System Design for Modular Tensegrity Robots

Tianyuan Wang

Doctor of Philosophy

University of York
Physics, Engineering and Technology

December 2023

Abstract

In complex scenarios such as planetary exploration and post-disaster rescue, environmental challenges and task diversity impose high demands for robustness and versatility on deployed robots. Tensegrity, as a unique paradigm that strikes a balance between rigid and soft structures, offers exceptional robustness. While its inherent compliance and flexibility equip tensegrity-based robots with advantages, the structural irregularity also presents challenges. Existing research on tensegrity robots has demonstrated their various capabilities but largely focuses on specific applications, missing the versatility needed for multifaceted scenarios.

This thesis introduces the Modular Tensegrity Robot (MoTeR) and its constituent module, the Symmetrical Tensegrity Mechanism (STeM). MoTeR achieves the scalability and reconfigurability of tensegrity robots through modularising a three degrees of rotational freedom tensegrity octahedron. The design of the STeM module starts from the principles of tensegrity structures and introduces the concept of underconstrained transition region, achieving a seamless integration with rigid structures. This offers improved agility and connectivity of tensegrity structures for robot actuation. Leveraging the features of STeM, MoTeR effectively imitates natural animal morphologies and the corresponding gaits, and features a dual-mode locomotion capability using wheels as complementation. Through employing the force closure principle and CPG models, this thesis implements both low-level and high-level control for the robot. Evaluations conducted across aspects including control, structure, and locomotion confirm that, while retaining the inherent compliance and flexibility of tensegrity, MoTeR realises agile, controllable structural deformation and demonstrates stable polymorphic locomotion capabilities.

The characteristics of MoTeR underscore the broad potential of highly modular tensegrity robots in adapting to different scenarios and diverse tasks. The design philosophy developed in this thesis should offer valuable insights for future research in modular tensegrity robots.

Table of Contents

List of Figures

List of Tables

List of Acronyms

ADMM	Alternating Direction Method of Multipliers
ANCF	Absolute Nodal Coordinate Formulation
CAD	Computer-Aided Design
CDPM	Cable-Driven Parallel Mechanism
CPG	Central Pattern Generator
DoF	Degree of Freedom
EDL	Entry, Descent and Landing
FCC	Force Closure Check
FC	Force Closure
FEA	Finite Element Analysis
FEM	Finite Element Method
GUI	Graphical User Interface
HAM	Hydraulic Artificial Muscle
HASEL	Hydraulically Amplified Self-Healing Electrostatic
IMU	Inertial Measurement Unit
ISO	International Organization for Standardization
ISR	Interrupt Service Routine

MKL	Intel Math Kernel Library Pardiso
MoTeR	Modular Tensegrity Robot
NSC	Non Smooth Contacts
PAM	Pneumatic Artificial Muscle
PCB	Printed Circuit Board
PID	Proportional-Integral-Derivative
PLA	Polylactic Acid
PRC	Physical Reservoir Computing
PWM	Pulse Width Modulation
RTOS	Real-Time Operating System
STeM	Symmetric Tensegrity Mechanism
TAM	Twisted Artificial Muscle
UART	Universal Asynchronous Receiver-Transmitter
USB	Universal Serial Bus
YAML	Yet Another Markup Language

List of Supplementary Materials

Supplementary videos, providing a visual representation of certain experiments conducted in this thesis, are included and listed as follows.

- Terrain_Adaptability.mp4, also available with the link to the video [131].
- Polymorphic_Locomotion.mp4, also available with the link to the video [132].

Acknowledgements

I would like to express my deepest gratitude to my supervisors Mark A. Post and Andy M. Tyrrell, for their continuous guidance, support, and patience. Their unwavering belief in my capabilities and insights into the subject matter have been instrumental in shaping this work.

I wish to extend my heartfelt thanks to my beloved wife. Her steadfast companionship during this particularly special time, her enduring understanding, and her support and encouragement when I needed it most have been invaluable. I also wish to express my profound gratitude to my revered parents. Their quiet sacrifices and dedication behind the scenes have empowered me to immerse myself wholeheartedly in my studies and work.

I would like to extend my sincere thanks to my friends: James, Junbo, Tian and Yunlong. Beyond their invaluable support during my PhD journey, they have been a consistent source of joy in my life.

Last but not least, I remain deeply grateful to all who contributed, either directly or indirectly, to this work, where your influence has been indispensable.

Declaration

I declare that this thesis is a presentation of original work and I am the sole author. This work has not previously been presented for a degree or other qualification at this University or elsewhere. All sources are acknowledged as references.

Parts of this thesis have been published in academic journals where I am the first author. In instances where these publications were co-authored with collaborators, I am solely responsible for the material presented in this thesis.

Journal Articles

T. Wang and M. A. Post, “A Symmetric Three Degree of Freedom Tensegrity Mechanism with Dual Operation Modes for Robot Actuation,” *Biomimetics*, vol. 6, no. 2, May 2021

T. Wang, M. A. Post, and A. M. Tyrrell, “Articulating Resilience: Adaptive Locomotion of Wheeled Tensegrity Robot,” *Electronics*, vol. 11, no. 4, p. 666, Feb. 2022.

Tianyuan Wang
December 2023

Chapter 1

Introduction

1.1 Background and Motivation

Robots have shown remarkable capabilities in diverse applications over recent decades [1]. These include, but are not limited to, industrial automation [2, 3], surgical assistance [4], rehabilitation [5], and agricultural monitoring [6], all aimed at facilitating people for a better living. With the expansion of application scenarios from a closed definite field to an open unknown space, the expectations for contemporary robot capabilities are progressively escalating [7, 8]. Among these, it remains a significant challenge for robots to be capable of reliably and effectively operating in unfamiliar environments, which are often unpredictable, complex, dynamic, and in certain cases, hazardous to the robots on site [9, 10].

In post-disaster rescue contexts, prior to the environment being deemed safe for human intervention, robots can be deployed to identify casualties or locate objects of significance. These scenarios present challenges for robots as the extensive damage would cause surroundings to be potentially unknown and unpredictable. Robots should exhibit a high degree of flexibility, adaptability, and resilience to navigate rugged terrains, travel through confined spaces, and survive from malfunctions [7].

During planetary exploration missions, the natural terrain, filled with sands, gravels, and rocks, can be particularly challenging for robotic equipment. These external elements can cause damage and lead to malfunctions. Moreover, as the scope of these missions becomes more complex, there's a growing need for robots to be versatile, capable of handling multiple tasks. It underscores the importance of designing robotic systems that are both durable against environmental threats and adaptive to varied mission objectives [11].

In environments where humans and robots are both present, the robots must demonstrate a high level of compliance and flexibility [12]. Such traits are crucial to ensure that robots can operate efficiently without posing risks, and can adapt to unpredictable human movements or behaviors, so that robots can work alongside humans in a safe and collaborative manner.

Given the challenges and requirements in these scenarios, it places a demand for robots that exhibit both distinct robustness and versatility [13].

1.2 Problem Statement

In addressing the robustness challenge, soft robots offer superior capabilities compared to the conventional rigid counterparts. Typically constructed from elastic materials such as polymers, rubber, and silicone for the main body and moving parts [14], these robots inherit unique characteristics that effectively address many of the challenges discussed above [15]. However, there are some common limitations holding back the practical applications of soft robots. The first drawback comes from their actuation schemes, where one popular approach involves fluidic sources, either pneumatic or hydraulic. These sources are relatively cumbersome and are normally as a separate stationary equipment that powers the robot externally [16]. This severely restricting the mobility of soft robots. Another limitation is their load-bearing capacity [14]. Although soft robots possess an outstanding resilience to environmental hazards, they are to some extent too "soft" for some regular tasks such as carrying heavier loads as they do not have rigid skeletons to stably support the body weight.

To address versatility in such contexts, modular robots stand out for their flexibility in functionality [17–19]. In contrast to monolithic robots, which are designed and manufactured in their final form for dedicated tasks and are therefore limited beyond the target application scenarios, modular robots comprise multiple units with either similar or unique functions. Such a design makes them inherently scalable and reconfigurable, overcoming the constraints of their monolithic counterparts [11]. With reasonable unit combinations, modular robots can readily adapt to various tasks and environments, broadening their application scope. However, while modular robots, traditionally rooted in rigid structures, have commenced a shift towards soft structures, research in this domain remains in the preliminary stage, constrained by challenges associated with materials, fabrication, actuation, and connection methods [13].

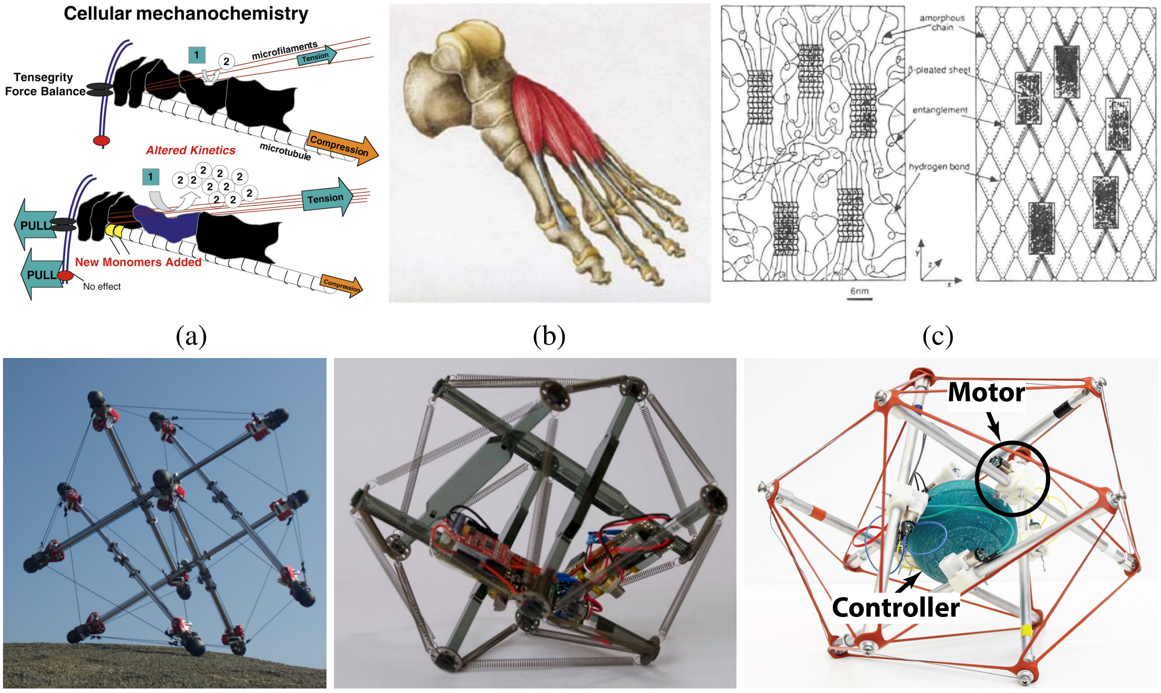

(a) (b) (c)

(d) (e) (f)

Figure 1.1 Tensegrity structures in the natural world and tensegrity robots. (**a**-**c**) Tensegrity structures in living cell, human body and spider silk, respectively [20–22]. (**d**-**f**) Robots based on tensegrity structures [23–25].

Tensegrity, although as a unique structure, is widely found in the natural world such as the living cell [26, 27], human body [21], and spider silk [21, 28, 29]. It is exclusively composed of discontinuous rigid elements in compression and a continuous network of elastic elements in tension [30], which are usually struts and threads, respectively. The elements of tensegrity irregularly expand in 3D space and are arranged in a sparse pattern that occupies a much greater volume than each individual element. The connectivity network of the elements establish a force equilibrium that the rigid elements are suspended in space without direct contact with each other through the constraints imposed by the tension elements. The coexistence of rigid and elastic elements makes tensegrity naturally compliant to external loads while retaining certain stiffness, that is, being soft and rigid at the same time, which mitigates the shortcomings of typical soft robots. In addition, tensegrity is inherently modular. Its constitute compression elements, serving as modules, can be connected in various topologies to configure the structure into corresponding shapes.

Tensegrity robots have been extensively investigated in emerging studies, especially for deployment in extreme environments, with an array of structural shapes being explored. However, while tensegrity structures are remarkable in structural efficiency, their motion efficiency tends to be lower. This leads to a commonly observed reduced mobility performance in tensegrity robots, prompting many studies to address this particular challenge. Furthermore, little research has been conducted with respect to the structural level modularity for tensegrity robots. Within this context, “modularity” is delineated as the incorporation of entire tensegrity structures as modules, diverging from the traditional approach of employing individual tensegrity elements. Such a modular approach augments the usability of robots, particularly when functioning as distinct modules. Existing studies toward this direction tends to chain modules of relatively simpler structures, each with a specific function, to attain complex capabilities [31]. This methodology, while promising, has its limitations: the practical use of these robots is hampered by the modules’ limited self-reconfiguration capabilities and versatility.

The main focus of this thesis revolves around designing modular tensegrity robots from a systemic perspective to augment their practical usability and versatility. Observing the aforementioned limitations inherent in tensegrity robots, it is clear that this endeavor goes beyond the modularisation in its lateral sense. It encompasses multiple facets such as structure, design, and control, implying an in-depth exploration into the essence of tensegrity. This thesis presents how these two aspects interconnect and mutually advance the characteristics of tensegrity robots, which is also a novel design philosophy formed in this study.

1.3 Thesis Contributions

This thesis offers meaningful advancements in the research of the design, control, and motion of modular tensegrity robots. The core contributions of this work are highlighted as follows.

1. This thesis proposes the design concept of the underconstrained transition region in Chapter 3, which optimises tensegrity structures for robotic applications. It introduces essential dexterity to tensegrity robots so that the deformation is in a more predictable and controllable way with expected motion freedom. It also simplifies the modularisation of tensegrity structures and the fusion with conventional rigid structures which broadens tensegrity structures’ potentials.

2. This thesis presents a paradigm design for tensegrity robots' modularisation with the Tensegrity Modular Robot (MoTeR) and its constituent module Symmetric Tensegrity Mechanism (STeM). The robot validates a high level of scalability and reconfigurability of tensegrity structures through the employment of rigid concatenations as introduced in Chapter 4. Discussed in Chapter 5, the module demonstrates the seamless integration of tensegrity and rigid structures while preserving the characteristics of the former, and distinct improvement in agility compared with typical tensegrity robots.
3. This thesis introduces the low level control of the STeM module and the high level control of the MoTeR in Chapter 5 and 6 respectively. Through employing the full actuation scheme and force closure principle, the fast and accurate control of the tensegrity structure's movement is realised. It is also presented the biomimetic gait generation of the MoTeR leveraging the distributed essence of the modules and Central Pattern Generator (CPG).
4. This thesis reveals the MoTeR's robustness in terms of its structural and locomotion characteristics. Its compliance and resilience to external loads are examined showing the robot's preservation of robustness in hazardous environments, as presented in Chapter 5. The adaptability to terrains with wheeled locomotion and the stability and polymorphism of biomimetic locomotion demonstrates the robot's robustness in navigating varied terrains, which are mainly discussed in Chapter 6.

1.4 Publications

The research presented in this thesis have led to several academic publications. Specifically, the findings have been foundational for the two journal articles, while the concepts developed were adapted for a conference paper. The relevant publications include [32–34] in the bibliography.

Journal Articles

- T. Wang and M. A. Post, "A Symmetric Three Degree of Freedom Tensegrity Mechanism with Dual Operation Modes for Robot Actuation," *Biomimetics*, vol. 6, no. 2, May 2021

- T. Wang, M. A. Post, and A. M. Tyrrell, “Articulating Resilience: Adaptive Locomotion of Wheeled Tensegrity Robot,” *Electronics*, vol. 11, no. 4, p. 666, Feb. 2022.

Conference Papers

- Y. Lian, T. Wang, J. Ingham, M. A. Post, and A. Tyrrell, “CPG-Based Locomotion Control of a Quadruped Robot with an Active Spine,” in *Towards Autonomous Robotic Systems*, Springer Nature Switzerland, 2023, pp. 177–189.

1.5 Thesis Outline

The remaining chapters of this thesis is arranged as follows:

Chapter 2 provides a comprehensive review of the application of tensegrity structures in robotics. Tensegrity, as a unique structure, its composition and structural characteristics are introduced first. Then existing tensegrity robot researches related to the scope of this thesis are critically analysed. Lastly, the design factors that affect the overall performance of tensegrity robots are discussed.

Chapter 3 proposes the concept of the underconstrained transition region. It is a type of specifically designed tensegrity structure that can be introduced into multi-unit tensegrity structures as intermediate stages to improves the original structures’ motion efficiency. The inspiration and principle of the underconstrained transition region is firstly discussed. Its potential configurations are then described.

Chapter 4 describes the STeM module which integrates a tensegrity structure with three degrees of rotational freedom and a modular robot framework. Firstly, the realisation approach of the STeM is introduced. Then, the physical implementation of the STeM including structure, mechanics, electronics, and software are detailed. Lastly, the construction of the simulation environment is presented.

Chapter 5 analyses the characteristics of the STeM from both structural and motion perspectives. The workspace and control strategy are firstly explained. Then, the STeM is evaluated with respect to the actuation such as accuracy and internal force distribution and structure such as resilience and fault tolerance, as well as the wheeled locomotion such as passive and active terrain adaptation as capabilities endowed by the design.

Chapter 6 presents the MoTeR built on top of the STeM modules, which imitates the morphologies and gaits of natural animals. Several example morphologies and the natural inspirations are firstly described, followed by the control approaches of corresponding gaits. The result reveals the broad potentials of STeM in robotic applications.

Chapter 7 summarises the previous chapters in relation with the proposed contributions to give a clear logic flow of the thesis and concludes the whole from a overall perspective. It also discusses the future work of this study, including focuses on the MoTeR itself, the tensegrity robots, and the potential application in broader fields.

Chapter 2

Literature Review

2.1 Introduction

Tensegrity robots are a relatively new category in the robotics field which have many exceptional advantages. This chapter reviews the current situation of tensegrity robots and generates critical analyses related to their development in three aspects from the structure itself, to existing studies, and to design factors.

Section 2.2 describes the fundamentals of tensegrity including the definition, classification and characterisation. Existing studies on tensegrity robots with regard to their structure, performance and limitations are analysed in Section 2.3. Section 2.4 discusses the design factors such as topology, control and tools for tensegrity robot development. This structure gives the basic principles first, then point out strengths and weaknesses of existing studies and finally analyse design essentials for a novel tensegrity robot addressing present issues. Chapter 2.5 gives a brief summary of the chapter.

2.2 Concept of Tensegrity

Unlike conventional structures that are fully rigid or soft, tensegrity structures expand in three dimensional space in an unusual and non intuitive way, arranging many repeating elements in equilibrium to form a whole, as mentioned in Section 1.2. A basic triangular tensegrity prism is illustrated in Figure 2.1.

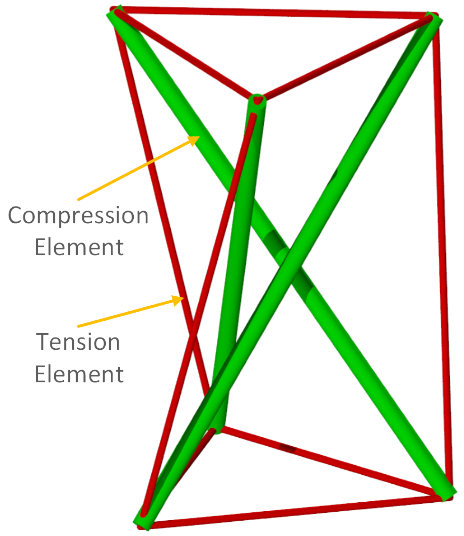

Figure 2.1 A basic tensegrity triangular prism structure. The green and red cylinders represent the compression and tension elements, respectively.

The structural principle of tensegrity to date is still ambiguous. In 1998, a more concise definition was proposed that "a tensegrity system is a stable connection of axially-loaded members" [35]. Another definition is given by Oxford English Dictionary as "A stable three-dimensional structure consisting of members under tension that are contiguous and members under compression that are not" [36]. These definitions have different constraints on minimum dimensions of the structure and the force situation of compression elements, which lead to the classification of tensegrity structures explained in Section 2.2.1. To summarise, a common characteristic of tensegrity structure is that the structure is composed of compression and tension elements. The compression elements are normally rigid making the structure expand and the tension elements are normally elastic making compression elements equilibrated in space.

2.2.1 Definition and classes of tensegrity

The classification of tensegrity remains unclear as a result of the ambiguity of its definition. While there is consensus regarding tension elements, confusion arises concerning compression elements. Specifically, the issues revolve around the types of connections between compression elements and their individual geometries. To bring clarity to the classification of tensegrity, this thesis proposes a definition that consolidates the commonalities of previous definitions:

“A tensegrity structure is a stable equilibrium consisting of continuous elements under tension and presence of discontinuous elements under compression.”

This definition allows compression elements to have various geometries in addition to straight struts, and direct contact between each other. The most critical point is that, from an overarching perspective of the structure, there must exist non-direct contact among compression elements. Only in this way can it be distinguished from conventional rigid structures, and retain the characteristics of tensegrity. Building on this definition and drawing from prior research, two primary classification criteria are given, which are typical/atypical tensegrity and Class k tensegrity.

Typical tensegrity - straight struts and threads

Typical tensegrity structures have a trait that their compression elements are normally straight struts, either directly connected to each other or not. Such configuration makes the most of the characteristics of tensegrity that there is no bending or shearing on the elements leading to a strong structure. However, when it comes to robotics, the form finding and control of typical tensegrity structures brings adverse effects since a small physical change, normally lengthening or shortening, on an individual element also distributes throughout the whole structure.

Atypical tensegrity - compression elements in higher dimension and threads

Contemporary research in tensegrity related to robotics has expanded to a broader field, that the compression elements feature various geometries in two or three dimensions such as the term biotensegrity explained in [37]. Such a classification is hereafter termed atypical tensegrity. Within a specific segment of the entire tensegrity structure, it spatially extends through the compression elements alone, rather than a composite of struts and threads. This leads to an improved agility and controllability since elements are more independent. It also simplifies the heuristic structure design process. Conversely, potential drawbacks include diminished structural strength and deployability, among others.

Class *k* tensegrity

The original criterion of the Class *k* tensegrity is given as “A Class *k* tensegrity structure is a stable equilibrium of axially loaded elements, with a maximum of k compressive members connected at the node(s)” [38]. In this definition, the classification is limited to typical tensegrity because of “axially loaded elements”. For the study herein, since atypical tensegrity is involved, the phrase “axially loaded” is substituted with only “compression” and it is then rewritten as follows.

“A Class *k* tensegrity structure is a stable equilibrium of compression elements, with a maximum of *k* compression elements connected at the node(s).”

With both classification criteria defined, Table 2.1 illustrates the relationship and combination of different classes of tensegrity. Among these configurations, typical tensegrity structures are commonly seen in both Class 1 and Class k ($k > 1$), while atypical tensegrity is rarely combined with Class k ($k > 1$).

Tensegrity classes	**Typical**	**Atypical**
Class 1	Typical Class 1	Atypical Class 1
Class *k* (*k* > 1)	Typical Class *k*	Atypical Class *k*

Table 2.1 Tensegrity classification based on two criteria.

2.2.2 Advantages of tensegrity

Tensegrity structures possess a range of unique advantages, as detailed in existing literature [38, 39]. Specifically, for the domain of robotics, these advantages include:

Stability: For most materials, a longitudinal element is more vulnerable under compression than under tension. When loaded, a compression element loses stiffness while a tensile one gains stiffness. Therefore, the tensegrity structure gains stiffness due to the use of more tension elements. Additionally, tensegrity structure elements are unusually but stably arranged since they are self-equilibrated in position by prestress. With such configuration, the structure also spans large areas with a moderate number of elements. This provides a high volume to weight ratio benefiting larger ground contact area, larger deformation room, less element collision probability and therefore further stability.

Efficiency: Given a stiffness condition, orthogonal architecture, such as beams, plates and columns in civil structures, does not lead to a minimal mass usage [40]. In practice, material is needed only in essential load paths and through this way it achieves higher efficiency than in orthogonal paths. A high ratio of use of longitudinal elements in an unusual pattern makes tensegrity structure more mass efficient as the load path of longitudinal elements aligns with the longitudinal axis. Meanwhile, the wide use of tension elements that leads to stability also contributes to efficiency since tension elements are inherently material efficient.

Deployability: The volume of tension elements of tensegrity structures is negligible so that the material volume is mostly donated by compression elements. The compression elements are either non-directly connected or connected with the ball joint. This makes large inter-elements displacements and deployment possible, which is advantageous for transport and operation that is volume sensitive.

Easy tunability: It is the same principle as deployment. A fine tuning could be achieved by making small displacements, or adjustments, to tensegrity structures.

Promoting integration of structure and control: The tension and compression elements of tensegrity structures can have alternative functions, not just as load-carrying materials. They could be easily integrated with sensors and actuators, or serve as insulators and electric wires. Thus it blurs the boundaries between structure, mechanics and control.

Biology motivated: Tensegrity is a building architecture favoured by nature. It exists not only in large scales like human bodies, but also in nanoscales like the molecular structure of the spider fiber [21]. Thus it becomes feasible for tensegrity structures to be as efficient as natural systems.

Reconfigurability: Tensegrity can get reconfigured with various patterns for different tasks. Tensegrity structures are repeating geometries like many biological and geometric structures thus are inherently modular. Therefore, they can be built, scaled and reconfigured all with the same elements conveniently. This reduced workload of designing and building modular robots.

Failure tolerance: Tensegrity structures are redundant and reliable. Tensegrity robots will not fail globally as conventional ones given failure of a single component. When local failure occurs in a tensegrity structure, it normally results in a change in morphology and degraded functionality, while the robot remains operational.

Simplicity of design: Two kinds of elements, struts and threads, either passive or active, can compose tensegrity robotics. All struts can share similar designs as well as threads and thus reduce the demand of dedicated designs. Tensegrity robotics can be driven by an active struts only or an active threads only strategy, which further simplified the design.

2.2.3 Form Finding of Tensegrity Structure

Tensegrity structures form complex geometries by arranging simple elements with various unusual patterns. This makes infinite shapes of tensegrity structures possible. Over the last few years, research into tensegrity robotics have been widely carried out in tensegrity sub-categories including form finding, static stability, dynamic and control. Among these, form finding, which discovers a tensegrity structure's potential shapes and defines the ceiling of its performance, is the foundation for tensegrity robots [41, 42]. It is composed of two steps of which the first is to determine the connections of elements, topology, and the second is to determine the spatial arrangement, geometry [43, 42].

Form finding for general tensegrity structures

Although the morphology finding is the second step, it was pointed out a that a majority of form finding methods assume a given topology for further analysis [44]. Tibert and Pellegrino classified the approaches of form finding into two main categories, which are kinematical methods and statical methods [45]. The kinematical methods share a characteristic that the lengths of either struts or threads are kept constant and adjust the others to optimal lengths. This is similar to the way of building tensegrity structures in practice. The characteristic of statical methods is that it sets up the relationship between equilibrium configurations of a structure with a given topology and force conditions at the first step and then analyses the relationship for new stable configurations.

Regarding the topology finding, the approaches are diverse. A method for searching connectivity patterns for arbitrary tensegrity structures using evolutionary algorithms was presented in [44]. Masic et al. introduced an approach to find the topology, geometry and pre-stress of a structure using nonlinear programming [46]. Rieffel et al. developed an evolutionary algorithm to produce large efficient and scalable irregular tensegrity structures in [43]. Ehara and Kanno employed mixed integer linear programming to maximise the number of struts and minimise the number of threads from a given ground structure, as well as minimise the strain energy for tensegrity structures [47, 48]. However, most of these pioneer studies focused on searching for large and static tensegrity structures, especially typical class, of arbitrary geometries, to expand in space or fill a given space. These, however, are not optimal for tensegrity applying in robotic applications.

Engineering oriented form finding

In terms of tensegrity for robotic applications, it usually explores potentials with simpler structures and ease of control. Form finding based on this often uses methods of heuristic guidelines and hierarchical design, such as biotensegrity and staged tensegrity [49]. The tensegrity structures reviewed by Carreño and Post are good examples of potential usage in robotics [42]. These include structures from as basic as triangular and quadrangular prism to truncated dodecahedron and spiral vertebral mast, as well as tetrahedral vertebral mast which is bio-inspired. These examples have some common characteristics such as symmetrical, recursive and bio-inspired. Tetrahedrons were employed by the Tetraspine robot developed in [50, 51] in a staged connection for the robot's crawling on the ground. Inspired by fish fins, Bliss et al. demonstrated a fishlike robot made up with a three cell, Class-2 tensegrity swimmer [52]. A tensegrity joint inspired by the human elbow was proposed in [53]. Böhm et al. presented several multi stable tensegrity structures using springs as elastic elements [54, 55]. The mixed integer linear programming presented in [56] modified by reserving restriction zones for payload is a potential approach for generating typical tensegrity structures suitable for robotic applications.

2.3 Review of Existing Tensegrity Robots

Robotics research utilising tensegrity structures serves various objectives, ranging from early studies focusing on the robustness, to endeavors aimed at enhancing the mobility through diverse approaches, and further to the improvement of the versatility. Centred around the core topic of modular tensegrity robots, this section offers an in-depth analysis of currently representative tensegrity robots, encapsulates their capabilities, and highlights some common challenges in existing cases that this research aims to address.

2.3.1 Pioneering Research Oriented Towards Robustness

As one of the key advantages of tensegrity, the distinct stability and structural efficiency enable tensegrity robots to have a high strength-to-weight ratio. By introducing flexibility into its elements, the robots could be more compliant interacting with the external environment, which leads to an improved robustness. Additionally, the failure tolerance further consolidates this characteristic. This is particularly notable for tensegrity icosahedron based robots that aggressively expand in space, among which the SUPERball series is an iconic paradigm [57, 23].

SUPERball series

As a part of a series of research on planetary exploration robots, a modular tensegrity robot called Reservoir Compliant Tensegrity Robot (ReCTeR) was presented in 2014 [58, 59], shown in Figure 2.2a. The robot uses 6 struts, 24 passive and 6 active spring-thread assemblies to form an icosahedron. By changing the length of the 6 active elements, it realises a flopping locomotion ability. The robot could also loosen its active threads to fold flat for easy transportation. ReCTeR demonstrated the locomotion and reconfiguration capabilities of tensegrity icosahedron robots and was soon evolved to a second generation called SUPERball shown in Figure 2.2b [60, 61, 57, 59, 62]. The new design removes the 6 active spring-thread assemblies of ReCTeR and makes 12 of the 24 originally passive assemblies actuated. The SUPERball exhibits an improved robustness as all external springs in line with the threads are moved inside the struts leaving only threads exposed to the environment. It also features an increased modularity that each strut, containing two independent autonomous units, is independently functional. According to the report to NASA Innovative Advanced Concepts (NIAC) program, the SUPERball is capable of locomotion along planned trajectories and over a variety terrains [63]. In terms of planetary exploration, it could withstand a maximum landing speed of 15 m/s with payload undamaged, and at the same time provide a high payload ratio by taking the job of both landing and exploration. In 2018, the SUPERball was further evolved to SUPERball v2 for stronger robustness during long term deployment [64]. It also employs a full actuation scheme which expands the robot's dynamic range to facilitate the large deformation required for packing and unpacking.

Although SUPERball series robots demonstrated steerable locomotion [23], its velocity and efficiency was not mention in the published literature. Upon analysing the supplementary video provided with the literature, it can be estimated that the robot's average velocity is approximately 7 cm/s. This velocity, when compared with its 1.95 m strut length, underscores that the mobility is not one of the primary strengths of this robot. This mobility limitation is a trait frequently observed in tensegrity robots with an icosahedron geometry.

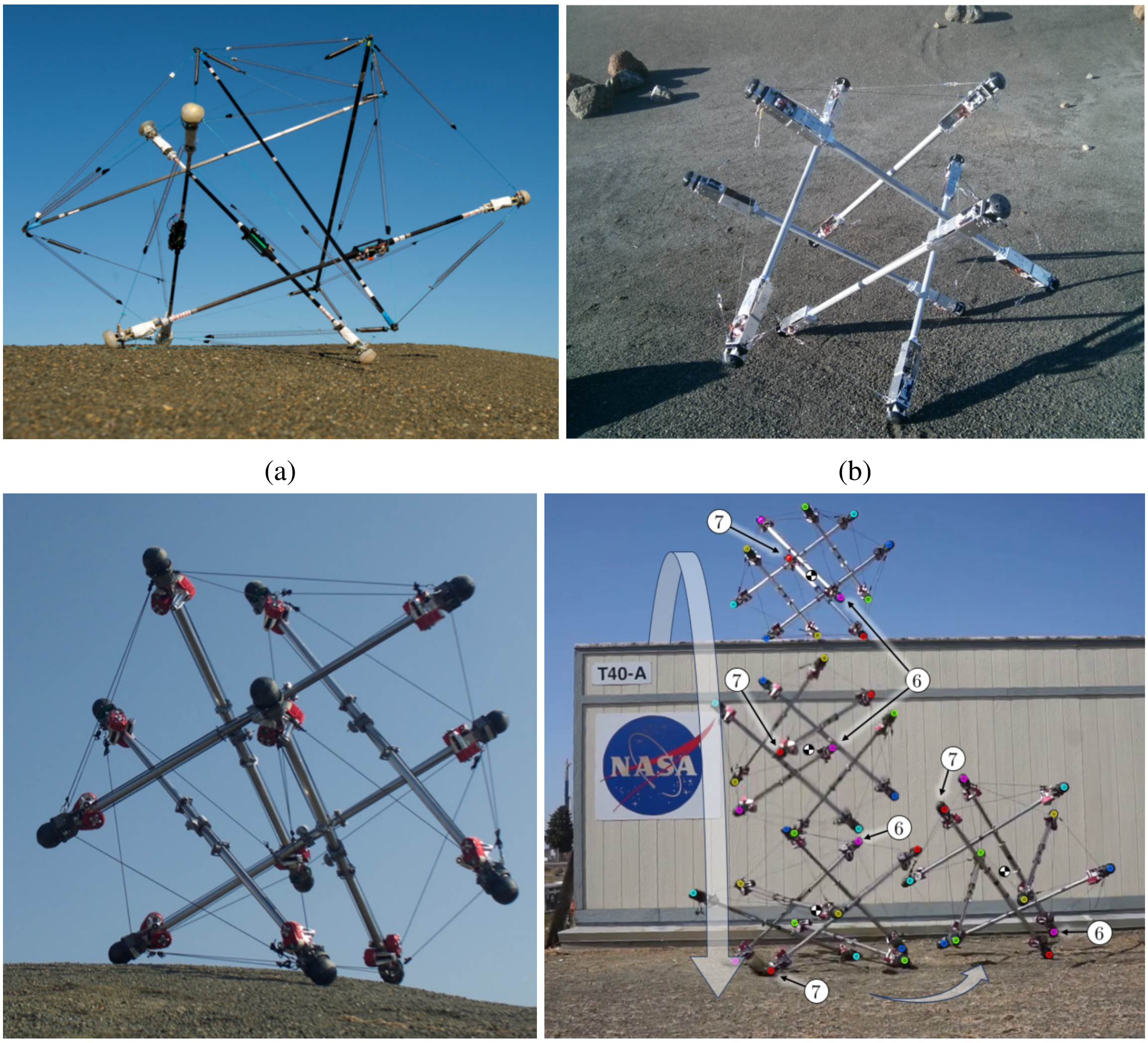

(a) (b)

(c) (d)

Figure 2.2 Robots developed in SUPERball series research. (**a-c**) The ReCTeR, SUPERball and SUPERball v2 robot, respectively[60, 57, 23]. (**d**) The SUPERball v2 robot drop test from 3.4 m rooftop.

Several factors contribute to this restricted speed. Firstly, the robot's trajectory in its intended locomotion direction is not a straight line but rather follows a zigzag pattern, introducing additional locomotive overhead. Secondly, the actuation of the elements within the robot are mutually constrained, which diminishes an efficient operation. Lastly, the robot's unique locomotion pattern requires complex algorithmic optimisation to ensure optimal efficiency.

2.3.2 Subsequent Research Focusing on Mobility

Since tensegrity robots are inherently outstanding in robustness, some research has shifted its focus towards enhancing the mobility. Tensegrity robots oriented for mobility are normally no longer limited to typical Class 1 tensegrity. In addition, these robots typically adopt a modular or segmental framework, with serial configurations being a prevalent choice.

Thin artificial muscle driven tensegrity robot

Built upon tensegrity icosahedrons as was SUPERball and TT-4mini, the soft tensegrity robot presented in [65] concatenates five icosahedron modules in series forming a typical Class 2 configuration, as shown in Figure 2.3a. It employs thin artificial muscles as the actuation source and adopts a special "4/3 muscle winding" which produces large contraction of the icosahedrons in two modes. The longitudinal contraction generates approximate 40% shrinkage in the axial direction and approximate 25% elongation in the radial direction. The lateral contraction generates approximate 25% elongation in the axial direction and approximate 20% shrinkage in the radial direction. Through driving the five modules' contraction in a specific sequential and alternate pattern, the robot realises a locomotion pattern like an earthworm and is capable of move between walls of width ranging from 150 mm to 240 mm with speeds of approximate 0.9 mm/s to 6.4 mm/s (strut length 130 mm), as illustrated in Figure 2.3b. As the connection between modules are soft, it can also passively adapt to the spatial shape of the environment such as tunnels, enabling effortless navigation 2.3c.

The thin artificial muscle driven robot exhibits distinct passive adaptation potentials in navigating complex terrain. However, the pneumatic source it relies on is provided externally. It can be observed from the photos of the robot that there is little space on the robot available to install extra instruments for actuation, which significantly limits the reachable workspace. Furthermore, the locomotion speed issue remains unsolved which could potentially affect task efficiency if applied in practice.

Tetraspine

The Tetraspine is another tensegrity robot based on a segmental arrangement but instead of straight struts, its compression elements adopt biotensegrity concept taking shapes of

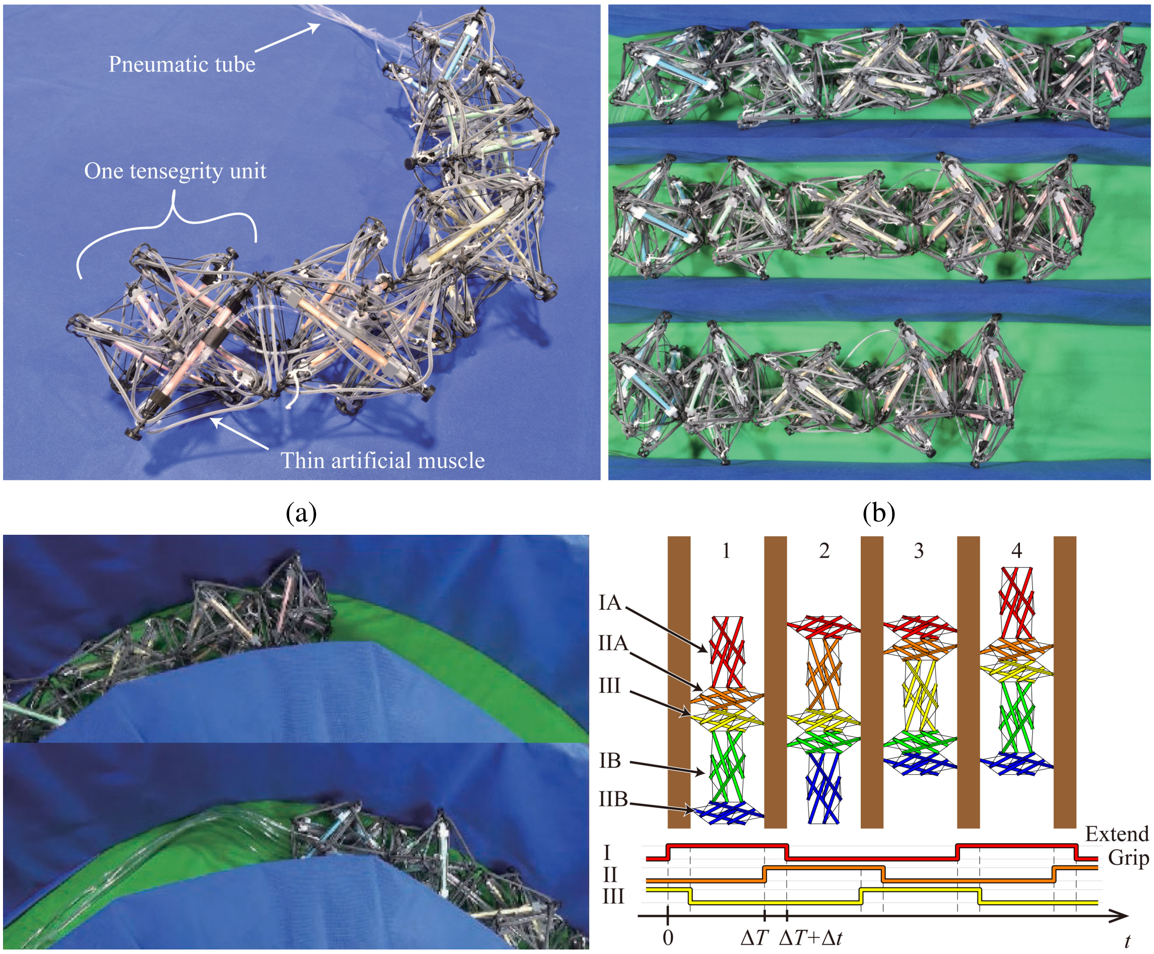

(a) (b)

(c) (d)

Figure 2.3 Soft tensegrity robot driven by thin artificial muscles. (**a**) The whole robot demonstration. (**b**) The robot travelling between walls of different width. (**c**) The robot adapting to curved path. (**d**) The driving principle of the robot. [65]

tetrahedron, tetrapod, and octahedron [50, 66, 67, 51], shown in Figure 2.4. Taking the tetrahedron model, of which the feasibility is validated with a physical implementation, as an example, the robot is cascaded that the tip vertex of one tetrahedron is held inside another tetrahedron adjacent to it. Each two segments are interconnected by six threads, three on the inside and three on the outside, all actuated. The outer threads one-to-one connect the outer vertices of the adjacent tetrahedron segments. The inner threads connect the tip vertex of one tetrahedron to the outer vertices of the other one. The outside threads pull two tetrahedrons closer while the inside threads pull them apart. Such arrangement gives three active degrees of freedom (DoF) between segments, which are axial translation, pitch and yaw, as well as passive compliance for the whole robot. The robot realises locomotion through a crawling gait on the ground generated with Central Pattern Generator (CPG). For each segment on the move, it will be lifted, pulled forward, and put down successively. The gait as a whole is similar to a rectilinear wave.

The simulation demonstrated the robot can climb over a wall 80% of the height of the segment. It can also crawl over different irregular terrains including slopes, bumpy surfaces, and randomly placed obstacles. Based on its compliance property, the robot could passively adapt to terrains and reduce the demand of sensors for accurate world knowledge modelling and operation decisions. In subsequent studies, the Tetraspine was updated to new morphologies by substituting tetrahedron segments with tetrapods [66, 67], where it uses eight threads between each two segments and achieves all six active degrees of freedom.

Through introducing tetrahedron compression elements to the system, the Tetraspine presents higher manoeuvrability as it can proactively adjust its direction of movement. In addition, the tetrahedrons allow simpler threads connectivity which reduces the complexity and improves efficiency of actuation. However, such a configuration also brings about adverse effects that thread damages, especially the outer threads, could cause significant degradation of the robot's structural integrity as there is less threads redundancy in the structure compared with tensegrity icosahedrons.

DuCTT

The aforementioned robots are all for general locomotion tasks. The DuCTT series is specifically designed for duct exploration and maintenance tasks [68, 69]. Similar to the Tetraspine but in a different arrangement, the DuCTT is composed of two nested tetrahedron frames interconnected by eight actuated threads and each tetrahedron also contains a linear actuator, as illustrated in Figure 2.5. This means the DuCTT employs a hybrid actuation scheme instead of threads-only approach. The principle for its climbing in the duct is similar to how an inchworm moves. The robot clamps the front tetrahedron within the duct and moves the rear tetrahedron forward. Then it clamps the rear tetrahedron and moves the front tetrahedron forward.

The robot overcomes three main challenges for duct travelling. First, since one of the horizontal strut in the tetrahedron is made of linear actuators, the robot could change its width to climb through ducts of different diameters. Second, the actuated thread network enables a 6-DoF motion. The tetrahedron could tilt with a large angle relatively to the other. This enables the robot to turn in sharp corners and duct T-junctions. Third, the robot's use of struts

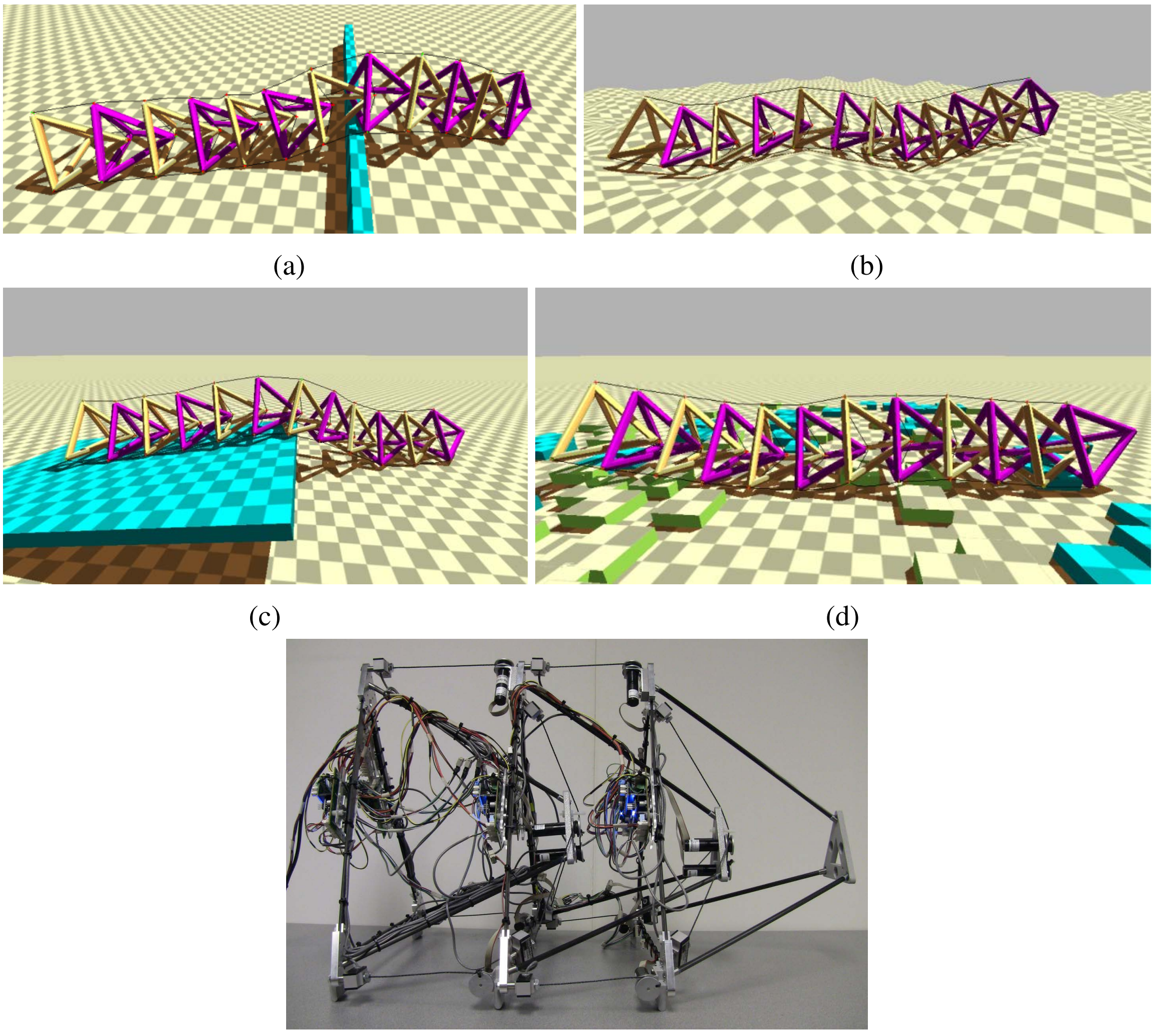

(a) (b)

(c) (d)

(e)

Figure 2.4 The Tetraspine robot (tetrahedron segment model). (**a**-**d**) The robot crawling on different terrains in simulation. (**e**) The prototype of the robot. [50, 66]

and threads results in a smaller cross-sectional area, thus minimally affecting the flow of substances in the duct. In addition, at the terminal end of each thread, a high stiffness spring is introduced to provide passive compliance for the system. Compared with conventional inchworm robots, this reduces the requirements on precise spatial positioning. The robot also features a symmetrical design that actuators act in parallel pairs which results in reduced power requirements and weight for each actuator.

The DuCTT robot demonstrates a high level of adaptability in duct travelling applications. It innovatively employs a method to precisely control a specially designed tensegrity structure. However, while this robot was tailored for a specific application, its design might not be

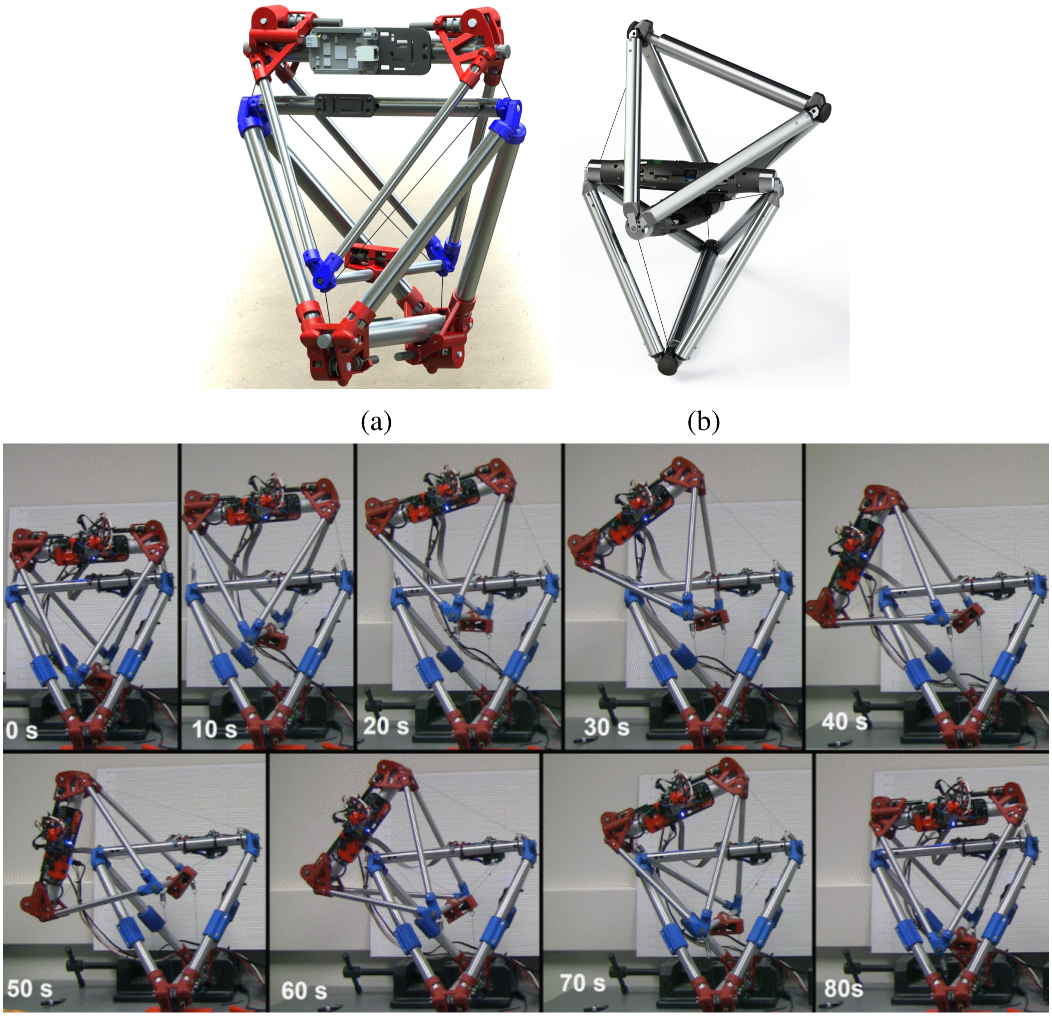

(a) (b)

(c)

Figure 2.5 The DuCTT robot series. (**a**, **b**) The DuCTT robot version 1 and 2, respectively. (**c**) The sequential images of the robot performing tilt movement. [68, 69]

directly transferable to broader contexts. Yet, it undeniably showcases the vast potential of unconventional tensegrity robots.

2.3.3 Diverse Locomotion Strategies

The deformation competence enables tensegrity robots to move solely on its structure without introducing extra moving parts. This is what most of tensegrity robots' locomotion relies on. Not limited to the flopping and crawling locomotion strategies presented in Subsection 2.3.1 and 2.3.2, other strategies, shown in Figure 2.6, have also been explored such as walk,

Robot	Locomotion Strategy	Maximum average velocity	Class	Framework	Platform	Morphology	Reference
SUPERball series	flopping	not given	typical C1	monolithic	practical	icosahedron	[57, 23]
Artificial muscle tensegrity robot	crawling	6.4 mm/s	typical C2	5 segments	practical	serial	[65]
Tetraspine	crawling	6.6 cm/s (30 cm edge length)	atypical C1	12 segments	simulation	serial	[50, 51]
DuCTT	two-anchor crawling	1.4 cm/s	atypical C1	2 segments	practical	serial	[68, 69]
TR-3	walking	45 cm/s	typical C1	monolithic	simulation	triangular prism	[70]
		1 cm/s			practical		
TR-4	walking	27 cm/s (1 actuator damaged)	typical C1	monolithic	simulation	quadrangular prism	[70]
		20 cm/s (2 actuators damaged)					
MoutainGoat	walking	13 cm/s	atypical C1	monolithic	simulation	quadruped	[71, 72]
TT-4mini	flopping	6.32 cm/s @ 0° slope 4.22 cm/s @ 10° slope	typical C1	monolithic	practical	icosahedron	[24]
Laika	walking	not given	atypical C2	5 segments	practical	quadruped	[73–75]
3-module soft robot	crawling	1.5 cm/s	typical C2	3 segments	practical	worm	[76]
Single actuated tensegrity structure	vibration	1.1 cm/s	atypical C1	monolithic	practical	tetrapod	[77, 78]
Vibration soft tensegrity robot	vibration	15 cm/s	typical C1	monolithic	practical	icosahedron	[79, 25, 80]
Random jumping exploration robot	jumping	not given	typical C1	monolithic	practical	spherical	[81]
Spherical curved robot	rolling	50 cm/s	atypical C1	monolithic	practical	spherical	[82–84]
Tensegrity swimmer	swimming	not given	typical C2	monolithic	practical	fish	[52]

Table 2.2 Comparison of tensegrity robot locomotion strategies.

vibration, rolling and jumping. A table summarising these locomotion strategies is shown in Table 2.2.

As observed from the table, tensegrity robots typically exhibit a modest locomotion speed, mostly hovering around or below 10 cm/s. This trend underscores the intrinsic challenges in achieving high locomotion efficiency with tensegrity structure, as an adverse effect of locomotion based on deformation of the structure.

The TR3 and TR4 robots employ the foundational tensegrity prism structure but exhibit an unconventional gait [70]. They achieve motion by lying on one side of the prism and alternating forward movement in the two bottom struts driven by threads. The locomotion pattern is categorised in the paper as walking due to the discrete ground contact of the struts. Although the movement in practice is slow, it offers notable benefits in terms of fault tolerance. The MountainGoat is another robot that employs a walking strategy, adopting a more traditional approach by imitating quadruped vertebrates [71, 72]. Various versions of the MountainGoat experimented with different configurations and control strategies, such as versions with and without feet, with short or long legs, and with either spine-only or leg-only actuation. The most optimal result is achieved with leg-only actuation. However, the study highlights the potential of combining spine and leg actuation for tensegrity robot locomotion, especially since spine-only actuation is demonstrated to be effective. The TT-4mini is a tensegrity icosahedron based robot similar to the SUPERball series. It incorporates six actuators responsible for the contraction and extension of threads [24]. Utilising a two-thread simultaneous control strategy, the robot can climb up to a 24° inclined surface and achieve a maximum average speed of 6.32 cm/s. Given its strut length of 25 cm, such a speed is rapid in the context of flopping tensegrity robots. The Laika robot presents a unique integration, introducing a traditional rotational actuator to its central tetrapod vertebra of the tensegrity spine in a quadrupedal configuration [73]. This design to a certain extent positions it within the category of atypical Class 2 tensegrity. The spine's design follows an under actuated approach. The bending is facilitated through the thread actuation, while twisting is managed by the rotational actuator [74, 75]. By integrating this actuated flexible spine, the quadruped robot demonstrates an enhanced ability to balance on obstacles without leg actuation. The 3-module soft robot presents a manipulation strategy similar to the thin artificial muscle driven tensegrity robot but with fewer segments. It utilises the "collapsibility" of the tensegrity icosahedron with a single servo motor in each module [76]. The servo motors contract and expand the icosahedrons sequentially to facilitate the robot's forward movement like peristalsis of earthworms.

While many studies focus on slow deformation such as flopping, crawling and walking approaches, the locomotion strategies of other research present interesting variations. For instance, the single-actuated tensegrity structure employs an electromagnet to induce specific-frequency vibrations in the robot [77, 78]. By adjusting these frequencies, the robot can alter its direction and speed of movement. Similarly, the vibration soft tensegrity robot utilises three vibrators arranged perpendicularly to each other to drive its motion [79]. Notably, this robot possess the capability to maintain fast and resilient movement, even when damaged. In a different approach, the random jumping exploration robot integrates additional mechanisms to generate thrust, enabling the robot to reach to specific heights along unpredictable trajectories [81]. The robot lacks landing gear but instead, it relies on the inherent compliance of the tensegrity icosahedron to absorb the impacts of landing.

Based on the velocity listed in the Table 2.2, the spherical curved robot claims the highest locomotion velocity among the presented tensegrity robots. Its design features two primary arc compression elements positioned opposite and orthogonal to each other. Together with an internal shifting mass, the robot achieves a seamless rolling motion along each arc, and employs a tip-over movement to alter its path. This robot underscores the heightened efficiency and speed of continuous rolling motion, a topic explored in greater depth in the subsequent discussion.

2.3.4 Integrating Rolling Locomotion

Although extensive studies have explored enhancing the mobility of tensegrity robots for diverse applications, it has been observed that locomotion velocity often remains constrained. The underlying reasons include the intricate dynamics of tensegrity structures, actuator limitations, and inefficiencies in adopted locomotion strategies. From the locomotion strategies discussed earlier, it is evident that the spherical robot, which employs two curved compression members, manages to achieve a relatively higher velocity by utilising continuous rolling locomotion. This movement paradigm, similar to wheel-based motion, effectively partitions one complete rotation into two distinct phases. Given these insights, in addition to looking into locomotion based on deformation of structures, adding rolling capabilities such as wheels to the tensegrity robots could be an approach to achieve a win-win performance, retaining the advantages of both tensegrity structures and rolling locomotion.

The locomotion speed of tensegrity robots based on wheels is primarily determined by the efficacy of its wheeled system. Additionally, wheeled locomotion is a mature technology,

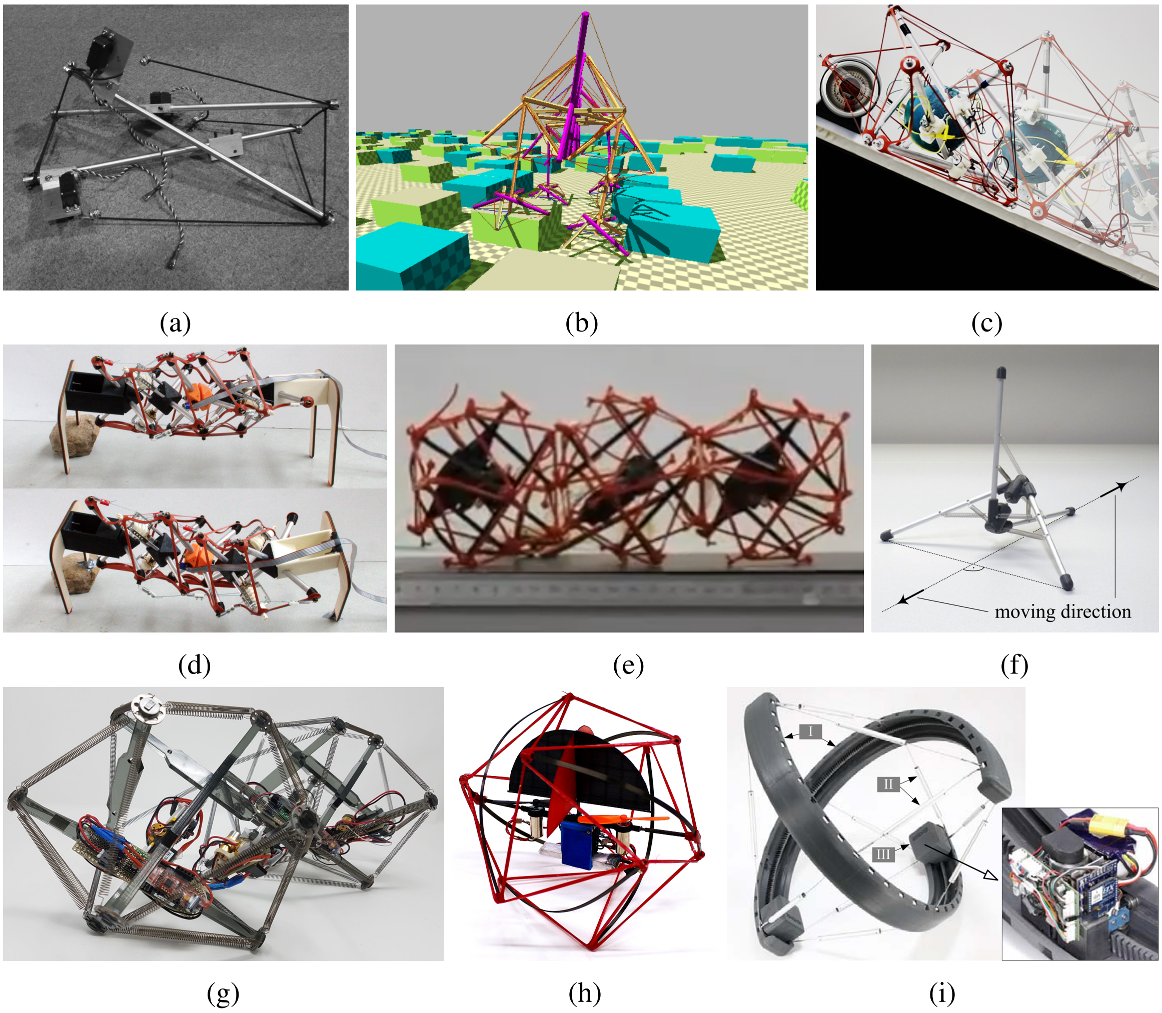

(a) (b) (c) (d) (e) (f) (g) (h) (i)

Figure 2.6 Tensegrity robots with diverse locomotion strategies. (**a-i**) The TR-3 [70], MountainGoat [71], TT-4mini [24], Laika [73], 3-module soft robot [76], single actuated tensegrity structure [77], vibration soft tensegrity robot [25], random jumping exploration robot [81], and spherical curved robot [84], respectively.

characterised by its predictability and ease of control. To date, only two wheeled tensegrity robots have been introduced to the research community the WTR [42] and the Tensegripede [85].

Wheeled Tensegrity Robot

The Wheeled Tensegrity Robot (WTR), shown in Figure 2.7, is specifically designed for traversing air ducts. It incorporates wheeled locomotion by integrating conventional rigid segments within its tensegrity framework [42]. The design comprises three wheeled rigid segments interconnected by two tensegrity spines, similar to the tetrapod model of Tetraspine. In this design, the tetrapod compression elements connect through eight threads. The rigid segments use springs to push the wheels against the air duct walls to generate traction, where the front and rear are motorised while the middle one is not. To connect the tensegrity and rigid components, the coupling terminal of the rigid segment replicates the shape of tetrapod and thus can be connected following a consistent pattern.

A distinct feature of the WTR is its enhanced speed within air ducts endowed by its wheeled design, increased from 1.2 cm/s to 70 cm/s. The robot has many passive degrees of freedom, enabling complex deformation including performing tight U-turns and navigating 90° duct branches. While the actuated turning was not implemented on the WTR prototype, a method for actively control the robot's heading using four additional actuated threads was demonstrated and validated through independent test findings.

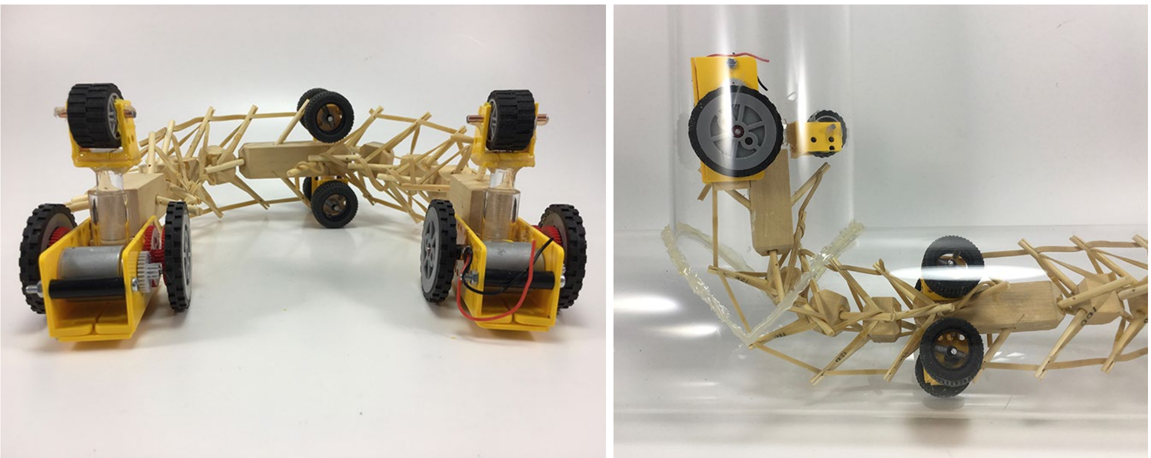

(a) (b)

Figure 2.7 The prototype of WTR. (**a**) The robot performing a U-turn. (**b**) The robot performing a 90° turn into a duct branch. [42]

Tensegripede

The robot presented in [85] is an intermediate prototype of Tensegripede, aiming ultimately to create a multipede robot with legged segments and tensegrity connections, shown in Figure 2.8. Nevertheless, this prototype showcased the potential of combining actuated tensegrity with wheeled locomotion.

The robot is composed of three conventional rigid segments, interconnected by actuated tensegrity structures. These structures feature a heuristic design having two anchoring bases, one with a strut attached, serving as the compression elements, and eight tension elements where four are passive springs and the remaining four are active threads. These springs are responsible for maintaining the stability of the strut's floating end, whereas the threads actuate the bases in two antagonistic pairs driven by two motors. Such a design facilitates active pitch and yaw movements while roll motion remains passive. The robot has the capability to navigate over obstacles that are 1.13 times the height of its wheel diameter. The design allows each segment to roll relatively to others within a certain range for adapting to irregular terrains. Additionally, the springs between segments can retain energy to reduce inter-segmental disruptions during external impacts.

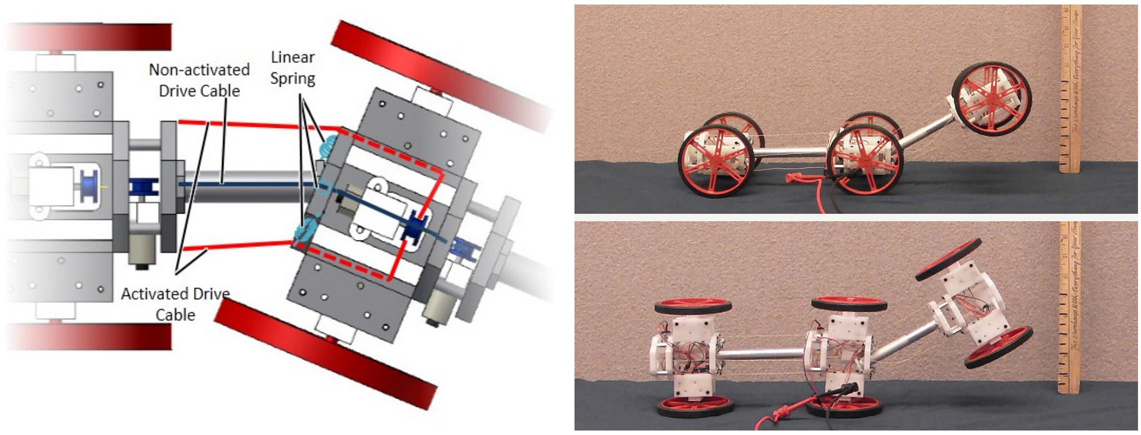

(a) (b)

Figure 2.8 The Tensegripede robot. (**a**) The configuration of its tensegrity structure. (**b**) The robot performing pitch and yaw motion. [85]

2.3.5 Improving Versatility

Compared to robots that rely on slow structural deformations for movement, both WTR and Tensegripede exhibit the potential of enhancing mobility through wheeled motion, indicating a new direction in a hybrid structural configuration. However, a commonality shared by these two and other robots discussed in this section is that they are tailored for specific applications or based on a general design. This considerably constrains the efficiency of tensegrity robots across diverse scenarios. There is limited research addressing the versatility issue of tensegrity robots. One reason for this scarcity is that, although tensegrity in its essence is modular and reconfigurable, the complexity of its elements' connectivity make it less adept at self-reconfiguration.

Thin Artificial Muscles Tensegrity Structure for Twist Manipulation

The tensegrity structure for twist manipulation driven by thin artificial muscles is a subsequent study of the robot presented in Subsection 2.3.2. In contrast to its predecessor, which only comprises the icosahedron contraction module, the new design incorporates torsion and grip modules which are also realised using tensegrity icosahedron [31], as shown in Figure 2.9. Its torsion module is capable of producing significant torsional deformations of up to $\pm 50^\circ$, with an associated height change as small as 10%. By connecting two torsion modules, one contraction module, and one grip module, the robot demonstrated the capability to unscrew plastic bottle caps, while also foreshadowing its potential to navigate through unknown confined spaces.

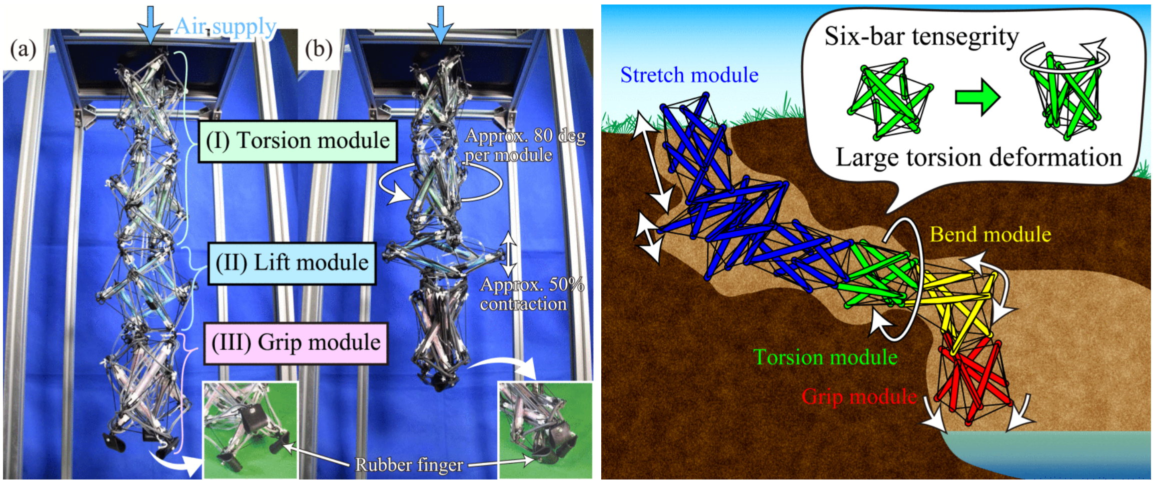

(a) (b)

Figure 2.9 The modular tensegrity robot driven by thin artificial muscles. (**a**) The robot unscrewing the plastic bottle cap in a naturally hanging posture. (**b**) The planned robot exploring unknown environment. [31]

However, given the soft nature of the inter-module connections, the robot only showcased operations in a naturally hanging posture. Not detailed in the literature, its passive adaptability in terrains is possibly only applicable for scenarios with continuous surfaces. Furthermore, its capacity for self-reconfiguration remains questionable, as individual modules lack inherent mobility. Nevertheless, the research does underscore the potential of tensegrity robot designs based on modules with distinct functionalities.

2.4 Review of design factors for tensegrity robots

Based on the analysis of existing tensegrity robot, two primary factors emerge as influential determinants of a tensegrity robot's general performance: mobility and versatility.

Mobility: Structural deformation-based locomotion strategies demonstrate adaptability across uneven terrains, whereas wheeled locomotion offers enhanced speed benefits. The efficiency of deformation, the degrees of freedom, and the operational workspace are primary considerations that influence deformation-based locomotion. When considering wheeled locomotion, the method of integrating tensegrity and traditional rigid structures becomes the primary concern.

Versatility: Present studies highlight the advantage of merging tensegrity structures with varied functionalities to achieve enhanced capabilities. Here, the challenge relates to efficiently and conveniently coupling and decoupling robot modules to realise scalability and reconfigurability.

Moreover, the control strategies for tensegrity structures play a pivotal role, especially in the context of deformation-based locomotion. For example, given the same tensegrity icosahedron framework, distinct control methodologies yield different locomotion speeds. This will also be discussed in this section.

2.4.1 Tensegrity Structure Optimised for Actuation Purposes

It is worth noting, when exploring factors that affect the mobility of tensegrity robots, research oriented towards actuation purposes, such as robot arms, offers insights from an alternative perspective. Compared to mobile tensegrity robot applications, these tensegrity based mechanisms typically adopt the atypical tensegrity and exhibit simpler topologies and geometries, facilitating easier modelling and manipulation. As a result, they often present advantageous agility in terms of motion efficiency, degrees of freedom, and operational workspace.

A bio-inspired tensegrity joint that emulates the human elbow is introduced in [86], Figure 2.10. This design employs three compression elements in non-direct contact to represent the humerus, olecranon, and a single complex of ulna and radius, with threads serving as muscles. Subsequently, the tensegrity elbow was combined with a tensegrity shoulder design to form a more complex tensegrity manipulator as illustrated in Figure 2.10c [87]. This assembly underscores the potential of utilising biotensegrity designs for simpler actuation strategies and larger workspace.

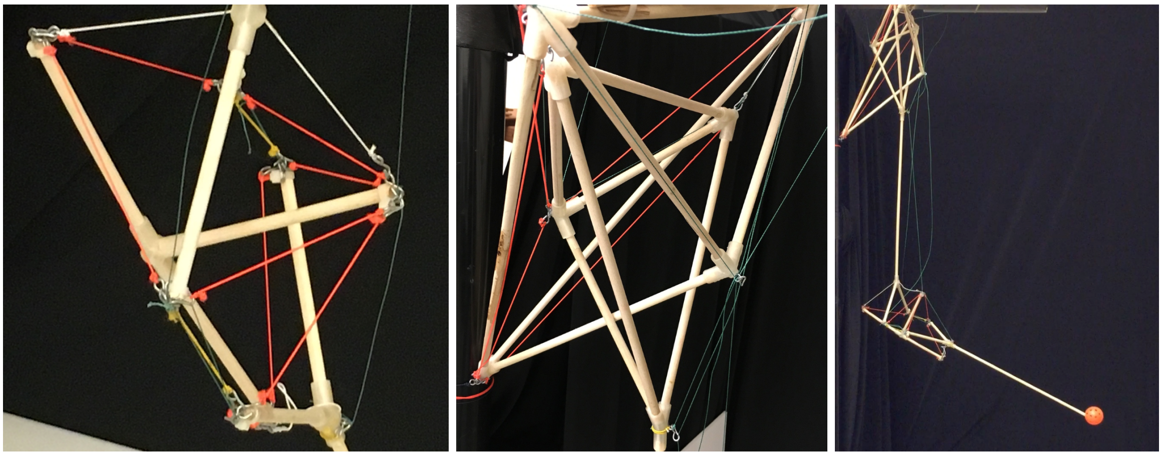

(a) (b) (c)

Figure 2.10 The tensegrity manipulator based on biotensegrity. (**a**-**c**) The elbow, shoulder and complete manipulator assembly, respectively. [87]

Another manipulator design achieves three degrees of rotational freedom in a single joint [88]. It introduces three passive threads to replicate the function of a spherical joint and six actuated threads to actuate the end effector of the manipulator, as shown in Figure 2.11. It employs a full actuation scheme so that the stiffness of the manipulator is adjustable. This design demonstrated how atypical tensegrity can be utilised to realise a rich and specific number of degrees of freedom.

Another robot designed for pipeline inspection demonstrates advantages in its operational workspace [89, 90]. Although the paper categorised the linkage, which provides compliance and actuation for the robot, as tensegrity, it doesn't strictly adhere to the definition of tensegrity. This is because all its compression elements are directly connected. The linkage consists of a universal joint serving as the compression element, complemented by three or four pairs of springs and threads acting as tension elements, as illustrated in Figure 2.12. However, viewing from a tensegrity perspective, if the universal joint could be replaced by a tensegrity structure as that for the 3-DoF tensegrity joint, this linkage design offers potential solution for a larger workspace and improved motion efficiency.


(a) (b)

Figure 2.11 The 3-DoF compliant tensegrity joint. (**a**) The prototype and geometric illustration of the joint. (**b**) The joint performing roll and pitch movement. [87]

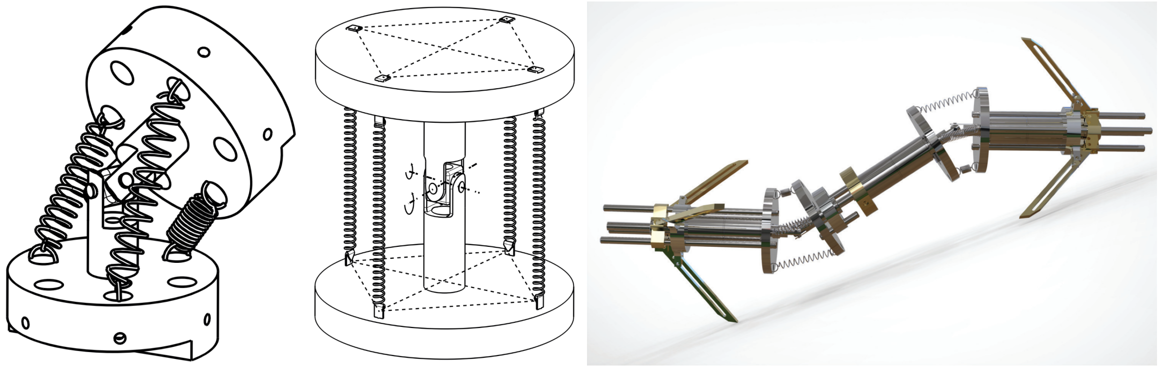
(a) (b) (c)

Figure 2.12 The pipe inspection robot based on tensegrity linkage. The threads run through the springs, which are not depicted in the figure. (**a**,**b**) The linkage with 3 and 4 spring-thread pairs, respectively. (**c**) The linkage applied to the robot. [89, 90]

2.4.2 Agility

Motion Efficiency

Motion efficiency is one of the direct factors affecting the mobility of tensegrity robots. While existing studies have explored various methods to enhance this characteristic, a comprehensive theory is yet to be formulated. A comparison between robots based on typical tensegrity and those on atypical tensegrity suggests a potential advantage for the latter.

Both structural design and actuation methods have a bearing on motion efficiency. Beginning with the actuation approach, fully-driven methods normally offer higher agility than under-driven ones. For instance, the SUPERball's actuation threads increased from 6 to 12 and then to 24, which led to improved locomotion controllability. However, the resultant rise in power consumption and dead weight, especially in the context of tensegrity structures with a greater number of threads and those relying on thread actuation, cannot be overlooked. This calls for targeted structure optimisation based on the required degrees of freedom and workspace, such employing antagonistic thread pairs and reducing detrimental constraints within the structure can be beneficial. The tensegrity elbow, for example, simulates the antagonistic muscle pairs providing motor actions of the human body.

Moreover, passive structural deformation is also one of the potential methods to enhance motion efficiency. For example, the thin artificial muscle driven tensegrity robot lack the capability to actively lift their bodies for obstacle traversing but can passively adapt to varying terrains. If a robot can exploit the compliance of tensegrity timely and appropriately, allowing itself to be "actuated" by the environment when active actuation isn't required, and engage active actuation when necessary, it can benefit from the best of both modes, thereby improving mobility.

Degrees of Freedom

As tensegrity is originally compliant with many degrees of freedom, the term degrees of freedom, hereafter, refers to the relative displacement between the compression elements in the structure without constraint, with minimal constraint, or with designated constraints exerted by the tension elements. Tensegrity structures with specifically designed degrees of freedom offer several benefits over those without.

When such a structure deforms within a designated degree of freedom, it usually will not impose unwanted movements in other deformable directions. This characteristic ensures more predictable and controllable motion. For example, the torsion module of the thin artificial muscle driven tensegrity robot without a designed degree of freedom, will cause an approximate 10% axial contraction when producing a 50° twist motion. In comparison, twist movements in the 3-DoF compliant tensegrity joint do not induce translational displacements among the compression elements.

With the introduction of degree of freedom designs, the structural elements usually have more specific functions. This, to a certain extent, simplifies the design and control challenges. For example, the 3-DoF compliant tensegrity joint uses three threads to replicate the spherical joint, the tensegrity elbow actuates each degree of freedom with an antagonistic thread pair, and the Tetraspine uses three threads to actuate its two rotational motion.

Moreover, such a structure exhibits more noticeable modularity, enabling larger workspace through cascading these motion freedoms. For example, when the tensegrity manipulator combines a 2-DoF elbow and a 2-DoF shoulder, its workspace no longer ends in a curved surface but spans a three-dimensional space.

When endowing tensegrity structures with specific degrees of freedom, there's often a greater emphasis on their rotational freedom. This is because it is easier to facilitate rotational displacement around nodes for the compression elements in the structure, while translational displacement demands coordinated actuation from multiple threads. For example, for the Tetraspine based on the tetrahedron model, axial translation between segments requires the involvement of six threads, whereas rotational motion, such as pitch, only needs actuation of three threads.

Workspace

In tensegrity robots, an expanded workspace typically implies a smaller turning radius and heightened capability to traverse obstacles. Even though precise workspace data are absent in some studies, the pipeline inspection robot's tensegrity linkage undeniably offers a larger workspace than the 3-DoF compliant tensegrity joint. This discrepancy is related to the different pivot point's positions in the structure across designs.

The study on the tensegrity linkage based pipeline inspection robot categorises these configurations as either pendulum or inverse pendulum setups. Within the pendulum configuration, one compression element's motion is constrained by other compression element, much like the restrictions seen in the Tetraspine's relative movement between its segments, aligning with the situation for the 3-DoF compliant tensegrity joint. Conversely, the inverse pendulum configuration allows for more extensive movement without collision, due to its pivot point situated between two compression elements. This design principle can be seen in the tensegrity elbow's interaction between the humerus and the radius-ulna assembly, as well as the movement between tetrapods in the WTR's tensegrity spine.

However, the realisation of the latter seems counterintuitive to the foundational principles of tensegrity. When two distant compression elements are solely connected by threads, especially for typical tensegrity, generating a separating force becomes a challenge. This might explain the incorporation of conventional universal joints in the tensegrity linkage design, while the tensegrity elbow realises the function of inverse pendulum through introducing an additional compression element and adopting a biotensegrity approach.

In addition, the workspace difference between passive and active operation should also be considered. For example, the tensegrity elbow has a passive pitch range of 215° while its normal actuated range is 36.33°. This indicates the tensegrity robot could realise greater passive displacements while actuated movement is not needed, providing improved flexibility.

2.4.3 Integration of Tensegrity and Conventional Structures

In terms of integrating tensegrity and conventional structure, a concept called transitional region was proposed as a part of the WTR's study. It refers to the coupling between the two types of structures. A properly designed transitional region could amplify the advantages of the tensegrity structure brought to the robot.

A hard transitional region means the transition is made exclusively of rigid elements. Commonly the connection end of the conventional member has a similar pattern of the tensegrity member. A soft transitional region leads to the one made exclusively of elastic elements. This connection needs its elements arranged in antagonistic configuration to attain equilibrium. For example, the WTR employs a hard solution. The struts on the wheeled segment have the same tetrapod pattern as the tensegrity mast. The Tensegripede prototype does not have an independent tensegrity structure between segments but since the compression elements are fixed to the segments, it also employs a hard transitional region.

The hard transitional region is more intuitive and structurally simple. The drawback is that rigid elements are fixed to the conventional parts resulting in potential bending and shear forces. In contrast, although the soft transitional region uses more complex antagonistic elastic elements, the integrity and robustness of the tensegrity structure could be well retained. In this case, the conventional part could serve as a mounting base to provide anchor points for elastic elements. In practical designs, a hard transitional region could give a general solution, but the soft transitional region should be preferred for improved performance.

2.4.4 Control for Tensegrity Structures

It has been summarised that tensegrity has an advantage of facilitation of high precision control [38], but the ease of controlling a tensegrity structure was not mentioned. Actually, the control of tensegrity structures, or dynamics, is non intuitive and complex, and is an ever-expanding research field.

As discussed in Subsection 2.2.2, it could be easy to integrate actuators into structural elements of tensegrity. But the force distribution property of tensegrity brings adverse effects to its controllability. Conventional mechanisms mostly move about independent axes or points while it is hard for tensegrity structures to act in this way. Any change on one element of the tensegrity structure would require essential changes of adjacent or even surrounding elements to retain equilibrium. This means a demand for more actuators so that the under actuation becomes a preferred approach in many tensegrity robots. The design trends of tensegrity structures could also reduce such complexity to some extent, through introducing antagonistic actuation pairs, simpler models, atypical compression elements.

Actuation Strategy

An important factor affecting the control complexity is whether the tensegrity structure is internally or externally actuated. The latter refers to adding extra elements for manipulation, where removal of these extra elements do not affect integrity of the original tensegrity structure.

Internal actuation: The internal actuation directly manipulates structural elements to realise deformation. This method could reserve the advantages of high precision control and fine tune of structure, especially with high stiffness materials. For instance, SUPERball, Tetraspine, DuCTT and Tensegripede all use internal actuation. However, it is relatively hard to model, and needs a number of actuators even when under actuated.

External actuation: The external actuation is employed by the ReCTeR, WTR, and 3-module soft robot. It employs extra elements, usually active threads, to pull structural nodes in a certain direction. It normally considers the tensegrity structure as a whole which has many degrees of freedom and leads to less demand for precise dynamics modelling. Thus it reduces complexity of control while providing reasonable performance. In addition, external actuation is inherently under actuated and uses fewer actuators yielding less power consumption. Such control strategy is suitable for scenarios requiring lower control accuracy, or when the topology is well designed.

Control Algorithms

In addition to optimising hardware design, the control algorithms are the key on the software side. The challenges include tensegrity's oscillatory nature, nonlinear coupling between elements, and overall complexity. To properly and efficiently control tensegrity structures, several algorithms have been explored by previous studies.

Coevolutionary control: The coevolutionary algorithm is an extension of the evolutionary algorithm that divides the search space into parts which can be conquered separately [91]. Coevolutionary algorithm could also be used for evolving various control functions through similar processes. The performance of cooperative coevolutionary algorithm, centralised evolutionary algorithm and hand-coded solution has been compared in controlling a tensegrity icosahedron [92]. The icosahedron is controlled by 24 active threads of which the lengths change according to a sinusoidal signal. As to the evolution process, the four parameters of the sinusoidal formula are evaluated and optimised based on the fitness function. The divide-and-conquer property of coevolutionary algorithms in this case not only speed up the search process but also fits the characteristic of tensegrity that the 24 controllers are not necessarily tightly coupled. The results reveal the evolutionary algorithm performs 400% better while the coevolutionary algorithm performs 800% better than a hand-coded solution.

Reactive Control: The reactive control is a traditional state recognition based algorithm and varies for different tensegrity structures. This algorithm has been employed to consecutively flop a icosahedron tensegrity [93]. The icosahedron stands still on the ground with three contact nodes at any time. The icosahedron is symmetrical so that only two types of contact triangles exist which are equilateral triangle, all three nodes connected, and isosceles triangle, two of the sides connected. Then actions, induced by contracting corresponding threads, are executed to make the robot flop over one of the five triangle sides. Based on the contact sensors' feedback, the robot could know which type of triangle it is standing on and flop in desired direction. The algorithm was also consolidated to smoothen discrete floppings for an improved rolling locomotion through coevolutionary algorithm presented above.

Central pattern generator (CPG): CPGs are inspired by neural circuits that can produce rhythmic activation patterns without sensory feedback or higher level control signals [94]. Control algorithms based on this technique are widely used for tensegrity robots of which the locomotion relies on rhythmic deformation of the structure. There are different methods to generate the oscillation for the CPGs.

The first is the phase oscillator based CPG. The Tetraspine uses a CPG arranged in three groups, each with 12 nodes, for the three lines of its outside threads [50]. Controlled by a phase bias parameter, the consecutive oscillators on each node in the line are shifted by $\frac{\pi}{2}$ so that each operation state of the segment could propagate from the spine's back to front. The top line nodes are also shifted by $\frac{\pi}{2}$ from bottom lines for a lift up and put down motion. Through this method, it realises a rectilinear wave-like crawling gait. The robot is immune to external perturbations and has a robust locomotion in irregular terrains.

The second is the Matsuoka oscillator based CPG employed as a part in the study to control a tensegrity icosahedron through physical reservoir computing (PRC) [95]. The CPG nodes are arranged according to the stress matrix of the structure with self feedback removed. The parameters of the CPG are generated randomly at the beginning. The output of CPG nodes are then adjusted with a constant offset and random gains. After that the results are used for directly controlling rest length of active threads. Since the optimal gait is unknown, the parameters are manually tuned through calculating normalised mean squared error for a target trajectory and screening the best ones. And eventually a slow crawling motion is achieved.

The reciprocal inhibition oscillator (RIO) based CPG was implemented with sensory feedback to control a three-stage Class-2 tensegrity structure [96]. The structure is only actuated on its base stage where two threads, actually steel wire and extension spring assemblies, lengthen and shorten antagonistically. Thus it is a 2-node CPG network. Nodes inhibit each other internally and get excited externally by the length change of actuated threads. Each node's nonlinearity is generated by a hyperbolic tangent function. Based on the RIO with sensory feedback, the system shows an improved robustness and efficiency than open-loop sinusoidal control since it exploits resonance of the structure and compensates the energy loss caused by damping.

Physical reservoir computing (PRC): The PRC was employed to control a tensegrity icosahedron [95] with a well tuned Matsuoka oscillator CPG used as a model for training. The tension sensor readings are used as feedback for online learning of the PRC. The PRC is trained to imitate the CPG control signals and along the learning process, the ratio of CPG is gradually decreased until PRC can generate reasonable control signals independently. With feedback introduced to the system, a trained PRC could control the tensegrity icosahedron robustly that it stops during and recovers after the lifting and constraining perturbations.

Among the algorithms presented above, the CPG and neural network are two of the more popular approaches, as well as a combination of the two. Compared with traditional control algorithms, these two approaches remove the need for precise dynamic modelling and require less sensory feedback. With sensory feedback, the CPG mitigates the actuation imperfections. The utilisation of neural networks allows the robot to evolve themselves to adapt to new and complex morphologies, which is beneficial for tensegrity robots with modularity.

2.4.5 Simulation for Tensegrity Robots

As the development of tensegrity robots could involve continuous modifications, minor adjustments and repeating experiments, it is beneficial to simulate the robot before hardware implementation for better parametric design process and ease of validation and evaluation. Existing simulation platforms are mostly developed for rigid body or specific purposes and are not good at solving elastic and close-loop structures, especially flexible multi-body problems. Studies to date have explored several simulation platforms. While each has its specific features, they all share certain limitations as outlined in the following sub-sections.

NASA Tensegrity Robotics Toolkit (NTRT)

NTRT is a simulator developed specifically for tensegrity, running on top of the Bullet Physics Engine [63] which is extended with more efficient models to simulate ropes and cables. It enables the convenient creation of robots consisting of only struts and threads using Yet Another Markup Language (YAML) descriptors. NTRT includes built-in libraries such as CPG and machine learning frameworks for controllers, allowing for sophisticated control strategies. It also supports customisation of terrains and obstacles, providing a versatile environment for testing. Notably, the simulator has demonstrated high accuracy, with less than 1% error in simulations of passive and semi-static controlled active tensegrity robots [63].

However, its focus on tensegrity structures means it falls short in simulating conventional mechanisms, limiting its broader applicability in the tensegrity-conventional hybrid robotics scenarios. These limitations manifest in several ways. Firstly, there is a lack of support for objects with irregular geometries, which are common in conventional robotic designs. Secondly, the types of constraints that can be applied to joints or between different objects are limited. Finally, its capabilities for handling interactions with external inputs are not extensive, which might impede simulations that require dynamic interaction with user inputs.

Open Dynamics Engine (ODE)

ODE is an open source library for simulating rigid body dynamics [97], widely used in robotics, game development and physical simulations. It excels in handling complex linkages between objects, offering advanced joint types such as hinges, sliders, and ball-and-socket joints. These features enable the creation of complex articulated systems in simulation. ODE has a robust integrated collision detection system completed with friction modelling. This is useful for realistic and high performance simulation of interactions between objects.

However, ODE has its limitations, particularly in simulating flexible materials such as threads and ropes. To address this, studies normally employ linear force pairs as a workaround, creating virtual threads that are massless, volumeless, and without collision detection [98, 70, 99]. By adjusting the rest length of these linear force pairs, it is possible to simulate the actuation of threads. Such an approximation allows for basic simulation of tension in threads where the exact dynamics are not critical. Additionally, due to the virtual nature of the threads, the absence of collision detection cannot faithfully reflect potential thread-to-object contact issues that could occur during motion.

Adams

Adams is a robust and comprehensive software system for multi-body dynamics simulation [100], renowned for its ability to facilitate cross discipline interaction and evaluation. These include motion, structure, actuation, and control, offering a versatile framework for various engineering and research applications. Its functionality is further enhanced by additional modules, such as flexible body dynamics, which allows the simulation of objects such as tires, durability, essential for long-term performance analysis, and vibration, critical for understanding the response of systems to oscillatory stimuli.

Several studies on static and dynamic analysis of tensegrity structures using the Adams platform have been presented [101–103]. However, these studies employed passive spring objects, which are large in volume, and prismatic actuators for active motion. This approach represents another approximation of threads, in addition to the force pairs representations in the ODE, which can potentially affect the precision and efficiency of simulations, especially those requiring intricate thread interactions. This reliance on substitutive components such as passive springs and prismatic actuators can sometimes limit the scope of simulations, making them less suitable for scenarios that demand highly detailed or dynamic analysis.

CoppeliaSim

CoppeliaSim stands out as a versatile simulator with an integrated development environment [104], primarily used for algorithm verification and development. Its distributed control architecture allows an effortless coordination of internal components and seamless integration with external programs. It supports rigid body simulation based on different physics simulation engines and uses an intuitive hierarchical structure for scenario construction.

However, CoppeliaSim's application in simulating tensegrity structures remains unexplored. Its focus on algorithm development might, to some extent, diminish its usability in physical simulations, which is an essential capability for tensegrity simulation. Additionally, similar to the ODE and Adams, its support for simulating rope-like flexible body objects is limited, although it could be a potential option for verifying high-level motion planning of tensegrity robots.

Project Chrono

Project Chrono is an advanced simulation platform encompassing a diverse array of multidisciplinary modules [105]. Its core is a multi-body and Finite Element Analysis (FEA) library, which serves as the foundation for its extensive simulation capabilities. This core can be augmented with additional functionalities, including fluid dynamics, vehicle simulations, parallel computing, and granular dynamics, allowing for a wide range of applications in different fields.

It provides native support for thread elements and conventional rigid bodies at the same time, making it a particularly promising platform in the simulation of tensegrity structures. In addition, it offers different constraints to simulate a variety of joint types which is indispensable for hybrid systems such as wheeled tensegrity robot. Although it does not provide a graphical user interface (GUI) which may slow down the construction process of simulation scenarios, it is competitive among aforementioned platforms.

Given the different features offered by these platforms and the specific demands in this thesis, Project Chrono was selected to construct the simulation environment. This decision was primarily driven by its capability to simultaneously simulate rigid structure collisions, soft structures, rigid-soft structure linkages, as well as its support for conventional mechanisms and constraints. These features address this thesis's requirements, especially for experiments involving a rigid robot as control group and the wheeled locomotion.

2.5 Summary

Tensegrity, characterised by its unique structural approach, has exhibited remarkable potential in the field of robotics. Notable studies including the SUPERball, Thin artificial muscle driven tensegrity robot, Tetraspine, DuCTT, and WTR have undertaken extensive exploration into attributes such as robustness, adaptability to uneven terrains, and capability to overcome obstacles. However, despite significant efforts to enhance the mobility of current tensegrity robots, their commonly employed movement based on structural deformation still presents limitations in terms of efficiency and performance. Furthermore, research oriented towards versatility is still in its early stages.

This chapter, after analysing common issues in existing robots, outlines several pivotal design factors that influence the overall performance of tensegrity robots, which encompass agility, structure integration, and control strategies. For tensegrity robots that move based on the deformation of the structure, the agility directly influences whether it can perform a fast, efficient, controllable, and large deformation to achieve a high mobility. Recognising the inherent agility issues of the common tensegrity robots, Chapter 3 introduces the underconstrained transition region concept, which offers changes to the underlying topology design to overcome these limitations. Existing research has highlighted challenges in the modularisation of tensegrity robots. Either making direct connections between tensegrity structures or using rigid structures as the intermediate stage presents their own sets of difficulties. In response, Chapter 4 employs the atypical tensegrity design in conjunction with the underconstrained transition region to achieve a seamless integration with rigid structures. The varied mobility performances exhibited by tensegrity robots of the same structure underscore the pivotal role of control strategies. Given the unique structure design and the modularity, Chapters 4 and 5 delve into both low-level and high-level control for the proposed robot to realise a polymorphic locomotion capability.

Chapter 3

Concept of Underconstrained Transition Region

3.1 Introduction

In Chapter 2, a comprehensive review of existing tensegrity robots was conducted, revealing key design factors encompassing agility, structure integration, and control strategies. Concerning agility, this chapter explains how motion efficiency, degrees of freedom, and workspace are closely interconnected and affect each other, as well as the pivotal role of degrees of freedom among them. Based on this, the concept of underconstrained transition regions is proposed, demonstrating the theory of introducing designated degrees of freedom to tensegrity structures for enhancing agility and facilitating modularity in robotic applications.

The effect, cause and solution of the agility issue are presented in Section 3.2 to 3.4. Example structures with one, two and three degrees of rotational freedom are demonstrated in Section 3.5, 3.6 and 3.7, respectively. The work is summarised in Section 3.8.

3.2 Problem of Agility in Robotic Applications

The inherent structural configuration of tensegrity offers high mass efficiency, allowing it to be lightweight while possessing considerable strength and stability. The complex connectivity of its elements significantly limits the relative displacement of each individual element within the structure. However, in robotic applications, it relies on the movement of parts to generate output to the real world (the robot). Such a situation presents a contradiction that tensegrity structures are expected to deform to facilitate robots' movement while they inherently tend to maintain their original geometry. For example, when driving a deformation of the structure by shortening the length of a certain element, the applied load distributes across the entire or a large region of the structure, as if the structure "fights" against the load, resulting in a decrease in agility and a higher requirement in actuator output power.

Employing the full actuation scheme in tensegrity structures offers a straightforward solution to accommodate the load distribution but the large number of elements, especially for more sophisticated structures, makes such an approach complicated and puts a barrier to practical implementations in robot actuation and locomotion scenarios. Although many existing tensegrity robots employ an under-actuated scheme, the fundamental issue remains unsolved.

3.3 Connection of Multi-Unit Tensegrity

Focused on the root cause of the agility issue, approaches such as multi-unit tensegrity is introduced, such as the thin artificial muscle driven tensegrity structure [65, 31] and the Tetraspine [50, 66] discussed in Section 2.3. In these cases, multiple tensegrity units, normally in a repeated pattern, are stacked and interconnected to form a larger scale structure. The deformation within each unit is to some extent isolated from one to another, which mitigates the effect of load distribution by confining the propagation in a smaller region. However, to maintain the structural integrity and stability, the connection between units still exerts complete constraints to the elements it covers, either when the structure is driven internally, where the actuation is applied on each unit, or externally, where the actuation is applied on the structure as a whole.

Therefore, the power requirement for the actuators is reduced but the agility such as the motion range and motion speed is not significantly improved to an expected level. The problem converges to the optimisation of interconnections between units in multi-unit tensegrity robots.

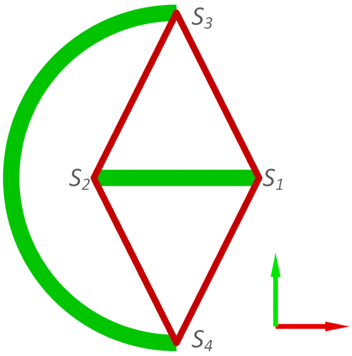

Figure 3.1 The C-Strut tensegrity structure consisting of two compression and four tension elements.

3.4 Inspiration from C-Strut Tensegrity

For all the figures in this chapter, the following conventions are used: the struts are represented by thick green and magenta cylinders, the threads are represented by thin red, yellow and cyan cylinders, the coordinate axes are indicated by the red, green and blue arrows for x, y and z respectively, and the available degrees of freedom are depicted by the rotation arrows on the axes indicators.

Figure 3.1 presents a configuration of the minimal tensegrity structures, the C-Strut, which is simply composed of a C-shaped strut and a straight strut. Considering it as a two-dimensional structure and assuming the C-shaped strut is fixed, the straight strut is stably constrained in both x and y axes with the tension of threads S_1-S_3-S_2-S_4-S_1. However, when positioned in a three-dimensional space, there are two degrees of freedom (DoF) available, which are the rotation about the axis passing through nodes S_1 and S_2, and the rotation about the axis passing through nodes S_3 and S_4, vice versa for the C-shaped strut. As discussed in Section 2.4, the term degrees of freedom denotes the relative displacement between the compression elements in the structure without constraint, with minimal constraint, or with designated constraints exerted by the tension elements.

These motion freedoms arise because there are only two nodes imposing constraints to the strut-thread assembly represented by S_1-S_2 and S_1-S_3-S_2-S_4-S_1, whereas in a completely constrained tensegrity structure, strut-thread assemblies are typically connected to three or more nodes, as that illustrated in Figure 3.2. The magenta strut and yellow threads in the assembly share a similar pattern as the C-Strut configuration and are constrained at nodes M_2

and N_3. But the additional constraints exerted by the cyan threads on nodes M_1 and N_1 limit the rotation movement about the axis passing through nodes M_2 and N_3.

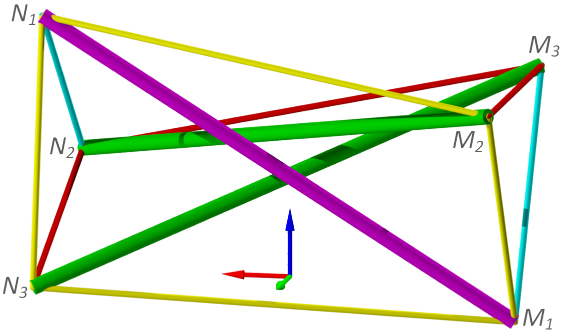

Figure 3.2 A stably constrained strut-thread assembly inside a tensegrity triangular prism. The assembly is represented by the magenta strut and the yellow and cyan threads.

Given the degrees of freedom, the C-Strut tensegrity structure, as well as its mutant, is ideal for the intermediate stage of two connected tensegrity units to introduce additional agility to the structure. Such configurations are hereafter named as the underconstrained transition region. The transition region only provides rotational freedom about the axes passing through node pairs where the translational displacement is consistently restrained. The structural integrity is thus reserved with respect to the motion out of the scope of the designated motion freedom. To drive the available DoFs, either internal actuation, where it applies on the transition region, or external actuation, where it applies in between tensegrity units can be employed. In practical implementations, the C-shaped strut and the straight strut can be replaced with other tensegrity structures that provide two nodes as the anchor points, such as the structure shown in Figure 3.3. The C-shaped and straight struts are replaced with two tensegrity icosahedrons of different sizes.

It is worth noting that in the C-Strut structure, the component composed of the straight strut and threads bears a certain resemblance to the D-Bar and T-Bar, particularly the D-Bar, presented in [21, 106]. According to definition in [21], they are “dual” to each other. Contrary to the composition of the component in the C-Strut, which consists of four threads and one strut, the outer elements of the D-Bar are replaced by four struts connected by spherical joints, while the central element is replaced by a thread. As a result, the D-Bar, in response to the direction of tension imposed from the C-shaped strut in the corresponding C-Strut, is supposed to bear compressive forces. This means that if the D-Bar concept is similarly extended and applied in transition for structures, it could also provide degrees of freedom for rotation around the central element under compression applied by the transited structures. However, for tensegrity structures, the pretensioned nature means that such transplantation is highly impractical. Moreover, due to the presence of the spherical joints, the two-dimensional D-Bar lacks stability in three-dimensional space. Even if a three-dimensional D-Bar is applied in transiting traditional structures that exert compressive forces, the benefits are significantly reduced due to the need for additional joints to allow rotation between the rigid elements in contact. Nevertheless, although the D-Bar and C-Strut serve completely different purposes, where the former focuses on structural engineering to optimise the mass of structures and the latter is applied in robotics to improve the agility of tensegrity structures, their similarity suggests the immense potential hidden in tensegrity structures with similar geometric configurations.

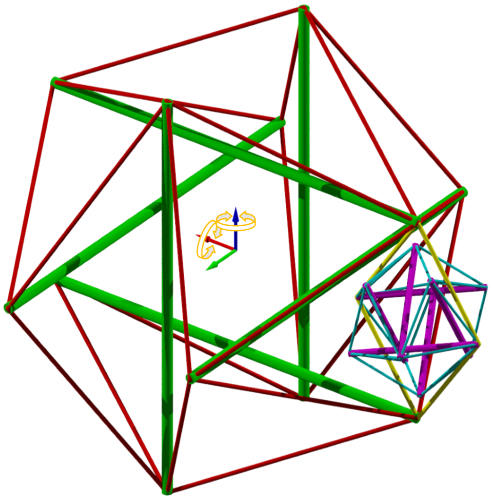

Figure 3.3 An example mutant of the C-Strut tensegrity. The nodes on the original C-shaped strut are replaced by the two closest nodes on the larger icosahedron, represented by the green and red elements. The nodes on the original straight strut are replaced by the two farthest nodes on the smaller icosahedron, represented by the magenta and cyan elements. The threads in the original C-Strut remain the same arrangement represented by the yellow elements.

3.5 One Degree of Rotational Freedom

To realise one rotational DoF between two connected tensegrity structures, one implementation is to have the two structures rotate about their longitudinal direction. An illustrative configuration is shown in Figure 3.4 which takes tensegrity triangular prism as the example structure being transitioned.

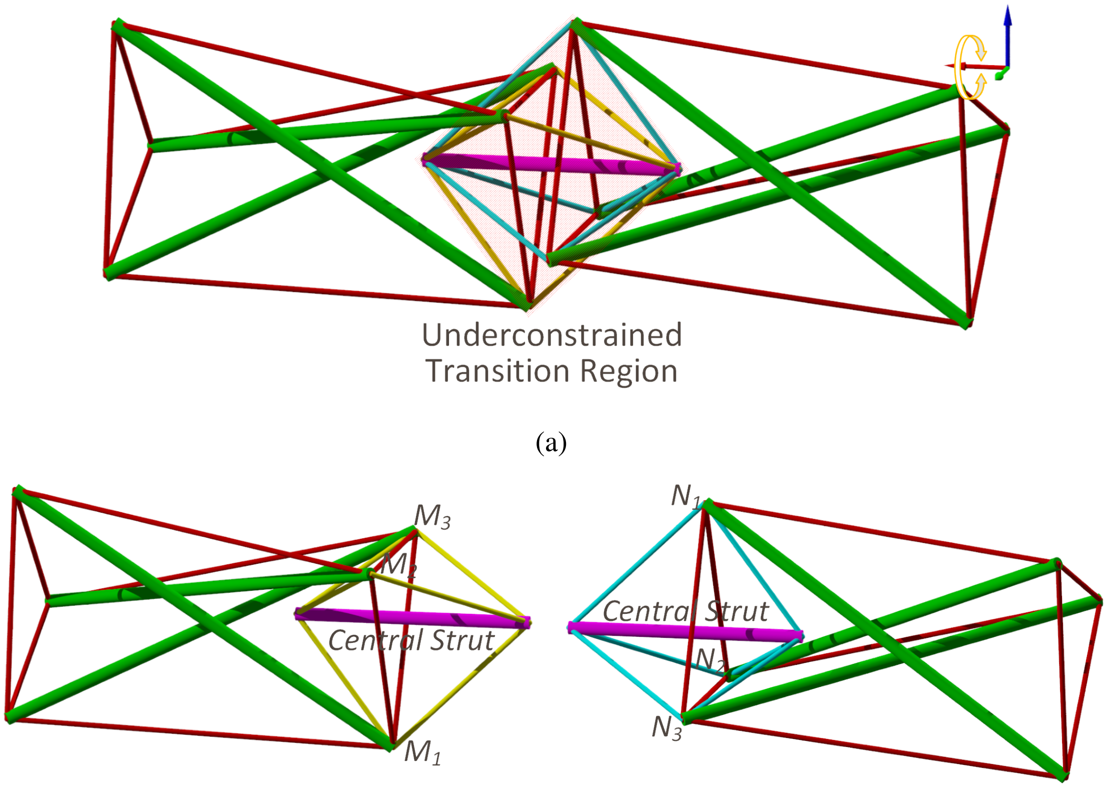

(a)

(b) (c)

Figure 3.4 A one rotational DoF three-stage tensegrity structure consisting of a central strut and two triangular prisms. (**a**) The whole structure. (**b**,**c**) The left half and right half of the structure connected to the central strut, respectively.

The 1-DoF tensegrity structure consists of three stages, which are the tensegrity triangular prism on the two sides and the transition region in the middle as shown in Figure 3.4a. Assuming the leftmost prism is fixed, the rightmost prism can rotate about the axial direction of the central strut. The whole structure has 7 struts and 30 threads. 12 of the threads serve the transition purpose.

Taking the left half shown in Figure 3.4b as an example, the central strut and each two nodes it is connected to, such as M_1 and M_2, form a C-Strut configuration, represented by the yellow lines C_1-M_1-C_2-M_2-C_1. Since the central strut is also connected to the third node M_3, represented by the yellow lines C_1-M_3-C_2, the rotation of the central strut about the axis passing through M_1 and M_2 is constrained while it is allowed in original C-Strut configuration. The same applies when analysing the remaining two node combinations of M_2M_3 and M_3M_1. With respect to the world coordinates, the central strut is significantly limited in rotation motion about the y and z axes and is thus stably suspended in 3D space. On the opposite side, the triangular prism takes the identical configuration with the central strut on the left side. It is placed rotated about the x axis by 180°. After the two halves are merged, it leaves only relative rotational motion around the x axis between them.

3.6 Two Degrees of Rotational Freedom

The idea of endowing two rotational DoFs between two tensegrity structures is to utilise the complete 2 DoF of the C-Strut on one side and only 1 DoF with a variant on the other side. An example structure based on the tensegrity quadrangular prism and icosahedron is illustrated in Figure 3.5.

The three stages of the 2-DoF tensegrity structure shown in Figure 3.5a are the quadrangular prism on the left, the transition region in the middle, and the icosahedron on the right. Assuming the tensegrity quadrangular prism is fixed, the icosahedron can rotate about the axial direction of the central strut and the axis passing through the nodes N_1 and N_2. The whole structure is composed of 11 struts and 48 threads, where there are 12 threads serve the transition region.

For the right half of the structure, where the central strut has two DoFs relative to the icosahedron, its topology is akin to that of the C-Strut configuration, represented by the cyan lines C_1-N_1-C_2-N_2-C_1. Nodes N_1 and N_2 provide anchor points for the central strut. Here the C-Strut replaced with a tensegrity icosahedron is to provide an example which applies the underconstrained transition region concept in typical tensegrity structures. For the left half which provides one DoF, it employs the same principle as that for the triangular prism configuration. However, in this case, if using the triangular prism, the distribution of its rightmost three nodes would result in asymmetrical motion range and limit the overall range. To address issue, the tensegrity quadrangular prism is introduced instead.

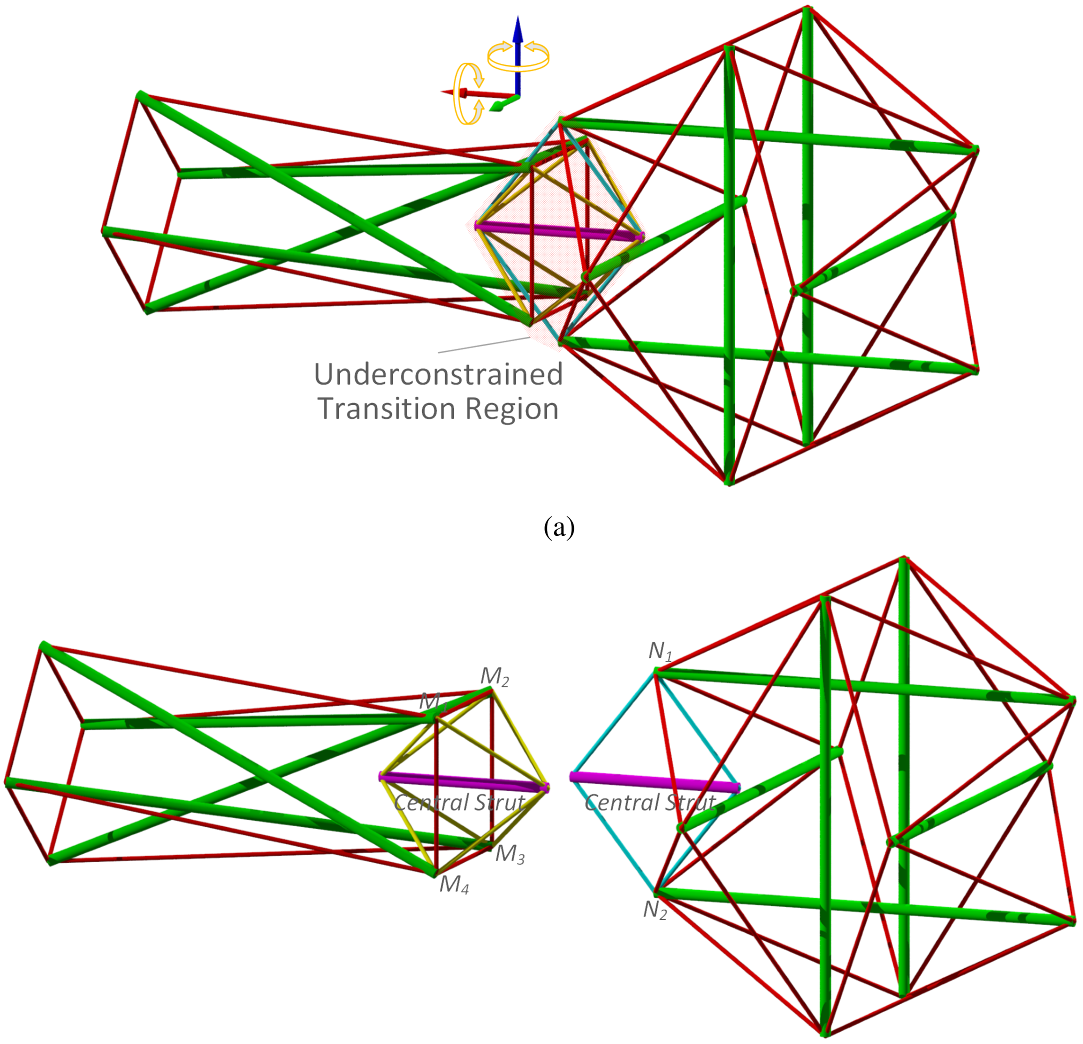

(a)

(b) (c)

Figure 3.5 A two rotational DoFs three-stage tensegrity structure consisting of a central strut, a quadrangular prism, and a icosahedron. (**a**) The whole structure. (**b**,**c**) The left quadrangular prism and right icosahedron of the structure connected to the central strut, respectively.

3.7 Three Degrees of Rotational Freedom

Since a single C-Strut structure provides rotational freedom about two orthogonal axes, the three degrees of freedom can be readily achieved by arranging two C-Struts orthogonally with one axis overlapping. An example structure built with tensegrity icosahedrons is shown in Figure 3.6.

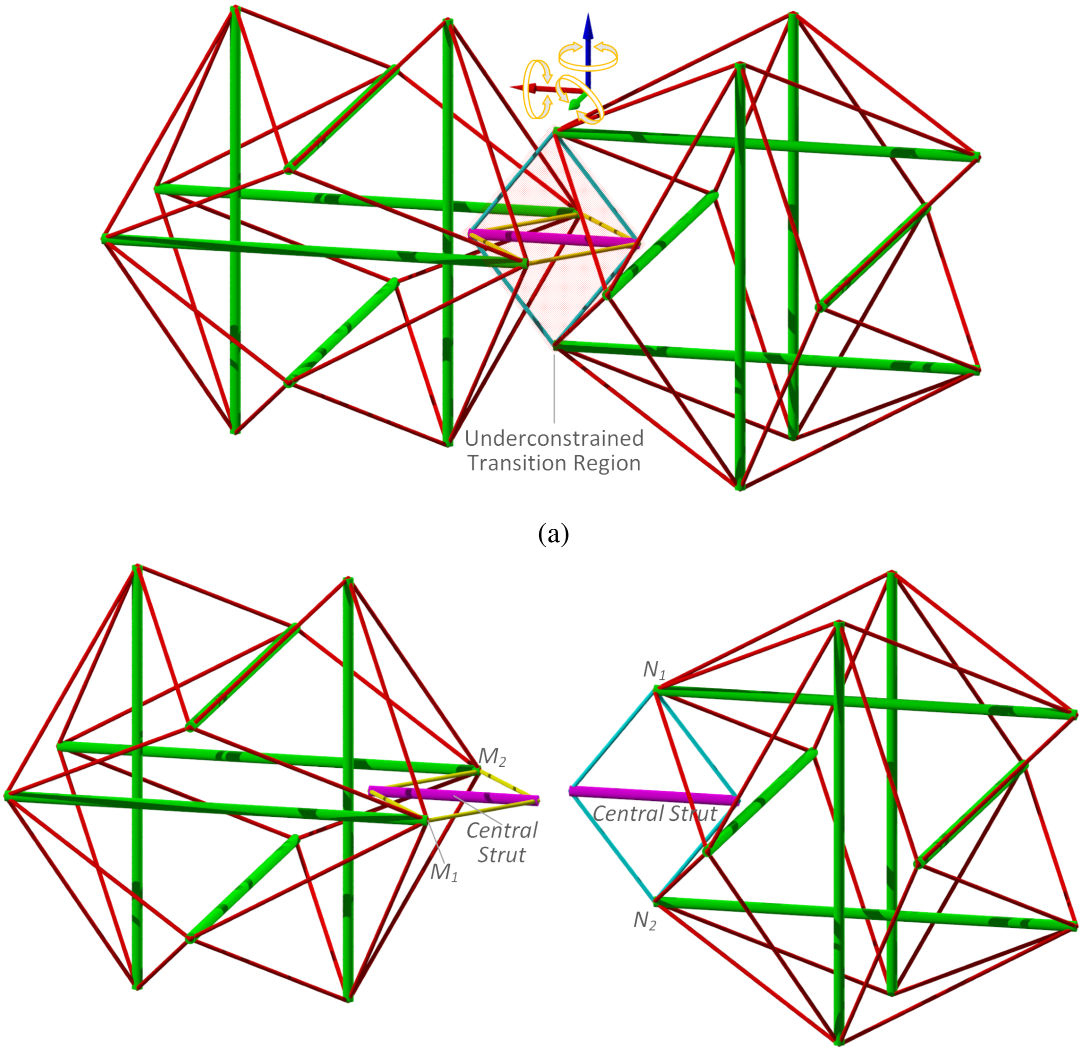

(a)

(b)

(c)

Figure 3.6 A three rotational DoFs three-stage tensegrity structure consisting of a central strut and two icosahedrons. (**a**) The whole structure. (**b**,**c**) The left and right tensegrity icosahedron connected to the central strut, respectively.

The constituent stages of the 3-DoF tensegrity structure shown in Figure 3.6a are the two icosahedrons on the two sides and the transition region in the middle. Assuming the left icosahedron is fixed, the right one can rotate about the axial direction of the central strut, the axis passing through the nodes M_1 and M_2, and that passing through N_1 and N_2. The whole structure consists of 13 struts and 56 threads, where 8 threads serve the transition region.

Similar to the right half of the 2-DoF example, in Figure 3.6b, the C-Strut suspended by the cyan lines C_1-N_1-C_2-N_2-C_1 allow the rotational movement of the central strut about its axial direction and the axis passing through N_1 and N_2. On the left side, the central strut is attached to the rightmost two nodes M_1 and M_2. The two halves are merged orthogonal to each other with the central strut overlapped and thus endowing three degrees of rotational freedom.

3.8 Summary

Inspired by the motion freedom in 3D space of the 2D tensegrity structure C-Strut, the concept underconstrained transition region is proposed. Through substituting the nodes of the C-Strut with the nodes in different tensegrity structures, its motion freedom can be readily embedded into these structures. Owing to the simplicity of the transition region's topology, of which the only compression element is a straight strut in most cases, the integration of two structures adopting such configuration is also straightforward. The example structures with one, two or three degrees of rotational freedom clearly exhibit the broad potential applications of the underconstrained transition region in various tensegrity structures.

In the next chapter, a robot module named Symmetric Tensegrity Mechanism (STeM) is implemented based on the underconstrained transition region concept. The integration approach of the tensegrity and conventional rigid structures are presented, as well as the prototyping and simulation setup for evaluation of the robot.

Chapter 4

Design, Physical Implementation and Simulation Model

4.1 Introduction

In Chapter 3, the theoretical foundation of a type of tensegrity for robotics application was described. In this chapter, the design of the Symmetric Tensegrity Mechanism (STeM) which integrates the proposed three degrees of rotational freedom tensegrity structure into a cubic robotic framework for modularity is presented. The prototyping, as well as the simulation model of the STeM are also described in detail.

The design process of the STeM and details on determining the geometry are introduced in Section 4.2. The design and fabrication of the prototype is detailed in Section 4.3. The construction of the simulation model and environment based on the Chrono Engine is described in Section 4.4. A brief summary of the chapter is given in Section 4.5.

4.2 Modularisation of Proposed Tensegrity Structure

The tensegrity structure adopting the concept of under constrained transition region presents great potentials in providing designated degrees of freedom for robot actuation purposes. However, when applying it in practical implementations, especially in modular robotic systems, the fusion of the tensegrity and conventional rigid structures is challenging. This includes how to embed tensegrity elements into rigid parts and how to properly actuate the available motion freedom.

4.2.1 Overall Geometry

The geometric model of the tensegrity structure is presented in Figure 4.1. The structure is composed of three compression elements and fourteen tension elements. The compression elements on the two sides feature the shape of triangular bipyramid. The third compression element is a normal strut. On the terminal ends of the compression elements, that is the nodes, there are multiple threads connected. The exterior surfaces of the tensegrity structure form an octahedron of which the top and bottom faces are equilateral triangles. The height *h* of the octahedron is equal to the diameter *d* of the circumscribed circle of the equilateral triangle faces, which is compatible with the specifications of the Sub-Modular Cube proposed in [107].

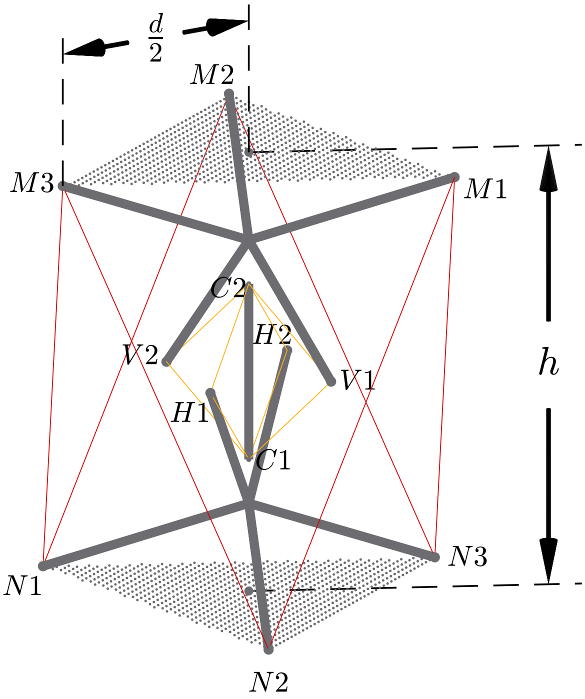

Figure 4.1 The geometric model of the tensegrity octahedron. The active and passive threads are represented by thin red and yellow lines, respectively. The compression elements, which are the central strut and the triangular bipyramids, are represented by thick grey lines. The shaded triangles denote the top and bottom faces of the octahedron.

From the perspective of function, the structure can be divided into two parts, the inner passive substructure and the outer active substructure. The passive substructure implements the concept of under constrained transition region. The active substructure provides external actuation to the structure. Based on such a substructure constitution, the tensegrity octahedron is able to retain its structural integrity without presence of the active threads.

4.2.2 Passive Substructure and Optimisation

The inner passive substructure consists of eight threads and five struts. The threads are arranged as a group of four, lying on two orthogonal planes. Four of the five struts are a part of the triangular bipyramids and the fifth is suspended in the centre of the structure by the passive threads. The passive substructure acts like a spherical joint while taking the form of tensegrity.

Since there is no constraint on the normal direction of the $H_1C_1H_2C_2$ and $V_1C_1V_2C_2$ planes of the passive substructure at neutral posture, it is critical to minimise potential displacement along such directions. Take thread H_1C_1 as an example, assuming an equivalent tension force for all candidate threads and a small displacement along the normal of the plane $H_1C_1H_2C_2$, the force F_d pulls the central strut to the neutral position provided by this cable is given by:

$$F_d = \frac{EA}{L} \cdot (\Delta l_0 + \Delta l_d) \cdot cos(\theta') \cdot sin(\alpha) \approx \frac{EA}{L} \cdot \Delta l_0 \cdot cos(\theta) \cdot sin(\alpha), \tag{4.1}$$

where Δl_0 and Δl_d are the length displacements of the cable H_1C_1 introduced by the original pretension and the small normal displacement, respectively. θ is the angle between H_1O and H_1C_1. θ' is the new θ resulted by the deviation. α is the angle of H_1O deviating from its neutral position. $\frac{EA}{L}\Delta l_0$ is a constant.

Meanwhile, the passive substructure should tend to retain its position for displacements along axial axis of the central strut. The displacement Δx_a for an axially applied force F_a is given by:

$$\Delta x_a = \frac{F_a \cdot L}{EA \cdot sin(\theta)} = \frac{F_a \cdot r_p}{EA \cdot sin(\theta) \cdot cos(\theta)}, \tag{4.2}$$

where r_p is the constant length of H_1O.

For the former case, F_d should achieve the maximum value for any given pretension force, while Δx_a seeks for the minimum value. Therefore, to determine the optimal value of θ, the equation for the derivatives of both cases with respect to θ is constructed as follows:

$$-EA \cdot \frac{\Delta l}{L} \cdot sin(\alpha) \cdot sin(\theta) = \frac{F_a \cdot r_p}{EA} \cdot (\frac{1}{cos^2(\theta)} - \frac{1}{sin^2(\theta)}), \tag{4.3}$$

Since $sin(\alpha)$ is negligible, the optimal point is the intersection between the right hand side and the x axis, which results in $\theta = \frac{\pi}{4}$.

4.2.3 Active Substructure

To actuate the available three degrees of rotational freedom provided by the passive substructure, the active substructure design takes inspiration from the shoulder complex and hip complex of the human body, which are tensegrity structures in nature with three degrees of freedom, given the function of the passive substructure is akin to that of the shoulder or hip's ball-and-socket joint. Since the movement of these joints is complicated and involves the coordinated action of many muscles, here the analysis focuses on the shoulder joint and rotator cuff muscles as their responsibilities are more intuitive. Although the rotator cuff muscles are not the primary movers in shoulder movement, the principle revealed by the muscles actuation mechanism holds the same. The anatomical illustration is shown in Figure 4.2.

It can be observed from the anterior and posterior views that the shoulder ball-and-socket joint, or more specifically, the head of the humerus in the glenoid cavity, is surrounded by the rotator cuff muscles which are supraspinatus, infraspinatus, teres minor, and subscapularis. These muscles pull in different directions to stabilise and actuate the humerus. For example, abduction motion is initiated by the supraspinatus, the infraspinatus and teres minor muscles facilitate external rotation, and the subscapularis is involved in internal rotation. These muscles, together with other muscles such as deltoid, pectoralis major, latissimus dorsi, and teres major, work in concert to actuate the shoulder joint and provide the humerus with various movements.

Learning from how the shoulder joint is actuated, the active threads are arranged in both parallel and intersection to actuate the passive substructure's three degrees of rotational freedom, where, in this case, the passive substructure act as the shoulder joint and the active threads act as the muscle group. For example, the bidirectional movement actuated by threads M_1-N_2-M_3-N_1 and M_1-N_3-M_2-N_1 on the $H_1C_1H_2C_2$ plane is similar to shoulder's external rotation controlled by infraspinatus and teres minor, and internal rotation controlled

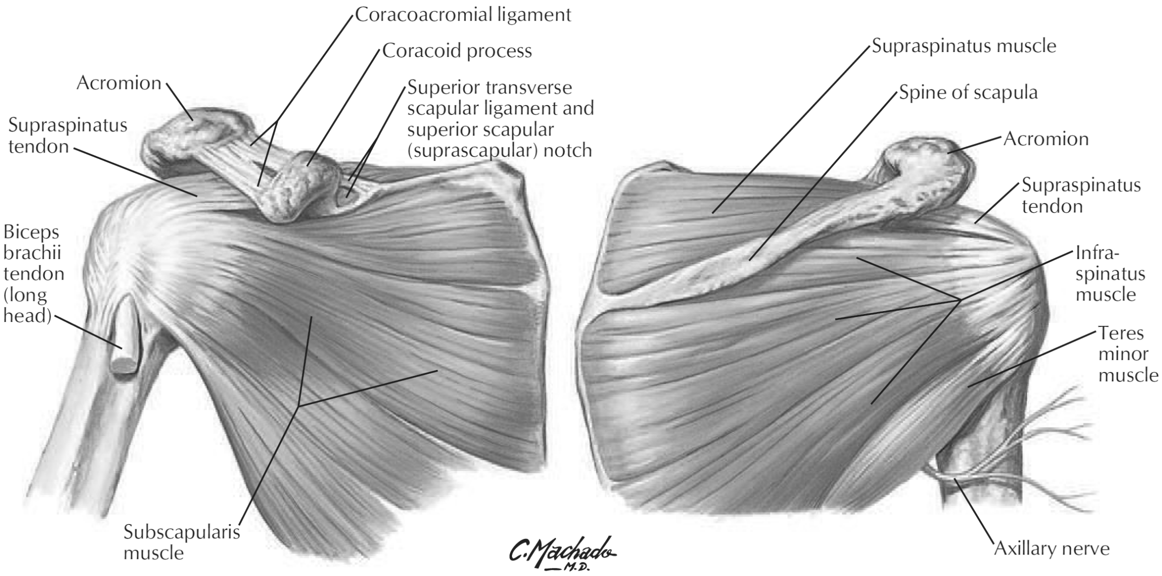

Figure 4.2 The anterior view (left) and posterior view (right) anatomy of the shoulder joint and rotator cuff muscles [108].

by subscapularis, pectoralis major, latissimus dorsi, teres major and anterior deltoid (non-rotator cuff muscles listed are not shown in the rotator cuff anatomy). However, affixing the threads directly to the lateral surface of the tensegrity struts by imitating the connection of muscles and bones would lead to a large load applied on the threads and actuators. As it is impracticable to significantly increase the diameter of the struts, to reduce such loads, a multi-strut compression element is introduced adopting the concept of biotensegrity. Together with the two struts required for the passive substructure, the “bone” forms the shape of triangular bipyramid.

A full actuation approach is employed on all the six active threads so that they work in antagonistic pairs similar to the flexors and extensors. This arrangement results in a geometry to some extent similar to the Stewart platform [109]. It eliminates the antagonism among the threads commonly existed within typical tensegrity structures and greatly improves the motion efficiency. Such a configuration uses threads extensively which features a thread to strut length ratio of approximate 38:1 at the neutral posture, leading to a high mass efficiency.

4.2.4 Integration with Conventional Rigid Structure

Analysing the geometry of the proposed tensegrity structure, one can readily observe that, compared to the less regular triangular bipyramid, the equilateral triangles at the top and bottom connected with active threads can be effortlessly embedded into conventional orthogonally arranged rigid structures. For typical tensegrity robots, the irregular arrangement of elements limits the installation of essential hardware so that it is challenging to properly attach the actuators and electronics to the struts. To make the tensegrity octahedron's more compatible with conventional bodies in a robot, the structural and other parts, such as mechanical and electronic, are separated. The latter parts are contained in the conventional body to avoid applying extra loads on the structure or exposing them directly to the environment. There are only thread routing through holes reserved on the faces of the conventional body for actuation. In addition, the triangular bipyramid can be further modified by replacing the five constituent struts with a plate with two struts to leverage the shape of conventional body. An illustration is shown in Figure 4.3.

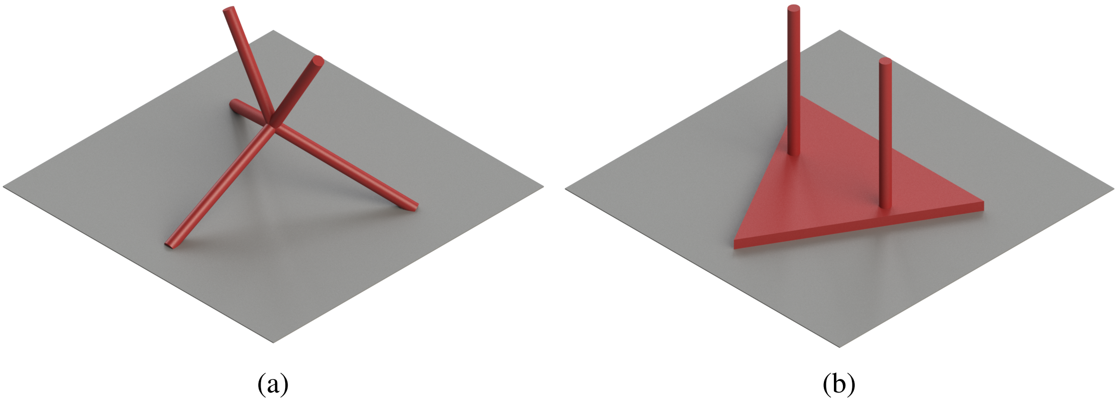

(a)

(b)

Figure 4.3 The modification to the five-strut triangular bipyramid for integration with conventional rigid structures. The red component represents the triangular bipyramid compression element in tensegrity. The grey component denotes the exterior surface of conventional rigid structures. (**a**) The original five-strut triangular bipyramid. (**b**) The plate-and-strut triangular bipyramid.

4.3 Physical Implementation

4.3.1 Mechanical Design

The mechanical design of the STeM mainly covers the design of structural components, actuation scheme and fixation of threads, arrangement of motors, sensors and battery, and magnetic connector coupling, as described in the following sub-sections. A general overview of the assembled STeM prototype from three orientations is shown in Figure 4.4.

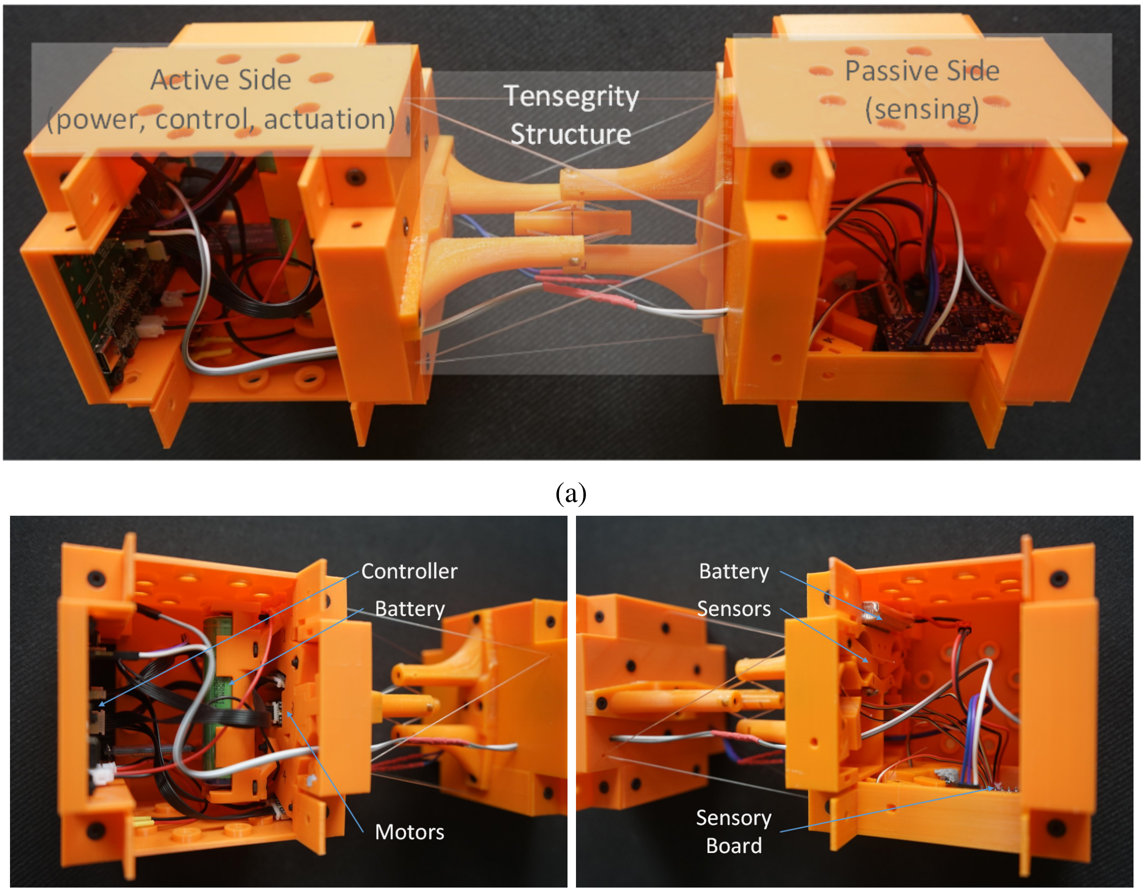

(a)

(b)

(c)

Figure 4.4 Three views from the (**a**) left, (**b**) front-left and (**c**) back-left orientations of the STeM prototype.

Structural Tiles

The structural tiles of the prototype are 3D printed with Polylactic acid (PLA) filaments and installed with corresponding hardware for different functions. Each tile has a dimension of $100 \times 60 \times 20$ mm. For normal operation of the STeM, these generally include the tensegrity tiles which contain the motors and sensors, controller tiles, and generic tiles. The controller tile is simply a tile fitted with the controller board. The generic tiles are used to enclose the robot and serve as the placeholder for tiles with other functions.

The tensegrity tiles are the main parts implementing the tensegrity structure of the STeM, which have six tiles, three on each side, five struts, and relevant accessories, as illustrated in Figure 4.5. The reason for using three tiles on each side is that the geometry of the proposed tensegrity structure has equal height and the diameter of circumscribed circles on the two sides. To comply with the specification of the Sub-Modular Cube system, the height is set at 10 cm. As a result, the vertices of the tensegrity structure cannot be fitted into one tile. The function of the struts connected to M_i and N_j vertices is embedded into and substituted by the tile body. The remaining two struts in each triangular bipyramid are mounted onto the tiles separately using screws and nuts. The central strut is suspended by threads in the middle of the tiles without direct contact.

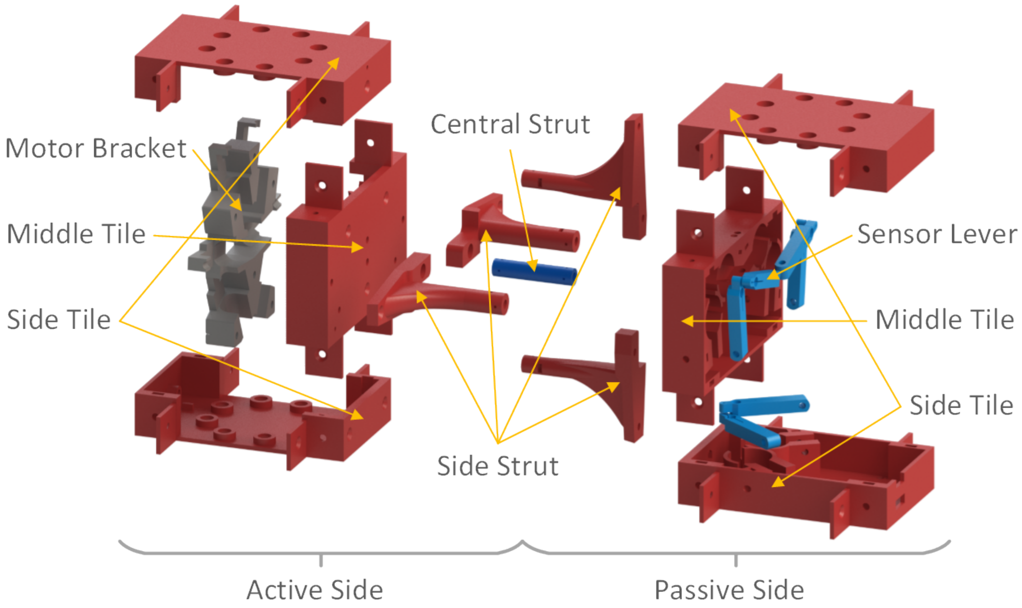

Figure 4.5 The essential structural parts of the tensegrity structure with sensory feedback in an exploded view. The parts on the left side constitute the active side which holds the motors, controller, and battery. The parts on the right side constitute the passive side which holds the sensors, sensory board, and secondary battery.

Motors

Inside the tiles, the actuation of the STeM is powered by the Pimoroni Micro Metal Gearmotor. The motor has a dimension of 40.5 × 12 × 10 mm including the gearbox, output shaft and back shaft, which is about the maximum allowed size to fit 6 motors inside one of the cuboid hub's faces. The motors are mounted onto the tiles using several holders and a bracket. They are arranged in a particular pattern so that the shaft is perpendicular to the threads exiting the shell. Given the limited tile dimension 100 × 60 × 20 mm, the motors take the space of three tiles - the complete volume of the middle tile and a 60 × 20 × 20 volume of each side tile, as shown in Figure 4.6.

The motor operates at 6 V nominal and provides a maximum torque of 0.9 kg.cm on its output shaft with a gear ratio ratio 110:1. It drains 600 mA current when stalled. The output shaft is 11 mm long and has a diameter of 3 mm thus providing a maximum pulling force on the threads of approximate 59 N.

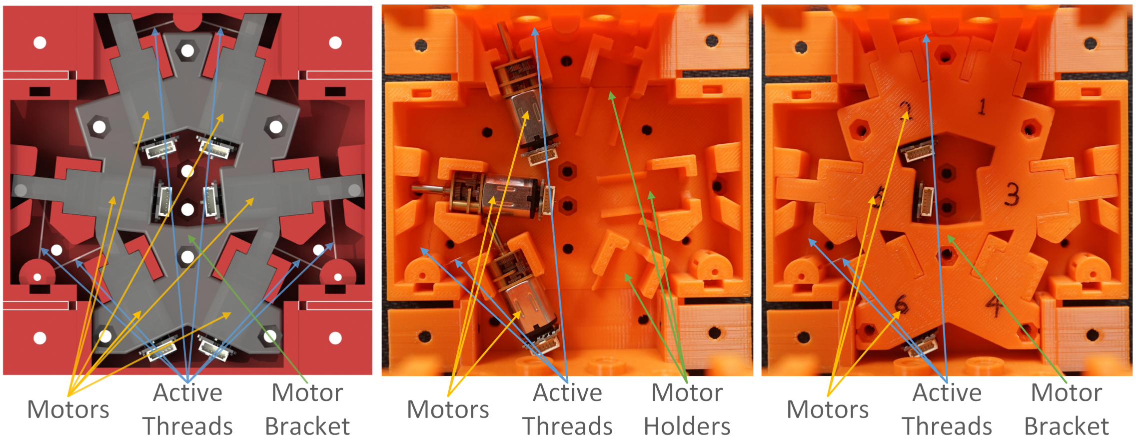

(a) (b) (c)

Figure 4.6 Arrangement and mounting of the motors. (**a**) The cross section view along the axial direction of the STeM showing the motor arrangement and thread routing, with the motor bracket rendered transparent. (**b**,**c**) The prototype with and without the motor bracket, with half of the motors populated.

Sensors

To measure the forces on the threads, there are six button load cells equipped on the opposite side to the motors. As the button load cells only sense compression, the pulling forces from the threads are converted to push forces on the button through a lever with a mechanical advantage of approximate 2.32. The levers have an identical design which has a thread through hole on the distal end, a button on the bottom face, and a rotation shaft through hole on the proximal end.

Four of the six load cells are mounted on the middle tile and the other two are placed on the side tile due to limited available space. A "L" shaped thread guide slot is reserved inside the side tile body to steer the threads by 90° since the encapsulated load cells are right-angle placed.

As each two threads pass through the same thread guide, as illustrated in Figure 4.7c, a stacked arrangement is employed to keep the perpendicular connection from the threads to

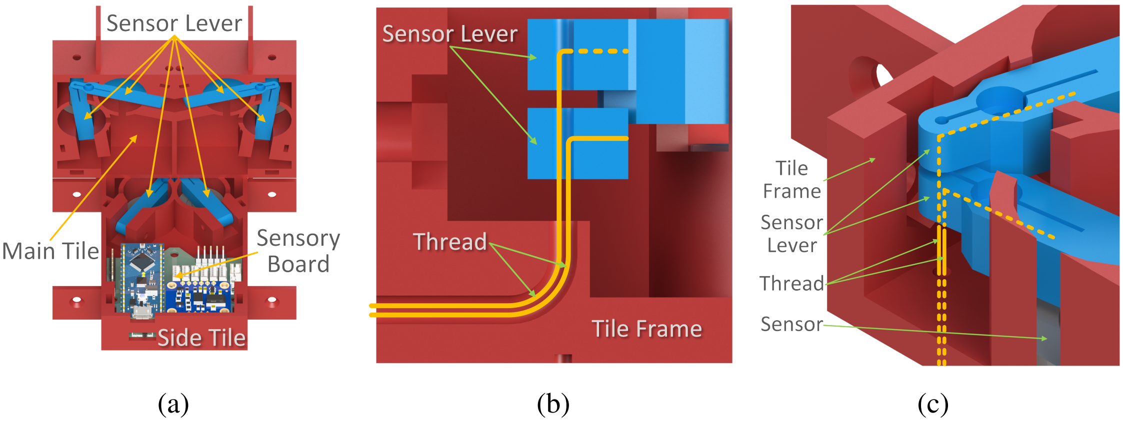

Figure 4.7 The force measurement design of the STeM. (**a**) The load cells arrangement inside the tiles. (**b**) The cross section view of “L” shaped thread guide slot. (**c**) The cross section view of the stacked lever design.

the levers, in order to minimise the systematic error. The two levers are kept apart with a certain angle to reduce the overall height while retaining enough thickness for its strength. The thread connected to the upper lever passes through the hole on the distal end of the lower lever so that both levers bear the thread pulling forces without interfering each other.

Thread Actuation and Fixation

The threads employed in the prototype are 0.5 mm Nylon fishing lines where double strands are used for the passive threads. The threads are actuated using a simple winch design. The active threads directly wind on the output D shaft of the motors. Since there is no enough space to install a spool to the output shaft, to prevent the threads from slipping off, the D shaft is secured with a stopper made up of a holder and bracket pair on the shaft distal end. A hole is drilled on the shaft proximal end using 1 mm diameter tungsten carbide drill bits for thread fixation. The thread is firstly wound around the half shaft for one turn, and then its terminal end is heated to melt into a small blob as a stopper, as demonstrated in Figure 4.8. Since there are only three nodes on each side in the geometric model, each two threads share the same guide hole on the tile (the same for the opposite side). Two guide slots are designed on the inside of the thread exit hole to split and align the threads with the motor shaft.

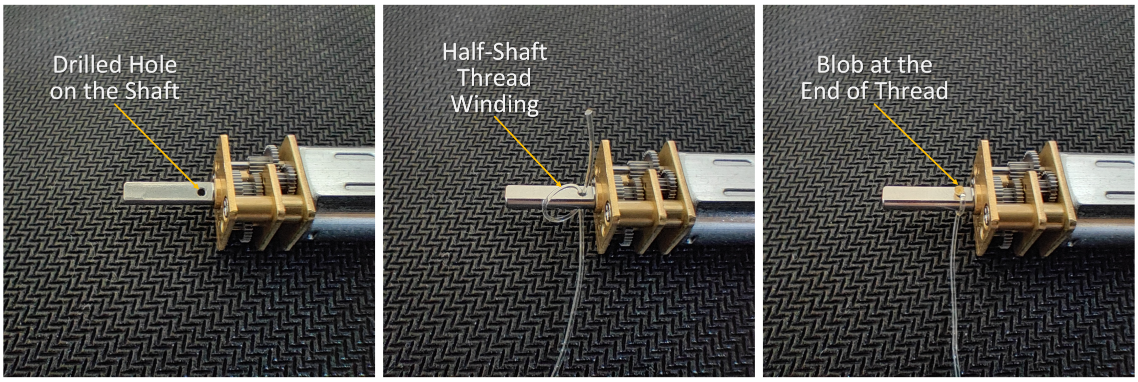

(a) (b) (c)

Figure 4.8 The fixation process of active threads to the output shaft of the motors. (**a**) The output shaft is drilled with a hole. (**b**) The thread is wound on the half of the shaft by one turn. (**c**) The end of the blob is heated to form a small blob.

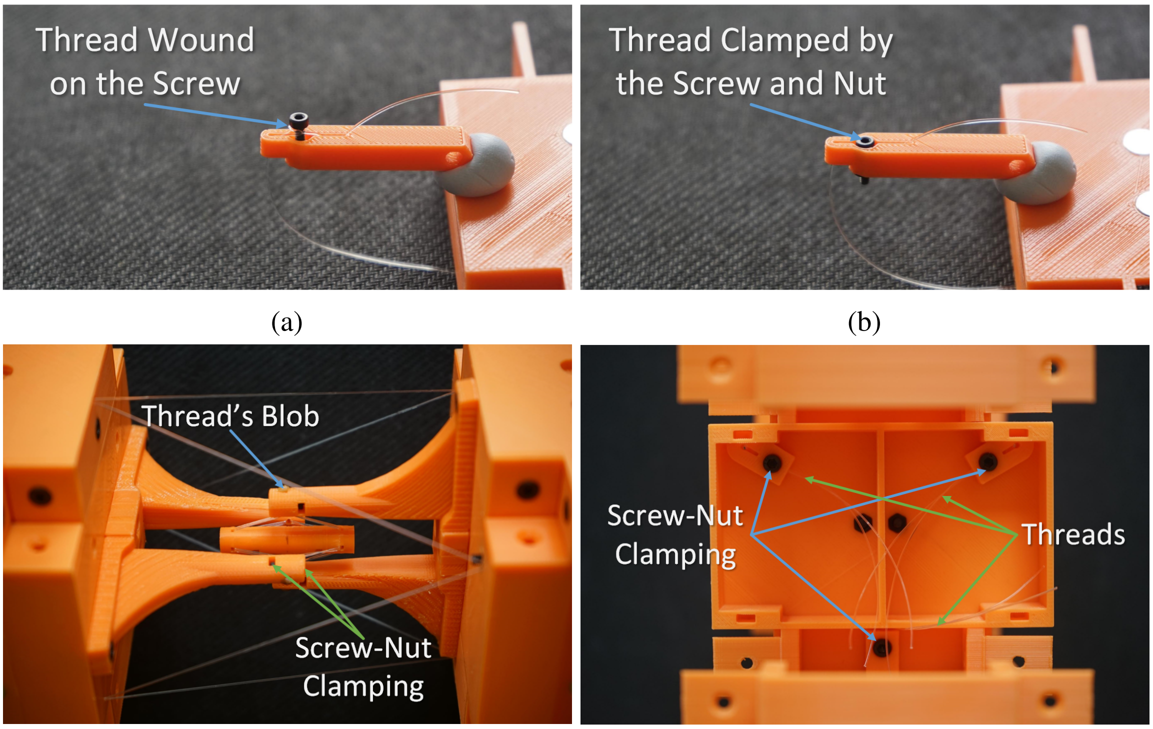

(a) (b)

(c) (d)

Figure 4.9 The fixation of threads to the structural parts or accessories. (**a**,**b**) The winding and fastening process of fixing threads to the levers. (**c**) The fixation of passive threads to the struts, with terminal end blob formed by heating. (**d**) The fixation of threads to the tiles without load cells.

On the other terminal end of the active threads, as well as for the passive threads, they are fixed directly to the tiles, struts or levers using screw and nuts as a grip. The thread is firstly wound on the screw with one turn. The screw is then tightened to push its cap onto the thread so that the thread is firmly clamped in between, as demonstrated in Figure 4.9. To introduce pretension to the passive substructure, a fixation process is designed. First, the five struts are held close to each other and threads are fixed to them. The struts are then mounted to the tiles which forces the nodes apart. It results in a theoretical pretension ratio of approximate 93%.

Battery Holder

The STeM and its constituted robot are designed to be self-contained. According to the design concept of the Sub-Modular Cube system, the STeM is supposed to be powered by a specialised power tile. However, a power tile is not available and the development of it is out of the study's scope, a simple battery holder mounted on top of the motor bracket is introduced to connect a single cell battery, as shown in Figure 4.10a.

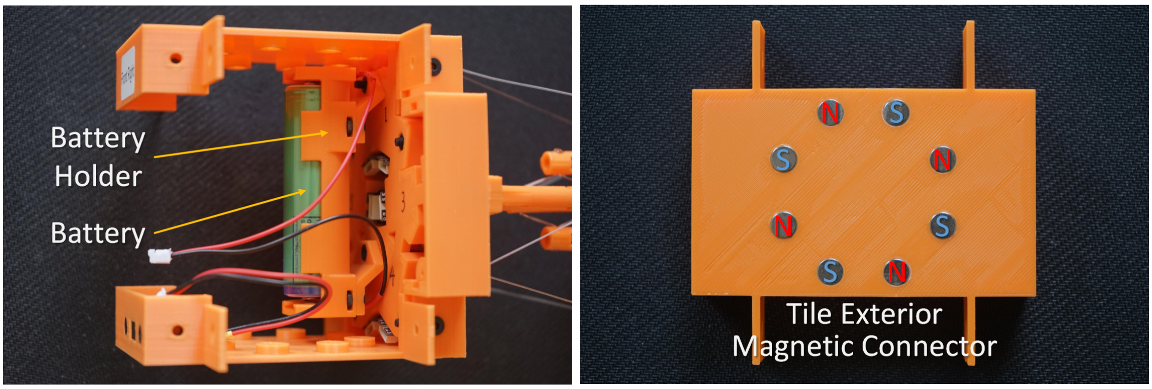

(a) (b)

Figure 4.10 The battery holder and magnetic connector. (**a**) The battery holder mounted on top of the motor bracket. The green object is the battery cell installed, connected to the wires through the spring contact plates fitted inside the holder. (**b**) The magnetic connector on the exterior face of the tiles.

Magnetic Connector

The concatenation between STeM modules is realised with the magnetic connectors on the exterior face of the tiles. The design is fully compliant with the specification of the Sub-Modular Cube system. Each connector consists of 8 cylinder magnets arranged in an octagonal pattern, as illustrated in Figure 4.10b. With opposing polarities between adjacent magnets, it realises a homogeneous coupling between each two connectors and expands in a Cartesian grid pattern with automatic alignment.

4.3.2 Electronics

The STeM's electronic system consists of the battery, power management, control unit, motor driver, communication, and sensors, making the robot self-contained. An overall block diagram of the system is shown in Figure 4.11. There were two printed circuit board assemblies designed, the controller board and the sensory board. The controller board is fitted inside the active side, which has motors installed. The sensory board is fitted inside the other side of the STeM, activated only for the force distribution test. There are 3 wires, 1 ground and 2 signals, connecting the 2 boards for establishing a UART (115200 baud rate) communication channel.

Controller Board

The controller board supports up to three parallel connected batteries for prolonged battery life while in this study, a single 3500 mAh protected INR18650MJ1 battery cell was employed. The batteries can be charged through the onboard charger (TP4056) by connecting external power to the USB receptacle. There are 3 boost converter (FP6291) and motor driver (TB6612) pairs regulating the voltage at 6 V. Each converter-driver pair is responsible for powering two motors (110:1 Pimoroni Micro Metal Gearmotor with 12 CPR encoder on the input shaft). Other components that drain 6 V power are supplied by the paralleled output of the boost converters and external supply. The microcontroller (STM32F417) and the logic circuit of the motor driver have a linear regulator (AMS1117) as an intermediate stage to provide 3.3V voltage.

The board can connect up to 6 motors. The microcontroller controls the output of the motor drivers and monitors the encoder feedback from the motors. The board is equipped with a HC-05 module to provide the UART (baud rate 921600) communication carried by Bluetooth between the board and host computer, as well as a CP2102 USB to UART bridge chip for the wired communication. There are 4 RJ12 sockets reserved for controlling external motors but sharing multiplexed connection with the onboard motors. The microcontroller is to be

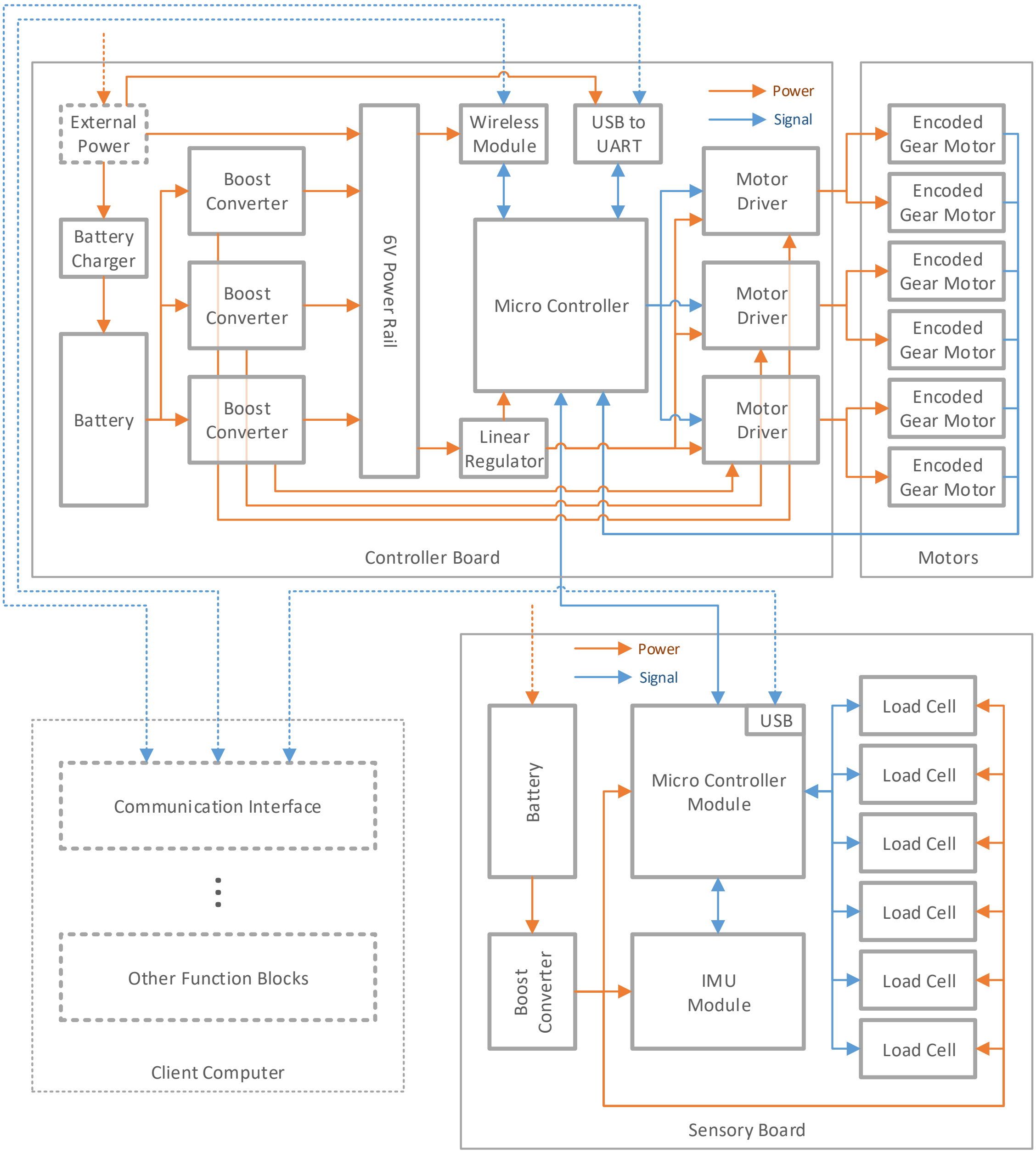

Figure 4.11 A block diagram of the STeM's electronic system. The solid lines denote the components or connections contained by the STeM. The dashed lines denote the external devices or interfacing that are optional for operation.

programmed by the ST-Link interface connected through the 5th RJ12 socket as well. A front view of the controller board in shown in Figure 4.12.

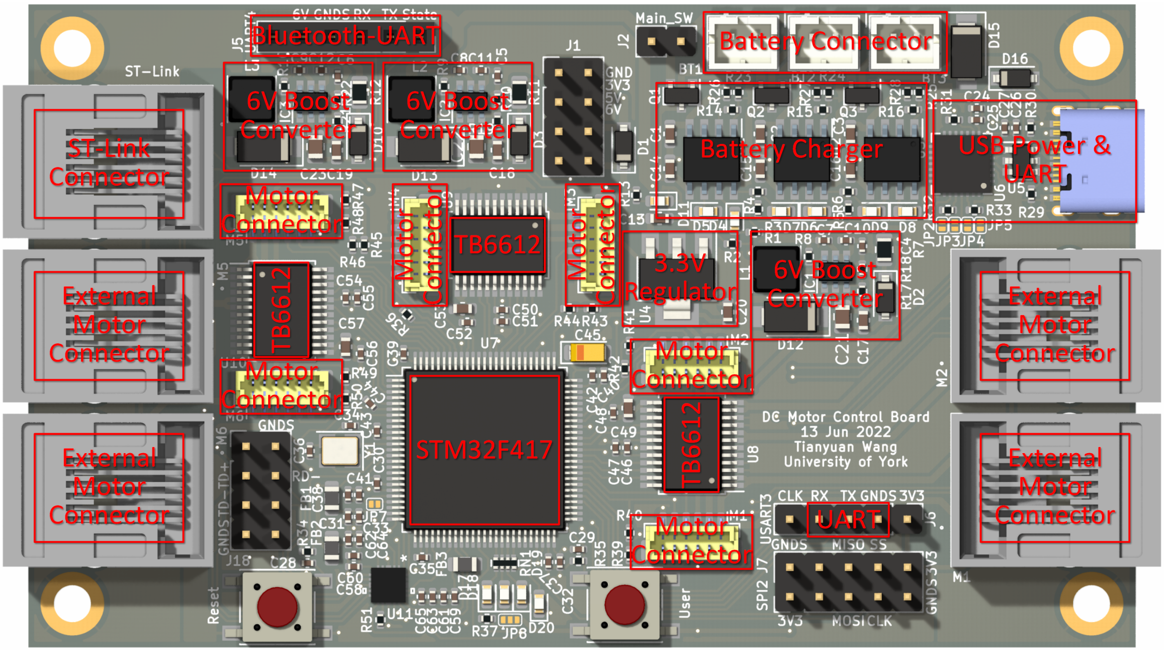

Figure 4.12 The front view of the controller PCB with components populated. The Bluetooth to UART module connects to the board through the connector labelled J5 on the top left corner of the board. The dimension of the board is 95.6 × 55.6 × 12 mm.

Sensory Board

The sensory board is powered by a smaller Li-Po battery (750 mAh 902540 package). There is only one boost converter regulating the output voltage at 5 V and no linear regulator or onboard charger. The battery is charged by external charger when depleted. There are two hardware modules stacked on the board, a microcontroller module (Arduino Nano Every) and an IMU module (Adafruit BNO055). Both modules have embedded voltage regulator supplying the 3.3 V rail for their onboard peripherals. There are six load cells (FX29K0-040A-0025-L) connected to the board and powered directly by the 5 V rail. The microcontroller module reads the measurement from the load cells and the absolute orientation information from the IMU module, both through the I2C bus. It synchronises the data with the controller board through the UART protocol carried by the wired connection between them. The front view of the sensory board is shown in Figure 4.13

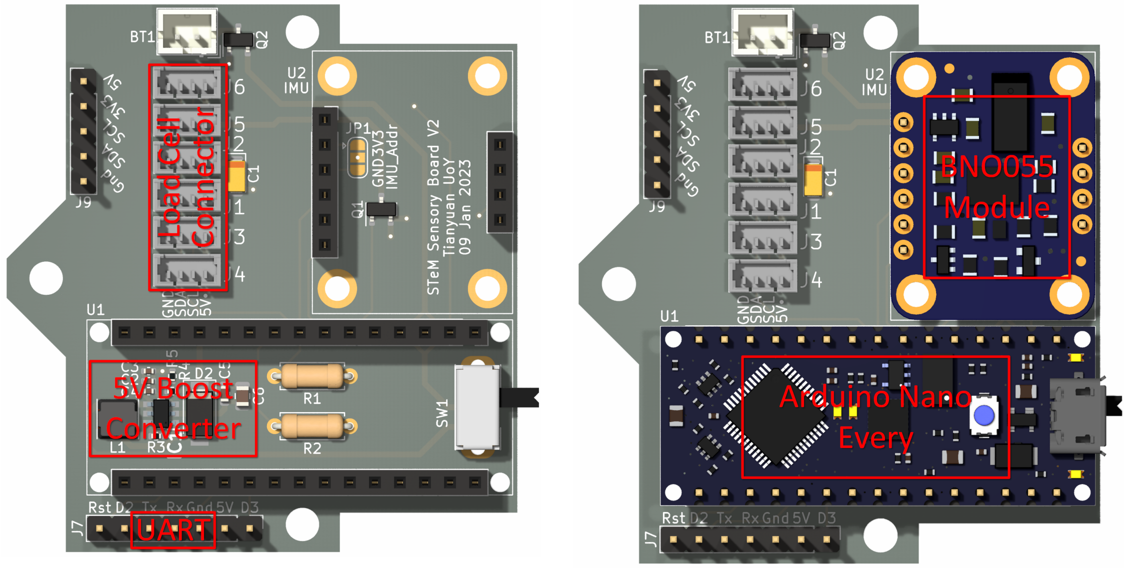

(a) (b)

Figure 4.13 The front view of the sensory PCB without and with the microcontroller and IMU modules populated. The dimension of the board is 51.8 × 55.6 × 17.8 mm.

4.3.3 Embedded Program

The embedded program running on the STM32F417 is responsible for low-level control of the STeM and is coded in C++. The program features a hierarchical design where each class corresponds to a component or function of the STeM, complemented by the event-triggered and timed schedulers that orchestrate their operation. A block diagram of the overall framework of the program is illustrated in Figure 4.14. The STeM class provides the unified access to all encapsulated attributes and methods (here the attribute and method follow Python's naming conventions to avoid ambiguity), which contains a state logger, a sensor transceiver, a control transceiver, and a control unit instance. Inside the control unit, there are 6 actuator instances controlling the 6 motors. Some additional libraries are employed to facilitate the calculation of vectors, quaternions and matrices.

The time sensitive tasks are triggered by the hard interrupts such as UART packet reception, timer timeout and encoder overflow events. They are executed inside the interrupt service routines (ISRs) with logical higher priorities than the real-time operating system (RTOS) kernel. Other tasks such as execute received commands, report and log latest states, and control wheels are managed by the relative RTOS tasks created at boot up, where the key first task is explained in detail in the following subsection.

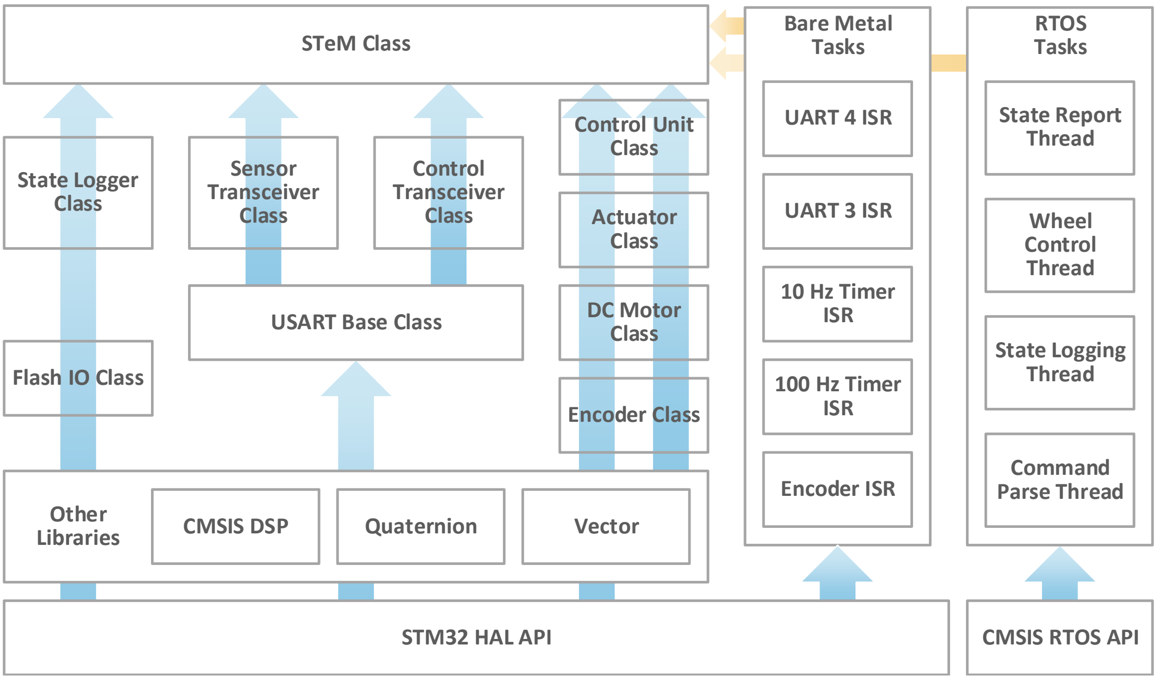

Figure 4.14 The structure of the embedded program running on the STM32F417 microcontroller. The blue arrows represent the inheritance and containment relationship of classes. The yellow arrows denote the referencing of the functions.

Thread Actuation RTOS Task

Among the RTOS tasks, the thread actuation task is the one that directly controls the tensegrity structure. It periodically calls functions of the STeM class to parse the received commands and perform the work accordingly. From the perspective of the workflow, the active threads are monitored by a length updater and a cascaded PID controller, as shown in Figure 4.15. The length updater calculates the threads' expected length based on the input posture and converts the length to the motor positions. The position PID loop updates at 10 Hz providing expected speed to the speed PID loop which runs at 100 Hz. The output of the speed PID is mapped to the PWM signal's duty cycle to drive the motors.

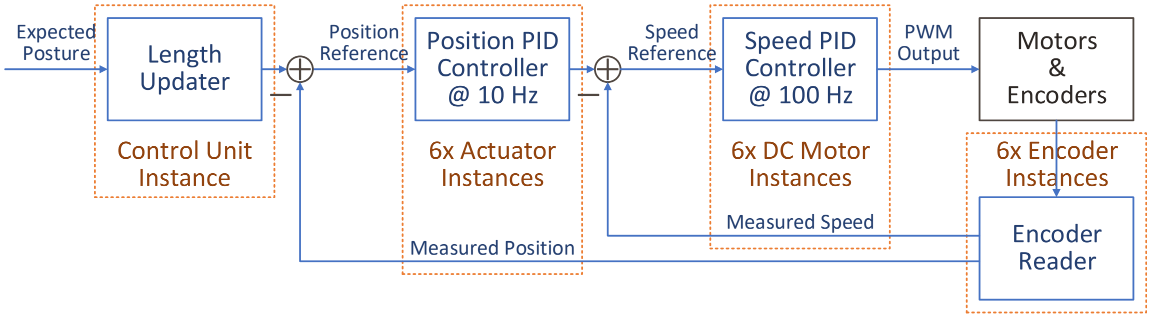

Figure 4.15 The workflow for controlling the motors that actuate the active threads. The solid blue boxes represent the data processing stages. The dashed orange boxes represent the classes where the enclosed processing happens. The solid black box represents the plant being controlled.

4.3.4 Graphical User Interface

The computational power provided by the STM32 microcontroller does not meet the requirement for high-level control of the modular robot, such as inter-module coordination and locomotion. However, given the development of an onboard computer module is not within the scope of designing a modular tensegrity robot, a GUI program was developed to manage the high-level control of the robot, as well as to facilitate the status monitoring, test sequence control and data collection on the client side for physical experiments. To simultaneously control all the modules of the robot, the communication between the GUI and the modules employs a point-to-multipoint topology, carried by Bluetooth. The GUI directly transmits commands to and receives report from each module through virtual UART ports emulated by the Bluetooth device. A screenshot of the interface is shown in Figure 4.16.

The GUI program is coded in Python, primarily relying on two libraries, PyQt5 and pySerial. The code consists of three modules, the GUI, serial, and CPG module. The GUI module is responsible for rendering the interface front end and initialise the signal connection to the back end. The serial module establishes standalone communication with the STeMs in separate threads that can be accessed by the front end and other functions. The CPG module iterates the CPG model and provides results as reference motion signals to the serial back end. The program structure of the GUI is shown in Figure 4.17.

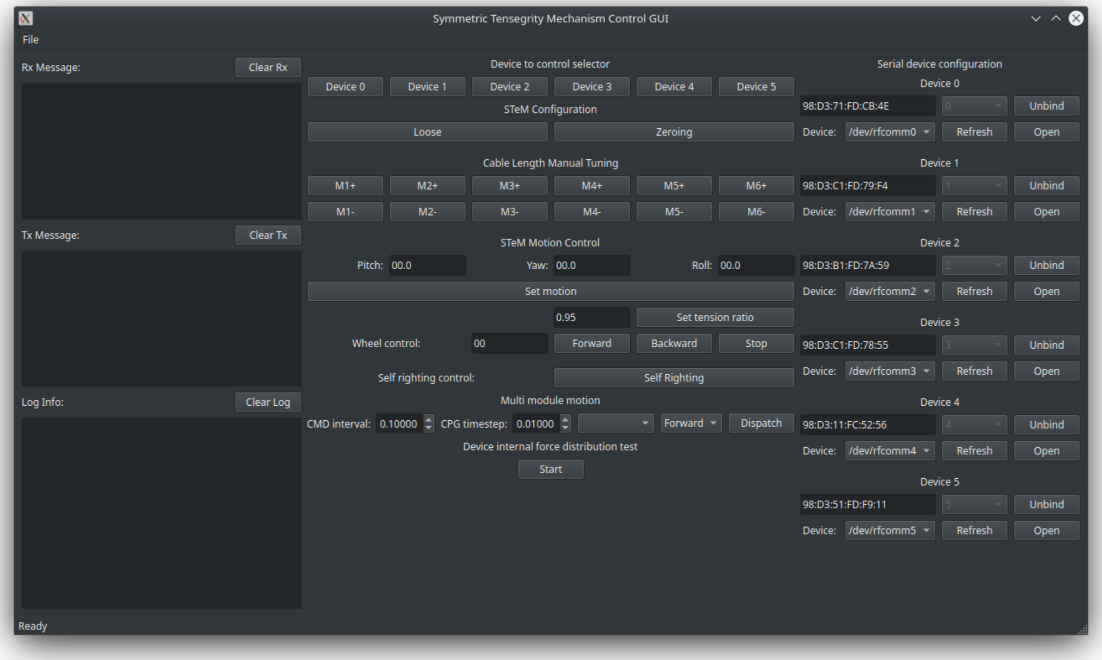

Pitch: 00.0
Yaw: 00.0
Roll: 00.0
0.95
Wheel control: 00
CMD interval: 0.10000
CPG timestep: 0.01000
Forward

Device 0
98:D3:71:FD:CB:4E
0
Device: /dev/rfcomm0

Device 1
98:D3:C1:FD:79:F4
1
Device: /dev/rfcomm1

Device 2
98:D3:B1:FD:7A:59
2
Device: /dev/rfcomm2

Device 3
98:D3:C1:FD:78:55
3
Device: /dev/rfcomm3

Device 4
98:D3:11:FC:52:56
4
Device: /dev/rfcomm4

Device 5
98:D3:51:FD:F9:11
5
Device: /dev/rfcomm5

Figure 4.16 A screenshot of the graphical user interface running on the client computer. The transmitted and received messages and the associated log information are displayed on the leftmost panel. The manual control and test sequence management of the STeMs (up to 6 entities) are located in the central panel. The communication connection management are grouped in the rightmost panel.

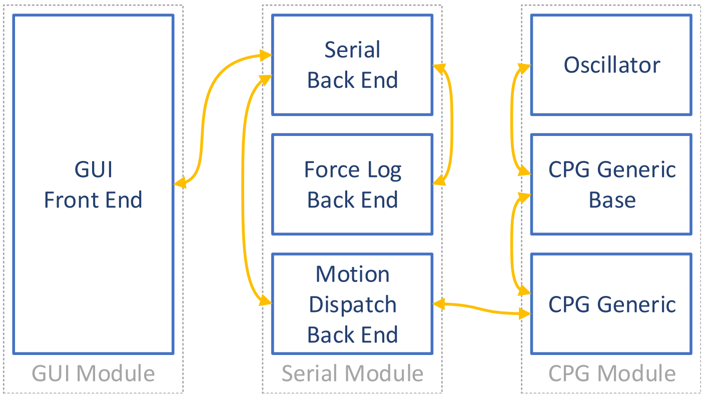

Figure 4.17 The structure of the GUI program. The solid blue boxes and dashed grey boxes represent the classes and modules, respectively. The yellow arrows indicate the interaction between classes.

4.4 Simulation Model

For some experiements that are difficult to implement in practice due to material constraints such as impact test and those that require fine control and reading of variables such as loads in contact with the ground, a simulation environment was designed and constructed. The simulation of the STeM is constructed on Chrono Engine, an open source multi-physics dynamics engine with validated fidelity [110, 111]. The NASA Tensegrity Robotics Toolkit (NTRT) simulator is a commonly used platform [63]. However, it is developed for tensegrity structures only, which means it cannot simulate tensegrity robots containing conventional linkages or robotic elements such as wheels as a complete system. Through employing the Chrono Engine, it enables an integrated simulation of tensegrity structure and conventional rigid body robots to be produced in one scene. A screenshot of the STeM simulation scene with one module populated is presented in Figure 4.18. The coordinate system of the simulation follows the ISO vehicle axes convention, where in the figure z axis points upwards, x axis points leftwards representing the head direction, and y axis points out of the paper denoting the left direction. The simulation employs the Chrono Engine's Non Smooth Contacts (NSC) system to solve collisions. It uses the hybrid solver which combines the Alternating Direction Method of Multipliers (ADMM) and Intel MKL Pardiso (MKL) solvers provided by Chrono Engine. The time stepper and time step are set to Euler implicit linearized and 0.001 s, respectively. The framework of the simulation program is demonstrated in Figure 4.19.

4.4.1 Rigid parts

The rigid parts of the STeM such as the tiles, struts and wheels, as well as the ground are created with the "ChBody" elements. The default density is set at 1.15 g/cm^3. When necessary, it is scaled at the object creation stage to match the mass in simulation with the prototype. The friction coefficient and the restitution are set at 0.5 and 0.2, respectively. To avoid anomalies in collision simulation, these parts are modelled using primitive shapes such as box and cylinder where the cubic hub of the STeM is composed of six cuboids contained by one "ChBody" instance. Their collision shapes are automatically generated with an outward envelope set at 0.3 mm for collision detection and an inward margin of 0.1 mm for the solution stage. The mass and moment of inertia are also auto-generated assuming the material is homogeneous.

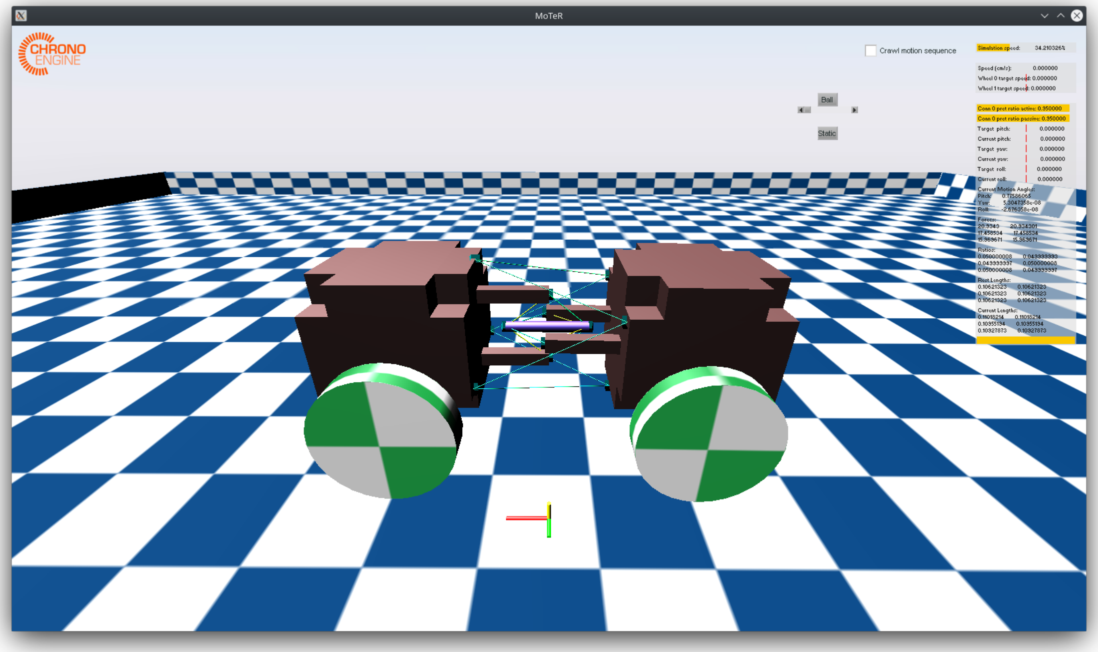

```
Simulation speed:        34.210326%

Speed (cm/s):            0.000000
Wheel 0 target speed: 0.000000
Wheel 1 target speed: 0.000000

Conn 0 pret ratio active: 0.950000
Conn 0 pret ratio passive: 0.950000
Target  pitch:           0.000000
Current pitch:           0.000000
Target  yaw:             0.000000
Current yaw:             0.000000
Target  roll:            0.000000
Current roll:            0.000000
Current Motion Angles:
Pitch:      0.77586065
Yaw:        5.3047358e-08
Roll:      -2.676358e-08
Forces:
20.9343       20.934301
17.458534     17.458534
15.969671     15.969671
Ratios:
0.050000008     0.049999993
0.049999997     0.050000008
0.050000008     0.049999997
Rest Lengths:
0.10621323     0.10621323
0.10621323     0.10621323
0.10621323     0.10621323
Current Lengths:
0.11018214     0.11018214
0.10955194     0.10955194
0.10927873     0.10927873
```

Figure 4.18 An example simulation scene based on Chrono Engine. A STeM module is presented in the centre of the screenshot. The floor is rendered with blue and white checkered pattern. The GUI showing status data is on the top-right panel.

4.4.2 Threads

The threads of the STeM are simulated using Finite Element Method (FEM). They are created with the "ChElementCableANCF" elements, which is based on the Absolute Nodal Coordinate Formulation (ANCF) that has been validated according to the technical report [112]. The threads are configured to match Nylon material, 2.7 GPa Young's modulus and 1.14 g/cm^3 density, with a diameter of 0.5 mm and 0.707 mm for the active and passive threads respectively, matching the prototype. The default pretension ratio of the passive threads is set at 95%. Each thread object is connected to the rigid parts through the nodes on its two terminal ends using a link called "ChLinkPointFrame", which acts as a spherical joint. An illustrative topology is shown in Figure 4.20.

4.4.3 Actuators

Incorporating collision simulations for FEA objects introduces extra complexity to the system and significantly elevates computational demands. Given this and considering that the threads

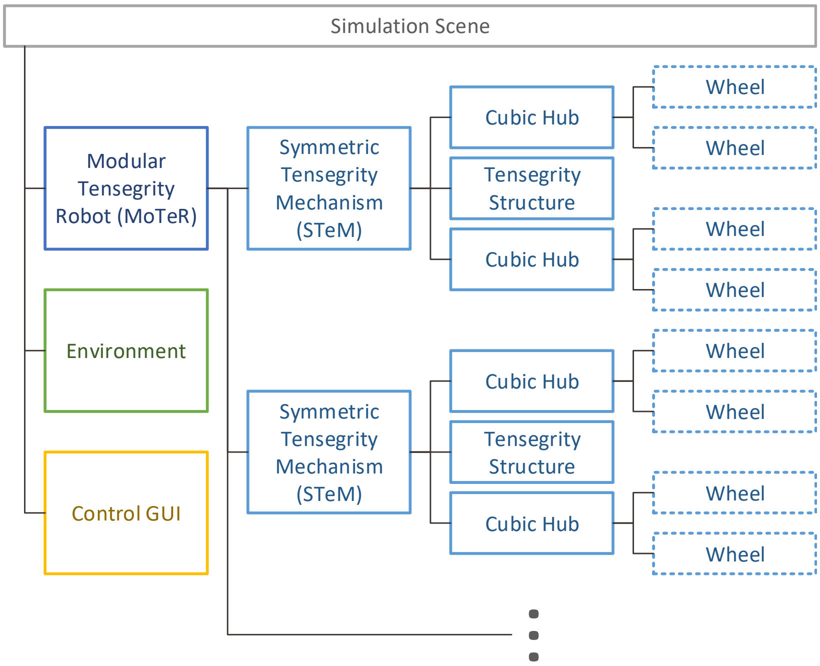

Figure 4.19 The framework of the simulation program. The scene is composed of the robot, environment and control GUI. The robot can be constituted by a single or multiple modules. The wheels are optional components depending on experiment requirement.

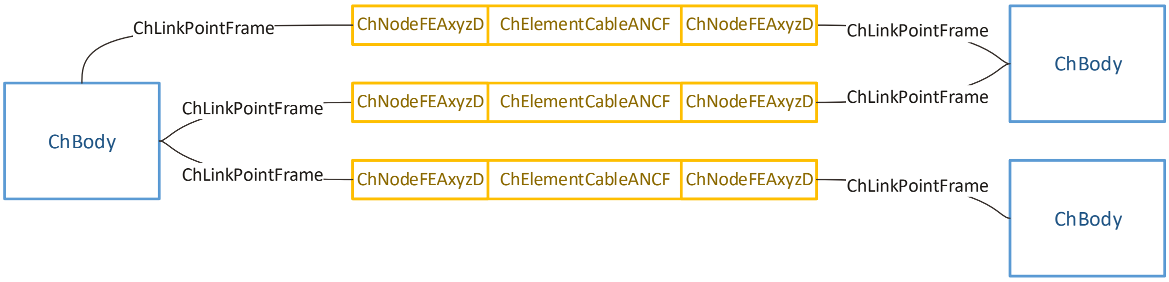

Figure 4.20 An example topology of the links (“ChLinkPointFrame”) connecting the threads (“ChElementCableANCF” and “ChNodeFEAxyzD”) and rigid parts (“ChBody”) in simulation. Each rigid part can be attached with multiple links at the same or different positions on its body while each node can only be connected to one rigid part.

do not collide with other parts during operation, the actuation of threads is not realised by replicating its physical implementation which winds the thread on the motor output shaft. Instead, the threads’ length change is represented by directly setting the rest length of the threads. The tension state of the threads is achieved by setting a shorter rest length of the calculated distance between two nodes.

4.4.4 Sensors

Benefiting from the convenience of simulation, the sensor data is obtained by directly accessing the state data of corresponding objects. In simulation experiments, several types of data are collected including the orientation and position of the cubic hubs and tensegrity nodes with respect to the world, the relative orientation between hubs, actual length and internal force of the threads, contact force of the rigid parts, and acceleration and velocity of the cubic hubs.

4.5 Summary

This chapter has described advancing the under constrained transition region introduced to the tensegrity structures oriented for robotic applications, the hybrid robot module Symmetric Tensegrity Mechanism (STeM) is designed which seamlessly integrates the tensegrity and conventional rigid structures. The STeM retains the topology of the proposed three degrees of rotational freedom tensegrity structure and endows the robot with motion freedom with actuated movement inspired from biological paradigms. The prototyping of the STeM which covers how to physically implement the design is also detailed in this chapter, as well as the construction of the simulation scene using an open source platform.

In Chapter 5, given the design, prototype, and simulation ready for use, the STeM is analysed and evaluated to gain comprehensive knowledge of its characteristics as an indispensable preparation stage for subsequent exploration of the modular robot.

Chapter 5

Symmetric Tensegrity Mechanism

5.1 Introduction

In this chapter, the analysis and evaluation of the Symmetric Tensegrity Mechanism (STeM) described in Chapter 4 are detailed in terms of the workspace, control, and properties of actuation, mechanical and functional. The naming convention of the symbols denoting the structure elements is consistent with the geometry illustration shown in Figure 4.1 in Chapter 4. The STeM is the fundamental building block that augments the robot with the properties of tensegrity.

The workspace of the STeM is analysed in Section 5.2. The control strategy is discussed in Section 5.3. Experiments and results are covered in Section 5.4 to evaluate the STeM's properties such as the force distribution, motion accuracy, stiffness, fault tolerance, and adaptability as a single or coupled configuration. The work is summarised in Section 5.5.

5.2 Workspace Determination

As discussed in Chapter 4, the STeM is endowed with both passive and actuated operation modes. The two modes have different workspace which is determined by the physical constraints and geometric configurations. The workspace analysis is thus divided into the following subsections.

5.2.1 Passive Workspace

Regarding the passive mode, its maximum tilt, that is pitch and yaw, and roll angles are mainly limited by mechanical constraints of the rigid elements, as illustrated in Figure 5.1. Since the overall height h of the tensegrity structure is equal to the width d of the cubic hub and the pivot point is at the centre of the mechanism, it is clear that the individual pitch and yaw range are both $\pm 90^\circ$. The roll motion reaches its maximum angle when the side struts collide with each other. Therefore, the independent roll range can be simply calculated using the law of cosines. In the case of STeM's mechanical design, where r equals 1 cm and l equals 2.5 cm, the range is approximate $\pm 67^\circ$ symmetrically due to the orthogonal placement of the struts.

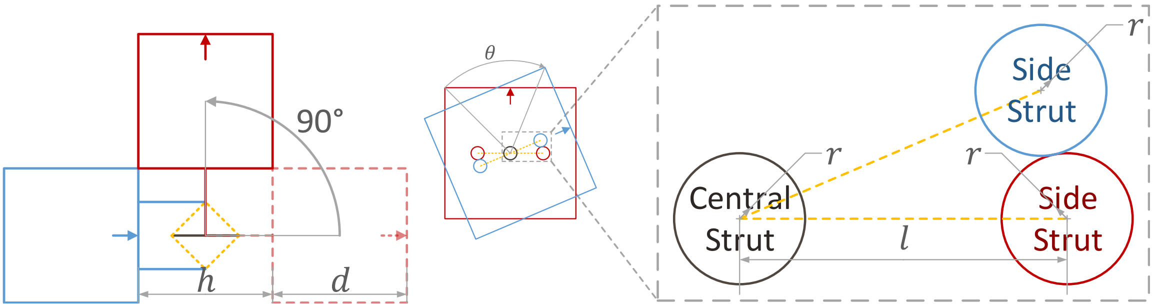

(a) (b)

Figure 5.1 The passive workspace of the STeM determined by the constraints of the rigid parts. (**a**) The workspace of tilt motion (pitch or yaw) is limited by the physical volume of the cubic hubs. (**b**) The workspace of roll motion is limited by the physical volume of the struts.

5.2.2 Inverse Kinematics

Prior to the determination of active workspace, the inverse kinematics need to be established so that given a desired posture, the resultant geometry of the structure can be calculated for subsequent analysis. As discussed in Section 4.2, the active substructure adopts a topology of parallel mechanism and is similar to the Stewart platform [109], but only rotates about the origin O, providing actuated three degrees of rotational freedom with limited translational freedom. An abstract model illustrating exclusively the rotational motion of the STeM is depicted in Figure 5.2.

Assuming one side of the STeM is fixed, here taking face $N_1N_2N_3$ as an example, the coordinates of vertices of face $M_1M_2M_3$ can be given by:

$$\begin{aligned}\boldsymbol{M}_i^{'''} &= \boldsymbol{R}_{yXZ}\boldsymbol{M}_i \\ &= \begin{bmatrix} c_1c_3+s_1s_2s_3 & c_3s_1s_2-c_1s_3 & c_2s_1 \\ c_2s_3 & c_2c_3 & -s_2 \\ c_1s_2s_3-c_3s_1 & c_1c_3s_2+s1s3 & c_1c2 \end{bmatrix}\boldsymbol{M}_i, \quad i=1,2,3\end{aligned} \tag{5.1}$$

with

$$\boldsymbol{R}_{yXZ} = \boldsymbol{R}_{zxy} = \boldsymbol{R}_y(\alpha)\boldsymbol{R}_x(\beta)\boldsymbol{R}_z(\gamma),$$

$$\boldsymbol{R}_y(\alpha) = \begin{bmatrix} cos(\alpha) & 0 & sin(\alpha) \\ 0 & 1 & 0 \\ -sin(\alpha) & 0 & cos(\alpha) \end{bmatrix},$$

$$\boldsymbol{R}_x(\beta) = \begin{bmatrix} 1 & 0 & 0 \\ 0 & cos(\beta) & -sin(\beta) \\ 0 & sin(\beta) & cos(\beta) \end{bmatrix},$$

$$\boldsymbol{R}_z(\gamma) = \begin{bmatrix} cos(\gamma) & -sin(\gamma) & 0 \\ sin(\gamma) & cos(\gamma) & 0 \\ 0 & 0 & 1 \end{bmatrix},$$

$$\boldsymbol{M}_i = \begin{bmatrix} \frac{d}{2}cos(\frac{2\pi}{3}(i-1)+\frac{5\pi}{6}) \\ \frac{d}{2}sin(\frac{2\pi}{3}(i-1)+\frac{5\pi}{6}) \\ \frac{h}{2} \end{bmatrix},$$

where α, β and γ are Euler angles (Tait–Bryan convention) following the Y–X–Z rotation sequence, respectively; $\boldsymbol{M}_i$ is the coordinates of face vertices M_1, M_2 and M_3 at reference frame and $\boldsymbol{M}_i^{'''}$ is the coordinate of these vertices after the third Euler rotation.

5.2.3 Active Workspace

To identify the mechanism's actuated workspace, the Force Closure Check (FCC) algorithm proposed in [113] is applied. The algorithm is originally used for checking high dimensional force closure condition of a cable-driven parallel mechanism (CDPM), which normally has a fixed infrastructure and a platform moving within the framework controlled by the cables connecting them. Assuming the threads can provide infinite tension forces, a specific posture

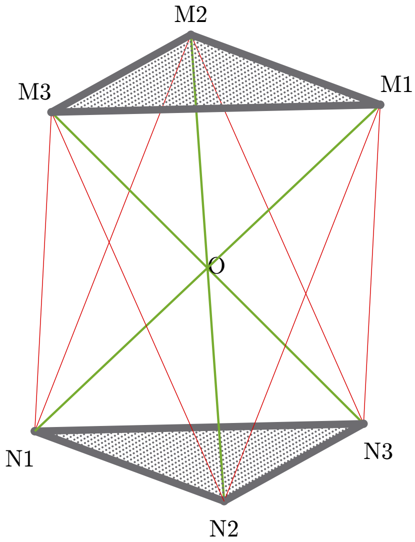

Figure 5.2 The abstract model exclusively illustrating the rotational motion of the STeM about the origin O.

of the STeM is considered within the workspace when it forms an equilibrium with all internal and external applied forces and torques.

To determine the force closure condition of a given posture, a structure matrix is firstly created to describe force and torque conditions of the STeM. The structure matrix is normally a 6-by-n matrix, where n corresponds to the total number of threads actuating the structure. From the first to last, each row denotes the resultant force along the x, y and z axes and the resultant torque about the x, y and z axes, respectively. For each column, it represents the force and torque imposed by a specific thread on the structure. Since the design of STeM significantly limits the translational freedom of the tensegrity structure, the first three rows' elements can be ignored without affecting the calculation and thus the matrix $\boldsymbol{A}_{3,6}$ can therefore be given by:

$$\boldsymbol{A}_{3,6} = \begin{bmatrix} \boldsymbol{M}_1''' \times \boldsymbol{v}_{13} & \boldsymbol{M}_2''' \times \boldsymbol{v}_{23} & \boldsymbol{M}_2''' \times \boldsymbol{v}_{21} & \boldsymbol{M}_3''' \times \boldsymbol{v}_{31} & \boldsymbol{M}_3''' \times \boldsymbol{v}_{32} & \boldsymbol{M}_1''' \times \boldsymbol{v}_{12} \end{bmatrix}, \tag{5.2}$$

with

$$\boldsymbol{v}_{ij} = \frac{\boldsymbol{N}_j - \boldsymbol{M}_i'''}{|\boldsymbol{N}_j - \boldsymbol{M}_i'''|}, \qquad ij \in \{13, 23, 21, 31, 32, 12\}$$

$$\boldsymbol{N}_j = \begin{bmatrix} \frac{d}{2} cos(\frac{2\pi}{3}(j-1) - \frac{5\pi}{6}) \\ \frac{d}{2} sin(\frac{2\pi}{3}(j-1) - \frac{5\pi}{6}) \\ -\frac{l}{2} \end{bmatrix},$$

where $\boldsymbol{v}_{ij}$ is the unit vector representing the force direction applied on vertex $\boldsymbol{M}_i^{''''}$, that is collinear with the active threads, and $\boldsymbol{A}_{3,6}$ is a 3-by-6 torque matrix where each column's elements represent a torque provided by the thread in the tensegrity structure.

For each torque vector in the matrix, the other torque vectors are projected onto the hyper plane orthogonal to this vector to form a lower dimension matrix filled with new non-zero torque vectors, recursively, until the column dimension is 1. Through this process, the structure matrix $\boldsymbol{A}_{3,6}$ is reduced twice on its column dimension to generate six 2-by-5 matrices and 6×5 1-by-4 matrices. For each row in all generated matrices, the sign of the elements is checked. Whenever there is an all negative or all positive row, the posture under inspection fails with FCC.

For the whole workspace, search trials were taken on pitch, yaw and roll angle combinations of range $[-90°, 90°]$ for each with a resolution of 1°, which results in a total number of $5,929,741$ FCCs. The full workspace of the tensegrity mechanism is illustrated in Figure 5.3, which consists of $2,141,901$ valid postures.

The full workspace result reveals that the maximum range of each rotation motion is variant and dependent on the values of the other two. Taking roll range output based on 0° yaw angle and $[\![-90°, 90°]\!]$ pitch angles as an example, the maximum swing decreases when the pitch angle is approaching the negative limit, as shown in Figure 5.4a. It can also be observed that the pitch motion could reach further in the positive direction for some specific roll angles. The remaining two combinations, which are roll range with respect to yaw range and yaw range with respect to pitch range, are illustrated in Figure 5.4.

To provide an intuitive estimation of the workspace, the absolute actuation ranges for independent pitch, yaw and roll rotation were investigated, where the results are $[-71°, 71°]$, $[-81°, 81°]$ and $[-59°, 59°]$, respectively, as visualised in Figure 5.5.

The FCC algorithm determines the theoretical maximum limits of the workspace. The physical constraints or influences of the practical system are not considered, such as the load capacity of threads and the maximum output power of actuators, as well as the variation among fabrication of prototypes, which refers to reality gap issues. Thus, the practical workspace is an implementation dependent attribute varying among designs and prototypes but smaller than these absolute extremes.

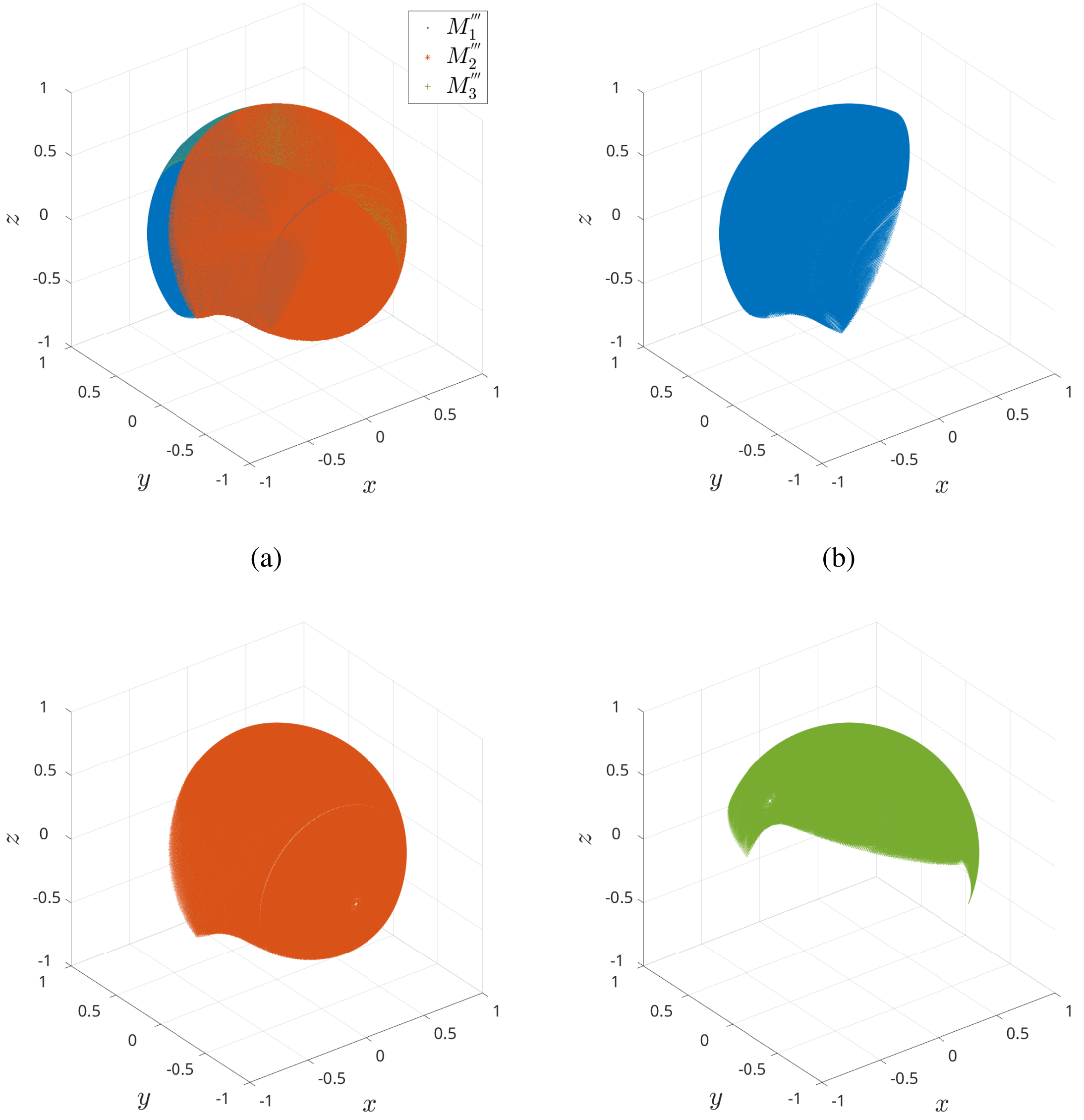

(a)

(b)

(c)

(d)

Figure 5.3 Active workspace of the STeM. (**a**) Full workspace encompassing all three vertices. (**b-d**) Individual workspace for each vertex M_1''', M_2''' and M_3''', plotted separately.

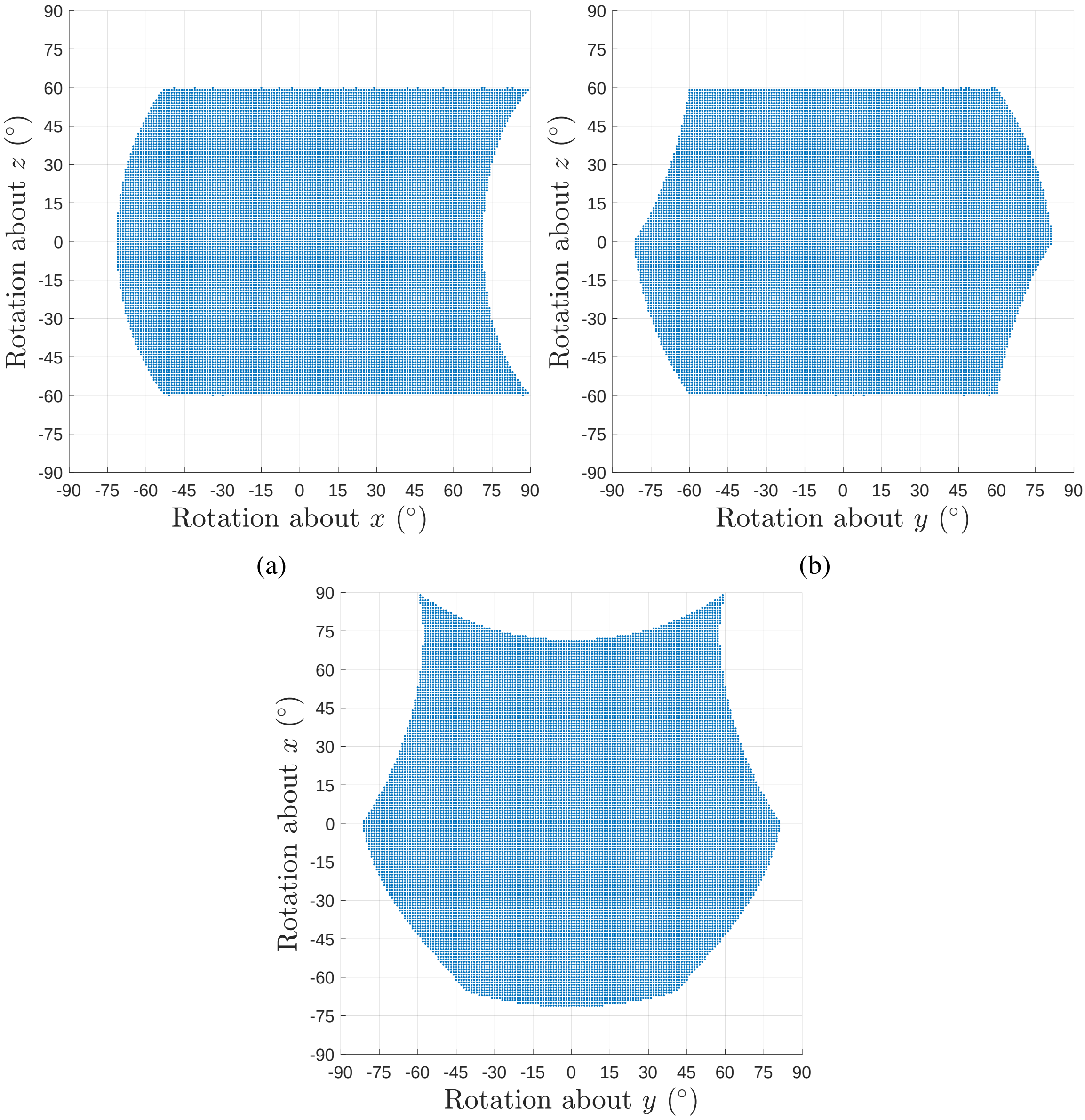

(a)

(b)

(c)

Figure 5.4 Workspace of the STeM about two rotation axes in combinations. (**a**-**c**) Range of rotation about *x*-*z* (pitch-roll), *y*-*z* (yaw-roll), and *y*-*x* (yaw-pitch) combinations, respectively.

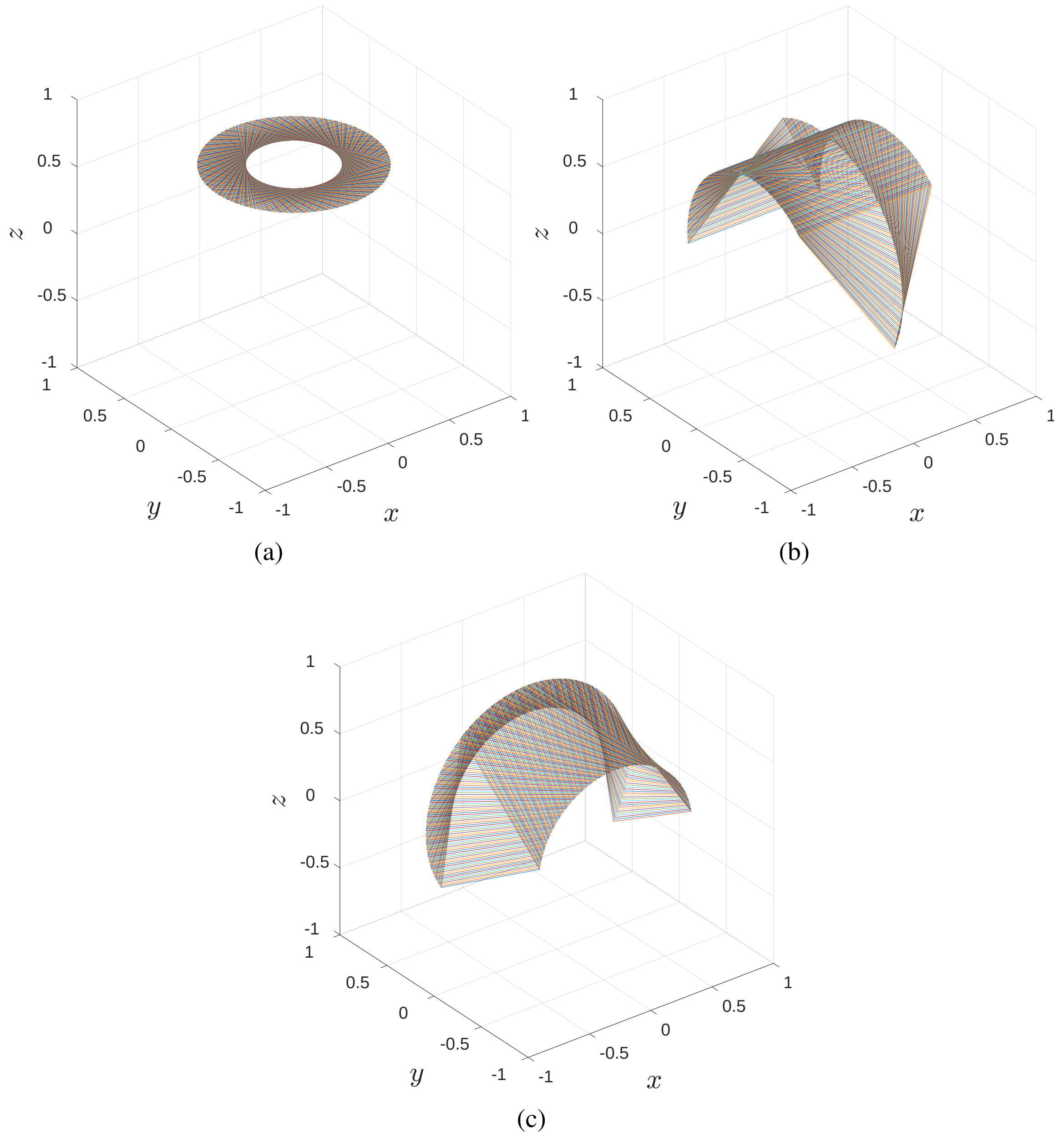

(a)

(b)

(c)

Figure 5.5 Workspace of the STeM for rotation about each axis. (**a**-**c**) Range of independent rotation about *z* (roll), *x* (pitch) and *y* (yaw) axis, respectively.

5.3 Control of the STeM

To maintain the stability of the tensegrity structure, it is inevitable to keep the structure pretensioned throughout its operation. Since the threads of passive substructure are not actuated and their rest lengths are determined with pretension at fabrication, the control problem for the STeM is solving the appropriate force distribution that should be exerted among the active threads. However, although constrained by the design of the passive substructure, the rotation pivot point of the STeM still experiences a small amount of displacement. To address this, modelling the STeM, which is a multi-body system, based on frameworks such as matrix differential equations or vector differential equations requires non-trivial calculations. To reduce the computation load for real time operation and at the same time leverage the characteristics of the STeM, a key strategy is applied to mitigate the control issues brought about by the structure's parallel essence and elasticity, which is the simplification of the structure.

As the threads are constantly fastened, the passive substructure of the STeM exerts constraints on the transitional displacement among the compression elements, which are the centre strut and side struts. Such displacement is significantly smaller compared with the rotational movement and thus the position of the pivot point can be assumed fixed with respect to the rotational movement. Given such a situation, two approaches can be employed which are the uniform pretension and the force closure based pretension, described in the following sub-sections.

5.3.1 Uniform Pretension

As suggested by its name, the uniform pretension method simply introduces the same pretension forces to all the active threads by shortening the threads by the same ratio of the length calculated from the inverse kinematics. Through this way, the overall pretension, or energy stored, of the structure is consistent from posture to posture, and therefore exhibiting a similar characteristic over time.

However, due to the active threads have different length of moment arm, the uniform pretension method will inevitable introduce extra inaccuracy to the control.

5.3.2 Force Closure based Pretension

In addition to determining the workspace of a CDPM, the force closure principle can also be used to calculate the required forces on the threads given a desired posture of the platform, by establishing the equation of force equilibrium between them using the structure matrix instead of directly analysing the matrix. The equation relies on the fact that there is a fixed enclosure infrastructure to provide anchor points for the threads, which result in the wrench applied on the platform. Although the geometry of the STeM is not similar to that of CDPMs, owing to the unique topology of the STeM, the force closure approach can be ported to the control of the STeM. During modelling, analogising the STeM with a typical CDPM, one side of the STeM can be considered as the virtual fixed infrastructure while the other side acts as the platform. Although the number of degrees of freedom is different, the principle still holds and can therefore be applied to facilitate the calculation of pretension forces.

Similar to the workspace determination, a structure matrix is also required to establish the equation of force equilibrium. However, the difference here is the structure matrix takes the size of 6x7 instead of 3x6 used in Section 5.2.3. Given the coordinates of the nodes, the structure matrix $\boldsymbol{A}_{6,7}$ can thus be organised as in (5.3).

$$\boldsymbol{A}_{6,7} = \begin{bmatrix} \boldsymbol{v}_{13} & \boldsymbol{v}_{23} & \boldsymbol{v}_{21} & \boldsymbol{v}_{31} & \boldsymbol{v}_{32} & \boldsymbol{v}_{12} & \boldsymbol{v}_{pvt} \\ \boldsymbol{M}_1^{'''} \times \boldsymbol{v}_{13} & \boldsymbol{M}_2^{'''} \times \boldsymbol{v}_{23} & \boldsymbol{M}_2^{'''} \times \boldsymbol{v}_{21} & \boldsymbol{M}_3^{'''} \times \boldsymbol{v}_{31} & \boldsymbol{M}_3^{'''} \times \boldsymbol{v}_{32} & \boldsymbol{M}_1^{'''} \times \boldsymbol{v}_{12} & \boldsymbol{0} \end{bmatrix} \tag{5.3}$$

The reason for employing six rows is to facilitate the calculation of the equation. In typical implementations, the platform of a CDPM normally havs six degrees of freedom and is actuated by no less than seven threads. This is true since the threads can only provide pulling forces so that it requires at least N+1 threads to constrain N degrees of freedom. When there are N+1 threads constraining the N degrees of freedom, it forms a completely-constrained parallel mechanism configuration for which the results can be obtained with the inverse of a square matrix.

The first row in the matrix denotes the direction of the forces generated by the threads while the second row denotes the corresponding torques. The first six columns denote the force and torque applied on the STeM by the threads similar to that of $\boldsymbol{A}_{3,6}$. The 7th column denotes a dummy force exerted by the constraint of the passive substructure. While the forces on the active threads pull the cubic hubs on the two sides towards each other, the dummy forces keep them apart. Since the dummy force passes through the virtual pivot point, the last column is represented by an element $\boldsymbol{v}_{pvt}$ representing the direction of the force and a torque element of $\mathbf{0}$. Then, the equation of equilibrium is given by:

$$\boldsymbol{A}_{6,7}\boldsymbol{f} + \boldsymbol{\omega} = \mathbf{0}, \tag{5.4}$$

with

$$\boldsymbol{f} = \begin{bmatrix} f_{M_1N_3} & f_{M_2N_3} & f_{M_2N_1} & f_{M_3N_1} & f_{M_3N_2} & f_{M_1N_2} & f_{pvt} \end{bmatrix}^T,$$

$$\boldsymbol{\omega} = \begin{bmatrix} \boldsymbol{f}_{ext} \\ \boldsymbol{\tau}_{ext} \end{bmatrix},$$

where $\boldsymbol{f}$ is the forces applied on the movable side by the threads and $\boldsymbol{\omega}$ is the external moment. Since STeM only actively rotates, the term $\boldsymbol{f}_{ext}$ is actually configured to zero. To simplify the calculation process, Equation 5.4 can be rewritten as:

$$[\boldsymbol{B}\ \boldsymbol{h}] \begin{bmatrix} \boldsymbol{f}_{act} \\ f_{pvt} \end{bmatrix} + \boldsymbol{\omega} = 0 \tag{5.5}$$

where $\boldsymbol{B}$ is a 6-by-6 square matrix representing the actuated threads and $\boldsymbol{h}$ is a column vector representing the virtual pivot point. $\boldsymbol{f}_{act}$ is the pulling forces of the actuated threads and f_{pvt} is the force applied at the virtual pivot point. The forces are therefore given by Equation 5.6.

$$\boldsymbol{f}_{act} = \left[-\boldsymbol{B}^{-1}\boldsymbol{h}\right] f_{pvt} + \left[-\boldsymbol{B}^{-1}\boldsymbol{\omega}\right] \tag{5.6}$$

It can be seen from the equation that the forces of the actuated threads are determined by two factors: the desired force applied at the virtual pivot point and the desired output torque at a specific posture, given by the first and second components in the right hand side of the equation.

Since the tensile force of the elastic thread with a given modulus of elasticity and cross-sectional area is linearly proportional to its fractional extension, the forces $\boldsymbol{f}_{act}$ can thus be controlled by the corresponding pretension ratios on the actuated threads, that is, by changing the rest length of the threads. The pretension ratios $\boldsymbol{\phi}_{act}$ for the actuated threads are given by:

$$\boldsymbol{\phi}_{act} = \boldsymbol{f}_{act} f_{base}^{-1} \phi_{base} \tag{5.7}$$

where f_{base} is the tensile force generated on the thread for the given pretension ratio ϕ_{base}. Therefore, the required changes of the rest length $\Delta \boldsymbol{l}$ that need to be controlled by the actuators are simply as that in Equation 5.8:

$$\Delta \boldsymbol{l} = \left[\boldsymbol{l}_{IK}\ \mathbf{0}_{6,5}\right] \boldsymbol{\phi}_{act} \tag{5.8}$$

where $\boldsymbol{l}_{IK}$ is the thread length obtained from the Inverse Kinematics stage.

5.4 Evaluation of STeM

With the control strategy established, the evaluation of the STeM was divided into three aspects, the actuation analysis which reflected its force distribution and accuracy properties as a basis, the structural examination which demonstrated its robustness as a soft structure from a low-level perspective, and the locomotion assessment which proved its high-level robustness endowed by the capabilities of the STeM design.

5.4.1 Actuation Analysis

In advance to the application of STeM in robotics actuation purposes, its actuation characteristics need to be investigated. The accuracy of the STeM's motion is one of the important criteria for intuitively evaluating it as a rotational actuator. Hidden behind, as a CDPM-like system, the distribution of the internal forces is the determinant factor to the accuracy. Therefore, these two properties are investigated in the following two sub-sections.

Force Distribution

The STeM maintains a specific posture through the force equilibrium of the structure, it is thus critical to distribute the forces on the threads as expected to ensure the motion accuracy. In addition, as the actuators have physical limitations in providing pulling forces, the force distribution also affects the performance and proper operation of the system.

To evaluate the effect of different control approaches, a sweep test was performed on each rotation axis within a target range of $[-30°, 30°]$. Since the uniform pretension method cannot compensate the effect of gravity, the output wrench $\boldsymbol{\omega}$ in the second component in (5.6) was set to $\mathbf{0}$ for the force closure based pretension as well. The dummy force f_{pvt} of the first component in Equation 5.6 was configured so that the resulted $\boldsymbol{f}_{act}$ was the same as the uniform pretension at the neutral posture. The direction of the force $\boldsymbol{v}_{pvt}$ applied at the pivot point was defined in parallel with the line connecting the geometric centres of the equilateral triangles on the two sides of the tensegrity structure. Aside from the comparison with the uniform pretension, two different baselines were applied to the force closure based approach during the calculation of the threads' pretension ratios: (i) to preserve a consistent overall pretension force in the tensegrity network, (ii) to preserve a consistent maximum pretension force across the actuated threads during operation. Such scaling of the forces on the actuated threads was feasible relies the property that these required forces are a linear combination of the desired internal pretension and output torque, which are given by the two components in Equation 5.6 respectively.

Figure 5.6 illustrates the comparison for the internal force distribution with the three pretension approaches in simulation as well as for the consistent maximum pretension force method implemented in the prototype. It can be seen from the results of uniform pretension, especially in Figure 5.6a and 5.6b, that the rising trend of the forces on the actuated threads gradually decelerates as the angle approaches the test range limitations. This is particularly obvious for threads A_2P_3 and A_3P_2 during the pitch motion. Due to the loss of pretension forces, the forces on threads A_2P_1 and A_3P_1 drops to zero at its positive maximum pitch posture which suggests a degradation of the stability. Figure 5.6d to 5.6f illustrate the improvement of internal forces using the FC based pretension. The slope of the forces are retained across the whole test motion stroke. However, to retain the same overall pretension force as the value at the neutral posture, the maximum force increases to compensate the decrement of forces on certain threads. The maximum force observed in the results of the consistent overall pretension force method is approximate 32.5 N while for the uniform pretension method stops at about 25 N. A greater pretension force exerted in the threads leads to a stiffer and more stable system. However, larger forces generated from the actuators also require higher power and more energy consumption, which worsens the common issue of tensegrity robots' motion efficiency. Therefore, for general scenarios where a higher compliance is beneficial, the second baseline can be employed to ensure a safe operation while not affecting the desired motion. For the second baseline, the consistent maximum force equal to the force at neutral posture is chosen as the upper limit for calculating the corresponding pretension ratios.

As shown in Figure 5.6g to 5.6i, the forces have a common characteristic that there is a sharp turning point at the neutral position for all the threads and motions. This is because the pretension ratios, that is, the forces of the actuated threads are linearly scaled with a different f_{base} value. From the perspective of the visualisation using graphs, it is presented by a proportional downward shifting of the lines in the second row and thus forms the turning point at the neutral posture in the third row. Based on this method, the maximum force observed is approximate 22 N. The minimum force is about 2 N and occurs on threads A_2P_1 and A_3P_1 at the positive maximum pitch motion as well. The corresponding force on threads A_1P_3 and A_1P_2 at this posture is about 19 N, which is 4.5 N smaller than that for the uniform pretension. This indicates the FC based pretension has a better distribution of the forces. Compared with the consistent overall force method, as the downward shift is a proportional scaling, the maximum required force is greatly reduced while the minimum force changes less. The results shown in the third row of Figure 5.6 reveals that the consistent maximum force method achieve a balance point between the stability of the structure and the requirement of the pretension forces.

The results of the prototype experiment is shown in Figure 5.6j to 5.6l for the practical validation of the control strategy. These figures illustrate a unique characteristic not existing in the simulation, which is hysteresis due to the threads' elasticity. Unlike the lines in the simulation figures, the lines of forces for the elongation and shortening paths does not overlap and forms a closed contour for the prototype test sweep motion. Such a difference is within expectation that this characteristic is common for elastic materials but not implemented in the simulation platform. Comparing figures in the third and fourth rows in Figure 5.6, the trends of the lines generally match each other apart from some threads such as A_2P_3 and A_3P_2 during the pitch motion and A_2P_1 and A_3P_1 during the yaw motion. Another difference is the value of the forces measured where the prototype forces are approximate 60% of the simulation value since the start at the neutral posture for each motion. These are potentially caused by the thread actuation scheme applied in the prototype where the threads are directly wound on the output shaft of the geared motors acting like a winch. The small friction and relatively large pulling forces allow the threads to slide on the shaft along their axial axis. This means the actual shortened length Δl for generating pulling forces is less than the expected value and thus the unwound "free" threads connecting the active and passive sides are longer than desired.

In general, through comparing the force distribution among different approaches, it is clear that the force closure based pretension combined with the consistent maximum force method effectively reduced the disparity of the forces among active threads. The alignment of force distribution patterns between the simulation and prototype results further underscored the efficacy of such approach applied in practical implementations.

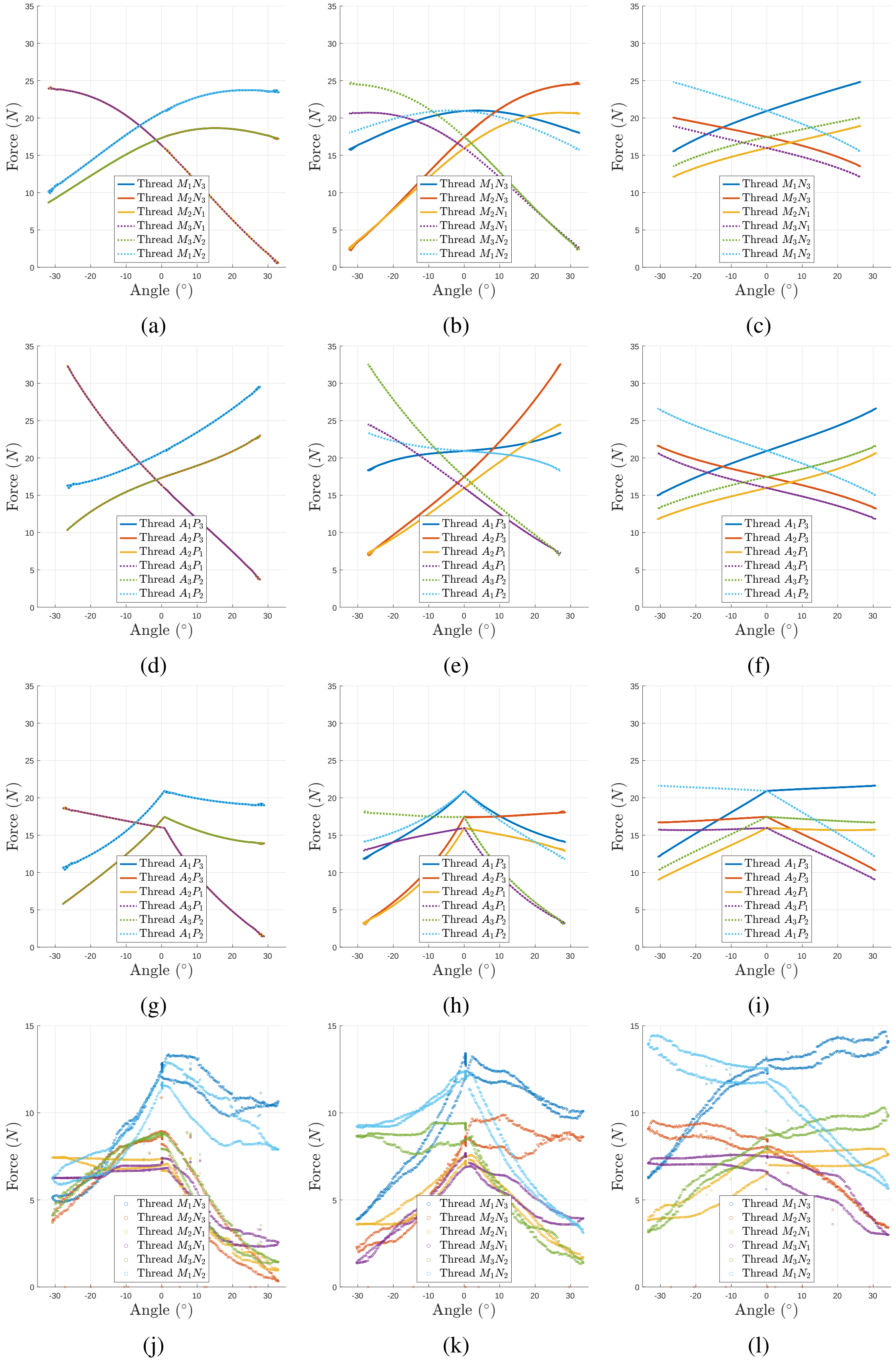

(a) (b) (c)

(d) (e) (f)

(g) (h) (i)

(j) (k) (l)

Figure 5.6 Force distribution of the active threads for each motion and experiment. (**a-c**) The uniform pretension in simulation. (**d-f**) The consistent overall force using FC pretension in simulation. (**g-i**) The consistent maximum force using FC pretension in simulation. (**j-l**) The consistent maximum force using FC pretension for prototype. Columns from left to right illustrate the force distribution of pitch, yaw and roll motion respectively.

Motion Accuracy

The STeM's motion was initially tested using the uniform pretension method as a primitive validation of the estimated large workspace in simulation. To avoid thread collisions with the rigid parts given the physical volume of the substructure and to prevent the STeM from moving out of the workspace, the maximum pitch and yaw angles were restrained to ±55° , and the maximum roll angles remained unchanged as ±60°. A comparison between the observed and expected motion of the movable cubic hub with respect to each active degree of rotational freedom is presented in Figure 5.7. With a uniform 95% pretension ratio, it is clear the observed motion waveform followed expected lines for all three rotational motions. The maximum observed range of pitch, yaw and roll motion were approximately $[-59.0°, 58.9°]$, $[-59.4°, 59.4°]$ and $[-47.1°, 47.1°]$, respectively. It should be noted that there was a continuous deviation between the observed and expected lines which increased over the growth of angle values. This was caused by the invariant uniform pretension ratio in all threads while the moment arms were continuously changing along operation. For pitch and yaw motions, the observed lines went beyond the inputs while the observed roll motion did not reach the input.

There was a continuous offset observed for the pitch deviation, especially at the neutral posture, revealing the inherent compliance of the STeM. With the Earth surface gravity and a pretension ratio of 95%, the mechanism gave a static pitch deviation of about 0.43° due to its self weight, while this value was about 2.5 times larger without pretension at about 1°. The oscillation during motion caused by the flexible tension elements was also perceivable as well as the settling time difference affected by the changes in tension force, which are explained in more detail in subsequent intrinsic frequency analysis.

The deviation of different expected motion angles are plotted in Figure 5.8a. The scatters are composed of both outbound and inbound for the two directions of the three rotational motions performed during the test. According to the results, although the deviation increased over the growth of motion angle, the pitch and yaw motions' growth curves gradually slowed down. In addition, the effect of gravity was perceivable over the whole pitch motion workspace as a persistent offset on its curve, making the curve not pass through the origin. To further investigate the effect of the uniform pretension, Figure 5.8b demonstrates the deviation values at a pitch angle of 33° (60% of the ±55° workspace limit) with respect to different pretension ratios. Note that the distribution was too narrow to visualise the box. The whiskers were given by the oscillation occurred at each steep change of the pretension ratio. The results generally exhibited a linear relationship for such pretension approach.

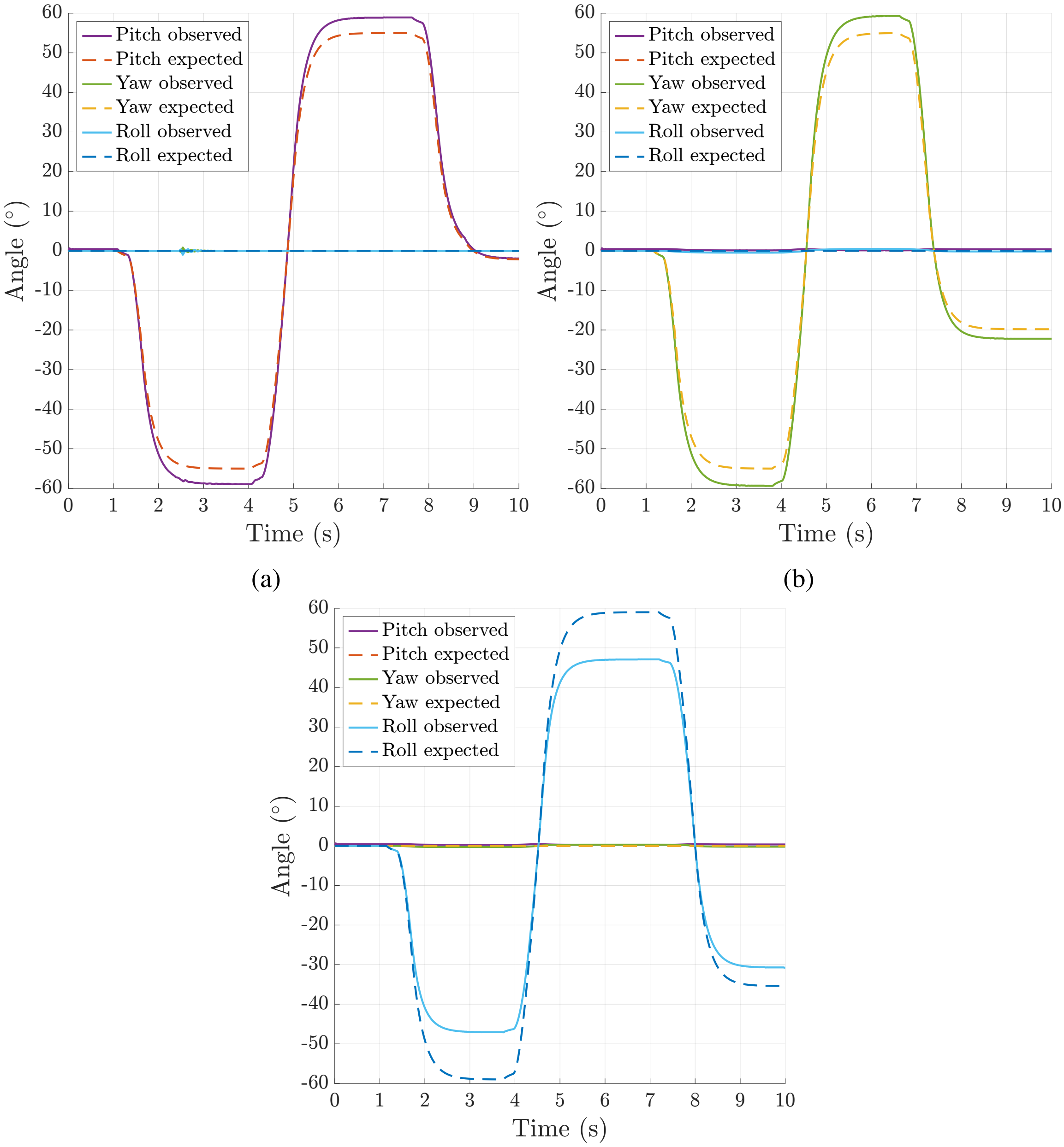

(a)

(b)

(c)

Figure 5.7 Waveform of observed and expected motion of the movable cubic hub over simulation time. (**a**-**c**) The pitch, yaw and roll individual motions, respectively.

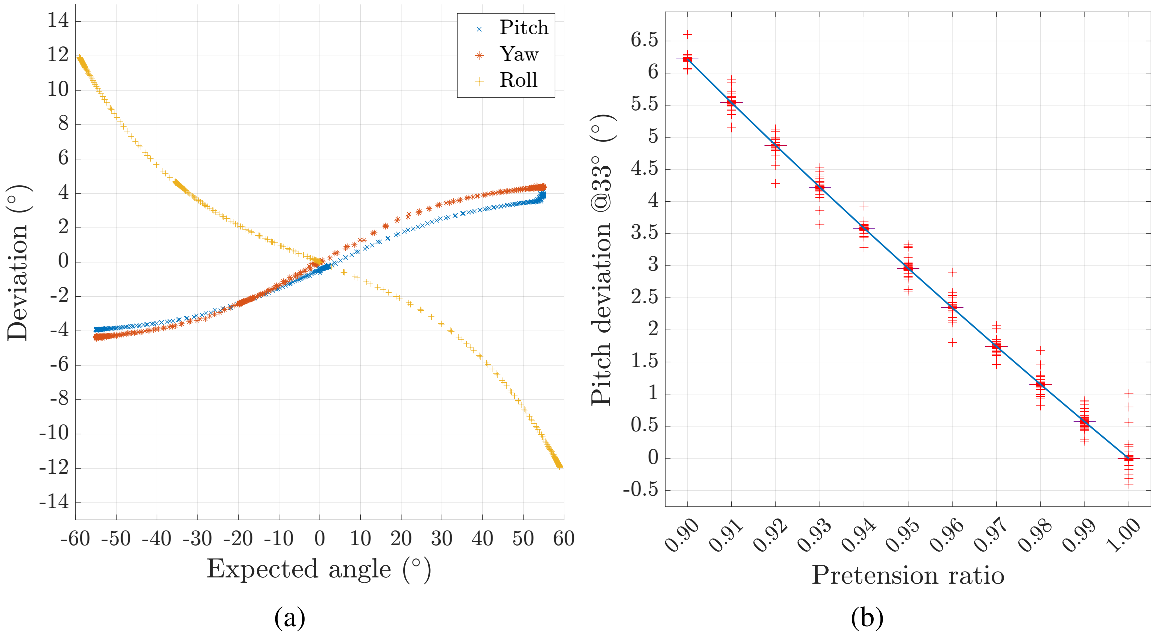

(a) (b)

Figure 5.8 Deviation of the STeM's motion in simulation. (**a**) The deviation with respect to expected angles for all three motions. (**b**) The deviation with different uniform pretension ratios at an expected pitch angle of 33°.

To compare the performance of the two control approaches, the force closure based pretension was also tested. As shown in Figure 5.9a, at the neutral posture, the uniform and force closure based pretension methods had the same deviation caused by the gravity as expected. A clear difference that can be observed between the two methods was the signs of the values. The expected angle and the deviation with the same sign suggested the actual motion goes beyond the target posture while an opposite sign indicated not reaching the target posture. Figure 5.9b shows the absolute deviation of the two pretension methods for a more intuitive view. It clearly revealed that the force closure based pretension performed better than the uniform method, especially for the roll motion where the deviation decreased approximate 83% from 3.6° to 0.6°.

However, when comparing the prototype and simulation experiment results for the force closure method, the signs of the deviation exhibited a combination of the characteristics of the uniform and force closure based methods. The same sign for the roll motion proved that the force closure based pretension worked well according to the results in Figure 5.9a and 5.9c. For the pitch and yaw motion, the prototype's actual motion also exceeded the target posture which was similar to the uniform pretension. This was assumed to have the same root cause as the low pretension forces observed in the force distribution experiment.

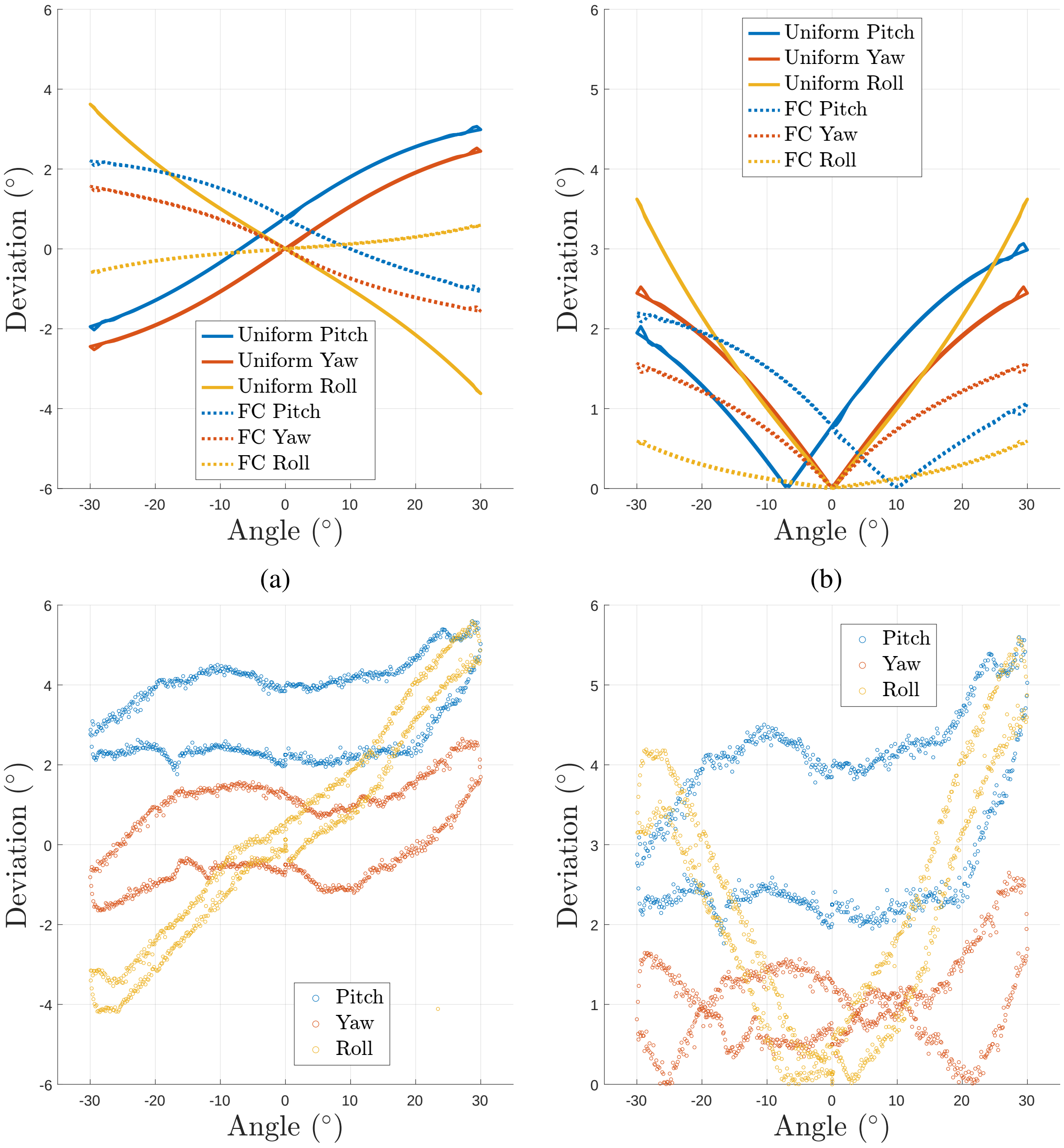

(a) (b)

(c) (d)

Figure 5.9 Comparison of the accuracy of STeM's motion with respect to the three rotational movement. (**a**-**b**) The raw and absolute deviation in simulation. (**c**-**d**) The raw and absolute deviation of the prototype test.

The direct cause can be explained using the changes of the threads' length. Comparing the forces in Figure 5.6b and the lengths in Figure 5.10, it can be observed that the threads with a longer length bore a higher pulling force. When the structure rotated about the pivot point, the moment arm for the shorter thread was longer than the opposite thread. Therefore, for the same pretension forces exerted on the two threads, a moment generated and rotated the structure to the short thread side. When the actuator did not shorten the thread precisely for the force closure method, the resulted motion deviated in a similar way to the uniform method.

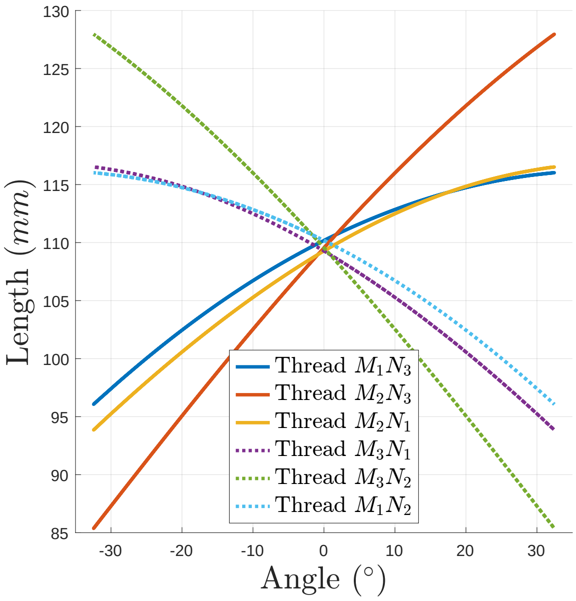

Figure 5.10 Cause of the deviation with respect to the changes of the threads' length during motion with yaw motion as an example.

5.4.2 Structural Examination

One of the primary reasons for incorporating tensegrity structures into the modular robot was to enhance its robustness, allowing it for example to deform to external loads, absorb impacts, and maintain stable states. Therefore, its characteristics as a soft structure need to be investigated to gain knowledge of the appropriate working conditions, including the stiffness, energy dispersion, intrinsic oscillation frequency, and fault tolerance.

Stiffness

As a tensegrity based mechanism, the robustness of the STeM is reinforced through its compliance under external loads and its resilience in returning to the neutral form when unloaded. These characteristics are closely related to the stiffness of the structure which is determined by the level of pretension. In this section, the stiffness of the STeM was examined through load bearing tests in simulation to investigate the static performance. During the test, a gradually increasing linear torque was applied to the free-moving cubic hub configured in the neutral posture along its x, y, and z axes with different pretension ratios. These axes correspond to the roll, yaw, and pitch motions, respectively. The simulation scene was configured with zero-gravity to eliminate external factors affecting the results. Subsequently, the resulting angles of rotation were recorded. To eliminate the interference from irrelevant motions, several constraints were introduced to each test sequence. A coaxial constraint was added to the roll motion test so that there was no pitch or yaw motion during the movement induced by external loads. In the same vein, the coplanar constraint was added to the pitch and yaw motions.

The static load results clearly demonstrate the STeM's compliance and resilience to external loads in a fully passive manner and revealed the effect of pretension ratios. According to the results illustrated in Figure 5.11, the rotation-torque curves shared a common characteristic that after crossing a smooth region, during which the deformation of the STeM gradually increased as the torque accumulated, they then entered a rapid growth stage up to the physical limitation of the structure. As for the differences, an obvious one was that the yaw and roll motion tests can recover from over-deformed states but not for the pitch motion. For the pitch motion, the STeM entered unrecoverable states with the final torque of approximately 3.42 N.m and 5.60 N.m for 99% and 90% pretension ratios, respectively. For the yaw motion's case, the values were approximately 2.74 N.m and 4.93 N.m, and started a late and sudden recover at a small load of around 2.42 N.m and 1.31 N.m, causing obvious vibrations. Since the physical constraints of the roll motion did not allow it to deform significantly, the recovery curves almost overlapped with the deform ones while the former contained slight vibrations at the start of the recovery stage. The torques were approximately 5.52 N.m and 9.83 N.m for 99% and 90% pretension ratios. The intermediate pretension ratios' results separated approximately evenly among these two extremes. As these results were obtained without gravity, in real word applications, sustained environmental loads, such as self-weight, are expected to occupy a part of the operational range and reduce its resistance to some extent. In such scenarios, it is beneficial to leverage the STeM's active actuation to compensate these effects.

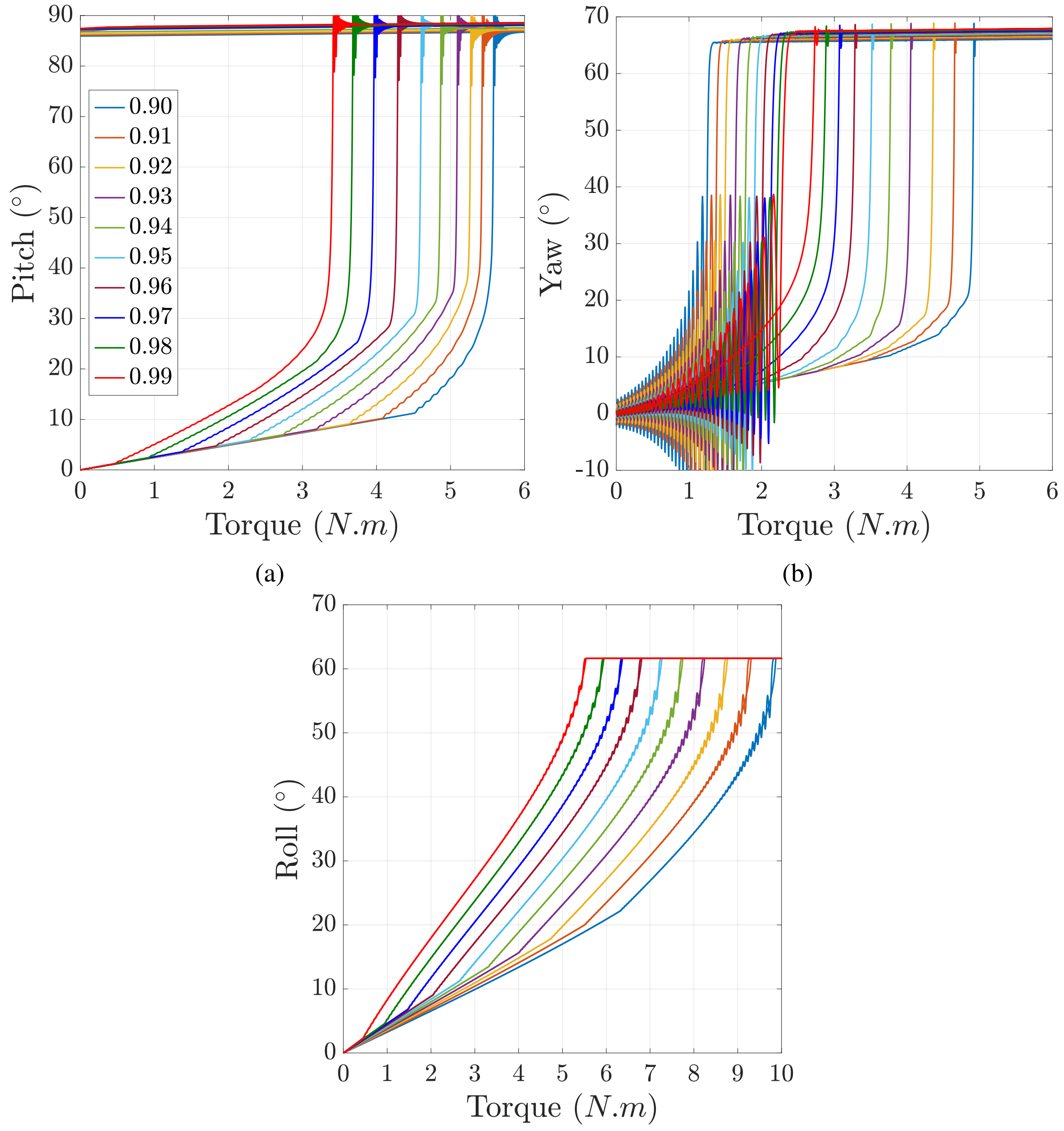

(a) (b)

(c)

Figure 5.11 The rotation caused by external loads applied on the free moving cubic hub. The horizontal and vertical axes represent the external torque and angle of the free moving hub, respectively. The path of each line denotes the hub's trajectory induced by the external load that gradually increased and decreased linearly. (**a**) The pitch motion caused by applying the force along the local z axis of the free moving hub. The force to torque conversion is based on its lever arm of 10 cm, which is the distance from the force application point to the pivot point. (**b**) The yaw motion caused by applying the force along the local y axis of the free moving hub. The force to torque conversion is the same as that of the pitch motion. (**c**) The roll motion caused by applying the torque along the x axis of the free moving hub.

Energy Dispersion

In addition to the stiffness in static scenarios, the energy dispersion property plays an important role to the robustness in dynamic scenarios and can be reflected by examining its impact resistance. To make the evaluation more effective, the robot under test was composed of two STeMs concatenated in series so that there were two stages absorbing the energy to ease the subsequent analysis. The robot was also attached with free rotating wheel tiles to mitigate the effect of friction of the STeM's bottom face with the ground. Pretension ratios of the tensegrity structure from 90% to 99% with a resolution of 1% were tested, as well as a comparison group performed using a rigid replica.

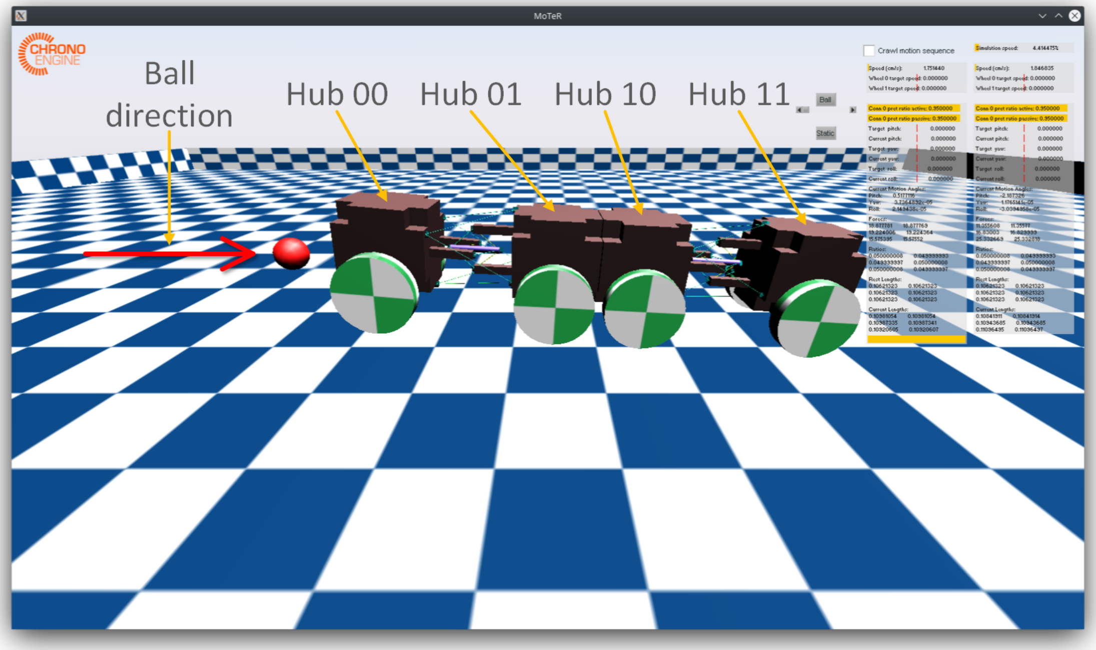

Figure 5.12 The robot composed of two concatenated STeMs, impacted by a solid sphere. The screenshot was captured moments after the collision.

The test was conducted in two configurations. The first configuration, referred as impact test hereafter, was performed by launching a solid metal ball along the longitudinal axis towards the robot, as illustrated in Figure 5.12. The solid ball had a diameter of 40 mm, a density of 8.05 kg/m^3, and was launched at 10 m/s velocity. The second configuration, referred as drop test hereafter, was conducted by making the robot roll freely down a slope and fall off onto a lower level, as shown in Figure 5.13. To obtain the same collision velocity, the robot was dropped from a fixed height of 0.2 m above and parallel with the slope. The angle of the

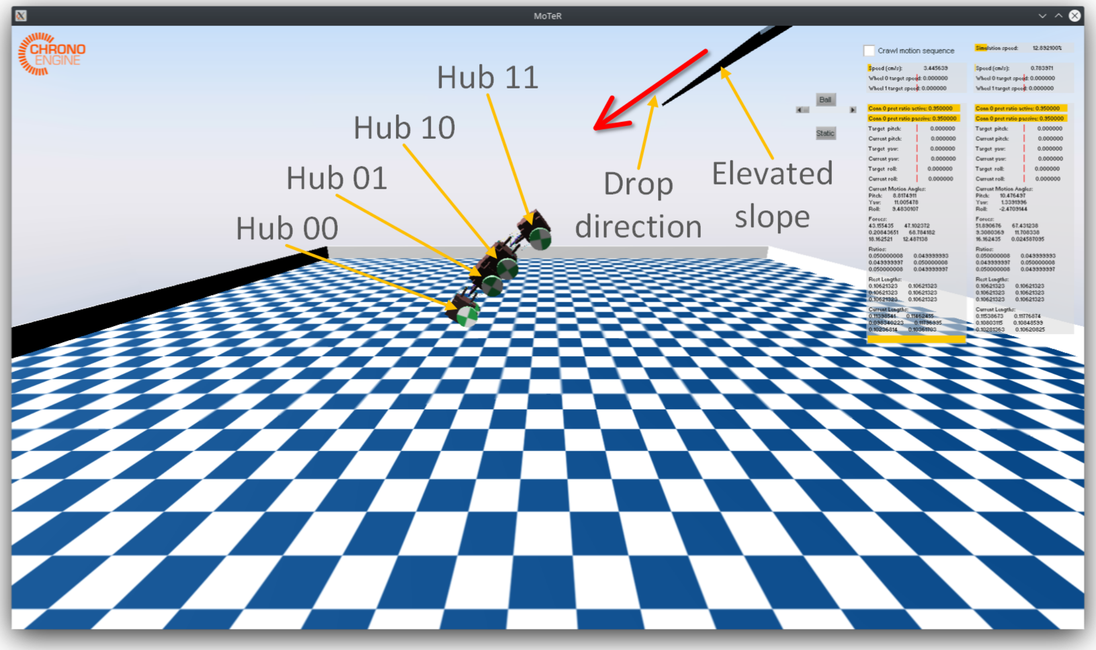

☐ Crawl motion sequence

Speed (cm/s): 3.445639
Wheel 0 target speed: 0.000000
Wheel 1 target speed: 0.000000

Conn 0 pret ratio active: 0.950000
Conn 0 pret ratio passive: 0.950000
Target pitch: 0.000000
Current pitch: 0.000000
Target yaw: 0.000000
Current yaw: 0.000000
Target roll: 0.000000
Current roll: 0.000000
Current Motion Angles:
Pitch: 8.8174911
Yaw: 11.005478
Roll: 9.4830107
Forces:
43.155435 47.102372
0.20843651 68.784182
18.162521 12.487138
Ratios:
0.050000008 0.049999993
0.049999997 0.050000008
0.050000008 0.049999997
Rest Lengths:
0.10621323 0.10621323
0.10621323 0.10621323
0.10621323 0.10621323
Current Lengths:
0.11398541 0.11462455
0.098340223 0.11736995
0.10236814 0.10361703

Simulation speed: 12.892100%

Speed (cm/s): 0.783971
Wheel 0 target speed: 0.000000
Wheel 1 target speed: 0.000000

Conn 0 pret ratio active: 0.950000
Conn 0 pret ratio passive: 0.950000
Target pitch: 0.000000
Current pitch: 0.000000
Target yaw: 0.000000
Current yaw: 0.000000
Target roll: 0.000000
Current roll: 0.000000
Current Motion Angles:
Pitch: 10.476497
Yaw: 1.3391996
Roll: -2.4709144
Forces:
51.890676 67.431238
9.3080369 11.708338
16.162435 0.024587095
Ratios:
0.050000008 0.049999993
0.049999997 0.050000008
0.050000008 0.049999997
Rest Lengths:
0.10621323 0.10621323
0.10621323 0.10621323
0.10621323 0.10621323
Current Lengths:
0.11538673 0.11776874
0.10803115 0.10848599
0.10281363 0.10620825

Figure 5.13 The robot composed of two concatenated STeMs, fall of from a slope onto a lower level. The screenshot was captured moments after the collision.

slope was 30° and the length of the acceleration stage on the slope was 0.5 m. The vertical distance from the edge of the slope to the lower ground was 1 m.

The impact test results are shown in Figure 5.14a. Hub 00 was the one directly facing the ball. Data were taken for 0.2 s starting from the time of contact. The maximum acceleration of its four hubs were almost the same as expected since it was rigidly articulated. Hub 00 of the tensegrity robot bore about two times higher maximum acceleration than the rigid one. In contrast, the rest of the hubs of the tensegrity robot held much lower maximum acceleration at about 1/3 of the rigid one. This proved that the tensegrity articulation prevented the impact from passing unattenuated through the whole network of the robot structure. It can be interpreted as a sacrifice by the hub of impact to protect the rest of the robot from externally inflicted damage. The robot can then decouple the incapacitated STeM and recover from malfunction.

The results of the drop test unveiled better protection of the robot than the impact test. As the robot was facing downwards with a certain angle during falling off, there were two major collisions occurred where the first was the robot head, hub 00, and the second is the robot tail, hub 11. In Figure 5.14b, the box chart presented the acceleration of each hub between

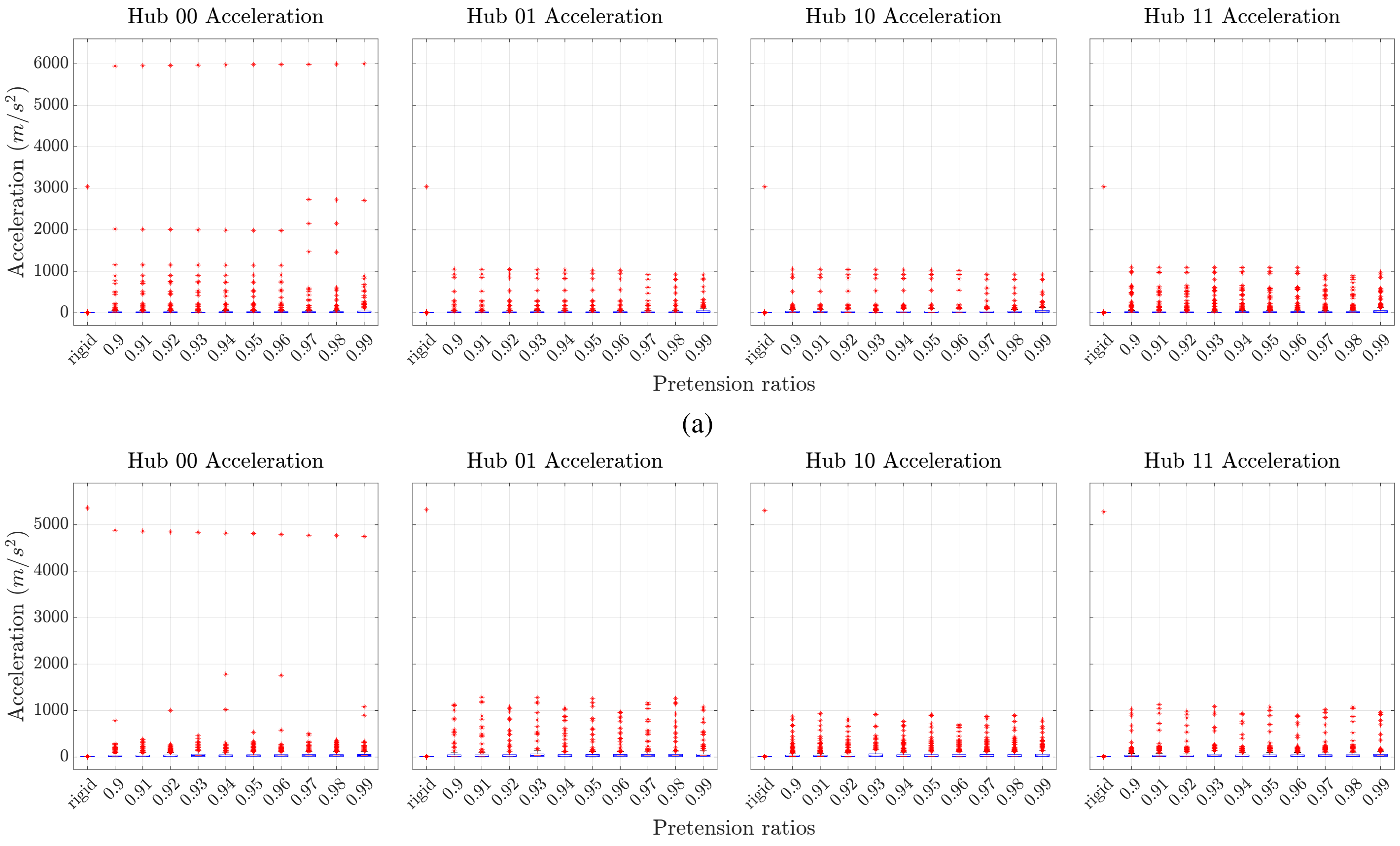

(a)

(b)

Figure 5.14 Acceleration box chart of cubic hubs after collision. (**a**) The impact test results with the ball hitting hub 00. (**b**) The drop test results with hub 00 contacting the ground first. The robot's four cubic hubs are numbered 00, 01, 10, and 11, where the first and second digit denotes the STeM index and the hub index, respectively. The label under each box denotes the pretension ratio used for the data set. The vertical axis represents the acceleration values recorded during the sampling period.

the two major collisions. For the comparison rigid robot, it received a very similar maximum acceleration for all the cubic hubs of approximately 5400 m/s2, where these high acceleration values were resulted from the simulation's use of entirely rigid objects. Hub 00 of the tensegrity robot bore a similar influence as that of the rigid one from the collision. However, for the rest of the hubs, the effect was significantly mitigated at a scale of approximately 80%. Along with the increment of pretension ratios, the maximum acceleration of the hub 00 slightly decreased due to smaller tension force held inside the structure. The results unveiled the improved survivability of the robot during a fall off situation to sustain functionality from such accidents.

Intrinsic Frequency

Aside from the robustness provided by tensegrity, the flexibility of such structure can also introduce potential oscillations into the system. Oscillation is one of the common characteristics of tensegrity, as well as other flexible structures. Such a system should avoid operating under external oscillating sources at its resonance frequencies. Therefore, knowledge of the natural frequency of the STeM is essential for robust operation.

The intrinsic frequency of the STeM was obtained by analysing the oscillation of the free moving cubic hub under Earth surface gravity while the other hub was fixed with respect to the world. The oscillation was generated by fastening the tensegrity structure rapidly from a loose state to act as an impulse applied to the system. The length of the threads were recorded during the oscillation as output.

To visualise the oscillation of the robot, the length of the active threads connecting nodes M_1 and N_3 is plotted in Figure 5.15. At the very beginning, due to the rapid fastening, the free moving hub vibrated and then entered the harmonic motion stage. Since the two hubs became closer due to a small displacement caused by tensioning, the waveform eventually converged to different stable lengths corresponding to the pretension ratios. The rate that oscillations faded away gradually decreased along with the decrease in the pretension amount, while the overall fading rate was slow, indicating a large Q factor and frequency rejection band. It revealed that different pretension ratios did not obviously affect the natural frequency of the mechanism. The 90% pretension ratio led to a intrinsic frequency of 14.9 Hz and a 99% pretension ratio led to 15.9 Hz, which gave an overall difference of 1 Hz and an approximately 0.11 Hz average difference between two adjacent samples.

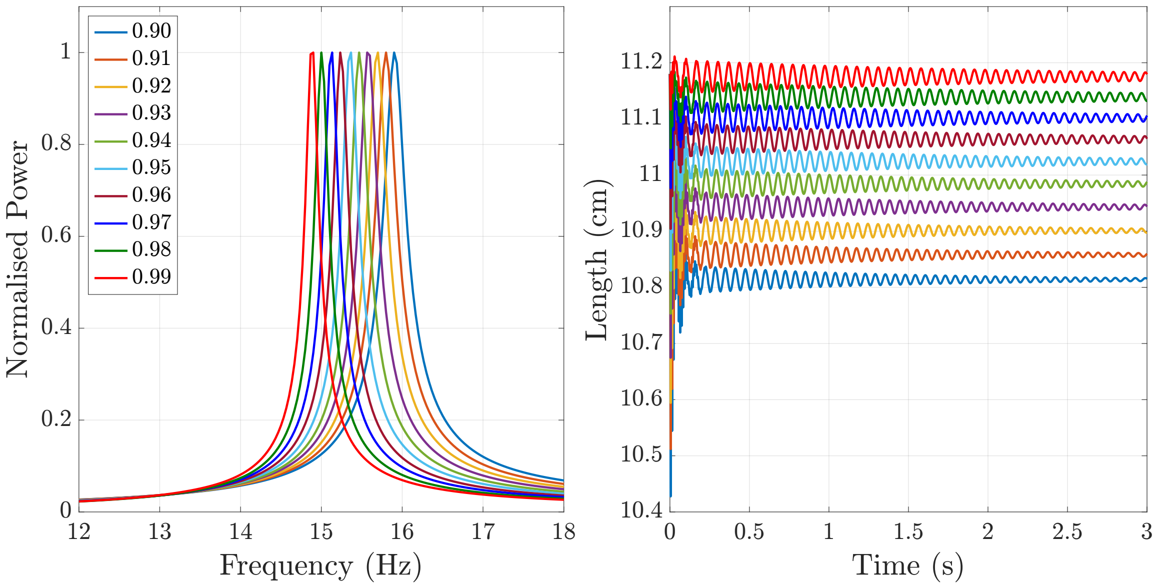

(a) (b)

Figure 5.15 Oscillation characteristics of the STeM. (**a**) The normalised spectrum showing the STeM's intrinsic frequencies with different pretension ratios at the neutral position. (**b**) The length of the thread connecting nodes M_1 and N_3 over a duration of 3 s from the time of sudden fastening.

Fault Tolerance

The fault tolerance is one other explicit factor that contributes to the robustness of the STeM, where it can potentially enhance the robot's survivability in extreme environments. To evaluate the fault tolerance, the consequences of broken threads were examined by unbinding threads from the tensegrity structure and observing if the STeM was still controllable to some extent or not in the simulation.

For situations with no more than two threads failures, whether the STeM can still operate is listed in Table 5.1. A full failure only occurred in three cases which share a common pattern that the two faulty threads are opposite to each other. This caused absence of indispensable force pairs to restrain the structure in a stable state. For cases that were still operational, the performance of the STeM was degraded to different levels correlated to combinations. In the context of three-thread failure scenarios, it was found that the sole operational configuration was the one in which the threads were evenly spaced, which were either M_1N_1–M_2N_2–M_3N_3 or M_1N_3–M_2N_1–M_3N_2. Such combination introduced non-eliminable roll motion but retains the functional pitch and yaw motion. Although the loss of threads results in smaller workspace and compromised accuracy, the STeM showed good performance overall in fault tolerance.

Thread	M_1N_3	M_3N_3	M_1N_1	M_2N_1	M_3N_2	M_2N_2
M_1N_3	✓	✓	✓	✓	✓	×
M_3N_3	/	✓	✓	×	✓	✓
M_1N_1	/	/	✓	✓	×	✓
M_2N_1	/	/	/	✓	✓	✓
M_3N_2	/	/	/	/	✓	✓
M_2N_2	/	/	/	/	/	✓

Table 5.1 Operation status of the STeM with no more than two threads failure. The combination of the same thread represents the one thread failure situation. The combination of different threads represents the two threads failure situation. A ✓denotes the STeM is still functional for the given combination while a × denotes an uncontrollable configuration.

5.4.3 Locomotion Assessment

The robustness of a robot is not only determined by the inherent properties of the structure in terms of the low-level aspect, but also contributed by the high-level capabilities such as the locomotion adaptation and failure recovery. To introduce locomotion capabilities to the STeM for examining these capabilities, the wheel tiles were attached to the STeM in the simulation. When coping with rugged terrains or obstacles, it is very likely for robots to get stuck or trapped during locomotion. These challenges can be potentially overcome by approaches such as enhancing the wheels' ability to maintain consistent contact with the ground, implementing alternative locomotion approaches, and self-recovery from failure. In addition, to fulfil essential conditions of the experiment, in this section, two STeMs were concatenated in serial to form a two-segment wheeled vehicle the same as that for the energy dispersion experiment.

Passive Adaptation

The passive adaptation was realised by configuring the active threads of the STeM in loose states during operation. The large passive workspace allowed the front and rear wheel pairs of each STeM to move relative to each other. This movement was similar to a wheeled rigid frame vehicle with a suspension system, without actually introducing a separate suspension mechanism. This is beneficial for challenging environments as the ground is rarely completely flat. Wheels without enough suspension travel can cause poor contact with the terrain and lead to balancing and stability issues during locomotion. The passive adaptation is expected to make the robot hold better to the surface to prevent or recover from unbalanced or stuck status.

To examine the passive adaptation of the STeM vehicle, an uneven terrain was generated which consisted of a matrix of rectangular blocks of pseudo random height using a constant seed, as shown in Figure 5.16. Two wheeled vehicles, the STeM vehicle and its rigid counterpart, were travelling on the terrain following the same straight track. The contact forces on each wheel over the complete journey were recorded for subsequent analysis. Here, the reason for using two STeMs was to eliminate the inevitable pitch motion when a single STeM operates in the passive mode.

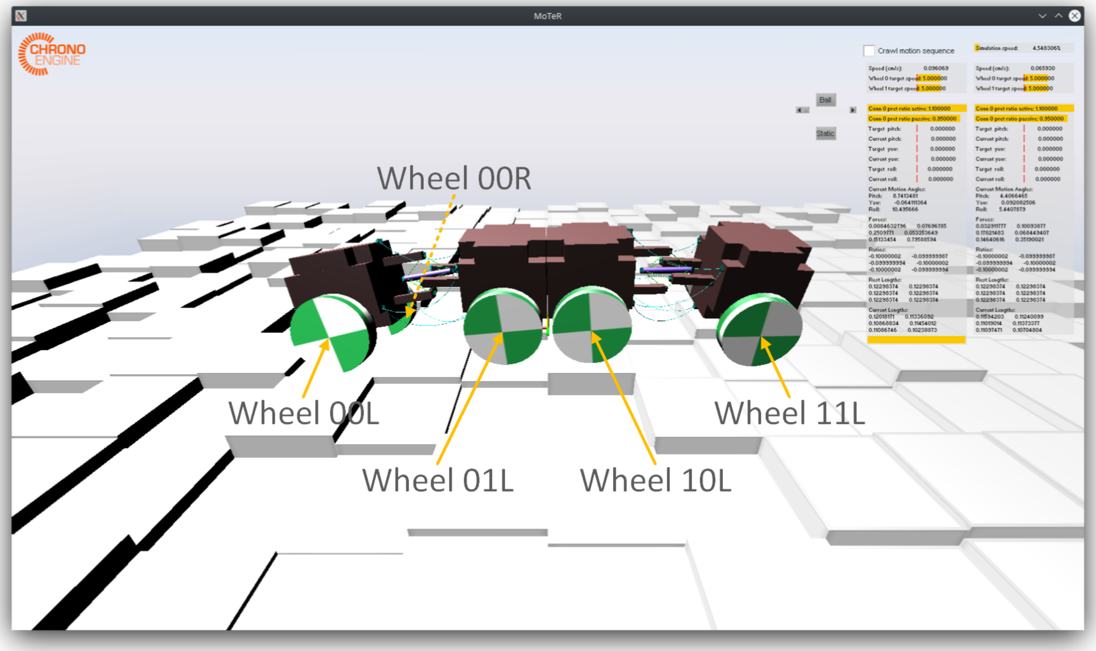

Figure 5.16 The robot composed of two concatenated STeMs traversing an uneven terrain, with active threads in loose states. Wheels not visible are not labelled with corresponding text.

The contact forces of the two vehicles are plotted in Figure 5.17. The active threads of the STeM vehicle were configured with 1.1 times the neutral length so that there were no constraints exerted by the active threads. Compared with the STeM vehicle, the rigid vehicle presented larger zero force bars, especially for wheels 00 and 11, indicating longer duration of improper contact with the ground. It was clear that the rigid vehicle's wheels bore greater average forces throughout the process when there were wheel contacts, while for the STeM vehicle the distribution was more uniform and fell within a lower range. This reflected a better adaptation to the uneven terrain of the passively operated STeM vehicle than the rigid one. It is worth noting that the STeM vehicle's wheels attached to the middle two cubic hubs had relatively high zero force bars. This was caused by the rigid concatenation between the two hubs, making it a similar configuration as the rigid vehicle but just for the wheels in the middle.

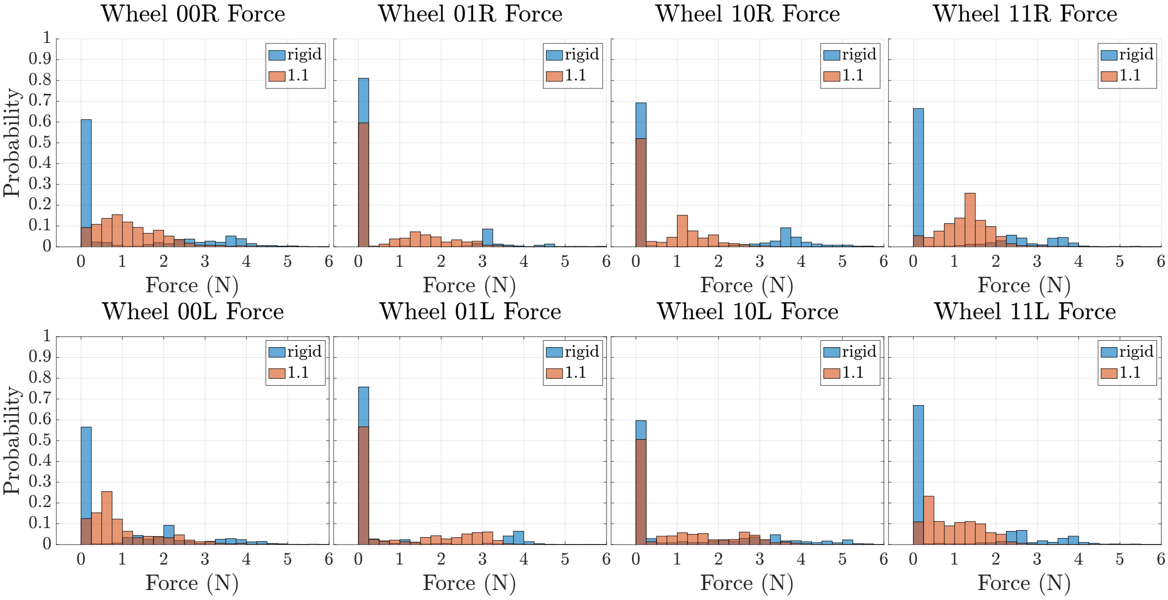

Figure 5.17 Contact force on the wheels when traversing the same uneven terrain for the wheeled STeM robot and the rigid comparison. The data series labelled "rigid" represents the rigid robot experiment results as the control group. The data series labelled "1.1" represents the wheeled STeM robot experiment results, where the active threads were 1.1 times the neutral length in loose state. The first digit in wheel index denotes the STeM module it belonged to in the vehicle. The second digit denotes the cubic hub it belonged to in each STeM. The last letter denotes the left or right side of the wheel.

Active Adaptation

For situations requiring navigating through more complex terrains such as high obstacles within narrow passageways and unavoidable steps, the active adaptation can be employed to traverse these obstacles. Here, the reason for using two STeMs was to guarantee enough mass of the stationary body for maintaining stable contact with the ground, while having the free moving hub pitch up to reach a higher level.

The obstacle was modelled by a simple step placed in the path of locomotion. The vehicle was preset to have knowledge of the distance to the step. The procedure of traversing the step was a predefined "pull-push" action sequence based on the distance information, as illustrated in Figure 5.18. Firstly, the front hub pitched up before reaching the step. After the front axle passed the step edge, the front hub pitched down to pull the robot upwards. Secondly, the rear hub pitched down after the second axle passed the step edge to push the robot up further and at the same time the front hub returned to the neutral posture. Finally, the rear hub returned to the neutral posture after the third axle passed the step edge. A test run was recorded using as a success measure if the fourth axle passed the step edge. The maximum obstacle traversing height was obtained by sweeping step heights from 50 mm upwards with a resolution of 10 mm, and then with 1 mm resolution from the maximum valid result of the 10 mm sweep.

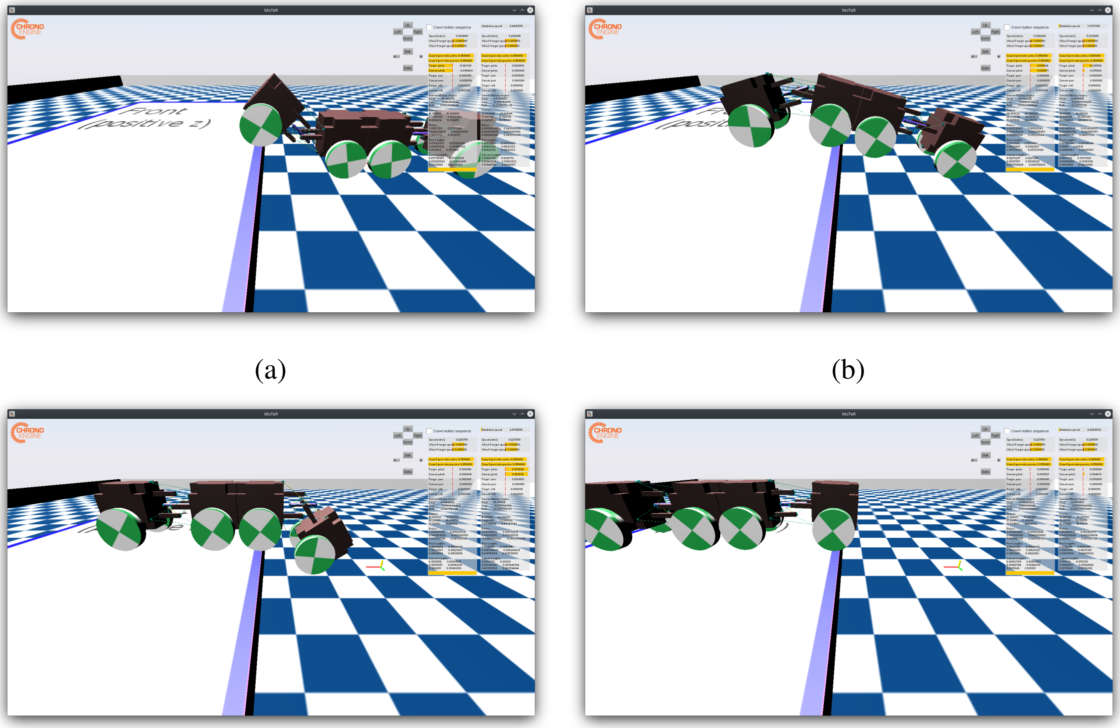

(a) (b)

(c) (d)

Figure 5.18 The "pull-push" action sequence of the robot for surmounting high obstacles.

The step traversing experiment presented a best result height of 93 mm. Without the active adaptation, the vehicle only crossed a step of up to 29 mm height. Since no noise was specifically introduced in the simulation, and the experiment's parameter sweeping procedure was controlled by a predefined script, these results were consistent across multiple experiments. For the vehicle, each cubic hub took a convex space of a 100 mm width with a wheel diameter of 90 mm. The wheels were attached 40 mm lower than the centre of gravity of the hubs, resulting in the bottom face of the hub being 35 mm above ground level. It turned out that the vehicle was able to traverse an obstacle of 68.9% of its total height, 103.3% of its wheel diameter, 265.7% of its ground clearance, or 320.7% of the non-actuated configuration, exhibiting a significant improvement of its traversability.

Failure Recovery

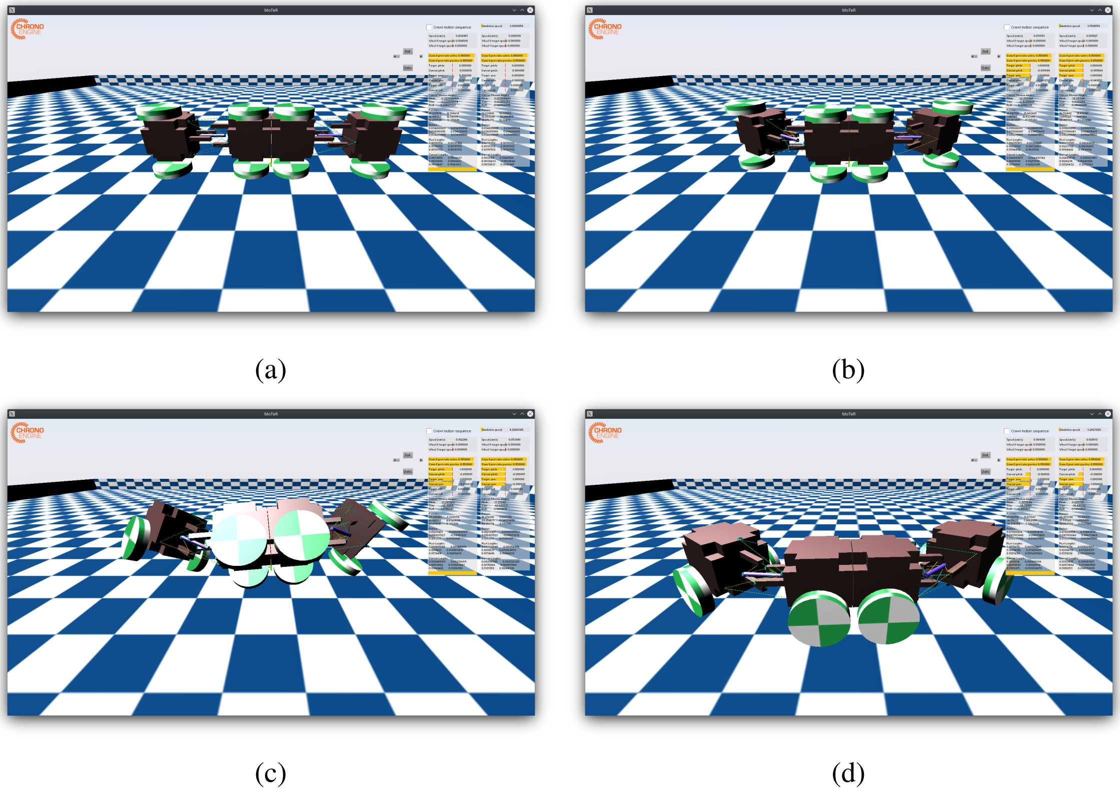

(a) (b) (c) (d)

Figure 5.19 The twisting-like action sequence of the robot for self-righting from a rollover. (**a**) The robot placed on its side on the ground. (**b**) The robot performing full pitch motion. (**c**) The robot carrying out both full pitch and yaw motion, causing it to flip towards upright position. (**d**) The robot performing full yaw motion, bringing it to a fully upright position.

In extreme and unpredictable environments, robots can get into unrecoverable states such as rollover and overturn, which can eventually lead to a complete failure of missions. In these scenarios, modular robots in biomimetic forms are normally able to recover from such situations by manipulating its "limbs" like human beings. For wheeled vehicles, even modular ones, it is difficult to recover from such failures as they do not have limbs that can extend outwards. However, owing to the rich degrees of freedom of the STeM, the two-module STeM vehicle can purposefully roll continuously on to its sides, to self-right from a rollover condition or twice from a overturn condition.

The vehicle was initially placed sideways on the ground to emulate a rollover scenario in the simulation. The self-righting procedure was achieved by a predefined motion sequence. The sequence was inspired by the behaviour of tortoises to flip back with the help of their neck given the vehicle had a similar configuration but with two necks available, while the resultant overall effect of the process is akin to twisting a U-shape bent soft stick with one's hand, as illustrated in Figure 5.19. The manoeuvre for a 90° flip was completed by symmetrically sweeping both heads by a quarter of a circle. From the perspective of pitch and yaw motions, it was a full transit from neutral, maximum pitch, maximum pitch and yaw, maximum yaw and finally to neutral, or vice versa. The orientations of each hub were recorded as the output.

The posture of the vehicle's front cubic hub with respect to the world is represented with solid lines in Figure 5.20. At the beginning, the roll motion was 90°, indicating a rollover state. Following a step by step sequence of the two STeMs' motion, plotted with dashed lines, the roll posture gradually decreased back to zero, representing a successful self-righting.

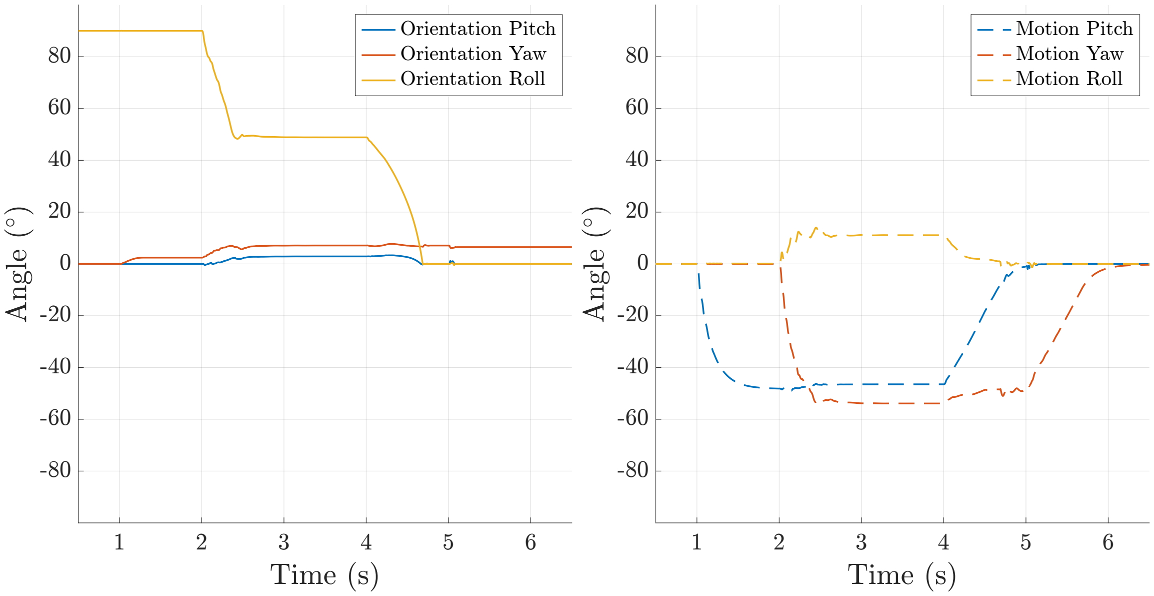

(a) (b)

Figure 5.20 States of the robot and STeMs during the self-righting process. The solid lines and dashed lines denote the orientation and motion of the robot, respectively. (**a**) The robot's orientation represented by the state of the middle two cubic hubs. (**b**) The motion of one STeM. The two STeM modules perform the same motion sequence.

5.5 Summary

When applying tensegrity structures in robots directly oriented for locomotion purposes, it is common that the accuracy of motion is not one of the primary criteria. The flexibility adds difficulty to this work, and from a holistic perspective, the coordination of elements in various motion patterns contributes more to the locomotion. However, the STeM as a mechanism responsible for robot actuation purposes, the accuracy plays an important role in affecting the overall performance of the robot. By incorporating the force closure control approach, the STeM has been proven to be a good substitution to conventional rigid joints for introducing soft characteristics to the robot system. Although its accuracy shown in the results is not comparable to the rigid counterparts, this is expected to be further improved by utilising more feedback such as the posture information during runtime.

Conversely, other results presented in this chapter clearly unveiled superior characteristics of the STeM than the rigid robotic joints. The compliance, resilience, fault tolerance exhibited endowed the robot with significantly improved robustness over their rigid counterparts. Building on top these low-level capabilities, the robot with a conventional wheeled locomotion based on multiple STeMs was enhanced with improved adaptability which further reinforced the robustness from a high-level perspective. These suggested that the STeM is capable of introducing robustness to the modular robots based on it.

In the next chapter, the modular tensegrity robot consisting of multiple STeMs is presented. The robot can be reconfigured into various morphologies which emulate the natural animals. In addition to the wheeled locomotion, the robot adopts a biomimetic locomotion approach implementing corresponding gaits of the morphologies using a bio-inspired control framework. The results include the convergence, speed and dispersion of each morphology's locomotion based on physical experiments.

Chapter 6

Modular Tensegrity Robot

6.1 Introduction

In the previous chapter, the development and evaluation of the STeM were presented. Its properties as a tensegrity structure including the compliance, flexibility, resilience, as well as the versatility and agility endowed from the atypical design, with respect to the robot articulation and actuation purposes are discussed. In this chapter, the Modular Tensegrity Robot (MoTeR) which is composed of multiple STeMs is explored in terms of the potential morphologies, locomotion gaits, control strategies and performance.

The MoTeR is primarily focused on the terrestrial locomotion capabilities in a polymorphic manner to demonstrate the great potential of such a class of robots based on the fusion of tensegrity structures and modular robotic systems. Four bio-inspirations, and the corresponding morphologies and gaits of the robot are introduced in Section 6.2. The realisation of the control approaches based on the Central Pattern Generator (CPG) for these gaits is presented in Section 6.3. The experiments for testing the locomotion performance of the robot are described in Section 6.4. A brief summary of the work is given in Section 6.5.

6.2 Morphology and Gait Analysis

Leveraging the large workspace, rich degrees of freedom and high connectivity of the STeM, the MoTeR can be readily reconfigured into various morphologies to accommodate the demands of different tasks. These morphologies can imitate the forms of completely different species of animals ranging from arthropods to mollusks, to more complex groups within vertebrates such as mammals and reptiles. In fact, each individual STeM is capable of locomotion on its own either through adding four wheel tiles or using an unstable primitive crawling gait, but the polymorphic locomotion relying on the coordinated movement of the robot's body or limbs provides an improved stability and adaptability to unstructured terrains in addition to the conventional wheeled approach.

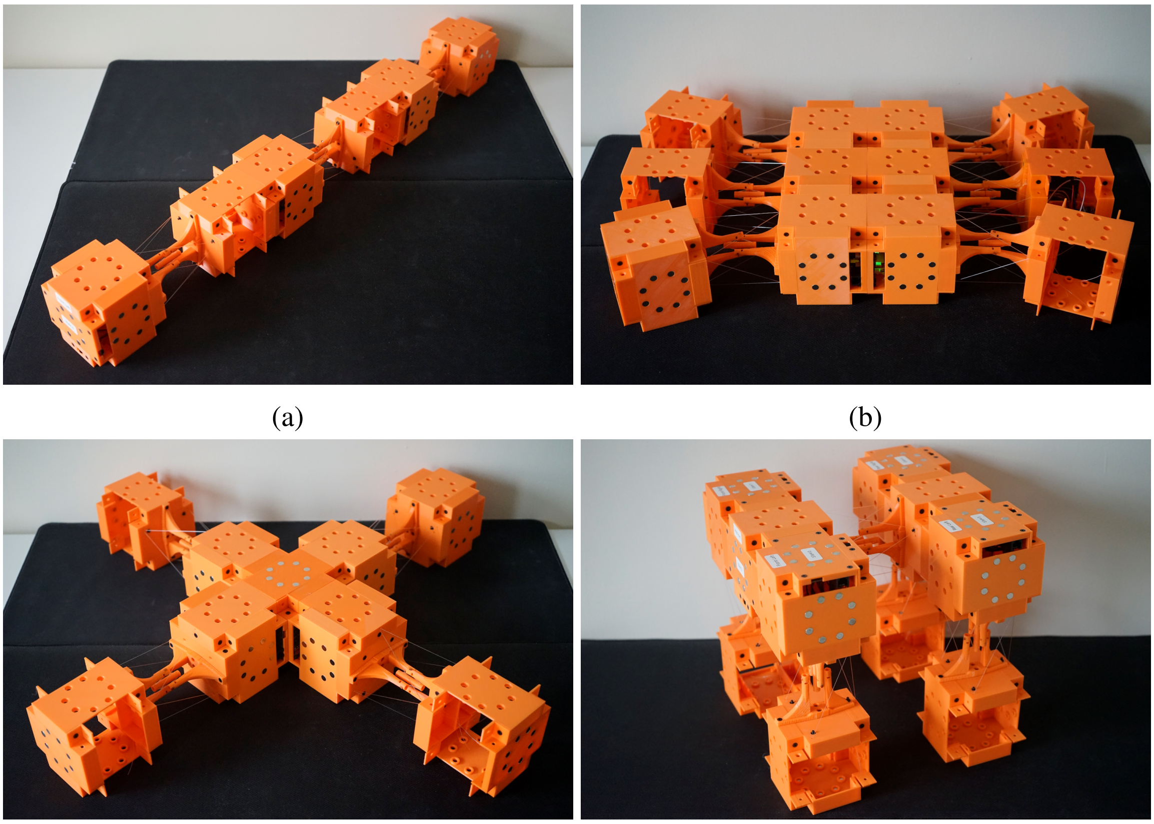

(a) (b)

(c) (d)

Figure 6.1 The four representative morphologies implemented of the MoTeR. From (**a**) to (**d**), the figures demonstrate the snake, hexapod, quadpus and quadruped morphologies, respectively.

In this study, the MoTeR were assembled in four different representative morphologies, which are snake, hexapod, "quadpus" (an octopus with only four limbs), and quadruped, as shown in Figure 6.1. Each morphology was explored with two locomotion behaviours, which are translational and rotational locomotion, except for the snake morphology where only translational locomotion was tested. The natural paradigm gaits of these morphologies vary in distinct forms include ophidia, hexapoda, cephalopoda, and tetrapoda, which results in different implementations on the robot such as body based, horizontally oriented and vertically oriented limb based. To simplify the gait analysis of the robot, the tensegrity structure of each module can be considered as a rotational actuator. They are firmly embedded into the modules and are therefore distributed through the robot in accordance with the topology of the modules. Thus, the gait control greatly varies from one morphology to another which requires an appropriate framework that can be applied to a variety of them.

Throughout the gait illustration figures in this section, the following conventions are used: the blue square represents the cuboid hub, the yellow dashed line represents the active tensegrity thread while the passive sub-structure is not depicted, the green arrow represents the direction of the limb's movement, the grey arrow represents the direction of locomotion, and the shaded shape represents the part in contact with the ground.

6.2.1 Snake

The snake morphology is the most straightforward configuration of the MoTeR which concatenates two or more STeMs in serial to imitate the structure of Serpentes, where a number of 3 modules were selected as a paradigm in this study as shown in Figure 6.1a. Under this morphology, the STeM actuates only the body movement, consistent with that of a natural snake. Since the length of the STeM is 3 times longer than its width, in this serial configuration, the distance between the rotation centres of adjoining body segments of the robot is relatively large. Thus, the deformation of the MoTeR body cannot be as continuous and smooth as that of its natural counterparts. However, by increasing the module quantity at the expense of total weight, the robot can better emulate the movements of natural snakes. Owing to the small cross-section area of the robot body, the snake morphology is ideal for locomotion in confined spaces such as tunnels and caves with unknown terrain conditions.

Although the term "gait" is typically used to denote the movement pattern of limbs during locomotion, for consistency, it is also employed to characterise the locomotion mode of snakes hereafter. Natural snakes have developed several common locomotion gaits such as rectilinear, sidewinding, serpentine, and concertina. In terms of the snake MoTeR, the serpentine and sidewinding gaits are suitable choices for its longitudinal and lateral locomotion respectively in general scenarios, as illustrated in Figure 6.2. For the serpentine gait, a natural snake bends its body to the left and right sequentially, that is the yaw motion, to generate a continuous virtual backward wave. Such body wave pushes against environmental anchor points to provide forward propulsion. To realise such gait, the subsequent body

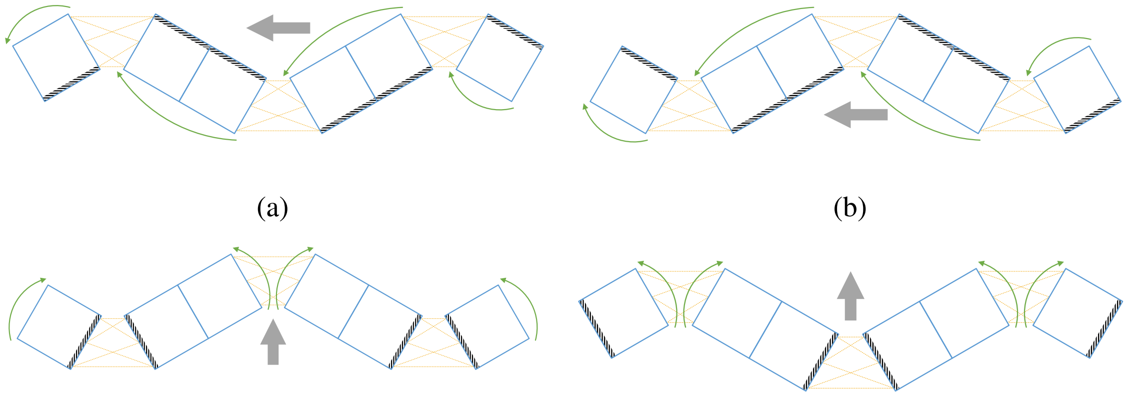

(a) (b)

(c) (d)

Figure 6.2 The alternating states in the gait cycle of the snake MoTeR's locomotion. See the text for shape, color and shading conventions. (**a**,**b**) The forward longitudinal locomotion based on the serpentine gait. The cuboid hub uses one of its side edges as contact point with the ground while the lifted up edge moves forward. Along the axial direction, the contact points of the hubs on the two sides of the tensegrity structure are opposite. They alternatively swap from left to right side or vice versa as illustrated from (**a**) to (**b**). (**c**,**d**) The right lateral locomotion based on the sidewinding gait. The cuboid hub uses one of its distal or proximal edges as contact point with the ground while moving the other edge to the right. Considering the two concatenated hubs as a whole, along the axial direction, the contact points of the hubs on the two sides of the tensegrity structure are symmetrical, while they are opposite for each adjacent modules as that swaps from (**a**) to (**b**).

segments need to closely follow the path of the segments ahead. However, due to the limited number of movable segments, it is not practical to fully replicate such pattern. In this context, modifications were introduced to the body segments' lateral undulation that instead of a continuous wave, an alternating motion between the adjacent modules is utilised that the body wave propagate backwards by two STeMs' length for each gait cycle in a discrete manner. To ensure there are still anchor points available, the robot needs to tilt its body using the roll motion so that one side of the body can move forward while the other side generally remains stationary with the ground, which is similar to that of the sidewinding gait below.

For the sidewinding gait, natural snakes intentionally lift up one side of its body and keep the other side in contact with the ground and at the same time incorporate lateral undulation for locomotion. Such pattern can be readily imitated by the pitch motion of the modules, while one module pitches down towards the ground results in the adjacent module pitching up away from the ground. The lateral undulation component in the sidewinding gait is akin to the modified serpentine gait using the alternating pattern. The lateral locomotion can thus be realised by the coordination of the pitch and yaw motion.

6.2.2 Hexapod

The hexapod morphology imitates the biological form of stick insects and cockroaches. The STeMs are arranged in a two-column, three-row configuration and oriented perpendicular to the forward direction of the robot as illustrated in Figure 6.1b. As there is no clearance between adjacent limbs, the leading and trailing STeMs in this morphology need to maintain a continuous outward tilt offset to avoid collision between the limbs during crawling. Since there is only one joint in each limb, the hexapod morphology doesn't have the lateral locomotion capability. Compared with the snake, although they are both suitable for unstructured terrains, the larger footprint of the robot's limbs for the hexapod morphology is expected to provide an improved stability.

For the hexapod morphology, the alternating tripodal leg coordination is a widely employed gait both in natural and robotics [114]. Each of the two tripods includes the front and rear legs on one side and the middle leg on the opposite side. To achieve the three-point contact with the ground during the stance phase and the six-point contact at touchdown and still state, the STeMs need to maintain a consistent pitch motion to lift up the six-cube body in addition to the yaw offset of the front and rear leg pairs. To crawl forward, the legs of each tripod moves in synchronisation and the two tripods alternatively provide support and swing forward to complete the stance and swing phase sequences. When turning in place, instead of moving forward or backward, the legs of each tripod follow a simultaneous clockwise or counter clockwise movement. A forward translational and a clockwise rotational locomotion based on the tripod gait for hexapod MoTeR is shown in Figure 6.3.

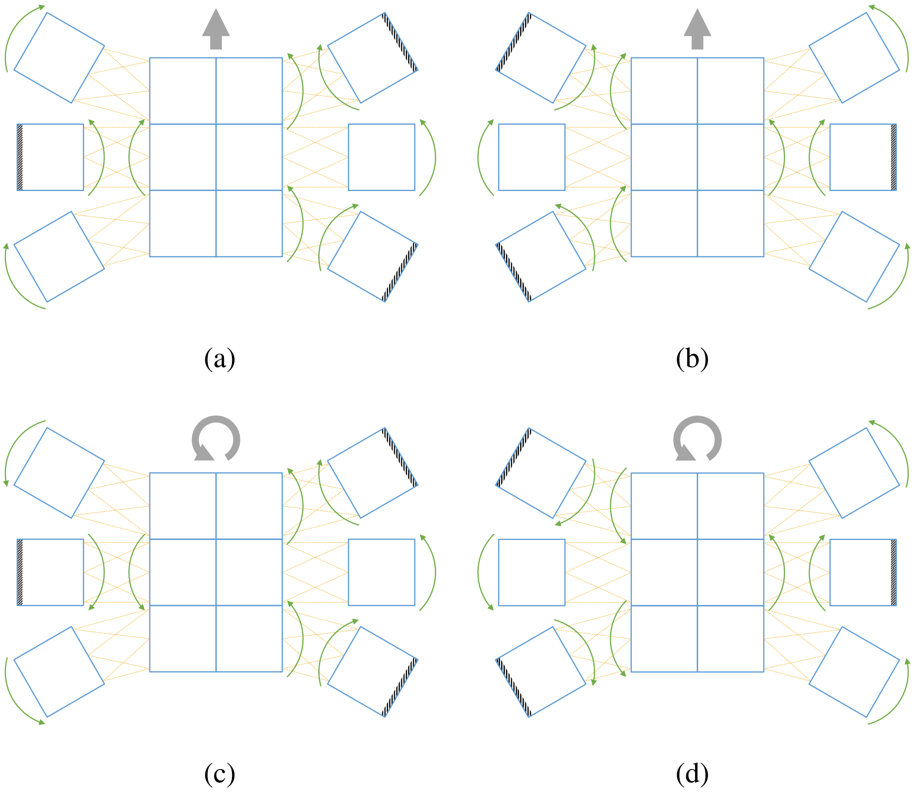

(a) (b)

(c) (d)

Figure 6.3 The alternating states in the gait cycle of the hexapod MoTeR's locomotion. See the text for shape, color and shading conventions. (**a**,**b**) The forward translational locomotion based on the tripod gait. During each half of the gait cycle, one of the tripodal sets of the limbs remains contact with the ground which is in stance phase, and meanwhile the lifted up limbs and the central body moves forward which is in swing phase. From (**a**) to (**b**), the tripodal sets swaps and vice versa to realise the stance and swing alternating pattern. (**c**,**d**) The counterclockwise rotational locomotion based on the tripod gait. The alternating tripodal pattern is the same as that of the forward gait. However for the limbs in swing phase, they all move in the same counterclockwise direction to generate angular propulsion.

6.2.3 Quadpus

As suggested by its name, the "quadpus" morphology is semi-bio-inspired by and modified from the octopus that it has only four limbs instead of the original eight, shown in Figure 6.1c. This is due to the STeM modules are arranged in the Cartesian grid pattern as stated in Section 4.3. It is difficult to fit eight limbs together equally and reasonably spaced while four limbs can provide adequate mobility performance. The STeMs are arranged in a cross shape acting as the limbs for locomotion, with an extra cuboid hub in the centre for physical connection. Each limb is able to provide independent lateral mobility in the quadrant in the horizontal plane. Therefore, MoTeR in this morphology can realise a holonomic crawling locomotion. It is also suitable for the confined situation that non-holonomic locomotion is limited but at the same time requires a movement with high agility and dexterity.

The limbs of the quadpus morphology, being a modification of the octopus, are not extensible and do not have as many degrees of freedom as those of the octopus. Thus it is not pragmatic to fully replicate the octopus' locomotion strategy on the sea bed or land. In addition, as a morphology with four limbs, it is feasible to mimic the locomotion gaits of tetrapod animals. However, in this work, another pattern is introduced, where all limbs of the robot are lifted and placed down simultaneously. This pattern is termed the 'synchronous gait'. The underlying principle of this gait is akin to that of a holonomic platform with four omnidirectional wheels. Each limb, that is STeM, can move its end point in a circle on the plane perpendicular to its longitudinal axis to generate propulsion in a similar way as wheels but in a rhythmic pattern. By varying and coordinating the motion amplitude and direction of the limbs, quadpus MoTeR can thus control of the direction and mode of the locomotion. The gait examples for forward translational and clockwise rotational locomotion are shown in Figure 6.4. During the swing phase, the body, that is the central five cuboid hubs, acts as an anchor point in contact with the ground providing support while the feet, that is the other four hubs, move freely in the desired direction. In the stance phase, the situation is reversed, with the edge of the feet in contact with the ground while the body moves. This also improves the stability through using the robot body as the support during the swing phase and all limbs as support during the stance phase. For translational locomotion, the limbs on the same side of the MoToR move in the same angular direction while for rotational locomotion, all limbs move in the same angular direction.

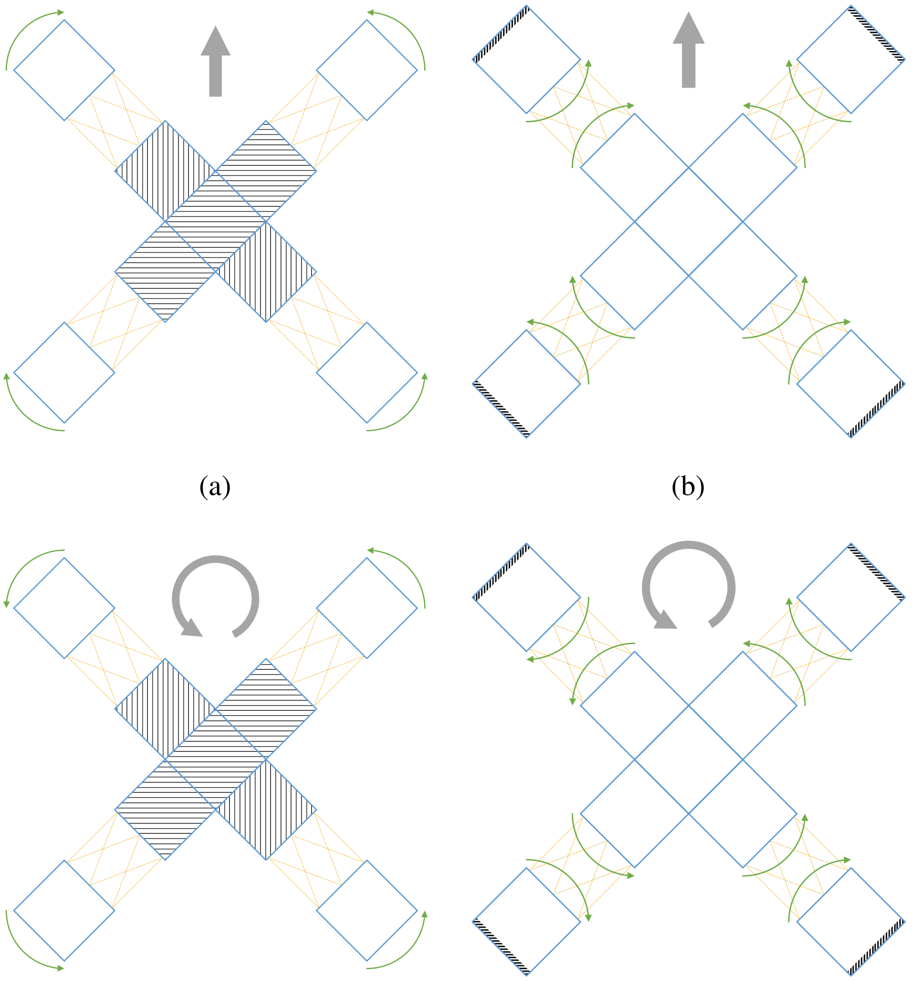
(a) (b)

(c) (d)

Figure 6.4 The alternating states in the gait cycle of the quadpus MoTeR's locomotion. See the text for shape, color and shading conventions. (**a**,**b**) The forward translational locomotion based on the synchronous gait. Since the motion of the limbs is synchronised, the contact points are fully symmetrical during each half of the gait cycle, either provided by the distal edge of the cuboid hub or by the bottom surface of the central body. The contact points swaps along with the state switching between the limbs swing phase (**a**) and the stance phase (**b**). The motion of each limb has a certain angle (±45○) relative to the direction of locomotion, but the resultant velocity is parallel with the direction of locomotion. (**c**,**d**) The counterclockwise rotational locomotion based on the synchronous gait. The pattern of the synchronised motion of the limbs is akin to that of the translational locomotion except that all four limbs move in the same counterclockwise direction to generate angular propulsion, which is similar to the hexapod rotational gait.

6.2.4 Quadruped

The quadruped morphology is designed in close imitation of quadruped vertebrates. Therefore, in addition to the four limbs, a fifth STeM is introduced to fulfill the function of a spine as shown in Figure 6.1d. The modules are arranged that the pitch motion provides upward and downward movement for the spine module and forward and backward movement for the leg modules. Typical quadruped robots with a rigid body normally require no less than two joints on each leg, of which the pivot points do not coincide to model the shoulder-elbow or hip-knee joint combinations, so that it can actively lift the feet during the swing phase. For quadruped MoTeR, however, each limb's three DoFs rotate about the same pivot point where its workspace is a dome-shaped surface with no room for independent vertical movement for feet lifting when it is vertically placed. Adding four more STeMs to take the role of thigh or calf from the existing four limbs is a potential solution to the issue but it will introduce extra complexity to the control of such an inherently flexible system. As a result, the typical limb-only topology and gait is not applicable for the quadruped MoTeR. To overcome this predicament, the fifth STeM spine is involved in the legged locomotion compensating the missing vertical workspace. With a proper coordination of the tensegrity spine roll motion and the limbs, the feet can be lifted during the swing phase and at the same time, the turning performance can also be improved with the spine's yaw motion. The quadruped morphology is a versatile configuration suitable for diverse general scenarios.

Quadrupeds use various gaits to move. These can be categorised into a number of common types such as walk, trot, pace, canter and gallop. Given the limitation of the available workspace of the legs compared with that of the specially designed counterparts and the symmetrical essence of the spinal movement, the trot gait is an ideal choice for the quadruped MoTeR's translational locomotion as it alternates the diagonally opposite legs in a symmetrical pattern. However, due to the existence of the spine roll motion during the steady state, the front and rear bodies of the robot will inevitably tilt to two sides, which results in the abduction of the legs in swing phase and the adduction of the legs in stance phase. To keep a vertical placement of the legs during locomotion, the yaw motion is thus introduced in coherence with the spine roll motion. For the rotational locomotion, although there is no specific gait for such maneuver, the principle of trot gait is well applicable in this scenario. This can be accomplished by intentionally utilising the abduction and adduction movement of the legs to facilitate the lateral motion of the front or rear bodies of the robot in the same polar direction with respect to the axis of rotation. Such leg movement is amplified by the roll motion of the spine, improving the efficiency of the motion. Additionally, a lateral locomotion of the whole robot can also be achieved while the front and rear bodies move in the same vector direction.

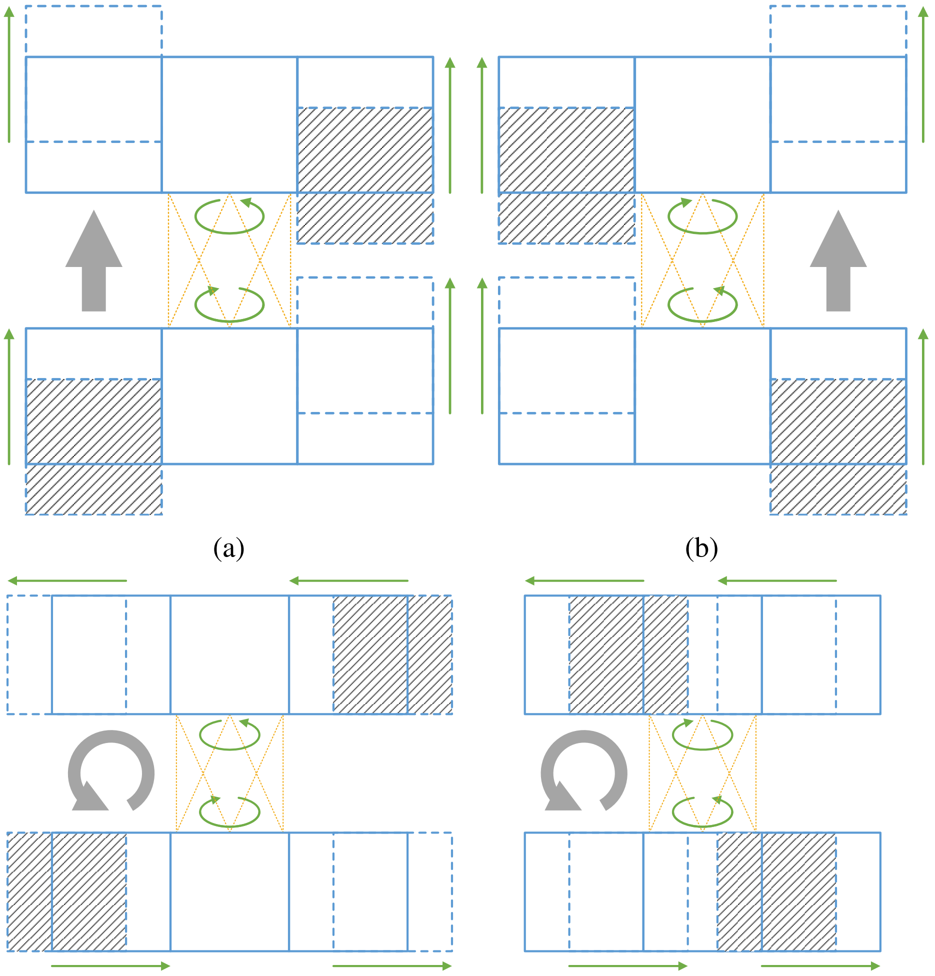

(a) (b)

(c) (d)

Figure 6.5 The alternating states in the gait cycle of the quadruped MoTeR's locomotion. See the text for shape, color and shading conventions. (**a**,**b**) The forward translational locomotion based on the trot gait. During the half of the gait cycle, one of the diagonal limb pairs that in stance phase pushes off the ground, while the other pair swings forward. In the meantime, the spine rolls in time with the forward movement of the swing limbs to lift them up. The states and movement swaps between the two limb pairs and the spine from (**a**) to (**b**) or vice versa. Due to the top view of the figure, the yaw motion of the limbs are not depicted. (**c**,**d**) The counterclockwise rotational locomotion based on the trot-like gait. The spine motion of the rotational locomotion is the same as the translational locomotion that it rolls to facilitate the lifting up of the limbs in swing phase. During each half cycle, the limbs of each diagonal pair move symmetrically instead of synchronised. This leads to the opposite states of all the limbs from one of the half gait cycles (**c**) to the other (**d**) or vice versa.

6.3 Gait Control by Central Pattern Generator

Central Pattern Generators (CPGs) are biological neural circuits that generate rhythmic motor patterns such as walking, breathing and chewing in the absence of rhythmic inputs [115]. They are widely observed in both invertebrates and vertebrates [116], and have an extensive application within the realm of robotics [94]. Through the intrinsic oscillation and the connectivity of the neurons, CPGs possess several properties that are beneficial to robotics including distributed control, perturbation rejection, and synchronisation convergence speed. Tensegrity as a bio-inspired structure, of which the elements are sparsely scattered and interconnected in the three dimensional space, is naturally compliant with the CPG network. For the case of MoTeR, its modularity essence and rhythmic pattern of STeM's motion make CPG an excellent choice for the implementation of its locomotion gaits analysed in Section 6.2.

In order to fully reflect the motion of STeM with a CPG network, the three rotational degrees of freedom of each STeM are managed individually by three pairs of back to back placed CPG motoneurons, that is six neurons in total. The neurons are modelled by means of the phase oscillator which controls the angular frequency of their output sinusoidal waveform at run time to coordinate the temporal relationship among them. The equations of the phase oscillator are given as follows [117]:

$$x_i = r_i(1 + cos(\theta_i)) \tag{6.1}$$

$$\dot{\theta}_i = 2\pi v_i + \sum_j |r_j| w_{ij} sin(\theta_j - \theta_i - \phi_{ij}) \tag{6.2}$$

$$\ddot{r}_i = a_i(\frac{a_i}{4}(R_i - r_i) - \dot{r}_i) \tag{6.3}$$

The burst of the CPG neuron is characterised by the positive output signal x_i of the oscillator i, which is determined by the state variables θ_i, the phase, and r_i, the amplitude. Equation 6.2 describes the modulation of the oscillator's angular frequency. The first term on the right-hand side of the equation denotes the intrinsic frequency determined by v_i that leads to the spontaneous oscillation. The second term represents the influence exerted by other connected oscillators due to the deviation from the expected phase bias phi_{ij}, with the strength scaled by the connection weights w_{ij}. The amplitude of other connected oscillators r_j is taken as the absolute value. This is to address the situation caused by the unique oscillator implementations in this study where the target amplitude is negative. Equation 6.3

illustrates the change in the oscillator's amplitude. It is a second-order critically damped system, where the convergence speed is controlled by the constant a_i, and the steady state value is controlled by the intrinsic amplitude R_i. In this study, the convergence speed of oscillators and the connection weights are all set to 50 and 10, respectively.

Within each neuron pair responsible for managing a degree of freedom in motion, the oscillators maintain a constant opposite phase difference. The output of the neuron pair, which is mapped to the angle of the corresponding motion, is obtained from the difference between the outputs of the two phase oscillators. This allows for the generation of a biased bipolar waveform, facilitating asymmetrical swing in the limb's movement. By defining the phase bias among the neuron pairs, the temporal relationship of roll, pitch, and yaw motion within each STeM, as well as the coordination among the STeMs, that is limbs, can be established. As the local CPG model for each STeM shares a similar connectivity, it possesses a modular nature akin to that of the STeM modules. Therefore, the global CPG model can be easily scaled and reconfigured in a modular fashion to closely reflect and control MoTeR's movements across various morphologies. Based on the CPG, the robot can self activate the gait from the stationary state based on the oscillators' intrinsic oscillation and transition from one gait to another smoothly owing to the excitation and inhibition among the oscillators.

When referring to the position and orientation of the STeM, the ISO vehicle axes convention is used throughout this section. Assuming the active side of the STeM points towards the X-axis positive direction, the coordinate system is established with right-hand principle with Y pointing to the left and Z pointing to the up. Based on this, the relationship between CPG output and STeM's rotation are thus defined as follows: assuming observation from the rear of the STeM along the X-axis positive direction, the positive CPG output corresponds to pitch down, yaw left, and roll clockwise motions, respectively.

Throughout the CPG illustration figures in this section, the following conventions are used: The blue, orange and green circles represent the pitch, yaw and roll oscillators respectively. The letter above the sinusoidal wave symbol in the circle indicates the module to which the oscillator belongs, while the letter below represents the type of oscillator and the direction of motion it produces. The inter oscillator connection is represented by arrow in grey, yellow and purple. The direction of the arrow indicates the influence from one oscillator (tail) to another (tip). The phase shift is denoted by the label next to the corresponding arrow. A positive value labelling the arrow denotes a phase leading relationship. The grey dashed rectangle envelopes oscillators which belong to the same module. The red shaded rectangle is used to highlight the difference between the two implemented gaits of a specific morphology.

6.3.1 CPG Model for Snake Morphology

The CPG models for the longitudinal and lateral, that is the serpentine and sidewinding, locomotion of the snake morphology, with 3 segments as an example, are illustrated in Figure 6.6 with the amplitude data shown in Table 6.1. As described in Section 6.2.1, the imitation of the serpentine motion is not entirely identical to that of a natural snake but on an alternating pattern, and it incorporates characteristics from the sidewinding motion. To make the robot body undulate laterally to generate a series of backward waves, the phases between each two adjacent modules' oscillators are directly connected and completely inverted. As a result, the subsequent body does not exactly follow the path of the one ahead. To provide the contact points in time with the lateral undulation for propulsion generation, the roll oscillators are closely coupled with the yaw oscillators within each module.

For the sidewinding motion, the robot's gait is more faithful to its natural counterparts. The body's staying contact with the ground and lifting up on the same side are controlled by the periodic output of the pitch oscillators. In collaboration with the yaw oscillators, which still define the essential lateral undulation, the modules generates propulsion to the left or right side of the robot.

Gait	Module	Oscillator	Amplitude	Oscillator	Amplitude
Serpentine	Front body	roll	0.50 0.50	yaw	0.50 0.50
	Middle body	roll	0.50 0.50	yaw	0.50 0.50
	Rear body	roll	0.50 0.50	yaw	0.50 0.50
Sidewinding	Front body	pitch	0.50 0.50	yaw	0.50 0.50
	Middle body	pitch	0.50 0.50	yaw	0.50 0.50
	Rear body	pitch	0.50 0.50	yaw	0.50 0.50

Table 6.1 Amplitude of the oscillators for the snake morphology CPG model.

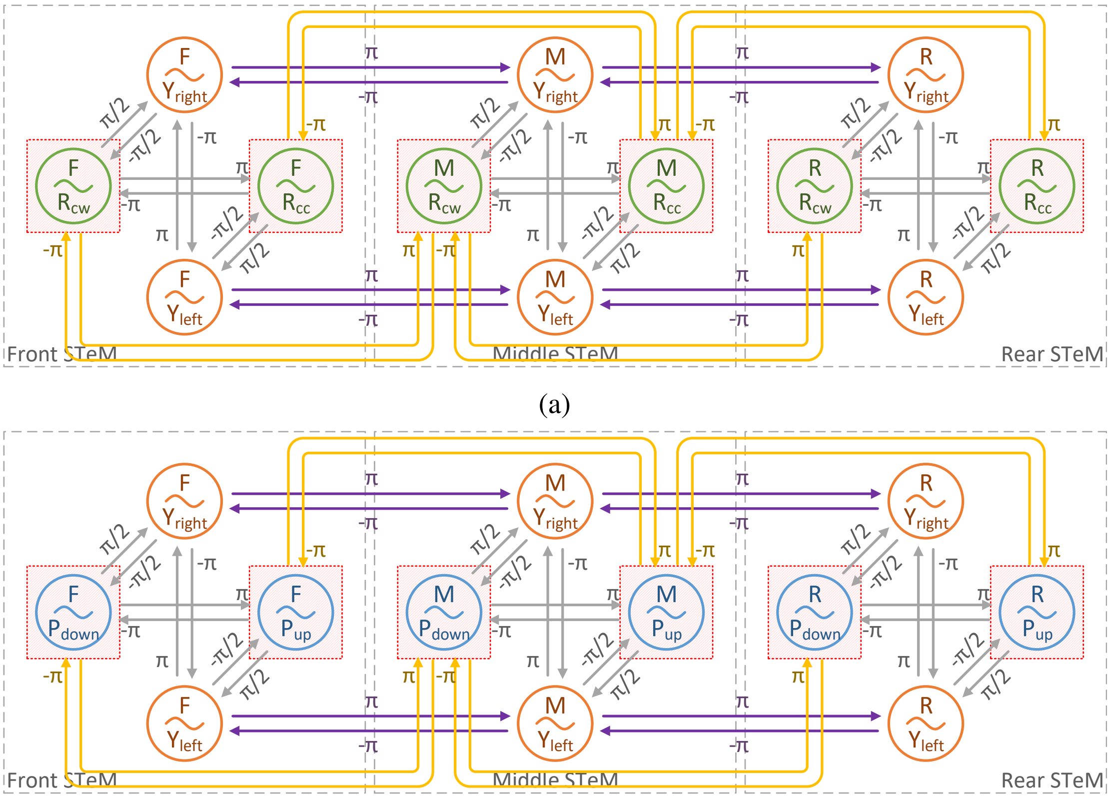

(a)

(b)

Figure 6.6 The CPG model of the snake morphology's locomotion gait. See the text for shape, color and shading conventions. (**a**) The forward translational, or serpentine locomotion. The intra-connectivity of the CPG within each module is identical. The phase of the oscillators within each pair are inverted. The roll oscillator pair is leading the yaw oscillator pair by $\frac{\pi}{2}$ for propulsion generation. The overall phase shift between the adjacent modules' CPG group is π where the oscillators of the same function are connected. (**b**) The left lateral translational, or sidewinding locomotion. The CPG model of the sidewinding gait is similar to the serpentine gait except that the roll oscillators are replaced with pitch oscillators. The pitch oscillators are leading the yaw oscillators by $\frac{\pi}{2}$ for moving to the left or inverting the value to move to the other side.

6.3.2 CPG Model for Hexapod Morphology

To synchronise the movement within each set of legs for the forward tripod gait of the hexapod morphology, a symmetrical two-rail serial connection in the central area is introduced where the corresponding oscillators are closely connected with the same phase as shown in Figure 6.7. The phases between the left and right side limbs of the robot in each row is inverted so that the alternating pattern is evenly distributed over time. For each limb, its propulsion is realised by the coordinated output of the pitch and yaw oscillators where the yaw oscillators are only connected to the pitch oscillators in the same module as a secondary stage. To maintain a constant abduction of the front and rear limbs, the amplitude of the yaw oscillator which controls the limb moving inwards is set to a negative value to realise an asymmetrical movement. Assuming the abduction motion reaches the maximum output of the oscillators, the value can be determined by evenly dividing the allowed workspace for the three limbs on an overall range from -1 to 1. In terms of supporting the robot body with a constant pitch offset, all pitch down oscillators are set twice the amplitude of the pitch up oscillators.

To convert the CPG model into the rotational gait, one simply needs to reverse the leading relationship between the pitch and yaw oscillators within one side's module to a lagging relationship, or vice versa, thereby generating opposite propulsion so that all limbs move in the same angular direction. The amplitude of the oscillators are listed in Table 6.2.

Gait	Module	Oscillator	Amplitude	Oscillator	Amplitude
Tripod Translational	Front left body	pitch	0.50 0.25	yaw	0.500 -0.167
	Middle left body	pitch	0.50 0.25	yaw	0.167 0.167
	Rear left body	pitch	0.50 0.25	yaw	-0.167 0.500
	Rear right body	pitch	0.50 0.25	yaw	0.500 -0.167
	Middle right body	pitch	0.50 0.25	yaw	0.167 0.167
	Front right body	pitch	0.50 0.25	yaw	-0.167 0.500
Tripod Rotational	Front left body	pitch	0.50 0.25	yaw	0.500 -0.167
	Middle left body	pitch	0.50 0.25	yaw	0.167 0.167
	Rear left body	pitch	0.50 0.25	yaw	-0.167 0.500
	Rear right body	pitch	0.50 0.25	yaw	0.500 -0.167
	Middle right body	pitch	0.50 0.25	yaw	0.167 0.167
	Front right body	pitch	0.50 0.25	yaw	-0.167 0.500

Table 6.2 Amplitude of the oscillators for the hexapod morphology CPG model.

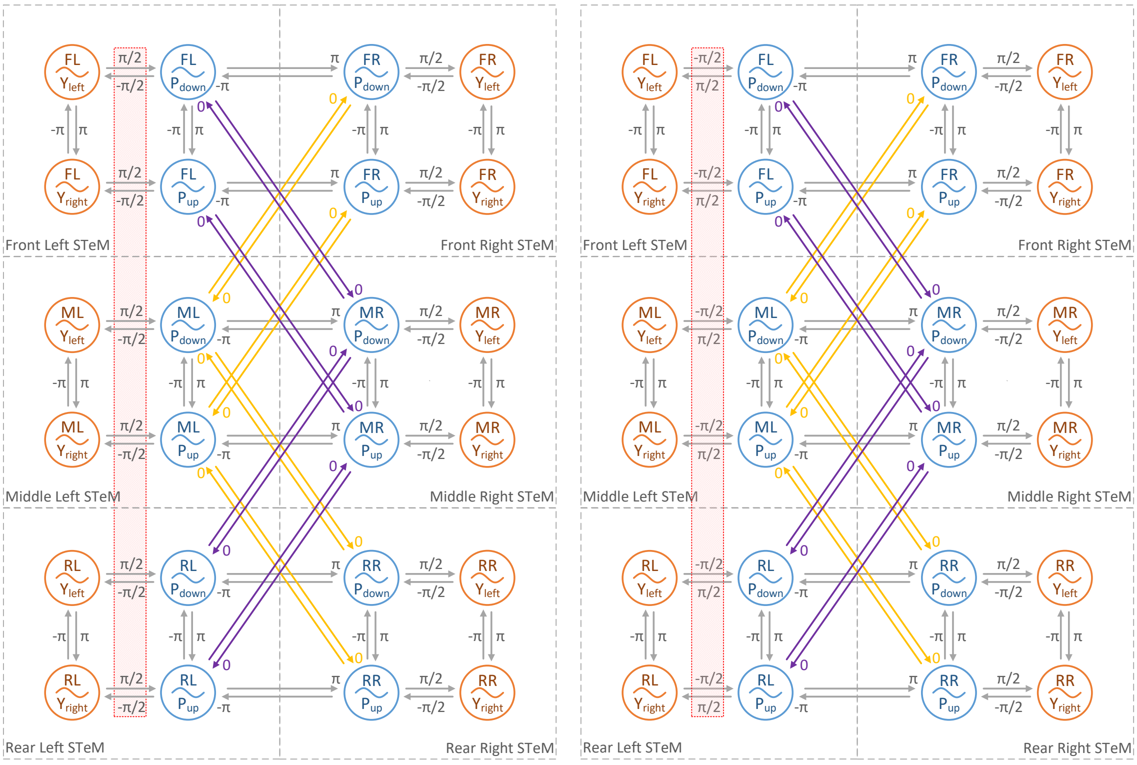

(a)

(b)

Figure 6.7 The CPG model of the hexapod morphology's locomotion gait. See the text for shape, color and shading conventions. (**a**) The forward translational locomotion. The CPG of each module is composed of the pitch and yaw oscillator pairs. On the right side, the pitch oscillators are $\frac{\pi}{2}$ leading the yaw oscillators, while on the left side the relationship is reversed, both for propulsion generation. All pitch oscillators on the two sides are connected with a phase shift of π for the alternating movement between the two. The pitch pair of the front left, middle right and rear left modules are directly connected without phase shifting to synchronise the tripodal motion, as well as that for the other three modules. (**b**) The counterclockwise rotational locomotion. The connectivity of the rotational gait is identical to that in (**a**) except that the pitch oscillators on the left side are leading the yaw oscillators by $\frac{\pi}{2}$, which is the same as those on the right side, generating movement with consistent angular direction for all limbs.

6.3.3 CPG Model for Quadpus Morphology

The main characteristic of the CPG model for the quadpus morphology is the circular coupling of the oscillators among all its limbs for different locomotion modes. This is to realise the synchronous gait of all the limbs proposed in Section 6.2.3. Each adjacent pitch oscillators are connected directly without any phase shift as shown in Figure 6.8. The lateral propulsion with respect to each module is generated by the combined output of the pitch and yaw oscillators. The yaw oscillators is either in-phase or 180 degrees out-of-phase between the two sides to realise a rotational or translational locomotion respectively. Through varying the amplitude of the oscillators especially the yaw oscillators, the quadpus is capable of steering during its translational locomotion. The amplitude of the oscillators for the gait in the two example locomotion modes is listed in Table 6.3.

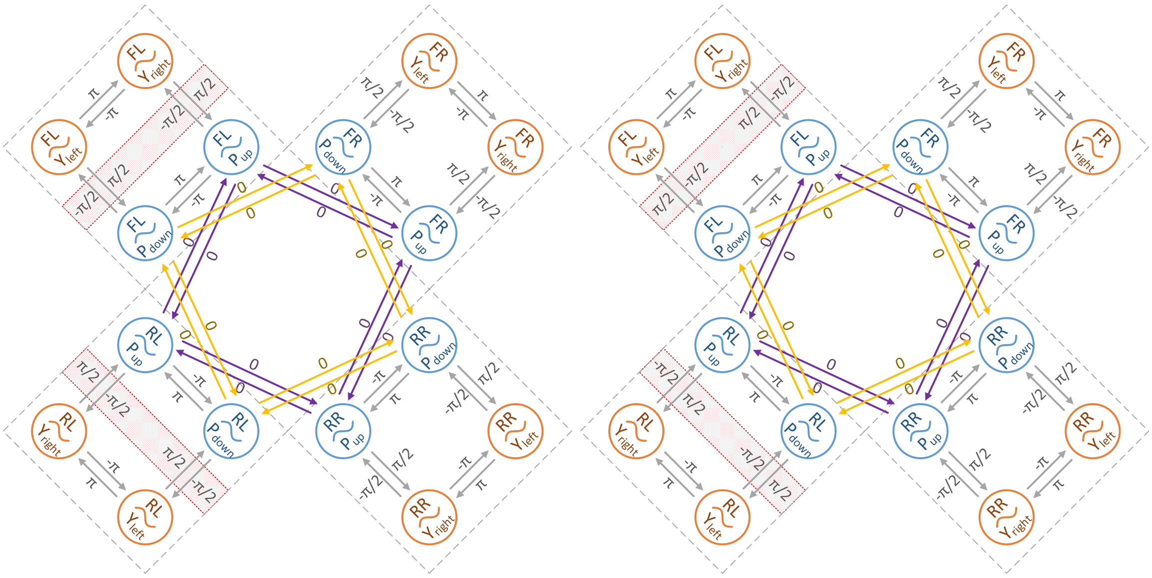

(a) (b)

Figure 6.8 The CPG model of the quadpus morphology's locomotion gait. See the text for shape, color and shading conventions. (**a**) The forward translational locomotion. The CPG of each module is composed of the pitch and yaw oscillators. Within the front right and rear right modules, the pitch oscillators are $\frac{\pi}{2}$ leading the yaw oscillators to generate propulsion, and vice versa for the modules on the other side. The inter module connection of the oscillators are fully synchronised in a circular pattern, with all pitch oscillator pairs on the loop. The yaw oscillators are indirectly synchronised as a secondary stage through the pitch oscillators. (**b**) The counterclockwise rotational locomotion. The only difference between the rotational and the forward CPG model is the phase shift between the pitch and yaw oscillators on the left side of the robot. The pitch oscillators are all leading the yaw oscillators by $\frac{\pi}{2}$, generating movement with consistent angular direction for all limbs.

Gait	Module	Oscillator	Amplitude	Oscillator	Amplitude
Synchronous Translational	Front right body	pitch	0.50 0.50	yaw	0.50 0.50
	Front left body	pitch	0.50 0.50	yaw	0.50 0.50
	Rear left body	pitch	0.50 0.50	yaw	0.50 0.50
	Rear right body	pitch	0.50 0.50	yaw	0.50 0.50
Synchronous Rotational	Front right body	pitch	0.50 0.50	yaw	0.50 0.50
	Front left body	pitch	0.50 0.50	yaw	0.50 0.50
	Rear left body	pitch	0.50 0.50	yaw	0.50 0.50
	Rear right body	pitch	0.50 0.50	yaw	0.50 0.50

Table 6.3 Amplitude of the oscillators for the quadpus morphology CPG model.

6.3.4 CPG Model for Quadruped Morphology

The coordinated movement of the limbs' pitch motion and the spine's roll motion is the primary source of the robot's propulsion from the perspective of each limb for the trot gait. They are thus the dominant oscillators in the network and are closely coupled together with the shortest distance. From the perspective of the inter-limb coordination, to realise the diagonal bipedal pattern, the left and right pitch oscillator pairs are connected with a constant phase shift of π, as well as the front and rear pitch oscillators, which use the spine as an intermediate stage to achieve the same phase shift indirectly. Here a reduced topology is introduced that the left and right pitch down oscillators together forms a pseudo oscillator pair as they are constantly in an anti-phase relationship. In this way, the pitch and roll oscillators are not connected in a pair-wise fashion where only the pitch down oscillators are connected as the agent of the pitch motion to one oscillator of the roll pair to reduce the potential communication overhead. On top of the spine involved network, a direct connection between the diagonal opposite oscillators are introduced to intentionally synchronise the pitch oscillator pairs for additional redundancy in case of abnormal synchronisation with the spine oscillators. To increase the stride length taking advantage of the yaw motion capability of the spine as that mention in Section 6.2.4, while the limbs on one side lift up controlled by the spine roll oscillators, the CPG model utilises the spine yaw oscillators to bend the robot body to the other side. Lastly, the yaw oscillator pair of the limb is connected to the pitch oscillator pair which is in turn connected at a secondary stage to the spine roll oscillators to compensate the limbs abduction and adduction movement.

For the spin in place movement CPG model, there are fewer oscillators involved. The angular propulsion from an individual limb is provided and controlled by the coordinated yaw oscillators output of the limbs and roll oscillators output of the spine. The topology of

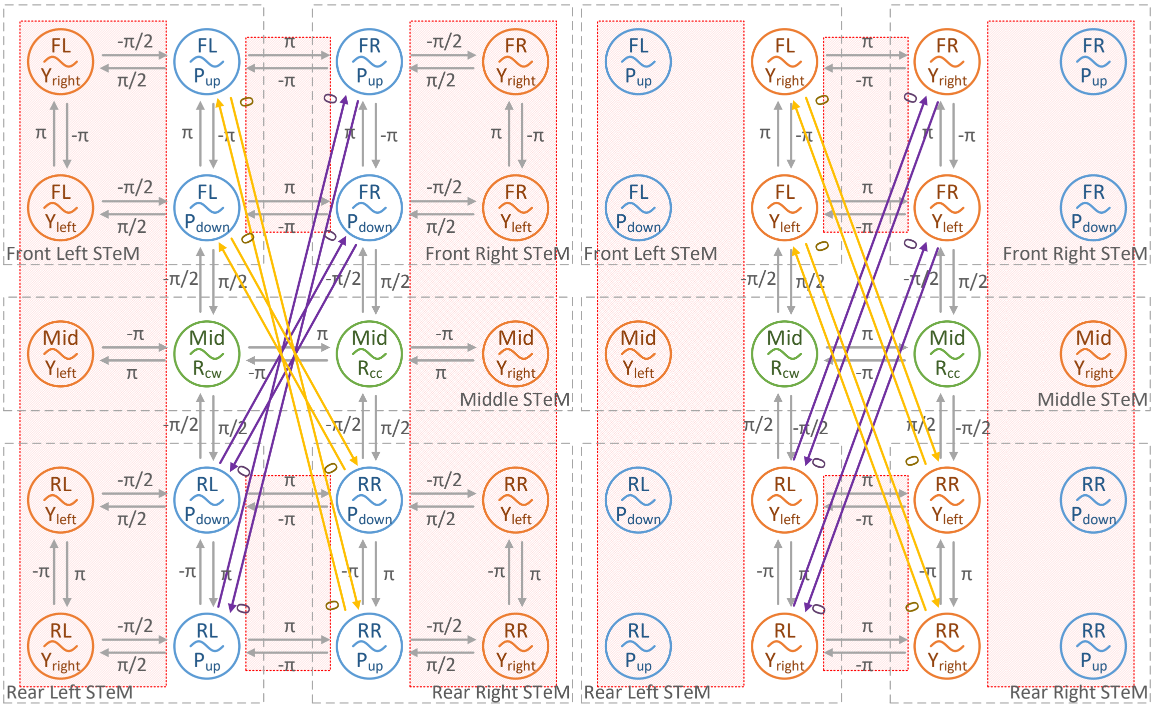

(a) (b)

Figure 6.9 The CPG model of the quadruped morphology's locomotion gait. The oscillators of the limbs in both sub-figures are placed axisymmetrically about the vertical and horizontal axes passing through the figure centre for clear arrangement. See the text for shape, color and shading conventions. (**a**) The forward translational locomotion CPG. The oscillators controlling the limbs consist of pitch and yaw pairs and those controlling the spine consist of roll and yaw pairs. The front left and rear right pitch down oscillators are leading and lagging the middle roll clockwise and counterclockwise oscillators by $\frac{\pi}{2}$ respectively for propulsion generation. The front left yaw motion is $\frac{\pi}{2}$ lagging the pitch motion to stay in-phase with the spine motion while the rear right yaw motion is $\frac{\pi}{2}$ leading the pitch motion to keep an anti-phase relationship, both for maintaining upright posture of the limbs during the gait cycle. To reinforce the inter-leg motion synchronisation, the front left and rear right pitch oscillator pairs are connected with a phase shift of 0. The same principle applies for the oscillators of the other diagonal limbs. The middle yaw motion phase is inverted to the roll motion to facilitate the further advancement of the limbs during swing phase. (**b**) The counterclockwise rotational locomotion CPG. The pitch oscillators for the limb motion and yaw oscillators for spine motion are not in use but kept to indicate the difference from that in (**a**). The front left and rear right yaw left oscillators are both leading the middle roll clockwise and counterclockwise oscillators by $\frac{\pi}{2}$ respectively for propulsion generation. The same principle applies for the oscillators of the other diagonal limbs. The inter-leg motion oscillators are also reinforced with 0 phase shift connection. It should be noted that the position of the pitch and yaw oscillators of the limbs are swapped between (**a**) and (**b**).

the spinal region is similar to that of the trot gait but the connections between the oscillator pairs are swapped. The left and right limbs' yaw left oscillators form a pseudo pair and are connected to the spine roll oscillators. The neighbouring connections of the CPG model result in the outputs of the oscillator pairs between the left and right being inverted while it is synchronised for the front and rear oscillators. The connections are consolidated by the diagonal direct connection to provide the whole-body propulsion. The connectivity and the phase shift of the CPG model for the quadruped morphology gaits are illustrated in Figure 6.9.

Gait	Module	Oscillator	Amplitude	Oscillator	Amplitude
Trot Translational	Front left limb	pitch	0.20 0.20	yaw	0.15 0.15
	Front right limb	pitch	0.20 0.20	yaw	0.15 0.15
	Middle spine	roll	0.30 0.30	yaw	0.20 0.20
	Rear left limb	pitch	0.20 0.20	yaw	0.15 0.15
	Rear right limb	pitch	0.20 0.20	yaw	0.15 0.15
Trot-like Rotational	Front left limb	yaw	0.20 0.20	pitch	N/A N/A
	Front right limb	yaw	0.20 0.20	pitch	N/A N/A
	Middle spine	roll	0.30 0.30	yaw	N/A N/A
	Rear left limb	yaw	0.20 0.20	pitch	N/A N/A
	Rear right limb	yaw	0.20 0.20	pitch	N/A N/A

Table 6.4 Amplitude of the oscillators for the quadruped morphology CPG model.

6.4 Terrestrial Locomotion Performance

As the control approach of the MoTeR is based on the bio-inspired CPG models and focused on the terrestrial locomotion, the evaluation of the performance is divided into two aspects. First is the coordination results of the motion of the limbs, which is to investigate the synchronisation properties of the CPG network, whether it achieves the desired behaviour, and generates and maintains stable gait. The second is to investigate the speed of the robot's locomotion in practice and compare the difference among different morphologies.

6.4.1 Gait Generation and Transition

The CPG output waveform of each tested gait is illustrated in Figure 6.10. All DoFs of the available modules start from the neutral position, which corresponds to the CPG oscillator

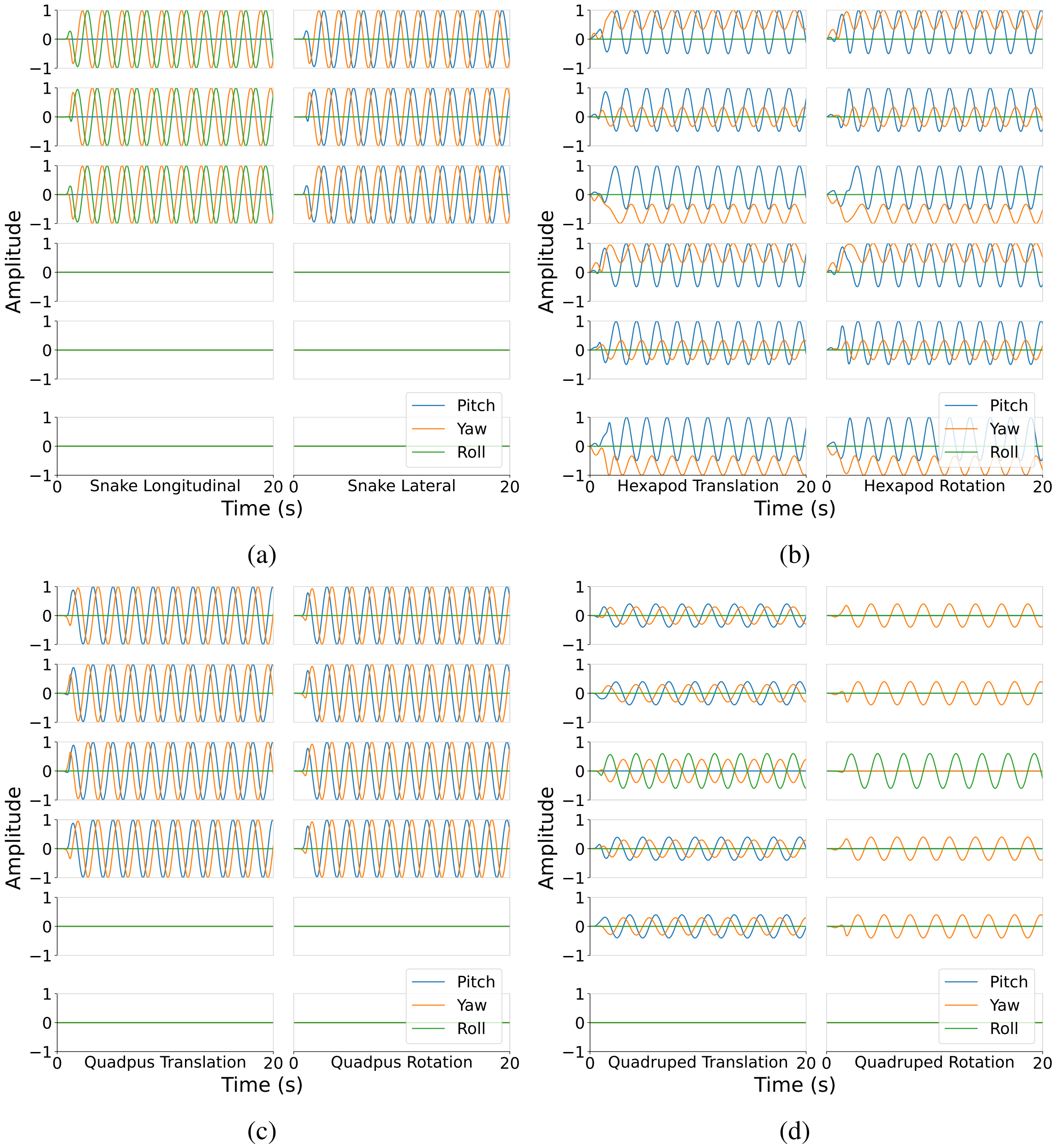

(a) (b)

(c) (d)

Figure 6.10 CPG output waveform of the MoTeR for the eight tested gaits. Each gait is plotted with a duration of 20s, starting from the all-zero neutral state. (**a**) and (**c**) show the forward, rotation and lateral locomotion gaits for the snake and quadpus morphologies. From top to bottom, the rows represent the modules arranged in a counter clockwise order for the quadpus morphology, the head to the tail along the longitudinal direction for the snake morphology. The forward and rotation gaits of the hexapod morphology are shown (**b**). From top to bottom, the rows represent the front left, middle left, till the front right module in the counterclockwise order. A continuous offset is introduced to the four front and rear modules to mimic the arrangement of the hexapod natural counterpart and avoid collision of modules during locomotion. (**d**) shows the forward and rotation gaits for the quadruped morphology. From top to bottom, the rows represent the front left, front right, middle spine, rear left and rear right modules respectively. The roll motion of the spine module is employed in the quadruped locomotion to actively provide vertical movement of the leg modules.

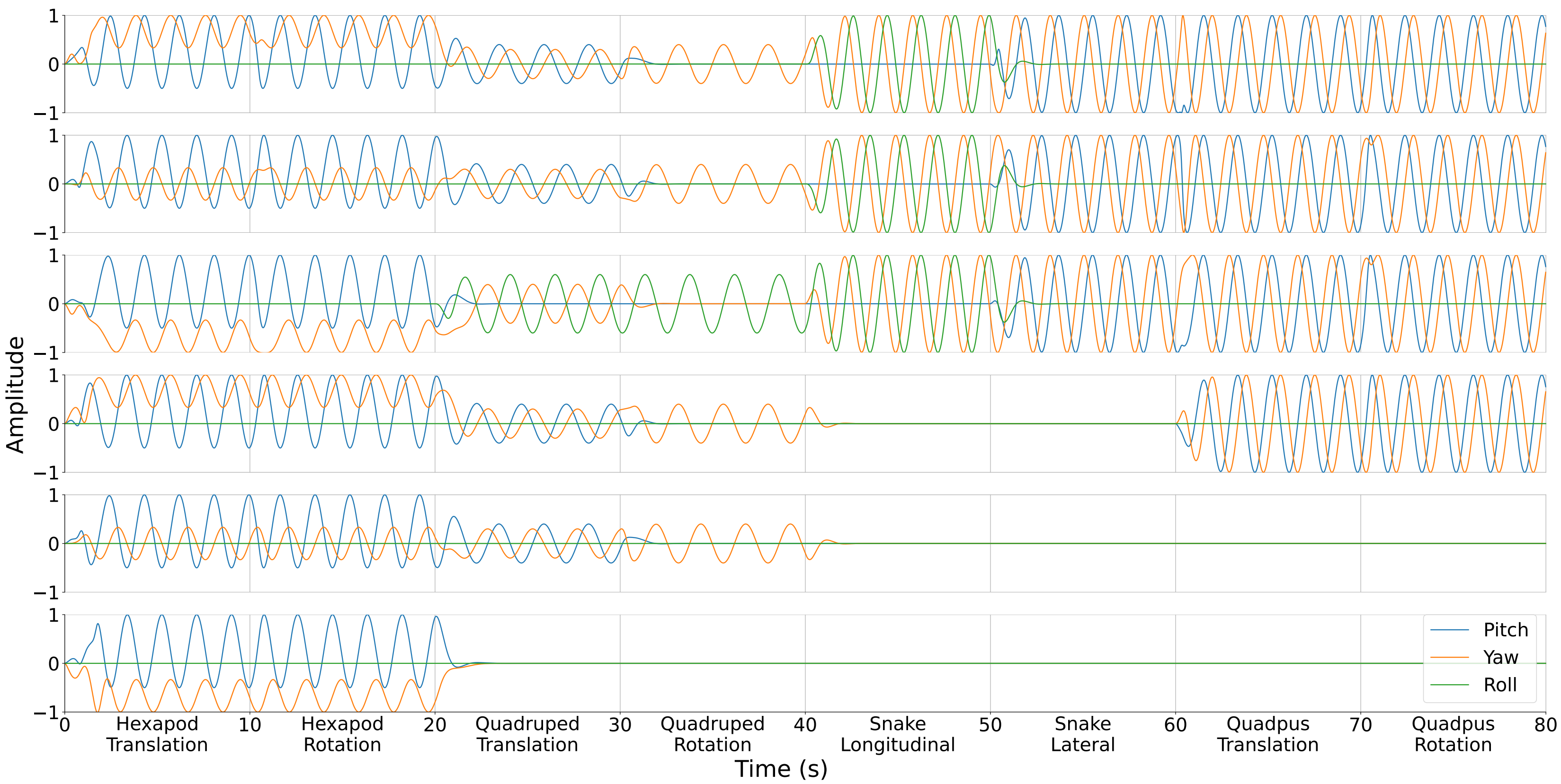

Figure 6.11 Overview of the CPG output waveform concatenated in a continuous timeline. The state of the oscillators will not be reset at the end of each gait. For the DoFs with no output, the intrinsic amplitude of the relevant oscillators is set to 0 while the intrinsic frequency remains the same as other oscillators that have an output. The order of the morphologies is rearranged so that both attenuation and oscillation of the CPG exist at the transition period.

output value 0. The maximum amplitude of the oscillator output is defined between -1 and 1. The results demonstrate that for various morphologies and gaits, the robot is capable of smoothly self exciting and gradually synchronising all the motion among the modules. For the snake, hexapod and quadpus morphologies, the intrinsic frequency of the oscillators is 0.5 Hz, while it is 0.4 Hz for the quadruped morphology for higher stability during locomotion. The connectivity patterns of the oscillators of the quadpus and snake morphologies are relatively simple, and are similar from the perspective of the resultant waveform. Both gaits of the morphology take approximate 0.8s for the CPG to initiate oscillations and converge at 2.3 s. For the quadruped morphology, the CPG oscillates at about 0.5 s, converges at 1.8 s and 2.5 s for the forward and rotation gaits respectively. In the hexapod gaits, due to the existence of the unipolar output, the CPG almost initiates the oscillation at 0 s and takes around 2 s to converge. The waveform diagrams clearly reveal that the corresponding CPG models applied to the MoTeR of various morphologies and gaits can rapidly and faithfully generate the anticipated gait with the desired amplitude and phase relationships.

By altering the connectivity during the operation of the CPG network, the transition from one gait to another can be realised. An overview of different gaits concatenated in a continuous timeline is shown in Figure 6.11 to demonstrate the transition characteristics. It is clear that during the transition period, the waiting and boosting behaviours can be observed for some of the oscillators to re-synchronise the CPG network in accordance to the updated phase shifts. In addition, when an oscillator has a new target amplitude of 0 from a non-zero value or vice versa, the output attenuates or regenerates smoothly, respectively. This suggests that for a morphology that is in the course of locomotion, it is capable of seamlessly proceeding to another gait without fully interrupting the current motion. The concatenated waveform also demonstrates the transition of the gaits from one morphology to another, although this is not applicable in practical applications for these four morphologies.

6.4.2 Locomotion Performance

To measure the translational velocity of the robot, an experimental fixed-length track of 50 cm was employed given that the MoTeR might deviate from its intended direction over longer distances without odometry feedback. The velocity of the robot was subsequently ascertained by measuring the time duration required for the robot to traverse the entirety of this predefined course. To assess angular speed, the time required for the robot to perform a complete 360 degree in-place turning was measured. For each gait, a total of 10 trails were conducted. The resultant speed data are illustrated in Figure 6.12.

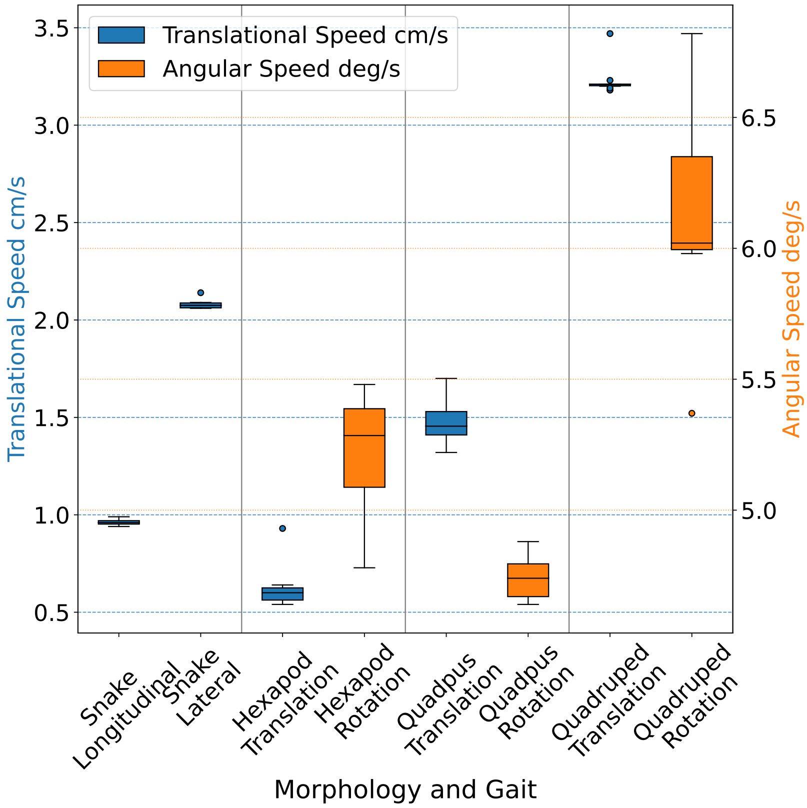

Figure 6.12 A box chart of the locomotion speed for each tested morphology and gait. Each two gaits of the corresponding morphology are grouped in the same section. The blue boxes (position 1,2,3,5,7) represent the translational speed, with values labelled on the left vertical axis. The orange boxes (position 4,6,8) denote the angular speed, with values labelled on the right vertical axis.

Among the four tested morphologies, the quadruped MoTeR demonstrates the most effective locomotion speed, achieving 3.23 cm/s in translational speed and 6.12 deg/s in angular speed. The speed difference among different morphologies has a relatively large span of 2.93 cm/s (174.93% of average translational speed 1.67 cm/s), and 2.19 deg/s (40.82% of average angular speed 5.35 deg/s), revealing the morphology's pivotal role in the speed performance. The hexapod morphology displays the lowest translational speed of 0.62 cm/s. This is mainly caused by the small available workspace of the legs due to the close arrangement of the legs.

The variability of each morphology's locomotion also varies. The snake robot demonstrates good consistency among test trails, with a standard deviation of 0.0152 and 0.0230. The quadruped morphology performs well for the translational movement, 0.0858, but not for the rotational movement, 0.3909. To reduce the influence of the speed and unit of different locomotion modes when making the comparison, the coefficient of variance is also calculated, listed in Table 6.5. Other results including the average speed and stride length ratio with respect to the body length in direction of travel are also included in the table. It is worth noting that, based on the short width of the snake robot, it achieves the highest stride length ratio of 37.83%, demonstrating an effective lateral locomotion using the sidewinding gait.

Morphology and Locomotion	**Average Speed (cm/s)**	**Average Stride Length Ratio**	**Standard Deviation**	**Coefficient of Variance**
Snake Longitudinal	0.96	1.95%	0.0152	0.0158
Snake Lateral	2.08	37.83%	0.0230	0.0111
Hexapod Translation	0.62	3.91%	0.1124	0.1804
Hexapod Rotation	5.22	N/A	0.2235	0.0428
Quadpus Translation	1.47	4.87%	0.1062	0.0721
Quadpus Rotation	4.74	N/A	0.0892	0.0188
Quadruped Translation	3.23	27.12%	0.0858	0.0266
Quadruped Rotation	6.12	N/A	0.3909	0.0639

Table 6.5 Experimental results of the robot locomotion through the predefined courses for different morphologies in terms of the average speed, average stride length ratio, standard deviation, and coefficient of variance.

6.5 Summary

Building on top of the capabilities of STeMs, a polymorphic modular robot which can be readily reconfigured into various morphologies to imitate specific natural species has been presented. The bio-inspired morphologies of the MoTeR exhibits significant differences in the number of modules, structural connection, and modes of locomotion. Through closely mapping the CPG network to the tensegrity modules and their corresponding motions required, the robot realises different terrestrial locomotion gaits in accordance with specific morphologies without creating the numerical model, which greatly simplifies the modeling of robot's motion control.

Based on the interpretation of experimental results, the performance exhibited by the MoTeR aligns relatively consistently with general expectations. On one hand, the more complex morphologies and corresponding gaits demonstrate superior performance in terms of speed, underscoring the immense advantages of an upright posture in achieving efficient rapid movement and enhanced agility. Conversely, simpler structures with associated locomotion patterns exhibit obvious advantages in stability, which is inline with the widespread employment of the sprawling posture in animals on irregular terrains. Additionally, since there are notable resemblances in the morphology and locomotion patterns between the hexapod and quadpus MoTeRs, the overall locomotive performance of these two morphologies is comparably similar, which is also evident from the experiment data.

From the perspective of the polymorphic robot applications, it can be learned that the selection of morphology should closely align with the requirements of the specific scenario. This alignment ensures:

- The properties such as the compliance, flexibility and resilience exhibited by each STeM, as discussed in Chapter 5, is harnessed to enhance the robustness of the robot in harsh environments.
- The agility endowed by the atypical tensegrity structure design, as well as the adaptability offered by the biomimetic morphology and locomotion control, is fully exploited.

By this means, it can finally lead to a high degree of versatility across different complex environments and variable tasks.

Chapter 7

Conclusion and Future Work

From a broader perspective, this chapter offers an overall review of this thesis. Firstly, centered around the main contributions proposed in Chapter 1, the roles played by each chapter in the core of the thesis, modular tensegrity robot, are summarised, illustrating how they are interdependent and complementary to each other. Subsequently, the focus shifts back to the original and ultimate goal, the system design of a modular tensegrity robot, discussing whether the original vision was achieved. Finally, potential future work that could further extend the work started in the thesis are suggested, and from a longer-term viewpoint, the possible implementations and applications of modular tensegrity robots are envisioned.

7.1 Chapter Summaries

This thesis provides a comprehensive investigation into the key facets of systematically designing a tensegrity robot, encompassing the motivation, philosophy, structure, and control. Chapter 2 surveys the state-of-art of tensegrity robots, thereby identifying the research gaps and key objectives that this study aims to address. In Chapter 3, theoretical foundations are proposed to address and challenge these identified needs. Chapter 4 explains the design and build process for the proposed tensegrity robot. Chapter 5 looks into and analyses the characteristics of the robot's modules from a microscopic perspective. Conversely, Chapter 6 evaluates the robot's polymorphic capabilities through a macroscopic lens. This section encapsulates and summarises the essence of these chapters as follows.

- Chapter 2, serves as a literature review, starting with foundational concepts, making modifications and supplementation to the prevailing definitions and classification methods of tensegrity structures. Specifically, it introduces the class of atypical tensegrity, which, as opposed to the typical class that only uses straight struts, incorporates compression components with non-one-dimensional shapes. This is essential given that the structural design philosophy proposed in this thesis deviate somewhat from conventional approaches, aligning it more suitably within the context of this thesis. Then, the chapter looks into a detailed analysis of existing tensegrity robots that have a strong correlation with this thesis, while also briefly compared with other representative research. The focuses of these studies vary. Initial explorations into tensegrity robots concentrated on leveraging the unique properties of the structure to enhance robots' robustness, resulting in the use of fundamental structures like tensegrity triangular prism and icosahedron. However, given that these traditional tensegrity designs exhibit outstanding structural performance but lack mobility, subsequent research shifted towards enhancing robots' locomotion capabilities. Innovative approaches beyond those exploiting slow structure deformations emerged during this transition, such as adopting vibration-induced movement and semi-circular rolling movement. Other strategies aimed to refine the tensegrity structure itself, integrating concepts like biotensegrity into their designs. Additionally, methods that combine conventional wheeled locomotion to enhance locomotion performance emerged, which is one of the approaches explored in this thesis. The chapter also offers a review on modular tensegrity robots although these are limited in current research. Although modular tensegrity robot research is sparse, this chapter offers an overview. Notably, while robots designed for improving mobility significantly advanced the field, they often remained circumscribed within this specific application. Consequently, the chapter's focus shifts to studies not primarily oriented for locomotion, such as robotic manipulators, which unexpectedly demonstrate superior agility of the structure—a critical factor influencing the mobility of tensegrity robots. For example, these designs often possess a larger workspace, increased controllable actuated degrees of freedom, and reduced energy consumption. These provide important insights for this thesis on integrating an efficient and agile tensegrity structure into a modular robot design. Furthermore, the chapter also reviews some bio-inspired and learning based control strategies for tensegrity robots, providing inspiration for the high-level control of the modular polymorphic robot presented in this thesis.

- Chapter 3 synthesizes inspirations from tensegrity robotic manipulators and experiences obtained from existing tensegrity robots. From a structure design perspective, it proposes the novel concept of the “underconstrained transition region”, which correlates to the first point of the thesis contributions. Initially, the chapter analyses the three determinant factors influencing agility of the structure identified in the literature review: motion efficiency, degrees of freedom, and workspace, underscoring their inherent interconnection. Often, when optimising with one factor as the guiding principle, certain improvement can concurrently be achieved in one or both of the other factors. Among these, degrees of freedom play an especially pivotal role. The underconstrained transition region is specifically designed to increase the degrees of freedom in tensegrity structures. The underlying principle originates from the distinctly different motion freedoms achieved when a fundamental 2D C-Strut tensegrity structure is placed in a 3D space. In fact, due to the unique connection pattern of compression elements in the structure, in typical tensegrities, the struts can somewhat be regarded as offering one degree of freedom about their axial direction. However, in traditional designs, since the structures are normally monolithic entities, this freedom is not practically usable. The underconstrained transition region, by employing the C-Strut as a bridge connecting two tensegrity structures, successfully exploits its inherent degrees of freedom. Moreover, designs based on this concept are not limited to using the C-Strut as the transition region but can employ other complete tensegrity structures, unveiling it as a comprehensive design concept. Building upon the underconstrained transition region, example designs applying it to typical tensegrity structures have been illustrated, including those with one, two, and three degrees of freedom. These examples, utilising C-Strut or its minor variations as transition region, combined with basic tensegrity triangular prisms and icosahedrons, demonstrate the concept’s broad generality in design. If applying to atypical tensegrity structures, the design becomes even more straightforward, hence no specific examples are provided. Indeed, this very approach is employed in the design of basic module of the proposed robot, which is subsequently presented in Chapter 4.

- Chapter 4 describes the design of the Symmetrical Tensegrity Mechanism (STeM), which employs the concept of the underconstrained transition region, as well as the prototype and simulation setups used in this thesis. Initially, it introduces STeM, the constituent module of the robot presented in this thesis, specifically explaining how high agility is achieved through the use of the underconstrained transition region. Unlike the examples shown in Chapter 3, which utilise typical tensegrity structures, STeM employs an atypical tensegrity design. The overall structure takes the form of an octahedron, with its compression elements shape as the triangular bipyramid. This design choice enables better integration with conventional rigid structures. The deeper rationale lies in allowing STeM to be modularised easily when interconnected with a rigid cubic tile system, thus substantially enhancing the robot's versatility—a point linked to the second contribution in this study. With the employment of the underconstrained transition region, it results in the STeM with a passive substructure which achieves three passive rotational degrees of freedom. The optimisation for the placement of elements within the structure is also discussed. The chapter then explains how the design of the active substructure draws inspiration from human shoulder complex to actuate these degrees of freedom. Given that the shoulder's skeletal structure is essentially a ball-and-socket joint inherently offering three degrees of rotational freedom, it utilises antagonistic muscle pairs to effectively control the joint with both independent and concurrent motions. Imitating this principle, the STeM integrates six active threads symmetrically distributed around the tensegrity structure, working in pairs to drive the entire mechanism. Subsequently, details regarding the physical implementation of the STeM are also provided. Owing to such a hybrid design, the STeM prototype used for physical experiments exhibits a high level of completeness. Its tensegrity part, located between two cubic hubs, is structurally supported by three tiles on each side, retaining a clear segmentation and preserving the topology and geometry of the original design. The actuation components are all encapsulated within the cubic hubs. Locally, it is protected by conventional rigid structures, while globally, by the tensegrity structure. Furthermore, the ample interior space within the cubic hubs accommodates additional controllers, sensors, and power sources, making each STeM self-contained. Combined with the homogeneous connector, the robot's scalability and reconfigurability are enhanced. The chapter also details the simulation experiment configurations of this thesis. Based on the Chrono engine, it successfully simulates both complex closed loop connected threads and traditional mechanical linkages in a single scenario, providing a suitable platform for the previously mentioned experiments involving wheeled locomotion.

- Chapter 5 presents the control methods for the STeM and offers a detailed analysis of its exhibited characteristics. Initially, the workspace of STeM is examined under both passive and active operation modes. Distinct from typical tensegrity structures, the STeM has a more predictable deformation pattern. Knowledge of the workspace is therefore critical for its normal operation in robot actuation applications. In this context, compared to the relatively simple passive workspace that is limited only by the physical structure, the determination of the active workspace is carried out through an algorithm called force closure check. Results reveal the interdependent nature of its three rotational motions' ranges, that the range of a specific motion is not fixed and depends on the states of the other two. Although the determined active workspace contains certain extreme conditions, it reasonably outlines the maximum tolerable deformation for the STeM in its active mode. Following this, a tailored strategy for effectively controlling the STeM is introduced, which correlates to the low-level control of the third contribution in this thesis. This control approach considers the STeM as a mechanism pivoting around a fixed point and incorporates force closure based control that originally adopted by cable-driven parallel manipulators. Given the STeM's over-actuated nature, to reduce computational overhead during operation, the approach introduces a virtual variable in the algorithm, which makes the calculation of the active thread's expected states a direct process, enhancing its real-time control feasibility. The chapter then investigates the characteristics of STeM from three perspectives: actuation, structure, and locomotion, which correlate to the module's robustness of the fourth contribution. For actuation, the improvement in accuracy for the force closure based control over the uniform pretension method is analysed and validated through prototype experiments, alongside an examination of certain disagreements between the two. Internally, the distribution of forces on the thread under different pretension modes is also analysed, proposing appropriate strategies to maintain consistent pretension of the STeM's tensegrity structure during operation. Regarding structure, STeM's robustness endowed by its encapsulated tensegrity structure is dissected through four facets, including static and dynamic loads, intrinsic frequencies, and fault tolerance. These include, how it passively complies to externally-induced deformations, how it absorbs inter-segment impacts, and how it remains functional under certain damages. Lastly, from a slightly higher level, the unique locomotion capabilities brought about by the STeM are tested under wheeled locomotion, in comparison with traditional rigid body robots or non-wheeled tensegrity robots. For example, in passive mode, the STeM equips the robot with improved adaptability to uneven terrains. In active mode, the robot can overcome higher obstacles. Additionally, an interesting and unique ability for self-recovery from a rollover state is also demonstrated.

- Chapter 6 delves into the Modular Tensegrity Robot (MoTeR) proposed in this thesis, which is constructed in various configurations with the STeM modules, alongside its corresponding high-level control strategies and the demonstrated locomotion characteristics. These correlate to the high-level control aspect of the third contribution and the polymorphic locomotion aspect of the fourth contribution. From an actuation perspective, the STeM offers exceptional agility, and in terms of modularity, STeM provides excellent connectivity. Analogising STeM to animals' joints or body parts, it provides broad potentials for the possible configurations of the MoTeR it composes.

Initially, the chapter introduces the bio-inspired morphology designs, demonstrating four implementations, describing how the polymorphic MoTeR emulates animals in the natural world. The first morphology is the snake, representing a limbless configuration. Three STeM modules are concatenated in series, constituting only the body segments of the MoTeR. In this configuration, MoTeR achieves longitudinal and lateral locomotion, by imitating the serpentine and sidewinding movements of snakes. Since the natural snake body have a great number of joints while MoTeR only has three, it cannot form continuous wave-like motions like the former, resulting in a more symmetrical and alternating motions between its adjacent modules. The second morphology is the hexapod, inspired by stick insects. Two sets of three STeMs are arranged side by side and then are connected end to end. Here, the central part comprising six cubic hubs forms the body, while the outer six hubs act as the legs. In this configuration, the MoTeR uses a tripod gait, demonstrating both translational and rotational locomotion. Since there is no preserved space between the front, middle, and rear legs of the hexapod MoTeR, the two outer pairs of STeMs retain a certain outward offset to provide clearance for the middle legs' movement. The third morphology is the 'quadpus', a semi-bio-inspired configuration. The octopus it imitates has eight tentacles, but due to the cubic shape of STeMs, it can only connect four limbs on a plane around an extra central hub. The quadpus MoTeR employs a heuristic synchronous gait, where all four limbs move simultaneously, offering independent traction in their respective quadrants. This is somewhat analogous to a four-wheeled omnidirectional vehicle, except that the rolling motion is replaced by rhythmic limb movement. The quadruped is the fourth morphology presented in the chapter, inspired by quadruped vertebrates and representing a more advanced MoTeR configuration. Four vertically arranged STeMs serve as the limbs. Then, to achieve legs' elevation movement while they have only one joint, a fifth STeM is introduced, functioning as the spine. The diagonally symmetrical motion of the spine makes the quadruped MoTeR ideal for the trot gait, where it achieves both translational and rotational locomotion. Given these bio-inspired morphologies and gaits as paradigms, the chapter further explores control strategies for stably generating these gaits and employs the Central Pattern Generator (CPG) which is also a biomimetic approach. Owing to the consistency and repetitiveness of STeMs in the MoTeR, the CPG model applied for controlling the MoTeR also features a high modularity. Each STeM is designed to be controlled by three back-to-back oscillator pairs for its pitch, yaw, and roll motions. Based on this, coordinated movements within and among the bodies or limbs are managed by phase relationships and connection strengths among oscillators. Through varying the oscillator's intrinsic amplitude, the STeM's movement can be regulated, and any irrelevant motion can be easily decoupled from the system by setting the amplitude to zero, suggesting the MoTeR's reconfigurability from a software perspective. Finally, the chapter presents physical experiments based on prototypes to investigate the locomotion performance of these polymorphic MoTeRs. The results reveals that, based on the self-oscillation of the oscillators and their mutual inhibitory and excitatory relationships, MoTeRs adopting a CPG control smoothly generate the stable gaits from a still state and seamlessly transit from one gait to another. This is critical for the MoTeR which has a great number of potential morphologies, as it eliminates the need for kinematic modelling in complex configurations with many modules. Moreover, the results also show that the quadruped MoTeR has the highest locomotion speed among the demonstrated configurations, while the snake MoTeR demonstrates the best consistency, aligning closely with their natural counterparts. Distinct from conventional tensegrity robots, which rely on slow structural deformations for movement, the MoTeR possesses advanced locomotion characteristics. Complemented with the wheeled locomotion presented in Chapter 5, it underscores the MoTeR's adaptability across various scenarios, and further affirms its outstanding versatility.

7.2 The Core Proposition of Modular Tensegrity Robots

The core proposition of this thesis—the system design of modular tensegrity robots—literally encapsulates two facets of work which are indeed inseparable. For the first aspect, the modularisation of tensegrity robots is not a straightforward piece of work. The inherent flexibility and irregularity of tensegrity structures present significant challenges. As mentioned in Section 1.2, such a modularity is with respect to the scope of functionality, which should be scalable and reconfigurable, rather than considering robot components that are not independently functional as modules. The underlying reason is to enhance the practical usability and versatility of tensegrity robots. This, especially in terms of versatility, remains in an early stage for many tensegrity robots studies. For the second aspect, an array of research on tensegrity robots pivoted to enhance their functionalities such as mobility and actuation after the robustness endowed by the structures was validated, which is a primary direction of this study. In fact, this also aligns with the intent for modularity proposed in this study. However, existing studies mainly focus on specific or one-for-all applications without considering broader contexts. Therefore, in the way for pursuing the practical usability of tensegrity robots, it can be seen that research into tensegrity could offer tangible functionality for the modules, where the modularity could in turn amplify such functions, which is indeed the study's original conception.

To realise this conception, in Chapter 2 the thesis begins with analysing the pros and cons of existing tensegrity robots, focusing on how they achieve various capabilities, such as various locomotion strategies and distinct actuation schemes. Fundamentally, these capabilities are related to a key factor—agility. The analysis reveals that the improvement of agility requires not only outstanding control algorithms, but also significant changes to the underlying structure design. Subsequently, the study offers a consolidation to the definition and classification of tensegrity, introducing the concept of the underconstrained transition region in Chapter 3. This concept, investigating into efficiency, dexterity, and space three critical factors for tensegrity's movement, modifies the original philosophy of highly redundant constraints on structures, which achieves a balance between excessive and inadequate structural integrity, thus ensuring a designable and controllable motion freedom. This significantly enhances the agility of tensegrity structures. This contribution is expected to be inspirational for future tensegrity designs. As this is a general enhancement to tensegrity, it is not directly related to modularity. Chapter 4 unveils the advantages of atypical tensegrity in a new classification. The MoTeR's modularisation is realised through integration with a rigid structure. The inherent challenges of dynamic inter-structure connection for tensegrity led to this decision. Typical tensegrity is exceptional in structural efficiency, but integrating with traditional structures often breaks the structural composition of typical tensegrity, diminishing its structural efficiency. As a result, in this study, atypical compression elements are employed in the junction with rigid structures, seamlessly endowing tensegrity structures with modularity. This contribution offers a paradigm for merging the two structures. With structure design available, Chapter 5 looks into the control and evaluation of the STeM module. Compared to conventional tensegrity robots, the MoTeR has an additional layer of low-level control for the STeM. Given its control objective is different from that for typical many-DoF tensegrity structures, a force closure based approach is employed for its real-time control. Based on this, the thesis comprehensively evaluates the robot from three main perspectives of control, structure, and mobility, which are highly correlated with tensegrity robots. The results underscore that STeM not only preserves the structure characteristics of tensegrity but also significantly enhances its agility as expected. This contribution could offer an image of characteristics for future tensegrity robots inspired by similar principles. In Chapter 6, the thesis unveils its primary objective, a Modular Tensegrity Robot constructed based on the original conception. Its modularity and versatility are robustly validated. By concatenating identical modules, the MoTeR readily emulates natural animals' morphologies. Leveraging traditional rigid structures, the reconfiguration of the morphologies can be instantaneous and dynamic, significantly enhancing the usability of tensegrity robots across diverse scenarios. Building upon these various morphologies, the thesis demonstrates their smooth generation of corresponding gaits and stable locomotion, which clearly reveals the realisation of the expected augmentation of tensegrity's functionality. This contribution unveils the broad potential of modular tensegrity robots. To summarise, this thesis, through making efforts in several aspects and focusing on two primary facets of work, shapes a comprehensive design philosophy. It initiates a novel, untouched direction for modular tensegrity robot research and in a certain level advances its progress towards practical applications.

7.3 Future Work

The research presented in this thesis encompasses multiple aspects of tensegrity robot development, offering rich potentials for its future work. These prospects extend beyond refinements of only the MoTeR, where these involve specific areas such as new forms of tensegrity robot actuation sources, precision control of tensegrity structures, and enhancements in polymorphic soft robots' gait, as well as broader applications such as substituting conventional robot joints and scaling to larger scale robot systems. Optimising the topology of MoTeR's tensegrity structure could lead to more effective constraints of unwanted translational displacements among components. In contrast to the commonly seen motor based thread actuation in tensegrity robots, the introduction of electrostatic actuation films makes their aquatic applications more feasible. The state estimation of tensegrity structures, when coupled with deep learning, could offer more accurate predictions. On the other hand, the employment of reinforcement learning could make possible a more natural gait compared with the current pre-knowledge only approach. Though the presented STeM is a small $30 \times 10 \times 10$ cm module, its underlying tensegrity design could be applied to and replace traditional robot joints. By doing so, it holds potential for larger outdoor robots, endowing them with heightened adaptability and robustness.

7.3.1 Advancements in Tensegrity Design

The design concept proposed in this thesis offers a novel perspective on tensegrity tailored for robotic applications. Yet, the possibilities within this domain remain vast and largely uncharted. This subsection looks into several potential areas, encompassing the design of structure topology, the choice of actuation scheme, and the estimation of structure states.

Topology Optimisation of Multi-DoF Tensegrity Structures

As discussed in Section 4.2, the lateral translational displacement of the three DoF tensegrity structure based on the underconstrained transition region utilised by the STeM is constrained through two sets of orthogonally arranged threads. However, in the neutral posture, it does not impose lateral constraints which is in contrast to the longitudinal situation. The intensity of these lateral constraints increases with the increment of the lateral displacement, introducing a certain level of hysteresis. As a result, there exists a difference in the lateral and longitudinal structural stiffness. This not only potentially impacts the adjustment of the structure's variable stiffness and the overall robustness, but also amplifies the challenge of precise control of the structure.

From a topological perspective, for the current three DoF underconstrained transition region, it is necessary to incorporate additional threads to ensure sustained lateral constraints to the transition region's central area even in its neutral posture. The design paradigm of the one DoF transition region can serve as a reference, suggesting that the tension elements between the two compression elements should form a certain angle other than a right angle in the constraint direction. Additionally, to less affect the originally required motion freedom, the angle's orientation should be opposite to that in the one DoF case, with the angle opening towards the central structure rather than outward. The central strut currently used in the STeM's design, due to its small cross-sectional area, which is theoretically zero, is not suitable for connecting multiple threads with a certain distance. This requires a more complex central structure which could be a quadrangular prism or a single atypical compression element. Although such a topology might somewhat constrain the structure's rotation movement around the longitudinal axis, considering that the struts used in tensegrity's physical implementations have a physical volume, these constraints, absent in abstract models, are already widespread in practical applications. Thus, when reasonably optimised in the geometry upon the topology, it could endow enhanced isotropy and robustness for tensegrity structures adopting the underconstrained transition region concept.

Unconventional Actuation Scheme

Full actuation holds advantages for tensegrity robots. Although motor based thread actuation is a common approach for driving tensegrity robots, as a form of exo-thread actuation, it does not offer superior benefits in this regard. The relationship between threads and tensegrity is akin to muscles in the human body. Hence, merging threads with actuation sources to form on-thread actuation could significantly broaden the potentials of tensegrity robots. Though existing research has made certain explorations such as using pneumatic artificial muscles (PAMs) [65, 31] and Twisted and twisted artificial muscles (TAMs) [118], some of these are even more cumbersome than motors, or exhibit slow dynamic properties.

In this case, electrostatic film actuators, such as the hydraulically amplified self-healing electrostatic (HASEL) actuators [119], might emerge as a promising alternative. Primarily, the HASEL lacks traditional mechanical components, aligning seamlessly with the philosophy of tensegrity, thereby suggesting enhanced durability and robustness. Compared to pneumatic powered artificial muscles, it offers higher control linearity, which is critical for precise control of tensegrity structures. Additionally, it can be embedded in series with threads, seamlessly integrating with the entire structure, thus effortlessly achieving a full actuation scheme. Furthermore, the design possibilities are greatly expanded as it can be constituted from numerous small units arranged in diverse configurations. Importantly, the HASEL is inherently waterproof, endowing tensegrity robots with enhanced capabilities for underwater applications, which is less observed in literature. With such a unconventional actuation scheme, future mechanical design work for tensegrity robots might be more compact and intuitive, making the robot even more "tensegrity".

State Estimation of Tensegrity Structures

The inherent multi-degree of freedom nature of tensegrity structures diverts many tensegrity robots away from traditional numerical modeling based motion control. Instead, they employ various heuristic [62], bio-inspired [50, 95, 96], and learning-based approaches [92, 95]. STeM, deviates from this trend, employing a force closure based method to achieve more deterministic motion. However, precise control, especially the estimation of the tensegrity structure’s state, holds practical significance for robots like the STeM, especially when operating in precision-demanding scenarios.

Given that tensegrity robots build upon soft structures, the variability in individual units fabricated often surpasses that of traditional rigid counterparts. In such a context, learning-based approaches could be a suitable choice for the STeM's state estimation. For example, the future work could leverage one of the deep learning methods in conjunction with developed simulation environments and prototypes, to facilitate extensive training of the robot across diverse environments and operational behaviors, thereby acquiring a comprehensive knowledge base for its state estimation. Inputs for such training could range from actuator outputs, force distribution within elements, intentionally introduced external perturbations, to the structure's state over specific duration. Alternatively, the reservoir computing could be employed, exploiting the inherent non-linearity of the tensegrity structure as the reservoir. Such an approach would be particularly suitable for the structures' low-level control systems demanding lower computational loads and higher real-time response.

7.3.2 Locomotion of Polymorphic Tensegrity Robots

In Chapter 6, four morphologies are presented as examples. However, the range of potential configurations is enormous, which amplifies the challenges in the robot's locomotion control. Key considerations include the robot's capability to self recognise its current morphology, whether the gait imitation is in its optimal configuration, and if such a system truly augments the effectiveness in initially proposed applications.

Self-Recognition of Morphologies

The polymorphic locomotion of the MoTeR demonstrated in this thesis mainly focuses on the proof of the robot's capability in imitating the gaits corresponding to the natural counterparts' specific morphologies. Thus, it is considered the robot has clear knowledge of its current configurations. However, during autonomous operations, the morphology employed by the robot often comes from its independent decisions based on both environment and requirements. This underscores the importance of the robot to have a precise recognition of whether it has achieved the intended configuration. With this, the robot can toggle between various gaits tailored to its current morphology or execute recovery procedures when its morphology is compromised.

MoTeR employs magnetic connectors for module concatenation, complying with the specifications of the Sub-Modular Cube system [107]. Within this system's vision, these magnetic connectors serve several purposes: they facilitate physical connection and are also responsible for transferring power and signals. The future work could involve assigning unique identifiers to each module and its constituent tiles, thereby enabling the robot to recognise its morphology through the underlying communication network topology. Such an approach requires a dynamic network management system capable of dynamically establishing or terminating inter-module communications and constructing route awareness in real-time. Progress in this direction has already been observed in another study based on the same modular system [120]. Such a system is particularly beneficial to MoTeR's CPG-based locomotion control. For example, to temporarily amplify traction during an uphill climb, a snake MoTeR could dynamically connect with an additional module or even another concurrently moving snake robot. Rapid morphology self-recognition would allow the system to update the CPG model in a timely manner, ensuring synchronised movement for the newly integrated part. Furthermore, if a module run out of power mid-operation, it is necessary for the system to recognise this morphological change and accordingly adjust the CPG parameters to preserve a level of locomotion capability.

Gait Optimisation with Deep Reinforcement Learning

While four morphologies accompanied with five corresponding gaits are realised in this thesis, these gaits draw inspiration from biological counterparts combined with heuristic methods, suggesting there's still room for further optimisation. The absence of thorough control variable experiments makes it difficult to ascertain where these pre-knowledge based configurations stand in terms of efficiency and adaptability among similar gaits. Additionally, the flexibility of tensegrity structures leads to discrepancies between the output of CPG and the actual limbs' motion. These underscore the necessity for further optimisation of the CPG models tailored to various gaits.

Given the temporal continuous nature of robots' gaits and the CPG models' continuity in their parameter space, deep reinforcement learning (DRL) becomes an ideal choice in this context. By employing DRL, the robot can continuously experiment with different gaits in actual operations, receiving feedback through environmental interactions. This feedback, in the form of rewards or penalties, can then be utilised to adjust its parameters. A potential advantage of this approach is the robot's capability to uncover efficient or specially adapted gaits for specific environments, aside from those close to the pre-knowledge based configurations, and that human designers never think of. Achieving this would require an appropriate DRL algorithm, especially a well-defined reward function to assess gait performance, which can then be implemented in the developed simulation environment for continuous refinement. In addition to optimising known gaits, this approach also makes possible for the robot to evolve, in post-deployment situation, new morphologies and corresponding gaits.

Locomotion Performance on Rough Terrains

This thesis presents a comparison of the implemented gaits in terms of performance and consistency, but the evaluation of these gaits was conducted on flat terrains. In contrast, uneven terrains, characterised by their irregular surfaces, obstacles, and varied inclines, introduce a number of additional challenges. These challenging terrains are, in fact, one of the original intended application scenarios for polymorphic robots, where it aims to offer optimal overall performance by adopting appropriate morphologies and gaits tailored to specific conditions. To faithfully validate and assess the robot's adaptability and versatility across practical environments, the future work could focus on its locomotion capabilities on rough terrains.

Given the robot's polymorphic nature, it is reasonable to have diverse types of rough terrains, ranging from continuous to segmented, solid to sandy, or even hybrid terrains that combines these characteristics. An important aspect of this work is identifying which gaits are inherently suited to which terrains. Not only limited to the critical metric of locomotion speed, this also encompasses other factors such as energy efficiency and stability. These findings could provide valuable guidance to the robot in dynamically identifying the ideal morphology and gait. From a deeper point of view, it is essential to evaluate whether the overall performance of these polymorphic robots on rough terrains surpasses that of conventional monomorphic robots. The underlying hypothesis suggests that, with their capability to switch between morphologies and gaits, polymorphic robots should consistently outperform traditional ones on various terrains. For example, certain gaits might be suitable for rocky terrains, while others are ideal for sandy environments. Such investigations also bring in challenges in identifying appropriate monomorphic robots for effective comparison.

7.3.3 Augmentations to Conventional Robots

The MoTeR design presented in this thesis, while facilitating wheeled locomotion through a hybrid approach, actuates the motion of the whole structure by the underlying tensegrity structures. Meanwhile, it also holds broad potentials for enhancing capabilities of conventional systems by employing appropriate actuation schemes for different requirements.

For example, some research has explored integrating tensegrity spines within traditionally actuated quadruped robots [34]. Based on the high compatibility of tensegrity structures adopting the underconstrained transition region in robot actuation applications, they can be seamlessly incorporated into conventional robot systems, introducing unique characteristics such as passive adaptability and lightweighting.

Hybrid Framework with Conventional Actuation

Within the STeM's design framework, its rigid structures comply with the specifications of the Sub-Modular Cube system [107]. By nature, any modular framework experiences certain overheads associated with modularity. This implies that, in certain contexts, the MoTeR, built upon the STeMs, might not perform as efficiently as specifically tailored traditional robots. However, since incorporated atypical tensegrity features, the STeM's active three DoF actuation, facilitated by the underconstrained transition region, can be seamlessly integrated into the design of these specialised robots, thereby amplifying certain attributes that are challenging for traditional systems.

Quadruped robots nowadays have exhibited superiority across diverse scenarios [121]. A common quadruped configuration possesses 12 degrees of freedom, with three on each leg powered by individual motors, while the main body remains a solid structure. In situations where the payload has particular requirements on stability and posture, such as on rough terrains with significant inclines, these robots can mitigate some impacts by adjusting leg biases. However, this compensation largely relies on the smoothness of control and the workspace of the legs. In this context, introducing a flexible multi-DoF spine could potentially better overcome these demands. Such a tensegrity spine, consisting of one or multiple segments, can operate similarly to a differential mechanism, allowing relative motion between the front and rear sections of the robot without affecting the main body's orientation. Concurrently, by absorbing and filtering vibrations during locomotion, it thus ensures payload stability.

Exploration of Large-Scale Robots

The MoTeR and its constituent STeM modules, as a small-sized robot, validate several groundbreaking concepts proposed in this thesis, including the underconstrained transition region, structure fusion, tensegrity modularisation, and polymorphic locomotion, while their potentials extend beyond these. During the physical implementation, the miniaturised nature of these robots caused some practical design and fabrication issues, such as reduced thread actuation precision and inconsistencies between individual units. While scaling up, as in the tensegrity spined quadruped robot discussed in Subsection 7.3.2, might mitigate some of these issues, it also introduces new challenges.

In larger scale implementations, influence of minor fabrication variations to the entire system significantly diminishes, and the precision issue of thread using motor's direct actuation can be compensated with additional mechanisms and algorithms. However, an increased size means motors bearing greater loads, a concern amplified in tensegrity contexts requiring continuous pretension. This could adversely affect the robot's energy efficiency. In addition, limited by the maximum allowed electrode distance and other factors, actuation schemes like HASEL are not ideal for these large-scale applications [119]. Although PAMs [122–126] and hydraulic artificial muscles (HAMs) [127–130] demonstrate advantageous power density, and in this context the cumbersome actuation source is no longer a issue, the actuation accuracy and dynamic response put a barrier for them [123]. Therefore, the future work could involve exploration into actuation systems tailored for larger scale tensegrity structures, with a focus on dynamic performance, accuracy, and energy efficiency.

Bibliography

[1] B. Siciliano and O. Khatib, *Springer Handbook of Robotics*. Springer Cham, 2008.

[2] F. Othman, M. A. Bahrin, N. Azli, and Others, “Industry 4.0: A review on industrial automation and robotic,” *J Teknol*, vol. 78, no. 6-13, pp. 137–143, 2016.

[3] T. Brogårdh, “Present and future robot control development—an industrial perspective,” *Annu. Rev. Control*, vol. 31, no. 1, pp. 69–79, Jan. 2007.

[4] R. H. Taylor, “A perspective on medical robotics,” *Proc. IEEE Inst. Electr. Electron. Eng.*, vol. 94, no. 9, pp. 1652–1664, Sep. 2006.

[5] N. Tejima, “Rehabilitation robotics: a review,” *Adv. Robot.*, vol. 14, no. 7, pp. 551–564, Jan. 2001.

[6] D. J. Mulla, “Twenty five years of remote sensing in precision agriculture: Key advances and remaining knowledge gaps,” *Biosystems Eng.*, vol. 114, no. 4, pp. 358–371, Apr. 2013.

[7] J. Delmerico, S. Mintchev, A. Giusti, B. Gromov, K. Melo, T. Horvat, C. Cadena, M. Hutter, A. Ijspeert, D. Floreano, L. M. Gambardella, R. Siegwart, and D. Scaramuzza, “The current state and future outlook of rescue robotics,” *J. Field Robot.*, vol. 36, no. 7, pp. 1171–1191, Oct. 2019.

[8] A. Fabris, S. Kirchgeorg, and S. Mintchev, “A soft drone with multi-modal mobility for the exploration of confined spaces,” in *2021 IEEE International Symposium on Safety, Security, and Rescue Robotics (SSRR)*, Oct. 2021, pp. 48–54.

[9] M. Calisti, G. Picardi, and C. Laschi, “Fundamentals of soft robot locomotion,” *J. R. Soc. Interface*, vol. 14, no. 130, May 2017.

[10] C. S. X. Ng and G. Z. Lum, “Untethered soft robots for future planetary explorations?” *Adv. Intell. Syst.*, vol. 5, no. 3, p. 2100106, Mar. 2023.

[11] M. A. Post, X.-T. Yan, and P. Letier, “Modularity for the future in space robotics: A review,” *Acta Astronaut.*, vol. 189, pp. 530–547, Dec. 2021.

[12] C. Majidi, “Soft robotics: A Perspective—Current trends and prospects for the future,” *Soft Robotics*, vol. 1, no. 1, pp. 5–11, Mar. 2014.

[13] C. Zhang, P. Zhu, Y. Lin, Z. Jiao, and J. Zou, “Modular soft robotics: Modular units, connection mechanisms, and applications,” *Adv. Intell. Syst.*, vol. 2, no. 6, p. 1900166, Jun. 2020.

[14] C. Lee, M. Kim, Y. J. Kim, N. Hong, S. Ryu, H. J. Kim, and S. Kim, “Soft robot review,” *Int. J. Control Autom. Syst.*, vol. 15, no. 1, pp. 3–15, Feb. 2017.

[15] A. J. Ijspeert, “Biorobotics: using robots to emulate and investigate agile locomotion,” *Science*, vol. 346, no. 6206, pp. 196–203, Oct. 2014.

[16] A. D. Marchese, C. D. Onal, and D. Rus, “Autonomous soft robotic fish capable of escape maneuvers using fluidic elastomer actuators,” *Soft Robot*, vol. 1, no. 1, pp. 75–87, Mar. 2014.

[17] J. Liu, X. Zhang, and G. Hao, “Survey on research and development of reconfigurable modular robots,” *Advances in Mechanical Engineering*, vol. 8, no. 8, p. 1687814016659597, Aug. 2016.

[18] A. Brunete, A. Ranganath, S. Segovia, J. P. de Frutos, M. Hernando, and E. Gambao, “Current trends in reconfigurable modular robots design,” *Int. J. Adv. Rob. Syst.*, vol. 14, no. 3, p. 1729881417710457, May 2017.

[19] J. Seo, J. Paik, and M. Yim, “Modular reconfigurable robotics,” *Annu. Rev. Control Robot. Auton. Syst.*, vol. 2, no. 1, pp. 63–88, May 2019.

[20] D. E. Ingber, “Tensegrity II. how structural networks influence cellular information processing networks,” *J. Cell Sci.*, vol. 116, no. Pt 8, pp. 1397–1408, Apr. 2003.

[21] M. C. Oliveira and R. E. Skelton, *Tensegrity Systems.* Springer, Boston, MA, 2009.

[22] Y. Termonia, “Molecular modeling of spider silk elasticity,” *Macromolecules*, vol. 27, no. 25, pp. 7378–7381, Dec. 1994.

[23] M. Vespignani, J. M. Friesen, V. SunSpiral, and J. Bruce, “Design of SUPERball v2, a compliant tensegrity robot for absorbing large impacts,” in *2018 IEEE/RSJ International Conference on Intelligent Robots and Systems (IROS)*, Oct. 2018, pp. 2865–2871.

[24] L. Chen, B. Cera, E. L. Zhu, R. Edmunds, F. Rice, A. Bronars, E. Tang, S. R. Malekshahi, O. Romero, A. K. Agogino, and A. M. Agogino, “Inclined surface locomotion strategies for spherical tensegrity robots,” in *2017 IEEE/RSJ International Conference on Intelligent Robots and Systems (IROS)*, Sep. 2017, pp. 4976–4981.

[25] J. Kimber, Z. Ji, A. Petridou, T. Sipple, K. Barhydt, J. Boggs, L. Dosiek, and J. Rieffel, “Low-cost wireless modular soft tensegrity robots,” in *2019 2nd IEEE International Conference on Soft Robotics (RoboSoft).* ieeexplore.ieee.org, 2019, pp. 88–93.

[26] N. Wang, K. Naruse, D. Stamenović, J. J. Fredberg, S. M. Mijailovich, I. M. Tolić-Nørrelykke, T. Polte, R. Mannix, and D. E. Ingber, “Mechanical behavior in living cells consistent with the tensegrity model,” *Proc. Natl. Acad. Sci. U. S. A.*, vol. 98, no. 14, pp. 7765–7770, Jul. 2001.

[27] D. E. Ingber, "Tensegrity i. cell structure and hierarchical systems biology," *J. Cell Sci.*, vol. 116, no. Pt 7, pp. 1157–1173, Apr. 2003.

[28] S. Kaewunruen, C. Ngamkhanong, and S. Xu, "Large amplitude vibrations of imperfect spider web structures," *Sci. Rep.*, vol. 10, no. 1, p. 19161, Nov. 2020.

[29] F. Fraternali, N. Stehling, A. Amendola, B. A. Tiban Anrango, C. Holland, and C. Rodenburg, "Tensegrity modelling and the high toughness of spider dragline silk," *Nanomaterials (Basel)*, vol. 10, no. 8, Jul. 2020.

[30] R. Buckminster Fuller and R. Marks, *The Dymaxion world of Buckminster Fuller*. Garden City, N.Y: Anchor Books, 1973.

[31] R. Kobayashi, H. Nabae, and K. Suzumori, "Large torsion thin artificial muscles tensegrity structure for twist manipulation," *IEEE Robotics and Automation Letters*, vol. 8, no. 3, pp. 1207–1214, Mar. 2023.

[32] T. Wang and M. A. Post, "A symmetric three degree of freedom tensegrity mechanism with dual operation modes for robot actuation," *Biomimetics*, vol. 6, no. 2, May 2021.

[33] T. Wang, M. A. Post, and A. M. Tyrrell, "Articulating resilience: Adaptive locomotion of wheeled tensegrity robot," *Electronics*, vol. 11, no. 4, p. 666, Feb. 2022.

[34] Y. Lian, T. Wang, J. Ingham, M. A. Post, and A. Tyrrell, "CPG-Based locomotion control of a quadruped robot with an active spine," in *Towards Autonomous Robotic Systems*. Springer Nature Switzerland, 2023, pp. 177–189.

[35] R. Skelton, W. J. Helton, and R. Adhikari, "Mechanics of tensegrity beams," *UCSD, Structural Systems & Contr. Lab. , Rep*, no. 1998-1, 1998.

[36] "tensegrity, oxford english dictionary," https://www.oed.com/dictionary/tensegrity_n, accessed: 2023-9-14.

[37] S. M. Levin, "16. tensegrity, the new biomechanics," in *Oxford Textbook of Musculoskeletal Medicine*, M. Hutson and A. Ward, Eds. Oxford University Press, 2016, pp. 155–156, 158–160.

[38] R. E. Skelton, J. William Helton, R. Adhikari, J.-P. Pinaud, and W. Chan, "An introduction to the mechanics of tensegrity structures," in *The mechanical systems design handbook: modeling, measurement, and control*, Y. Hurmuzlu and O. D. I. Nwokah, Eds. CRC Press, 2002.

[39] E. Komendera, "A survey of the computational modeling and control of tensegrity robots," Ph.D. dissertation, Prelim Exam in Computational Modeling of Complex Systems, University of . . . , 2012.

[40] A. G. M. Michell, "LVIII. the limits of economy of material in frame-structures," *The London, Edinburgh, and Dublin Philosophical Magazine and Journal of Science*, vol. 8, no. 47, pp. 589–597, Nov. 1904.

[41] Y. Chen, J. Feng, and Y. Wu, "Novel Form-Finding of tensegrity structures using ant colony systems," *J. Mech. Robot.*, vol. 4, no. 3, Aug. 2012.

[42] F. Carreño and M. A. Post, "Design of a novel wheeled tensegrity robot: a comparison of tensegrity concepts and a prototype for travelling air ducts," *Robotics Biomim*, vol. 5, no. 1, p. 1, May 2018.

[43] J. Rieffel, F. Valero-Cuevas, and H. Lipson, "Automated discovery and optimization of large irregular tensegrity structures," *Comput. Struct.*, vol. 87, no. 5, pp. 368–379, Mar. 2009.

[44] S. H. Juan and J. M. Mirats Tur, "Tensegrity frameworks: Static analysis review," *Mechanism and Machine Theory*, vol. 43, no. 7, pp. 859–881, Jul. 2008.

[45] A. G. Tibert and S. Pellegrino, "Review of Form-Finding methods for tensegrity structures," *Int. J. Space Struct.*, vol. 18, no. 4, pp. 209–223, Dec. 2003.

[46] M. Masic, R. E. Skelton, and P. E. Gill, "Optimization of tensegrity structures," *Int. J. Solids Struct.*, vol. 43, no. 16, pp. 4687–4703, Aug. 2006.

[47] S. Ehara and Y. Kanno, "Topology design of tensegrity structures via mixed integer programming," *Int. J. Solids Struct.*, vol. 47, no. 5, pp. 571–579, Mar. 2010.

[48] Y. Kanno, "TOPOLOGY OPTIMIZATION OF TENSEGRITY STRUCTURES UNDER SELF-WEIGHT LOADS," *J. Oper. Res. Soc. Japan*, vol. 55, no. 2, pp. 125–145, 2012.

[49] C. Paul, H. Lipson, and F. J. V. Cuevas, "Evolutionary form-finding of tensegrity structures," in *Proceedings of the 7th annual conference on Genetic and evolutionary computation*, ser. GECCO '05. New York, NY, USA: Association for Computing Machinery, Jun. 2005, pp. 3–10.

[50] B. R. Tietz, R. W. Carnahan, R. J. Bachmann, R. D. Quinn, and V. SunSpiral, "Tetraspine: Robust terrain handling on a tensegrity robot using central pattern generators," in *2013 IEEE/ASME International Conference on Advanced Intelligent Mechatronics*, Jul. 2013, pp. 261–267.

[51] B. T. Mirletz, I. Park, R. D. Quinn, and V. SunSpiral, "Towards bridging the reality gap between tensegrity simulation and robotic hardware," in *2015 IEEE/RSJ International Conference on Intelligent Robots and Systems (IROS)*, Sep. 2015, pp. 5357–5363.

[52] T. Bliss, T. Iwasaki, and H. Bart-Smith, "Central pattern generator control of a tensegrity swimmer," *IEEE/ASME Trans. Mechatron.*, vol. 18, no. 2, pp. 586–597, Apr. 2013.

[53] G. Scarr, "A consideration of the elbow as a tensegrity structure," *Int. J. Osteopath. Med.*, vol. 15, no. 2, pp. 53–65, 2012.

[54] V. Böhm, S. Sumi, T. Kaufhold, and K. Zimmermann, "Compliant multistable tensegrity structures," *Mechanism and Machine Theory*, vol. 115, pp. 130–148, 2017.

[55] ——, "Compliant multistable tensegrity structures with simple topologies," in *Mechanisms and Machine Science*, vol. 43. Kluwer Academic Publishers, 2017, pp. 153–161.

[56] K. Liu and G. H. Paulino, “Tensegrity topology optimization by force maximization on arbitrary ground structures,” *Struct. Multidiscip. Optim.*, vol. 59, no. 6, pp. 2041–2062, Jun. 2019.

[57] A. P. Sabelhaus, J. Bruce, K. Caluwaerts, P. Manovi, R. F. Firoozi, S. Dobi, A. M. Agogino, and V. SunSpiral, “System design and locomotion of SUPERball, an untethered tensegrity robot,” in *2015 IEEE International Conference on Robotics and Automation (ICRA)*, May 2015, pp. 2867–2873.

[58] K. Caluwaerts, J. Despraz, A. Işçen, A. P. Sabelhaus, J. Bruce, B. Schrauwen, and V. SunSpiral, “Design and control of compliant tensegrity robots through simulation and hardware validation,” *J. R. Soc. Interface*, vol. 11, no. 98, p. 20140520, Sep. 2014.

[59] J. Bruce, K. Caluwaerts, A. Iscen, A. P. Sabelhaus, and V. SunSpiral, “Design and evolution of a modular tensegrity robot platform,” in *2014 IEEE International Conference on Robotics and Automation (ICRA)*. IEEE, May 2014, pp. 3483–3489.

[60] J. Bruce, A. P. Sabelhaus, Y. Chen, D. Lu, K. Morse, S. Milam, K. Caluwaerts, A. M. Agogino, and V. SunSpiral, “SUPERball: Exploring tensegrities for planetary probes,” in *International Symposium on Artificial Intelligence, Robotics and Automation in Space (i-SAIRAS)*, 2014.

[61] A. P. Sabelhaus, J. Bruce, K. Caluwaerts, Y. Chen, D. Lu, Y. Liu, A. K. Agogino, V. SunSpiral, and A. M. Agogino, “Hardware design and testing of SUPERball, a modular tensegrity robot,” in *2014 Edition of the World Conference on Structural Control and Monitoring (WCSCM)*, 2014.

[62] K. Caluwaerts, J. Bruce, J. M. Friesen, and V. SunSpiral, “State estimation for tensegrity robots,” in *2016 IEEE International Conference on Robotics and Automation (ICRA)*, May 2016, pp. 1860–1865.

[63] V. SunSpiral, A. Agogino, and D. Atkinson, “Super ball bot - structures for planetary landing and exploration, NIAC phase 2 final report,” National Aeronautics and Space Administration, Tech. Rep., Sep. 2015.

[64] M. Vespignani, C. Ercolani, J. M. Friesen, and J. Bruce, “Steerable locomotion controller for six-strut icosahedral tensegrity robots,” in *2018 IEEE/RSJ International Conference on Intelligent Robots and Systems (IROS)*, Oct. 2018, pp. 2886–2892.

[65] R. Kobayashi, H. Nabae, G. Endo, and K. Suzumori, “Soft tensegrity robot driven by thin artificial muscles for the exploration of unknown spatial configurations,” *IEEE Robotics and Automation Letters*, vol. 7, no. 2, pp. 5349–5356, Apr. 2022.

[66] B. T. Mirletz, I.-W. Park, T. E. Flemons, and V. Sunspiral, “Design and control of modular Spine-Like tensegrity structures,” in *6th World Conference on Structural Control and Monitoring*. unknown, Jul. 2014.

[67] B. T. Mirletz, P. Bhandal, R. D. Adams, A. K. Agogino, R. D. Quinn, and V. SunSpiral, “Goal-Directed CPG-Based control for tensegrity spines with many degrees of freedom traversing irregular terrain,” *Soft Robotics*, vol. 2, no. 4, pp. 165–176, Dec. 2015.

[68] J. Friesen, A. Pogue, T. Bewley, M. de Oliveira, R. Skelton, and V. Sunspiral, “DuCTT: A tensegrity robot for exploring duct systems,” in *2014 IEEE International Conference on Robotics and Automation (ICRA)*, May 2014, pp. 4222–4228.

[69] J. M. Friesen, P. Glick, M. Fanton, P. Manovi, A. Xydes, T. Bewley, and V. Sunspiral, “The second generation prototype of a duct climbing tensegrity robot, DuCTTv2,” *Proceedings - IEEE International Conference on Robotics and Automation*, vol. 2016-June, pp. 2123–2128, 2016.

[70] C. Paul, F. J. Valero-Cuevas, and H. Lipson, “Design and control of tensegrity robots for locomotion,” *IEEE Trans. Rob.*, vol. 22, no. 5, pp. 944–957, 2006.

[71] D. Hustig-Schultz, V. SunSpiral, and M. Teodorescu, “Morphological design for controlled tensegrity quadruped locomotion,” in *2016 IEEE/RSJ International Conference on Intelligent Robots and Systems (IROS)*. IEEE, Oct. 2016, pp. 4714–4719.

[72] ——, “Morphological optimization for tensegrity quadruped locomotion,” in *2017 IEEE/RSJ International Conference on Intelligent Robots and Systems (IROS)*, Sep. 2017, pp. 3990–3995.

[73] A. P. Sabelhaus, L. J. van Vuuren, A. Joshi, E. L. Zhu, H. J. Garnier, K. A. Sover, J. Navarro, A. Agogino, and A. Agogino, “Design, simulation, and testing of a flexible actuated spine for quadruped robots,” *arXiv: Robotics*, 2018.

[74] A. P. Sabelhaus, H. Ji, P. Hylton, and V. Sunspiral, “Mechanism design and simulation of the ULTRA spine: A tensegrity robot,” in *ASME 2015 International Design Engineering Technical Conferences and Computers and Information in Engineering Conference*. unknown, Aug. 2015, p. V05AT08A059.

[75] A. P. Sabelhaus, A. K. Akella, Z. A. Ahmad, and V. SunSpiral, “Model-Predictive control of a flexible spine robot,” in *2017 American Control Conference (ACC)*, May 2017, pp. 5051–5057.

[76] D. Zappetti, S. Mintchev, J. Shintake, and D. Floreano, “Bio-inspired tensegrity soft modular robots,” in *Biomimetic and Biohybrid Systems*. Springer International Publishing, 2017, pp. 497–508.

[77] V. Böhm and K. Zimmermann, “Vibration-driven mobile robots based on single actuated tensegrity structures,” in *2013 IEEE International Conference on Robotics and Automation*, May 2013, pp. 5475–5480.

[78] V. Böhm, I. Zeidis, and K. Zimmermann, “An approach to the dynamics and control of a planar tensegrity structure with application in locomotion systems,” *International Journal of Dynamics and Control*, vol. 3, no. 1, pp. 41–49, 2015.

[79] J. Rieffel and J.-B. Mouret, “Adaptive and resilient soft tensegrity robots,” *Soft Robot*, vol. 5, no. 3, pp. 318–329, Jun. 2018.

[80] J. Karaul, A. Khan, G. Liu, and J. Rieffel, “Behavioral repertoires for soft tensegrity robots,” *2020 IEEE*, 2020.

[81] S. Mintchev, D. Zappetti, J. Willemin, and D. Floreano, "A soft robot for random exploration of terrestrial environments," in *2018 IEEE International Conference on Robotics and Automation (ICRA)*, May 2018, pp. 7492–7497.

[82] V. Böhm, T. Kaufhold, F. Schale, and K. Zimmermann, "Spherical mobile robot based on a tensegrity structure with curved compressed members," in *2016 IEEE International Conference on Advanced Intelligent Mechatronics (AIM)*, Jul. 2016, pp. 1509–1514.

[83] V. Böhm, T. Kaufhold, I. Zeidis, and K. Zimmermann, "Dynamic analysis of a spherical mobile robot based on a tensegrity structure with two curved compressed members," *Arch. Appl. Mech.*, vol. 87, no. 5, pp. 853–864, 2017.

[84] T. Kaufhold, F. Schale, V. Böhm, and K. Zimmermann, "Indoor locomotion experiments of a spherical mobile robot based on a tensegrity structure with curved compressed members," in *IEEE/ASME International Conference on Advanced Intelligent Mechatronics, AIM*, 2017, pp. 523–528.

[85] V. A. Webster, A. J. Lonsberry, A. D. Horchler, K. M. Shaw, H. J. Chiel, and R. D. Quinn, "A segmental mobile robot with active tensegrity bending and noise-driven oscillators," in *2013 IEEE/ASME International Conference on Advanced Intelligent Mechatronics*, Jul. 2013, pp. 1373–1380.

[86] S. Lessard, J. Bruce, E. Jung, M. Teodorescu, V. SunSpiral, and A. Agogino, "A lightweight, multi-axis compliant tensegrity joint," in *2016 IEEE International Conference on Robotics and Automation (ICRA)*, vol. 2016-June, May 2016, pp. 630–635.

[87] S. Lessard, D. Castro, W. Asper, S. D. Chopra, L. B. Baltaxe-Admony, M. Teodorescu, V. Sunspiral, and A. Agogino, "A bio-inspired tensegrity manipulator with multi-DOF, structurally compliant joints," in *2016 IEEE/RSJ International Conference on Intelligent Robots and Systems (IROS)*, vol. 2016-Noem. IEEE, Oct. 2016, pp. 5515–5520.

[88] J. M. Friesen, J. L. Dean, T. Bewley, and V. Sunspiral, "A Tensegrity-Inspired compliant 3-DOF compliant joint," in *2018 IEEE International Conference on Robotics and Automation (ICRA)*. IEEE, May 2018, pp. 3301–3306.

[89] S. Venkateswaran, M. Furet, D. Chablat, and P. Wenger, "Design and analysis of a tensegrity mechanism for a Bio-Inspired robot," in *ASME 2019 International Design Engineering Technical Conferences and Computers and Information in Engineering Conference*. American Society of Mechanical Engineers Digital Collection, Nov. 2019, pp. 1–10.

[90] S. Venkateswaran, D. Chablat, and P. Hamon, "An optimal design of a flexible piping inspection robot," *J. Mech. Robot.*, vol. 13, no. 3, pp. 1–37, Jan. 2021.

[91] L. Panait, "Theoretical convergence guarantees for cooperative coevolutionary algorithms," *Evol. Comput.*, vol. 18, no. 4, pp. 581–615, Jun. 2010.

[92] A. Iscen, A. Agogino, V. SunSpiral, and K. Tumer, "Controlling tensegrity robots through evolution," in *Proceedings of the 15th annual conference on Genetic and evolutionary computation*, ser. GECCO '13. New York, NY, USA: Association for Computing Machinery, Jul. 2013, pp. 1293–1300.

[93] ——, "Flop and roll: Learning robust goal-directed locomotion for a tensegrity robot," in *2014 IEEE/RSJ International Conference on Intelligent Robots and Systems*, Sep. 2014, pp. 2236–2243.

[94] A. J. Ijspeert, "Central pattern generators for locomotion control in animals and robots: a review," *Neural Netw.*, vol. 21, no. 4, pp. 642–653, May 2008.

[95] K. Caluwaerts, M. D'Haene, D. Verstraeten, and B. Schrauwen, "Locomotion without a brain: physical reservoir computing in tensegrity structures," *Artif. Life*, vol. 19, no. 1, pp. 35–66, 2013.

[96] T. Bliss, J. Werly, T. Iwasaki, and H. Bart-Smith, "Experimental validation of robust resonance entrainment for CPG-Controlled tensegrity structures," *IEEE Trans. Control Syst. Technol.*, vol. 21, no. 3, pp. 666–678, May 2013.

[97] "Open dynamics engine," https://www.ode.org/, accessed: 2023-5-27.

[98] J. Rieffel, B. Trimmer, and H. Lipson, "Mechanism as mind - what tensegrities and caterpillars can teach us about soft robotics," *ALIFE*, 2008.

[99] W. Du, S. Ma, B. Li, M. Wang, and S. Hirai, "Dynamic simulation for 6-strut tensegrity robots," in *2014 IEEE International Conference on Information and Automation (ICIA)*, Jul. 2014, pp. 870–875.

[100] "Adams - the multibody dynamics simulation solution," https://www.mscsoftware.com/product/adams, accessed: 2023-5-28.

[101] A. Luo, H. Xin, P. Cao, X. Hao, Y. Yu, P. Sun, and W. Tian, "Motion simulation of six-bar tensegrity robot based on adams," in *2016 IEEE International Conference on Mechatronics and Automation*, Aug. 2016, pp. 264–269.

[102] A. Luo, S. Che, and H. Liu, "The driving of the six-bar tensegrity robot," in *2017 IEEE International Conference on Robotics and Biomimetics (ROBIO)*, Dec. 2017, pp. 640–645.

[103] A. Luo, J. Wang, and H. Liu, "Four-bar tensegrity robot based on ADAMS simulation," in *2017 IEEE International Conference on Mechatronics and Automation (ICMA)*, Aug. 2017, pp. 1463–1468.

[104] "CoppeliaSim," https://www.coppeliarobotics.com/, accessed: 2023-5-28.

[105] "PROJECTCHRONO," https://projectchrono.org/about/, accessed: 2023-5-28.

[106] U. Boz, R. Goyal, and R. E. Skelton, "Actuators and sensors based on tensegrity d-bar structures," *Frontiers in Astronomy and Space Sciences*, vol. 5, 2018.

[107] M. A. Post and J. Austin, “Knowledge-Based Self-Reconfiguration and Self-Aware demonstration for modular satellite assembly,” in *10th International Workshop on Satellite Constellations & Formation Flying 2019*, Apr. 2019.

[108] Netter, *Atlas of Human Anatomy*, 7th ed., ser. Netter Basic Science. Philadelphia, PA: Elsevier - Health Sciences Division, Feb. 2018.

[109] D. Stewart, “A platform with six degrees of freedom,” *Proceedings of the Institution of Mechanical Engineers*, vol. 180, no. 1, pp. 371–386, Jun. 1965.

[110] A. Tasora, R. Serban, H. Mazhar, A. Pazouki, D. Melanz, J. Fleischmann, M. Taylor, H. Sugiyama, and D. Negrut, “Chrono: An open source multi-physics dynamics engine,” in *High Performance Computing in Science and Engineering*. Springer International Publishing, 2016, pp. 19–49.

[111] M. Taylor and R. Serban, “Validation of basic modeling elements in chrono,” University of Wisconsin-Madison, Tech. Rep., Apr. 2015.

[112] A. Recuero and D. Negrut, “Validation of a gradient-deficient ANCF beam element in Chrono::FEA,” University of Wisconsin-Madison, Tech. Rep., May 2016.

[113] C. B. Pham, S. H. Yeo, G. Yang, M. S. Kurbanhusen, and I.-M. Chen, “Force-closure workspace analysis of cable-driven parallel mechanisms,” *Mechanism and Machine Theory*, vol. 41, no. 1, pp. 53–69, Jan. 2006.

[114] T. Weihmann, P.-G. Brun, and E. Pycroft, “Speed dependent phase shifts and gait changes in cockroaches running on substrates of different slipperiness,” *Front. Zool.*, vol. 14, p. 54, Dec. 2017.

[115] D. Bucher, G. Haspel, J. Golowasch, and F. Nadim, *Central Pattern Generators*. Chichester, UK: John Wiley & Sons, Ltd, Dec. 2015, pp. 1–12.

[116] E. Marder and D. Bucher, “Central pattern generators and the control of rhythmic movements,” *Curr. Biol.*, vol. 11, no. 23, pp. R986–96, Nov. 2001.

[117] A. J. Ijspeert, A. Crespi, D. Ryczko, and J.-M. Cabelguen, “From swimming to walking with a salamander robot driven by a spinal cord model,” *Science*, vol. 315, no. 5817, pp. 1416–1420, Mar. 2007.

[118] D. Zhou, Y. Liu, X. Tang, J. Sun, and J. Deng, “A lightweight and multimotion crawling tensegrity robot driven by twisted artificial muscles,” *IEEE Trans. Ind. Electron.*, vol. 69, no. 11, pp. 11 447–11 457, Nov. 2022.

[119] N. Kellaris, V. Gopaluni Venkata, G. M. Smith, S. K. Mitchell, and C. Keplinger, “Peano-HASEL actuators: Muscle-mimetic, electrohydraulic transducers that linearly contract on activation,” *Sci Robot*, vol. 3, no. 14, Jan. 2018.

[120] J. White, M. Post, and A. Tyrrell, “A novel connection mechanism for dynamically reconfigurable modular robots,” in *Proceedings of the 19th International Conference on Informatics in Control, Automation and Robotics*. SCITEPRESS - Science and Technology Publications, 2022.

[121] P. Biswal and P. K. Mohanty, “Development of quadruped walking robots: A review,” *Ain Shams Engineering Journal*, vol. 12, no. 2, pp. 2017–2031, Jun. 2021.

[122] F. Daerden, D. Lefeber, and Others, “Pneumatic artificial muscles: actuators for robotics and automation,” *Eur. J. Mech. Environ. Eng.*, vol. 47, no. 1, pp. 11–21, 2002.

[123] K. C. Wickramatunge and T. Leephakpreeda, “Study on mechanical behaviors of pneumatic artificial muscle,” *Int. J. Eng. Sci.*, vol. 48, no. 2, pp. 188–198, Feb. 2010.

[124] S. Wakimoto, K. Suzumori, and J. Takeda, “Flexible artificial muscle by bundle of McKibben fiber actuators,” in *2011 IEEE/ASME International Conference on Advanced Intelligent Mechatronics (AIM)*, 2011, pp. 457–462.

[125] W. Liang, H. Liu, K. Wang, Z. Qian, L. Ren, and L. Ren, “Comparative study of robotic artificial actuators and biological muscle,” *Advances in Mechanical Engineering*, vol. 12, no. 6, p. 1687814020933409, Jun. 2020.

[126] C. De Pascali, G. A. Naselli, S. Palagi, R. B. N. Scharff, and B. Mazzolai, “3d-printed biomimetic artificial muscles using soft actuators that contract and elongate,” *Sci Robot*, vol. 7, no. 68, p. eabn4155, Jul. 2022.

[127] R. Tiwari, M. A. Meller, K. B. Wajcs, C. Moses, I. Reveles, and E. Garcia, “Hydraulic artificial muscles,” *J. Intell. Mater. Syst. Struct.*, vol. 23, no. 3, pp. 301–312, Feb. 2012.

[128] P. T. Phan, M. T. Thai, T. T. Hoang, N. H. Lovell, and T. Nho Do, “HFAM: Soft hydraulic filament artificial muscles for flexible robotic applications,” *IEEE Access*, vol. 8, pp. 226 637–226 652, 2020.

[129] S. Kittisares, H. Nabae, G. Endo, K. Suzumori, and R. Sakurai, “Design of knee support device based on four-bar linkage and hydraulic artificial muscle,” *ROBOMECH Journal*, vol. 7, no. 1, p. 16, Mar. 2020.

[130] Y. Feng, T. Ide, H. Nabae, G. Endo, R. Sakurai, S. Ohno, and K. Suzumori, “Safety-enhanced control strategy of a power soft robot driven by hydraulic artificial muscles,” *ROBOMECH Journal*, vol. 8, no. 1, p. 10, Mar. 2021.

[131] Wang, Tianyuan, “Terrain adaptability of MoTeR with wheeled locomotion,” Sep. 2023. [Online]. Available: https://www.youtube.com/watch?v=9ip5PrBI998

[132] ——, “A polymorphic modular tensegrity robot with biomimetic terrestrial locomotion,” Sep. 2023. [Online]. Available: https://www.youtube.com/watch?v=6-4QaDfBN2M

Appendix A

Schematics and Layouts of the STeM Controller Board

This appendix contains complementary materials of the STeM controller board introduced in Chapter 4.

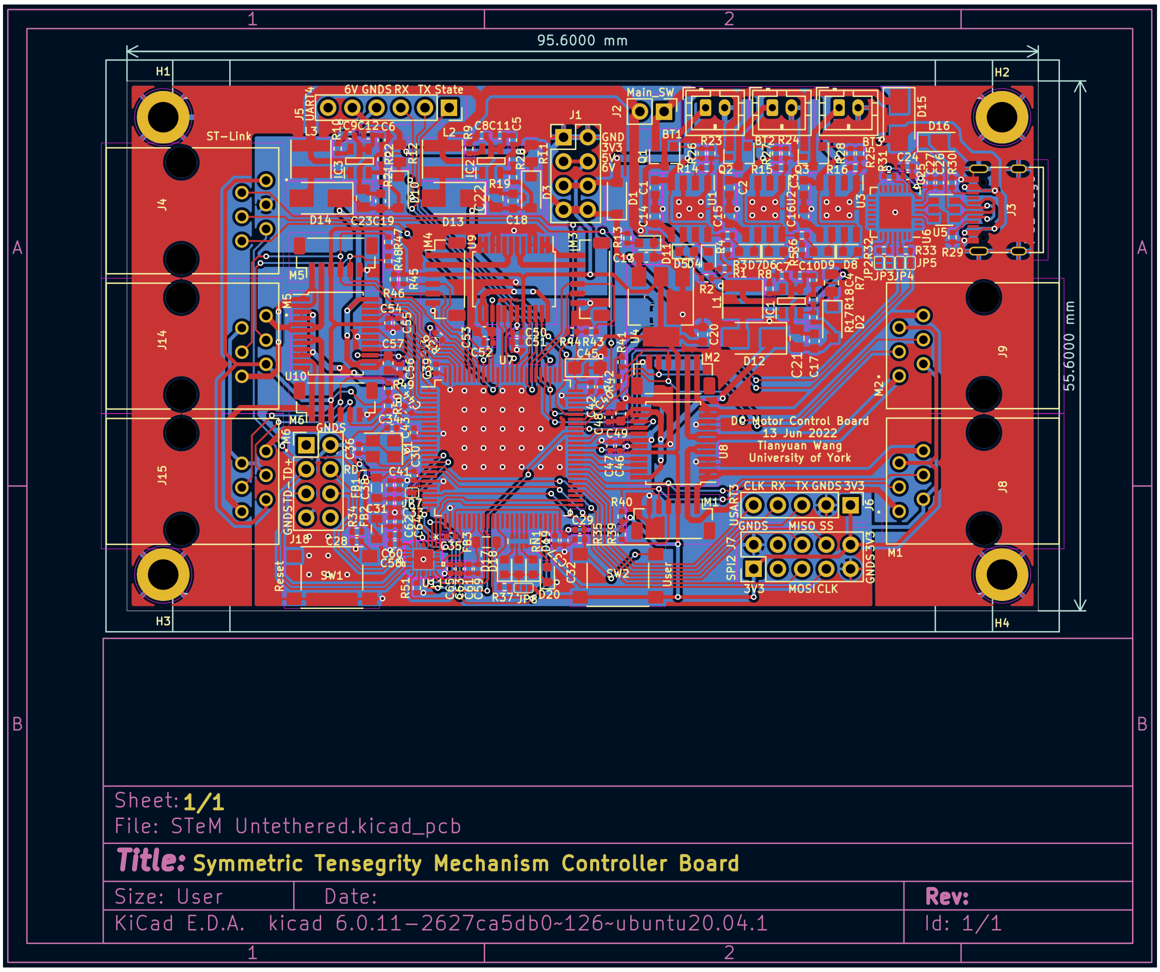

AO3401A P-MOS: Anti battery reverse MOSFET.
Body diode will bring MOS pin 2 (S) to approx 3.7V−0.6V.
Vgs then becomes −3.1V (g: 0V, s: 3.1V). MOSFET conduction state.
If 5V is applied, g will be pulled up to 5V, Vgs > 0, MOSFET cutoff, charging start.

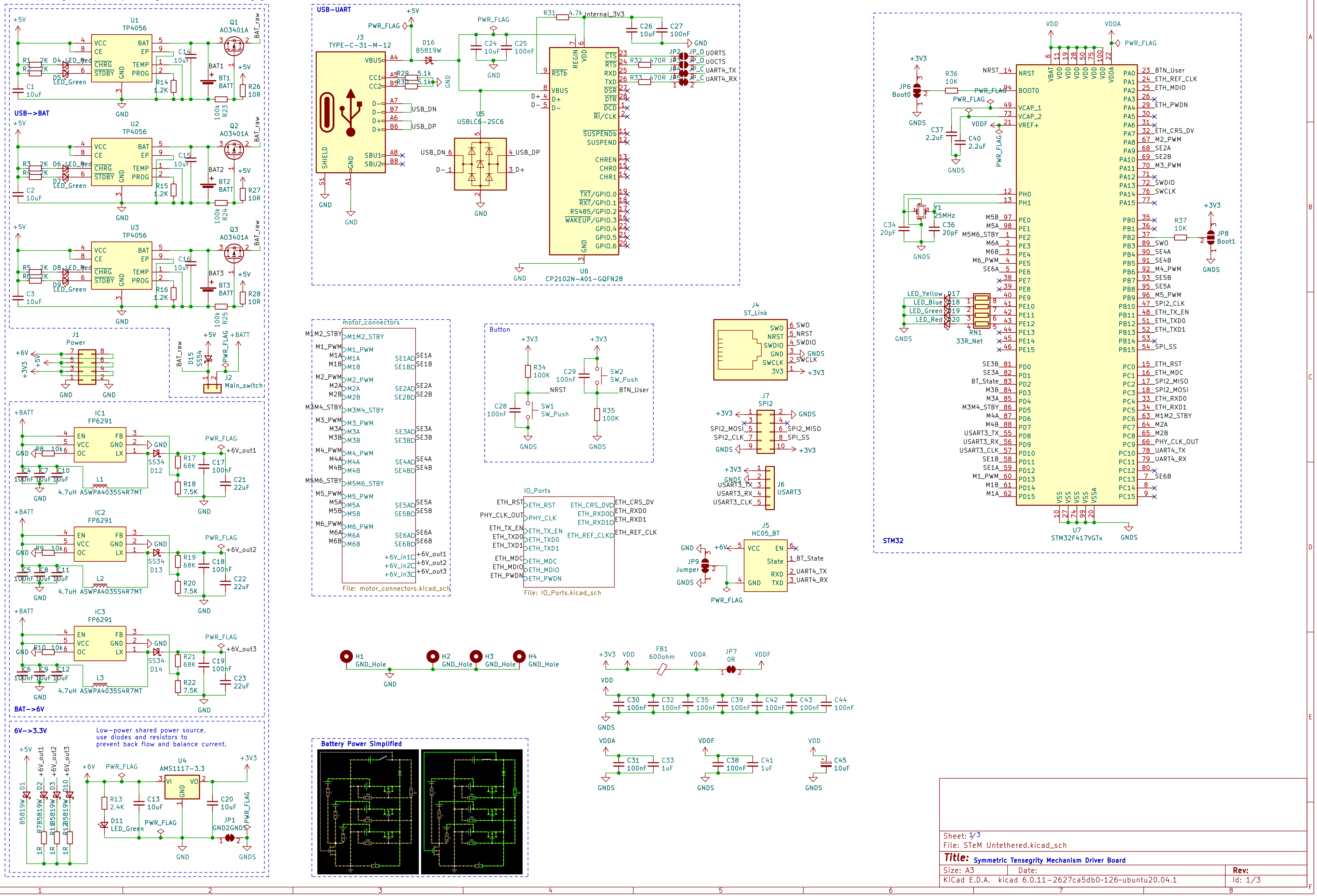

Sheet: /
File: STeM Untethered.kicad_sch

Title: Symmetric Tensegrity Mechanism Driver Board

Size: A3
Date:
Rev:
KiCad E.D.A. kicad 6.0.11-2627ca5db0-126-ubuntu20.04.1
Id: 1/3

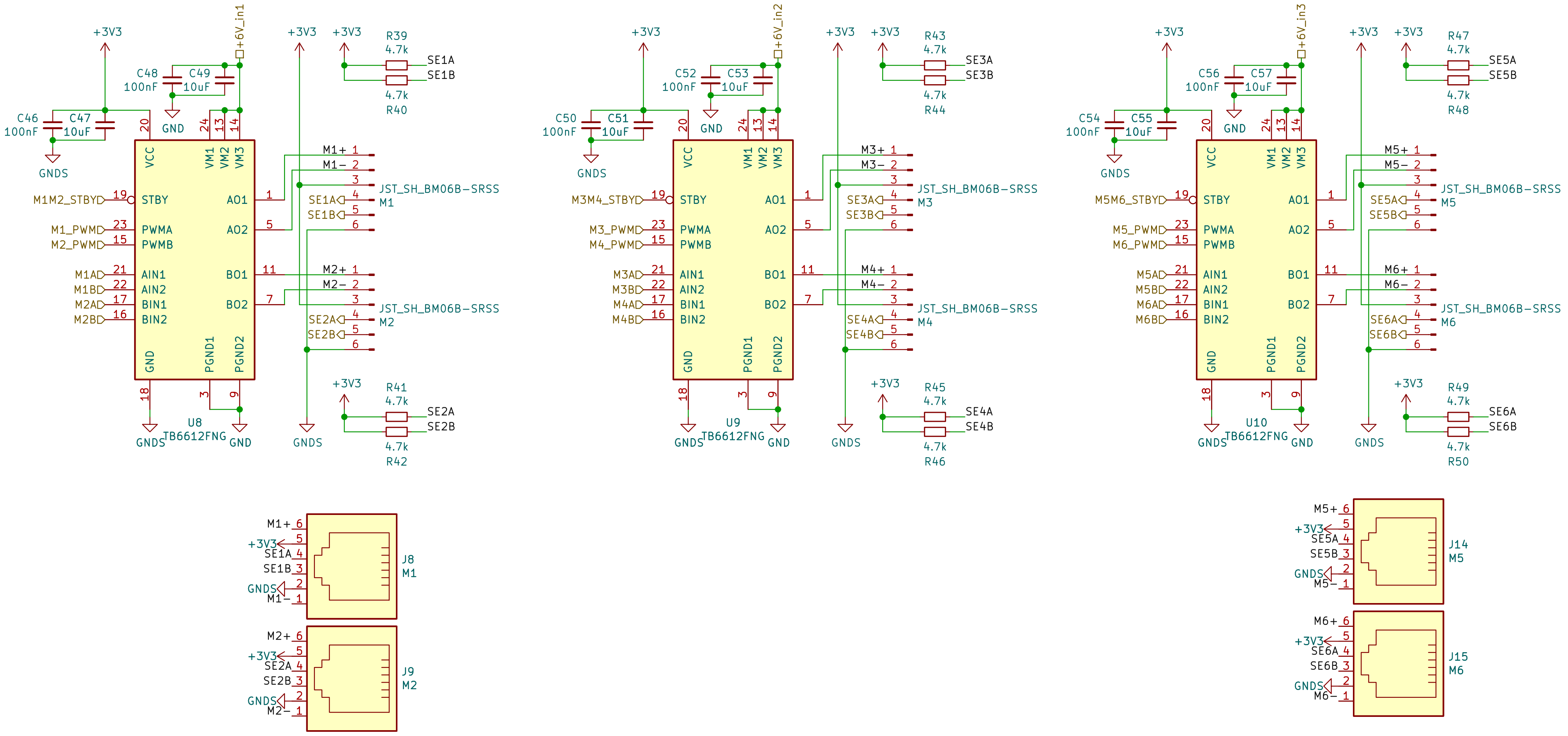

Sheet: /motor_connectors/
File: motor_connectors.kicad_sch

Title: Symmetric Tensegrity Mechanism Driver Board Motor Sub-Sheet

Size: A4 Date: **Rev:**
KiCad E.D.A. kicad 6.0.11-2627ca5db0-126~ubuntu20.04.1 Id: 2/3

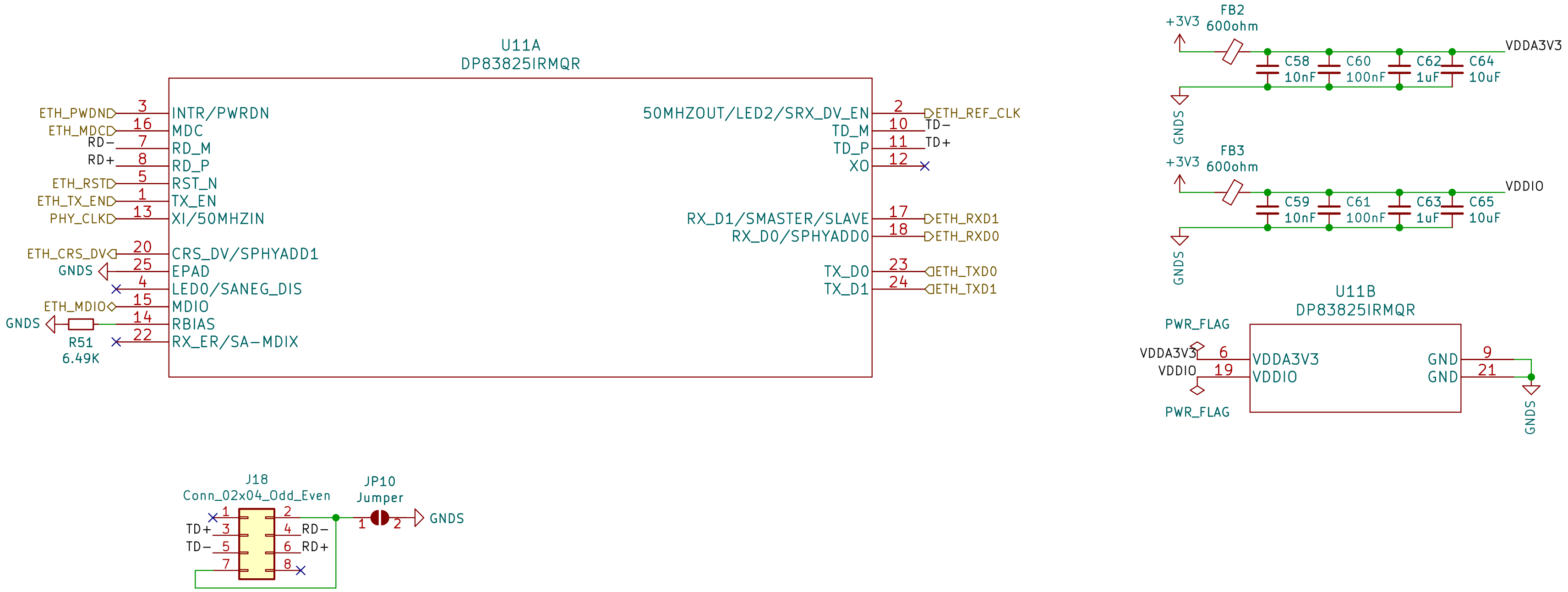

Sheet: /IO_Ports/
File: IO_Ports.kicad_sch

Title: Symmetric Tensegrity Mechanism Driver Board Ethernet Sub-Sheet

Size: A4
Date:
Rev:
KiCad E.D.A. kicad 6.0.11-2627ca5db0~126~ubuntu20.04.1
Id: 3/3

Appendix B

Schematics and Layouts of the STeM Sensory Board

This appendix contains complementary materials of the STeM sensory board introduced in Chapter 4.

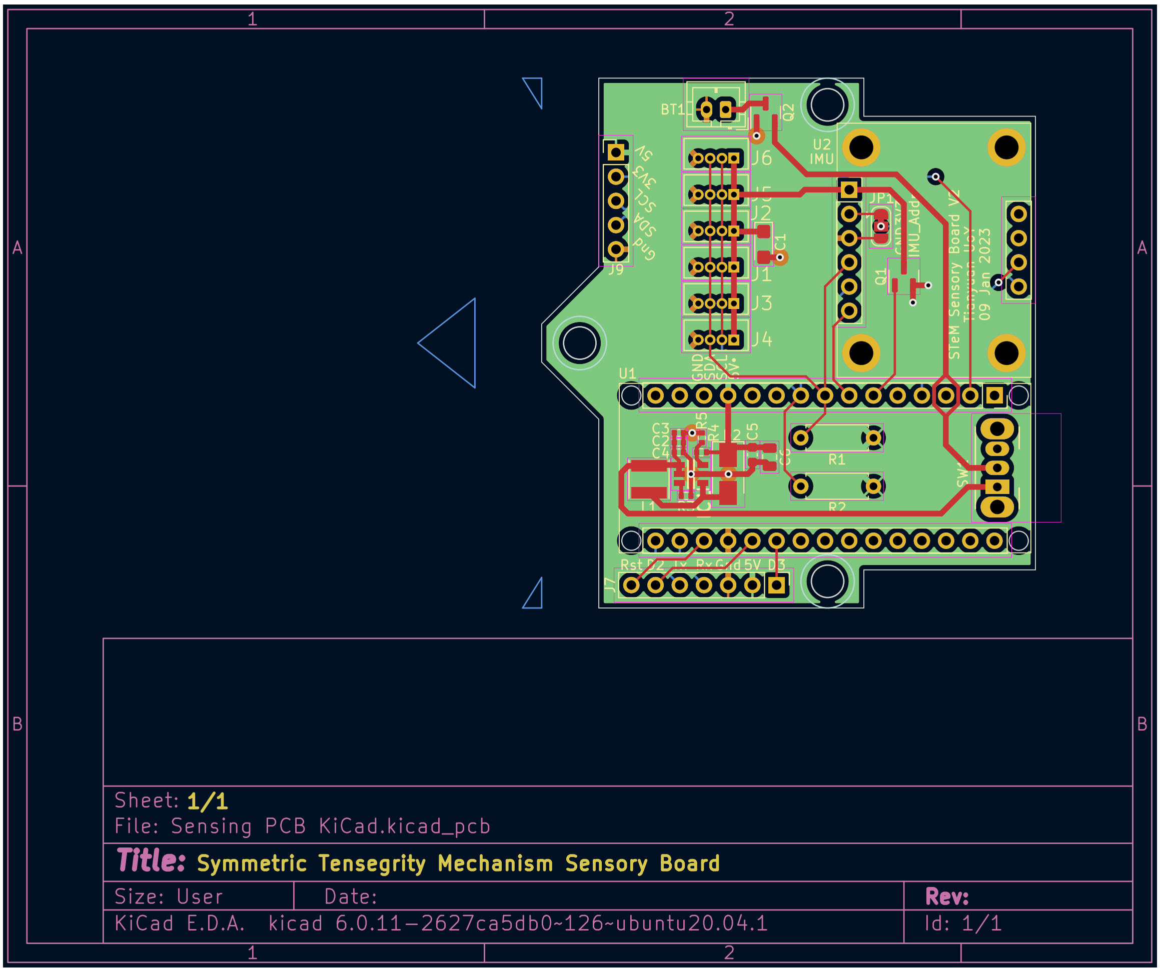

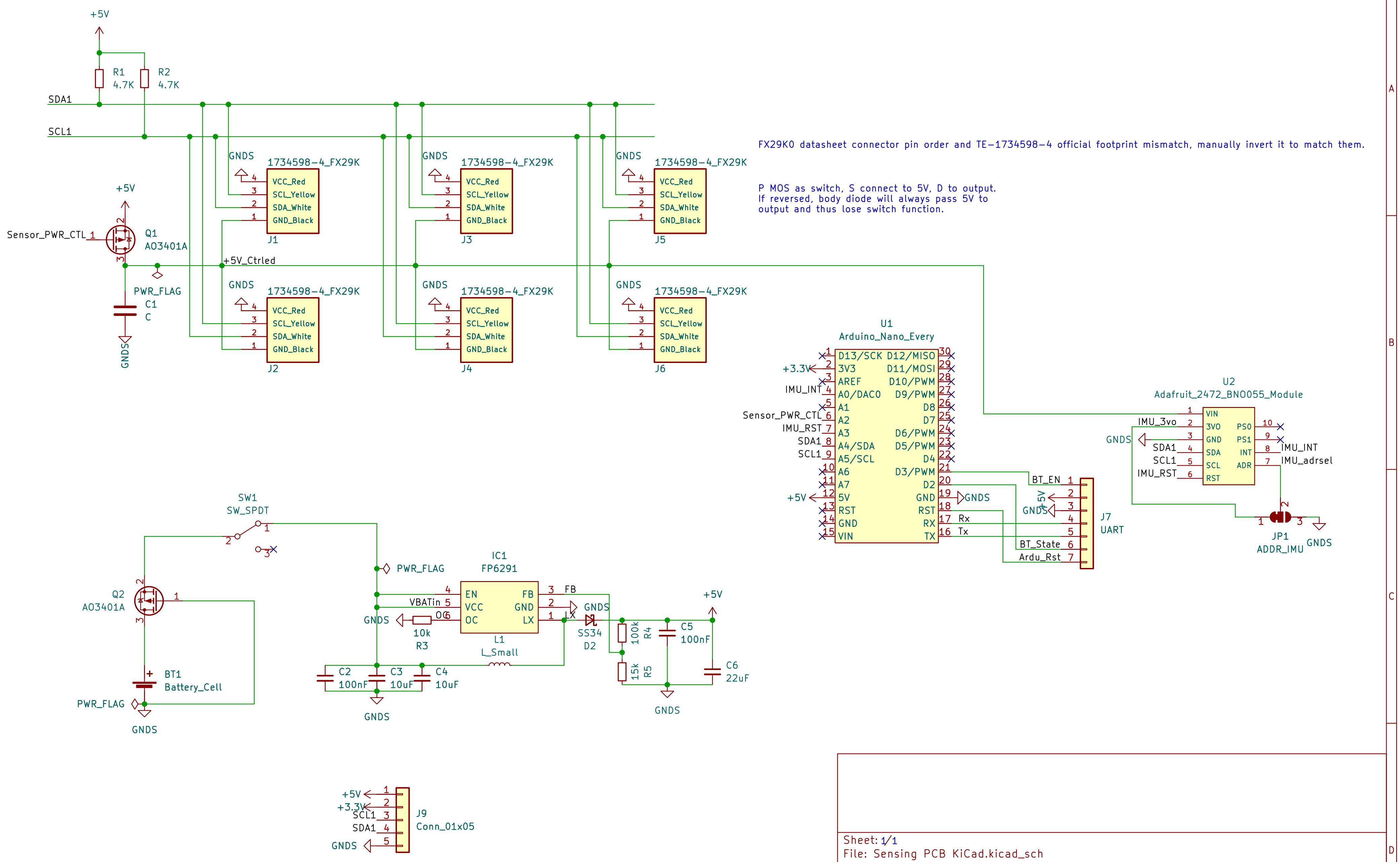

FX29K0 datasheet connector pin order and TE-1734598-4 official footprint mismatch, manually invert it to match them.

P MOS as switch, S connect to 5V, D to output.
If reversed, body diode will always pass 5V to
output and thus lose switch function.

Sheet: 1/1
File: Sensing PCB KiCad.kicad_sch

Title: Symmetric Tensegrity Mechanism Sensory Board

Size: A4 Date: Rev:
KiCad E.D.A. kicad 6.0.11-2627ca5db0~126~ubuntu20.04.1 Id: 1/1

Appendix C

STeM Wheel Tile Design

This appendix contains complementary materials of the STeM's wheel tile design, serving as a possible physical implementation of the wheeled locomotion shown in the simulation in Chapter 5.

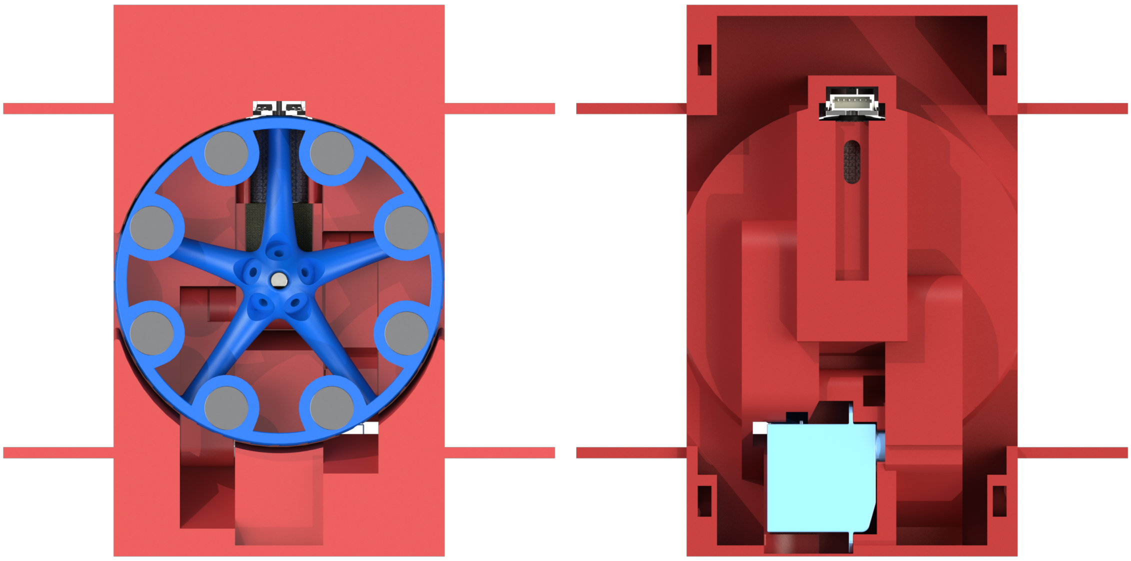

The front and rear view of the tile with the wheel retracted.

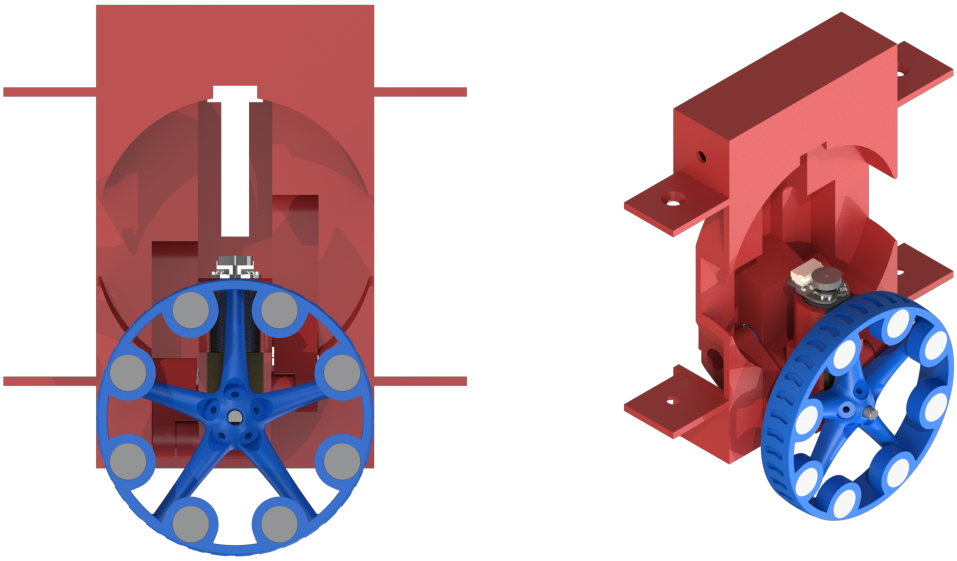

The front and trimetric view of the tile with the wheel deployed.